Gust Rejection in Insect Flight

A Thesis

Submitted for the Degree of

Master of Technology (Research)

in the **Faculty of Engineering**

By

Dipendra Gupta

Department of Mechanical Engineering

INDIAN INSTITUTE OF SCIENCE

BANGALORE – 560012
INDIA

February 2020

Dedicated to

My Maa, Papa

&

My Sisters

Declaration

I hereby declare that the matter embodied in the thesis entitled '**Gust Rejection in Insect Flight**' is the result of investigation carried out by me at the Department of Mechanical Engineering, Indian Institute of Science, Bangalore, India, under the supervision of Prof. Jaywant H. Arakeri and that it has not been submitted elsewhere for the award of any degree or diploma.

In keeping with the general practice in reporting scientific observations, due acknowledgement has been made whenever the work described is based on the findings of other investigators. I am the sole author of this thesis. I authorize Indian Institute of Science to lend this thesis to other institutions or individuals for the purpose of scholarly research.

Dipendra Gupta

Certificate

I hereby certify that the matter embodied in this thesis entitled '**Gust Rejection in Insect Flight**' has be carried out by Mr. Dipendra Gupta at Indian Institute of Science, Bangalore, India, under my supervision and that it has not been submitted elsewhere for the award of any degree or diploma.

Prof. Jaywant H. Arakeri

(Research supervisor)

“Nobody ever figures out what life is all about, and it doesn't matter. Explore the world. Nearly everything is really interesting if you go into it deeply enough.”

Richard P. Feynman

Acknowledgements

First and foremost, I would like to thank the institute – Indian Institute of Science (IISc), Bangalore for providing me an opportunity to carry out research here. The lush greenery and peaceful ambience always helped me focus on the studies and research. The services provided by the late-night cafes, canteens and gymnasium are really commendable. I would rather call them 'The recharge center', for they provide both great place and food required to keep oneself healthy. The time spent here would always be among the most memorable one.

I would like to express my sincere thanks and deep gratitude to my research advisor, Prof. Jaywant H. Arakeri for his constant guidance, motivation, advice, and support during the course of this work. It is difficult to describe him in words. To me, he is a true genius. His curiosity for science, ingenuity, innovative ideas, simple yet powerful insights into the problem, clarity and above all, his humbleness will always be a driving factor for me towards the better me. I will always appreciate the degree of freedom he gave and the trust he put in me during the work.

My heartfelt thanks to Prof. Sanjay P. Sane for allowing me to use the experimental facilities of his lab at NCBS, Bangalore. I really admire his technical suggestions during the work and motivations he gave me during the highs and lows in my personal life. His kind-hearted nature and compassion for others restored my belief in humanity in modern times and filled in me an aspiration to be a person like him. The open-minded culture, friendly and cheerful ambience at his lab further made my stay at NCBS a fruitful and memorable experience.

I would like to thank the Department of Mechanical Engineering, IISc and its faculty and staff members. In particular, I will be always indebted to Prof. Raghuram N. Govardhan for his motivating words – "You can do it" and also, helping me with the nuances of numerical simulation during my early days at IISc. "Enjoy the journey, the result that you are striving for will automatically follow" – said by Prof. M.S. Bobji on my very first day in IISc has always been a guiding path during the lows in research work. My sincere thanks to him. I also thank Prof. Namrata Gundiah for her constant motivation and encouragement during the research period. I would like to extend my thanks to Senior Scientist C. Dharuman for his invaluable suggestions, long technical discussions and also, helping me with the experimental facilities in the lab. I am also thankful to office staffs Mrs. Somavathi, Mrs. Chinnamma, Mrs. Mangala and all other who always helped me with the official formalities and requirements.

I owe my sincere thanks to Dr. Navneet Kumar who directly or indirectly taught me the nuances of experimental research, helped in framing and communicating my research to the general audience in a more concise and interesting way. I also thank Dr. Majid Hassan Khan for deep technical discussion on fluid mechanics and sharing some of his invaluable experiences with

me over tea. Special thanks to Suyog for helping me out in difficult times –in both academic and personal life. I will always be indebted to the generosity he showed towards me during the journey. I would also like to thank my lab mates and colleagues Ashok Balla, Rakshita Joshi, Visakh MG, Debendra Nath Sarkar, Deepan Sharma, Omshree Mahapatra and Parth Khokhani for making my research study pleasant and fruitful.

I had the privilege of having a beneficial association with Dr. Partha, Dr. Nitesh, Dr. Harshada, Umesh, Chinmayee, Simran, Vidur, Aditya and Shipra at NCBS. Special thanks to Maitri for helping me setting up experiments and with the required purchases, Dinesh for helping me with the programming and code, and Agnish and Abin for assisting me in high-speed videography. The experimentation with insects would have been really a difficult task without the help of Allan at NCBS. Thank you, Allan, for being such a wonderful friend.

I would like to thank Vishank (Kattappa), Shubham (Golu), Adhip (Himali), Ajay (Ajju) and Akshay (Chate) for all their support and encouragement from the day we met till now. They taught me the meaning of friendship and made my journey at IISc pleasant and memorable. No matter where we all will be and what we will be doing in coming years, the bonding we shared here will always be with me. You guys rock.

Suppliers, fabricators, and technicians, being an integral part of any experimental investigations, deserve special thanks. In particular, I am thankful to Dr. Sitaram (DESE, IISc) for helping me in developing a circuit diagram for a linear amplifier, Mr. Raja and Mr. Babu at IISc Mechanical workshop for helping me in the fabrication of a speaker box, and Mr. Dorababu (NCBS) for designing PCB for required electronic circuits, and Mr. Ravi (CPDM, IISc) for helping me with laser cutting and machining.

Finally, I thank my parents and my sisters for all the love and support during my studies. I hope this research thesis, to some extent, would justify the sacrifices they have made for me.

ABSTRACT:

Large commercial and military aircraft can fly in turbulent wind conditions except in extreme weather events like cyclones. Smaller man-made vehicles like Micro aerial vehicles (MAVs) and Nano aerial vehicles (NAVs) are more susceptible to normal fluctuations in wind speed encountered in the environment, and thus more difficult to control. Insects, on the other hand, stabilize themselves quickly in the presence of gustiness normally found in the atmosphere. However, very few studies have been carried out to understand the impact of gusts and turbulence on the flight performance of insects.

Keeping this practical relevance in mind and to fundamentally understand the flight stability of insects under gusty environments, we investigated the flight of a freely flying insect (black soldier fly) subjected to a discrete head-on aerodynamic gust under controlled laboratory condition. Gust was generated in the form of a vortex ring which, unlike conventional methods of perturbation, is well studied and highly controllable. The flow properties of the vortex ring were characterized using flow visualization and studying the motion of a light bead. Reynolds number of the vortex ring, based on its average propagation velocity and nozzle exit diameter, was 15000, while that of fly, based on its wingtip velocity and mean wing chord, was 1100. Flight motion of the fly was recorded using two highspeed cameras, and body and wing kinematics were analyzed for cases. In response to the gust, we observed some common features in the cases analyzed: 1) asymmetry in the wing stroke amplitude, 2) large change in the body roll angle, by as much as 160°, that happened on an average, in two wing beats ($\sim 20\ ms$), and with the recovery in about 9 wing beats, 3) change to pitch down attitude, and 4) deceleration in flight direction. The ability to respond at such a short time scale and use of both passive and active control responses to gusts give some insight into the flight control strategies of insects. This study will help in better design of MAVs and NAVs to respond to gusts and unsteadiness in the natural environment.

LIST OF FIGURES

LIST OF TABLES

NOMENCLATURE

a	*acceleration*
b	*wing span*
c	*wing cord length*
$\bar{c}$	*mean chord length*
C_L	*coefficient of lift*
C_{Lt}	*translational lift coefficients*
C_{Dt}	*translational drag coefficients*
C_{rot}	*rotational force coefficients*
$D_f(t)$	*Instantaneous drag*
D_0	*exit internal diameter of nozzle*
D_n	*dimensionless diameter of vortex ring* $= \frac{D}{D_0}$
F	*force*
f	*wing beat frequency*
F_a	*force due to added mass effect*
F_{inst}	*instantaneous force on flapping wing*
F_{rot}	*rotational force*
F_{trans}	*translational force*
F_{wc}	*force due to wing-wake interaction*
I	*moment of inertia*
L_c	*characteristic length*
L	*body length of fly*
L_f	*lift*
$L_f(t)$	*instantaneous Lift*
M	*mass*
T	*torque*
t	*instantaneous time*
R	*wing length, radius* $= \frac{b}{2}$
S	*planform area of wing*
T_n	*dimensionless propagation time of vortex ring* $= \frac{U_{avg}t}{D_0}$
t_1	*rise time of input signal*
t_2	*constant time of input signal+*t_1
t_3	*fall time of input signal+*$t_1 + t_2$
U_n	*dimensionless velocity magnitude of vortex ring* $(= \frac{Ur}{U_{avg}})$ *and fly* $(= \frac{U}{L*f})$
U_t	*wing tip velocity*
X,Y,Z	*global axis coordinates*
x,y,z	*body axis coordinates*
$X_{CoM}, Y_{CoM}, Z_{CoM}$	*postion of centre of mass along X, Y and Z axes respectively*
X_L,Y_L,Z_L	*dimensionless position of center of mass (CoM)* $= \frac{X_{CoM}}{L}, \frac{Y_{CoM}}{L}, \frac{Z_{CoM}}{L}$

X_n	*dimensionless axial distance from nozzle* $= \frac{X}{D_0}$
X_0	*axial distance from nozzle exit where fly gets hit by gust*
U	*forward speed of insect/ flying vehicles*
U_{avg}	*average velocity of vortex ring (gust)*
u_n, v_n, w_n	*dimensionless velocity of fly in X, Y and Z directions respectively*
U_r	*instantaneous Velocity of vortex ring (gust)*
V_{in}	*input voltage*

GREEK SYMBOLS

α	*angle of attack*
α_a	*angular acceleration*
β	*body pitch*
$\dot{\beta}$	*pitch rate*
β_T	*trajectory Pitch*
γ	*body roll*
$\dot{\gamma}$	*roll rate*
μ	*mean*
ν	*Kinematic viscosity of air* $=1.511 \times 10^{-5}$
ω	*angular velocity of wing*
ϕ	*deviation angle*
φ	*body yaw*
$\dot{\varphi}$	*yaw rate*
φ_T	*trajectory Yaw*
ρ	*density of air*
ρ_{bead}	*density of Styrofoam bead*
σ	*standard deviation*
τ	*dimensionless time; number of wing beats* $= t * f$
θ_r	*stroke angle of right wing*
θ_l	*stroke angle of left wing*
θ_o	*stroke amplitude*
$\Delta\theta_o$	*difference in stroke amplitude of right and left wings*

ABBREVIATIONS

AR	*Aspect ratio* $= \frac{b^2}{s}$
Cam	*Camera*
CMOS	*Complementary Metal oxide Semiconductor*
CoM	*Center of Mass*
DAC	*Digital to Analog Converter*
DARPA	*Defence Advanced Research Projects Agency*
DC	*Direct Coupled*
DLT	*Direct Linear Transformation*
FPS	*Frame Per Second*
FRD	*Fly Releasing Duct*
IR	*Infra-Red*
LE	*Leading Edge*
MAVs	*Micro Aerial Vehicles*
NAVs	*Nano Aerial Vehicles*
NI-DAQ	*National Instrument- Data Acquisition System*
PVC	*Polyvinyl Chloride*
ROI	*Region of interest*
Re	*Reynolds Number* $= \frac{UL_c}{\upsilon}$
RMS	*Root Mean Squared*
3-D	*Three Dimensional*
TTL	*Transistor-Transistor Logic*
2-D	*Two Dimensional*
WB	*Wing Beat*

Table of contents

Chapter 1. **Introduction**

1.1 Background

Standing outside on a windy day and watching an insect or a small bird fly makes us curious about their flight ability. Atmospheric winds offer a considerable challenge to any flying organism to maintain its flight trajectory. The upper-speed limit of flight of a living or non-living flying organism is determined, in nature by a combination of mean atmospheric wind speed and inherent gustiness of its environment. A summary of flying speed, indicating wind conditions for different flying animals is shown in Table 1-1 (Tennekes & Pennycuick 1996).

Table 1-1: Cruising speed of various insects, birds and aircraft, Tennekes & Pennycuick (1996)

Airspeed	**Windspeed (m/s)**	**Cruising speed of**
Light air	0.5-1	Butterflies, damselflies
Light breeze	2-3	Gnats, flies, dragonflies
Moderate breeze	6-8	Bees, wasps, beetles
Fresh breeze	9-11	Sparrows, starlings, swallows
Strong breeze	11-13	Crows,
Near gale	14-17	Plovers, knots, godwits
Gale	18-21	Swans, ducks, geese
Strong gale	21-24	Sailplanes
Violent Storm	29-32	Diving Hawks
Hurricane	>32	Diving falcons

Larger commercial and military aircraft can fly in all but the most extreme weather conditions such as cyclones. In contrast, smaller artificial vehicles like Micro aerial vehicles (MAVs) and Nano aerial vehicles (NAVs) are highly susceptible to normal wind speed fluctuations in their environment. They easily lose their control, even leading to complete structural failure and hence the failure of assigned missions. Despite turbulence, unsteadiness, and gustiness in the natural environment, the ability of small insects and birds to rapidly stabilize serve to inspire us to study their flight capabilities.

Understanding the flight control of insects and birds under severe environmental conditions may help us improve the design of MAVs and NAVs to ensure that they autonomously sense the environmental fluctuations and accordingly adjust their body attitude. Despite having such practical relevance, very few studies have been carried out to understand the impact of gusts and turbulence on the flight performance of insects and birds. This is the prime interest of the present study, which investigates the kinematic response of freely flying insects to a discrete gust. Their response time to the gust, change in body attitude and wing kinematics provided clues about the aerodynamic mechanisms of aerial stabilization in insects.

1.2 How do insects fly?

Despite their small size, the fight ability of insects in diverse natural environments has inspired many papers in engineering and biomechanics journals. However, the terminologies in both fields are different and often confusing. Hence, before addressing the aerodynamic mechanisms of insect flight, we must establish the common terminologies and conventions associated with wing morphology and kinematics.

1.2.1 Basic terminology

The key parameters of interest are:

a. ***Leading Edge****: Front margin of the wing.*

b. ***Trailing-Edge****: Hind margin of the wing.*

c. ***Wingspan****: Distance between wingtips when stretched laterally, denoted by* b.

d. ***Wing length****: Distance between wing root and tip in fixed-wing, also called wing radius for a flapping wing. Ignoring thoracic width, it is half of the wingspan and denoted by* $R = b/2$.

e. ***Chord length***: *Distance between leading and trailing edge at any position across wingspan, denoted by* c.

f. ***Aspect ratio***: *Ratio of wingspan to its chord denoted by* $AR = b^2/S$ *where* S *is the planform area of the wing.*

g. ***Stroke plane***: *Plane swept by the line joining wing tip and its base.*

h. ***Forward stroke or downstroke***: *Dorsal to ventral movement of wing. During this phase, wing moves forward and downward in direction of flight.*

i. ***Reverse Stroke or upstroke***: *Ventral to dorsal movement of wing. The wing moves backward and upward in this phase.*

j. ***Supination***: *Rotation of wing at the end of downstroke that brings its ventral surface to face upwards.*

k. ***Pronation***: *Rotation of wing at the end of upstroke that brings its ventral surface to face downwards.*

l. ***Reynolds number***: *Ratio of inertial to viscous force.*

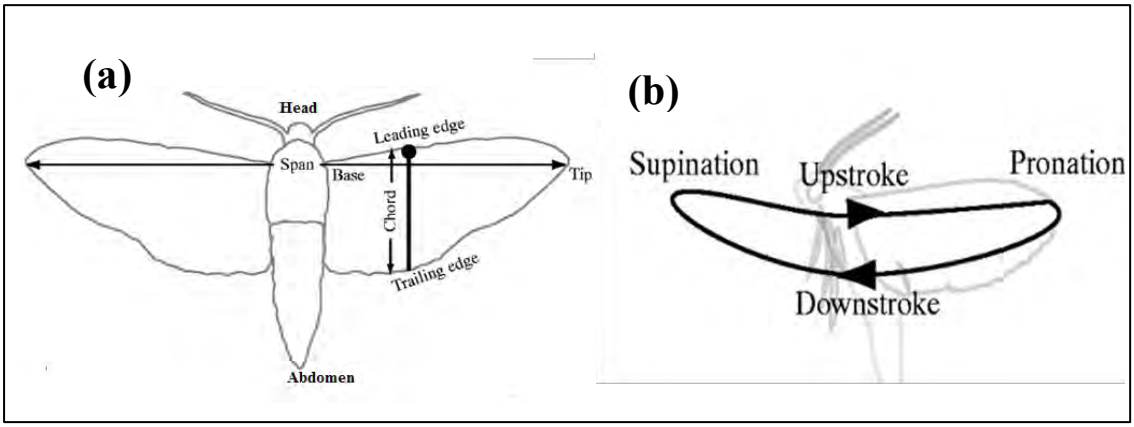

Figure 1-1: Basic terminology of insect morphology and wing motion, reproduced from Sane (2003). (a) Different parts on insect body and its wings. (b) Terms associated with different phases of flapping motion of wing consisting of two translational phase – upstroke and downstroke, and two rotational phase – pronation and supination. During upstroke, the wing moves upward and backward simultaneously before supinating at the end of this phase. Similarly, it pronates at the end of downstroke while simultaneously moving downward and forward.

1.2.2 Kinematic Parameters

A. Pitch

Pitch is defined as the rotation about lateral axis. It can be computed as the angle of elevation of a vector joining head and abdomen of the insect with respect to horizontal plane (see Figure 1-2 (a)).

B. Yaw

Yaw is defined as the rotation about vertical axis. Mathematically, it is calculated as the azimuthal angle on horizontal plane, i.e. angle between global horizontal axis and a vector joining head and abdomen of the insect (see Figure 1-2 (s)).

C. Roll

Roll is defined as the rotation about longitudinal axis. Mathematically, it can be computed as the angle of elevation of a vector joining a wing base to center of mass of body (see Figure 1-2 (a)).

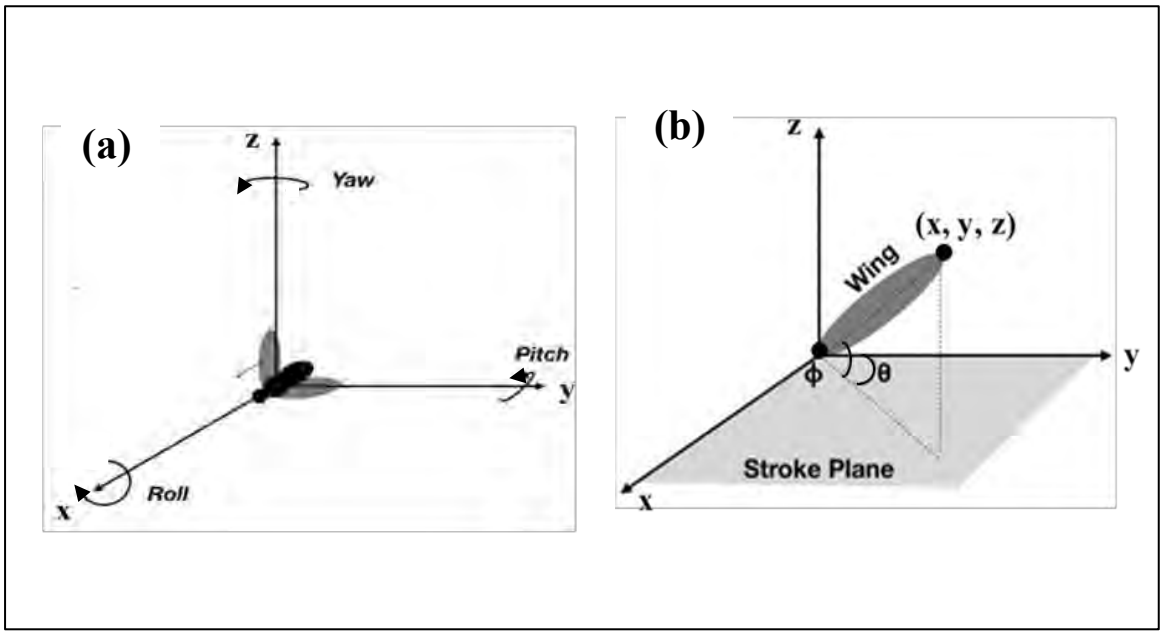

Figure 1-2:. (a) Axis system fixed on body of insect with its center of mass as origin. Roll occurs about body longitudinal axis (i.e. x axis), pitch about lateral y-axis and yaw about vertical z-axis. (c) Kinematic parameters of a wing. Θ represents stroke angle about horizontal stroke plane, Φ is deviation angle

D. Stroke amplitude

Stroke amplitude is the maximum azimuthal angle that a vector joining the wingtip to its base makes in a half cycle on a stroke plane relative to body reference system. The average stroke amplitude of a soldier fly in a normal flight is approximately 110° [see Figure 1-2(b)].

E. Deviation angle

Deviation angle is the elevation angle of a vector joining wing tip and its base to a stroke plane [see Figure 1-2(b)].

F. Angle of attack

Angle of attack is the local angle between the chord line and incident airflow. Wing rotation gives a measure of its angle of attack.

G. Wing beat frequency

Number of wing strokes in one second is called its wingbeat frequency (f). It is given by reciprocal of time period taken by wingtip to traverse from one end of the stroke to another.

1.2.3 Flight Mechanism

1.2.3.1 Biological Mechanism

The flight muscles of an insect can be broadly divided into two types: a small number of larger power muscles and a large number of control or steering muscles (Dickinson & Tu 1997; Hedenström 2014).

Power muscles contract cyclically to move the wings up and down, whereas steering muscles control the transmission of power from power muscles to wings and hence aids in fine control of wing motions. The power muscles may be attached directly (direct flight muscles) or indirectly (indirect flight muscles) to the wing base. The working of these muscles is shown in Figure 1- 3, adapted from (Hill et al. 2012) and briefly explained below.

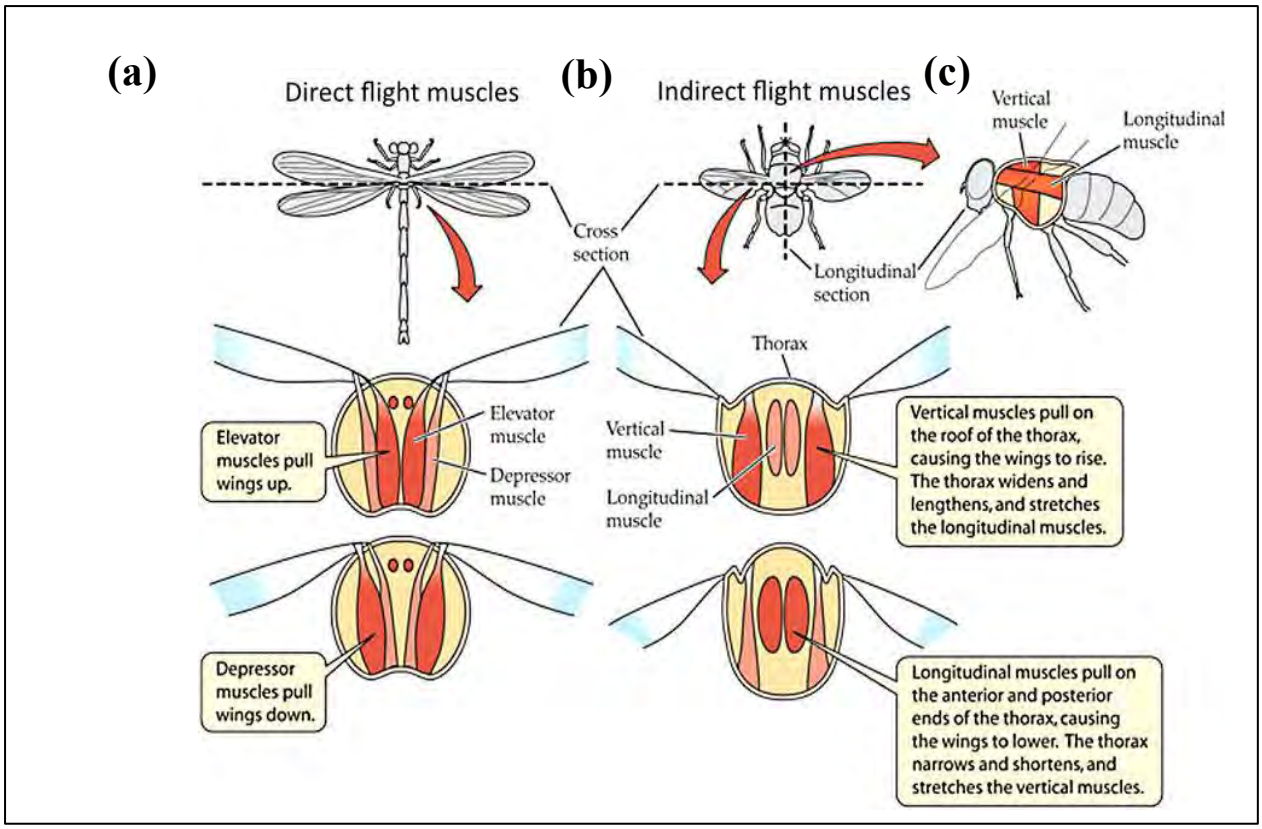

Figure 1- 3: Working of direct and indirect flight muscles. Muscles in contraction are shown in red while relaxed muscles in pink. (a) Mechanism of direct muscles in a dragonfly. Contraction in elevator muscles moves the wings up, while contraction in depressor muscles moves the wing down. (b) Mechanism of indirect muscles in a housefly. Vertical muscles pulls down the roof of the thorax and stretches longitudinal muscles, leading to upward movement of wings. Longitudinal muscles are antagonistic to vertical ones and moves the muscles down. (c) Arrangement of indirect muscles in a thorax of housefly. Vertical muscles run from roof of thorax to its floor while longitudinal muscles from its anterior to posterior end and perpendicular to vertical ones. Figures adapted from (Hill et al. 2012).

A. Direct Flight muscles

Direct muscles are attached to the wing base and directly actuate the wings. Typically, they consist of two sets of muscles that bring the flapping action of wing: elevator muscles attached just inside to wing bases and depressor muscles attached outside the wing bases. Elevator muscles on contraction raise the wing up, while depressor muscles on contraction lower down the wings. The contraction of a set of muscles relaxes the other and vice-versa. These two sets of muscles work in tandem, i.e. alternating contractions to move the wings up and down.

Direct muscles are always synchronous muscles (require nerve impulse for each contraction) and found in primitive group insects like dragonflies (Odonata) and mayflies (Ephemeropteara). Typically, wingbeat frequencies are less than 100 Hz because the muscles require a nerve impulse for each contraction (Smith 1983).

B. Indirect Flight muscles

In insects such as flies and mosquitoes (Diptera), bees and wasps (Hymenoptera), and butterflies and wasps (Lepidoptera) and beetles (Coleoptera), etc, wings are actuated through indirect flight mechanism (Dickinson & Tu 1997; Hill et al. 2012). Here, the flight muscles are not directly connected to the wing bases. Instead, vertical and longitudinal muscles are attached to the thorax wall (see Figure 1- 3b and Figure 1- 3c). Vertical muscles run between the base and roof of the thorax, whereas longitudinal muscles from anterior to posterior end of thorax. These mutually antagonistic pairs of muscles use elastic properties of thorax. On contraction, vertical muscles pull down the roof of thorax and stretch the longitudinal muscles, thereby raising the wings while longitudinal muscles on contraction bulge up the roof of the thorax and stretch the vertical muscles leading to movement of the wings in downward direction. The alternate contraction and lengthening of these perpendicular muscles depend on resonant mechanical properties of thorax and wings and these properties determine the wingbeat frequency (Hedenström 2014; Hill et al. 2012).

Indirect muscles are typically asynchronous (individual muscle contractions are not synchronized with individual nerve impulses, i.e. a single nerve impulse can initiate many contractions). The operating frequency for asynchronous muscles can range from 20 Hz in large belostomid bugs (Barber & Pringle 1966) to more than 1000 Hz in small midges (Sotavalta 1953). Asynchronous muscles are proposed to be more powerful and efficient than synchronous ones (Syme & Josephson 2002).

1.2.3.2 Aerodynamic Mechanisms

When an insect moves its wings through air, forces are produced both in direction of motion of wing and perpendicular to that motion. The force perpendicular to the motion of wing is called lift and that opposite to the direction of motion of wing is called drag. Reynolds number (Re), for insect, can range from $10 - 10^4$ (Wang 2005). The flapping of a wing is usually analyzed by treating the wing as a flat plate. Depending on the phases during wing strokes, the aerodynamic mechanisms are sub-divided into six mechanisms: added mass, leading-edge vortex and absence of delayed stall, Kramer's effect (rotational circulation), clap and fling, and wing-wake interactions and Wagner effect (Sane 2003), which are briefly explained below and presented in Figure 1-4, adapted from (Sane 2003; Chin & Lentink 2016).

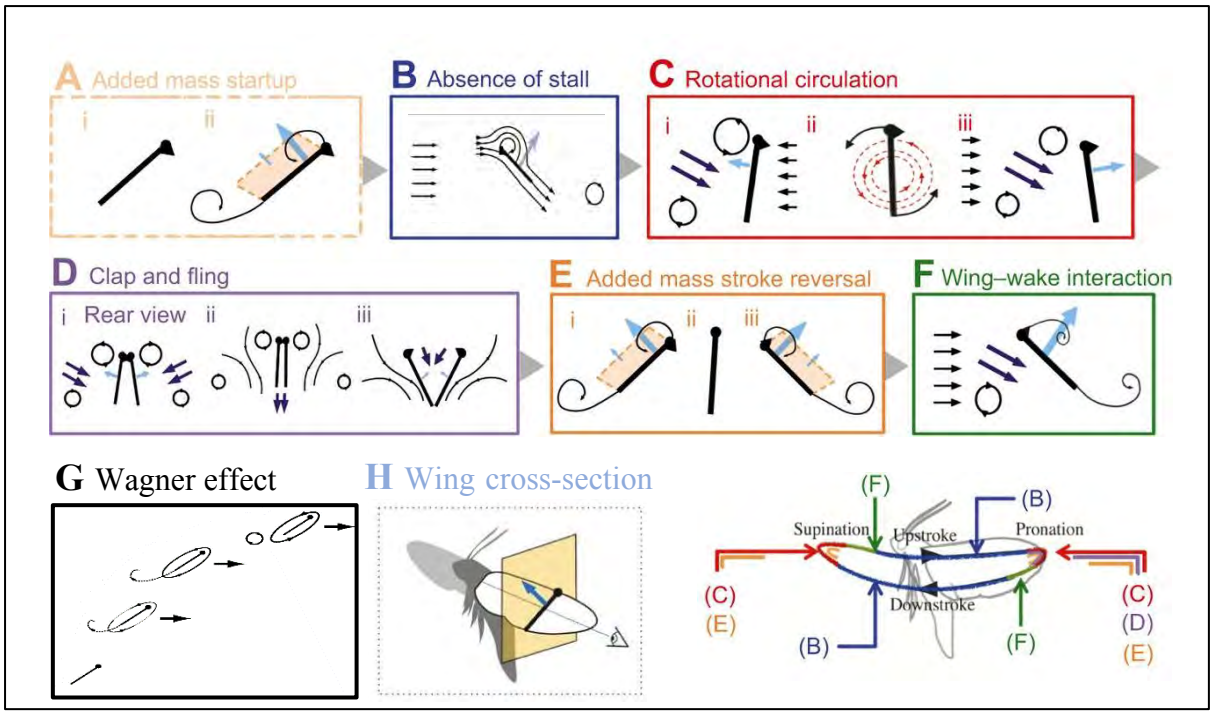

Figure 1-4: Different aerodynamic mechanism of flapping motion of insect wings. (A) Added mass (shown in orange box) on wing accelerating from rest. (B) Formation of leading edge vortex during mid-upstroke and mid downstroke resulting in prevention of stall. (C) Development of rotational circulation (red dashed arrows) during rotational phase. (i) shows wing before (ii) during and (iii) after rotation. (D) Clap and Fling phenomena found in some insects. (i) Leading edge approaching each other during clap (ii) End of clap leading to cancellation of opposite circulation on each wing and also a flush of jet of fluid enhancing thrust (iii) On onset of fling, leading edges move apart and surrounding fluid rushes in. (E) Added mass due to (i) deceleration during (ii) rotation and (iii) acceleration during translation. (F) Wing may interact with wake generated during previous stroke. (G) Wagner effect: Trailing vortices delay the growth of circulation around wings. (H) Cross section of wing, as represented in all figures by a chord line, when viewed along spanwise direction. Mechanisms (B) to (F) are repeated as wingbeats continue. Lowermost right diagram shows relative timings of each mechanisms. Black arrows indicate airflow, dark blue induced velocity and light blue net forces. Upper left diagram shows Black triangle indicates top surface of leading edge of wing. Figures adapted from (Sane 2003; Chin & Lentink 2016).

A. Added mass

When a wing moves from rest, the fluid attached to the wing gets accelerated and, in turn, imparts a reaction force on the wing (see Figure 1-4A). This reactive non-circulatory force is called added mass inertia (Sane 2003; Sane & Dickinson 2001). Added mass effect can be experienced on deceleration of wing during pronation and supination, and acceleration during translation phase, resulting in a pressure force on the wing.

B. Leading Edge Vortex and absence of stall

When the wings translate at high angles of attack, flow separates at the sharp leading edge. The separated boundary layer (a sheet of concentrated vorticity) rolls up to form a stable leading-edge vortex (LEV) on the top surface of each wing during mid-upstroke and mid-downstroke (see Figure 1-4B) (Dickinson et al. 1999; Ellington et al. 1996; Bomphrey et al. 2006; Lentink

& Dickinson 2009). The flow, however, reattaches to the wings after LEV, imparting a greater downward momentum to the fluid, and thereby substantially augmenting the lift (Sane 2003; Dickinson et al. 1999; Ellington et al. 1996). The reattachment allows the fluid to flow smoothly from the trailing edge of the wing and, hence, establishes the Kutta condition.

The LEV remains stably attached to the wing due to a steady spanwise flow from wing base to approximately three-quarters of distance to wingtips, at which point LEV detaches from wing surface (Ellington et al. 1996; Maxworthy 2007). In other words, spanwise flow reduces the momentum of flow along chordwise direction, causing LEV to remain smaller. A smaller LEV allows flow reattachment more easily, thereby preventing the wing from stalling, in stark contrast to LEV formed in fixed-wing that grows with angle of attack until it gets separated and shed as trailing vortex (Sane 2003). Consequently, insects can generate large lift forces and fly at a high angle of attack. LEV also extends continuously from wingtip to tip and across thorax (Bomphrey et al. 2006; Fuchiwaki et al. 2013) or may not be connected across thorax (Bomphrey et al. 2010). LEV pair in the latter case is less efficient than the former one (Bomphrey et al. 2010).

C. Rotational circulation or Kramer's effect

During rotational phase of flapping, the wing undergoes pronation and supination about spanwise direction. During rotation, flow around the wing deviates and stagnation point moves away from trailing edge resulting in a deviation from Kutta condition (Sane 2003). To ensure that Kutta condition is re-established around trailing edge, circulation is generated in surrounding fluid. The circulation thus generated in response to wing rotation is called as rotational circulation (see Figure 1-4C) or Kramer's effect, the magnitude of which depends on angular velocity of the rotation. The circulation leads to instantaneous peak in aerodynamic forces during translation, their enhancement or attenuation being subject to the timing and direction of rotation relative to each stroke (Sane 2003; Sane & Dickinson 2002).

D. Clap and fling

Clap and fling mechanism, also called as clap and peel, Weis-Fogh effect, comprises two distinct aerodynamic mechanisms occurring during pronation of wing (Weis-Fogh 1973). During clap, the leading edges of each wing touch each other, cancel the opposing circulations around each wing, leading to no or at most low strength trailing vortices being shed as stopping vortices. Absence of or low strength trailing vortices enhances the rate of formation of bound circulation around wing (see 0, Wagner effect), resulting in an extension of period of lift generation for downstroke (Lehmann 2004). Further, a jet of fluid is flushed out when the wings clap, enhancing thrust (Ellington et al. 1996).

During fling, leading edge of each wing moves apart, creating low-pressure region between them. This results in flow of air into the region, aiding build-up of bound circulation (Sane 2003; Lehmann 2004). The wings then, with opposite circulations, translate away from each other, each generating lift. Clap and fling is not observed in all insects, and it has been argued that the clap and fling may be the outcome of insects trying to maximize their stroke amplitude to augment flight forces (Sane 2003).

E. Wing-wake interactions

During stroke reversal, the wings interact with vortices shed during the previous stroke (see Figure 1-4F). As the wing reverses its stroke, leading and trailing edge vortices are shed in the flow giving rise to a region of wake. These vortices induce strong inter-vortex velocity field. After stroke reversal, the wing encounters these induced velocity fields thereby enhancing aerodynamic forces.

F. Wagner effect

An impulsive movement of an inclined wing leads to a generation of starting vortex due to roll-up of trailing vortices shed downstream in the flow (see Figure 1-4G). Unless it gains steady-state size, the starting vortex counteracts the growth of bound circulation around the wing. This delay in development of circulation around wing is called Wagner effect. Wagner effect attenuates the aerodynamic forces on start-up of wing motion. Experiments on 2D translation (Dickinson & Gotz 1993) and 3D flapping translation (Dickinson et al. 1999) of wings has indeed shown very little evidence of Wagner effect over range of Re insects fly.

Each unsteady effect explained above has some aerodynamic force associated with it. The total aerodynamic force generated at any instant during the starting wing stroke can thus be given as the sum of the force generated during each effect. Ignoring the frictional drag and Wagner effect, the force at any other stroke can then be given using the equation below (Sane & Dickinson 2002).

$$F_{inst} = F_a + F_{trans} + F_{rot} + F_{wc} \quad (1)$$

Where F_{inst} is the total instantaneous force generated on a flapping wing, F_a is the force due to added mass, F_{trans} is translational force, F_{rot} is rotational force (generated during pronation and supination), and F_{wc} is the force that is generated due to interaction of wing with wakes of previous strokes.

Quasi-steady assumption, according to which the instantaneous aerodynamic forces generated on a flapping wing are equal to those during steady motion at the same instantaneous velocity and angle of attack (Ellington 1984) has been followed since (Osborne 1951) to analytically predict this instantaneous force total. However, the earlier quasi-steady model has been found

insufficient to predict the mean force measured in experiments. To account for this deficiency, (Sane & Dickinson 2002) revised the quasi-steady model which, in addition to translational force components, accounts for rotational force generated during a wing stroke. Based on this revised model, lift and drag generated during wing translation can be estimated using the following relation:

$$L_f(t) = \frac{1}{2}\,\rho U_t^2 S \hat{r}_2^2(S) C_{Lt}^2(\alpha) \tag{2}$$

$$D_f(t) = \frac{1}{2}\,\rho U_t^2 S \hat{r}_2^2(S) C_{Dt}^2(\alpha) \tag{3}$$

Where $L(t)$ and $D(t)$ are instantaneous lift and drag , ρ is density of air, U_t is wing tip velocity, S is wing wet area, $\hat{r}_2^2(S)$ is non-dimensional second moment of area, α is instantaneous angle of attack, and C_{Lt} and C_{Dt} translational lift and drag coefficients respectively. The net aerodynamic force can be found using vector addition of these orthogonal forces.

Similarly, the rotational force component can be predicted as below.

$$F_{rot} = C_{rot}\rho U_t \omega \bar{c}^2 R \int \hat{r}\hat{c}^2(\hat{r}) d\hat{r} \tag{4}$$

Where F_{rot} is instantaneous rotational force, ω is angular velocity of wing, $\hat{r}$ is non-dimensional radial pitch along the wing, $\bar{c}$ is mean chord length, $\hat{c}(\hat{r})$ is non-dimensional chord length R is wing length and C_{rot} is rotational force coefficient.

Even though this model does not account for unsteady effects like wing-wake interaction, Wagner effect and added mass effect, and it is based on inviscid flow conditions, the predicted force values closely agree with experimental values. The model thus provides us considerable mathematical simplicity at a relatively low cost in accuracy (Sane & Dickinson 2002).

1.3 How do insects control their flight during airborne?

Insects control their body attitude by manipulating wing kinematics like stroke amplitude, angle of attack, deviation angle, and also in some cases, by changing their posture by elevating abdomen and hindlegs (Taylor 2001). They shift their center of pressure relative to center of mass to control pitch by moving their wing more dorsally forward or backward (Dickinson & Muijres 2016; Ristroph et al. 2013). To bring any roll stability, they modulate stroke amplitude, wing rotation (and hence angle of attack) and wing path during supination of a wing relative to the other such that a differential lift is generated and roll is brought in intended direction (Dickinson & Muijres 2016; Beatus et al. 2015). Similarly, they differentially change angle of attack to drive yaw maneuvers (Ristroph et al. 2010). Each wing has different projected area

due to difference in angle of attack, leading to different drag force on each wing. The differential drag force leads to yaw.

To mediate such fine control of these wing kinematics, most insects, especially *Diptera* (Flies, wasps, beetles etc.) have about 18 pairs of control or steering muscles (Dickinson & Tu 1997). Insects flapping their wing at more than 100 Hz. must have maximum latency of response less than 10ms. Such insects cannot rely merely on visual feedback, the response latency in which case is greater than 10 ms (Sherman & Dickinson 2003). Instead, such insects may rely on mechanosensory feedback from antenna (Sant & Sane 2018; Sane et al. 2007) or sensory fields on wings (Dickerson et al. 2014; Pratt et al. 2017) which have faster response latency (Sherman & Dickinson 2003). Dipterans have a pair of halteres that act as mechanosensors. Halteres are a modification of hind wings that oscillate anti-phase to wings and act as gyroscope to sense any Coriolis forces due to any rotation of body (Pringle 1948; Deora et al. 2015; Deora et al. 2017).

1.4 How do insects maintain their flight in gusty and turbulent environment?

The aerodynamics of flying insect has been characterized by studying the flow field over wings of tethered and free-flying insect, and also by direct force measurements on dynamically-scaled robotic wing model of insect wings (Dickinson et al. 1999). Most studies were carried out in still air or in laminar airflow in wind tunnels. However, a majority of the insects fly in lower parts of atmosphere, where the wind conditions are highly unsteady. The properties of wind are dictated by pressure differences due to meteorological phenomena, Coriolis forces arising from the rotation of earth, and the local terrain (Watkins et al. 2008; Stull 2012). Wind speeds can vary from 0 to 10 m/s, except under extreme conditions (Watkins et al. 2010; Stull 2012). Moreover, turbulent convective flow is dominant in the lower part of the atmosphere and can affect the flight of insects. Thus, under natural conditions, air is full of turbulence in lower parts of the atmosphere.

Wind turbulence in the environment comprises of discrete gusts and random continuous turbulence (Etkin 1981). Discrete gusts refer to a sudden and sharp change in wind speed, as encountered in the wakes of large objects or at edge of convective disturbances. The latter can be referred as a chaotic motion of atmospheric wind and is usually described using statistical approach in terms of stationarity, isotropy, homogeneity, time and length scales, correlations and spectra. Such complex environmental airflows present severe flight challenges to insects. As such, the effect of turbulence and gust on the flight performance of insects has received very little attention in the literature.

Combes & Dudley (2009) first reported the impact of turbulence instabilities on the flight performance of wild orchid bees. They found that bees were most susceptible to turbulence

about their roll axis perhaps due to the lowest moment of inertia about that axis. They actively responded to this destabilization by ventrally extending their hind legs in response to turbulence instabilities at moderate and high wind speeds. Although the hind legs weigh about 6% of total body mass, their extension increases the moment of inertia by more than 50%. It also increases aerodynamic drag on the body. They concluded that extending hind legs, despite increasing energy cost, is a mechanism that bees employ to mitigate roll instabilities. They also found that turbulence limits the maximum speed of the bees beyond which they crashed and ceased flying.

Ravi et al. (2013) investigated the impact of flight in the von Karman wake on control responses of bumblebees. A von Karman street was generated in wind tunnel using cylinder (diameter =25mm~ b, b being wingspan), both in vertical and horizontal orientations at mean speed of 2.55 m/s, such that vortex shedding occurred at 23 Hz. Such disturbances can also be considered as a form of periodic gusts. This study confirmed the finding of Combes & Dudley (2009) that bees are most sensitive to disturbances along roll axis and that forward flight speeds of bees were reduced in presence of gusts. They also noted that some abdominal deflection may contribute towards pitch stability. However, they did not observe any leg extension in this case, as was noted by Combes & Dudley (2009) in orchid bees. They further stated that bees made use of roll axis for any lateral maneuvers or correction, based on a strong positive correlation found between roll angle and lateral acceleration (i.e. rolling of bees in any direction also causes it to accelerate in the same direction) and lack of such correlation between yaw and lateral acceleration. Also, pitch was lower compared to roll in all flow cases, suggesting that bees were passively more stable to disturbances along pitch axis.

These findings are in contrast to those reported by Ortega-Jimenez et al. (2013) who carried out similar experiments on hawkmoth in von Karman Vortex behind vertical cylinder and observed yaw and roll oscillation both synchronized with vortex shedding frequencies (2-8 Hz), but maximum fluctuations in yaw than in roll. These differences may be due to differences in experimental conditions; whereas bees were actively flying upstream (Ravi et al.(2013), hawkmoths were in stationary position at a flower in oncoming flow (Ortega-Jimenez et al. (2013). Further, the differences can also be attributed to different body and wing morphology, flapping frequency and wing loading. Consistent with the finding of Combes & Dudley (2009) in orchid bees, hawkmoths also extended their fore-legs when flying in the wake of cylinder at 2 m/s, and their response in unsteady flow shifted more towards steady flow as the hawkmoths are moved further apart from cylinder, possibly due to decay of vortices with downstream distance. They found a 10% increase in wingbeat frequency in presence of von Karman vortex street. Similarly, (Ortega-Jimenez et al. 2014) found that hawkmoths modulated angle of attack, stroke amplitude and body pitch to maintain control in tornado-like vortical flow. Unlike their earlier study, they did not notice any change in flapping frequency of hawkmoth.

Ravi et al. (2016) experimentally and numerically, studied the flight motion of bumblebees in presence of von Karman Vortices behind a vertical cylinder only. They observed casting motion (flight trajectory with large amplitude low-frequency lateral motion combined with roll) in both steady and unsteady flow, indicating strong positive correlation of roll angle and lateral acceleration, as noted in earlier study, thus provide support for helicopter model in case of low-frequency casting motion. In the helicopter model, direction of motion can be altered if insects orient their body attitude accordingly, keeping the net aerodynamic force vector unaltered relative to the body. Thus, insects change their body pitch for longitudinal acceleration or deceleration, and their body roll for any change in lateral direction. The presence of low-frequency casting motion in steady flow indicates that these motions were mostly voluntary. However, high-frequency motion was also observed, but only at cylinder's vortex shedding frequency. Their numerical simulation showed that the motion was caused by passive interaction of vortices in von Karman effect. Because von Karman effect induced this high frequency periodic lateral disturbance on bee flight, like a sailboat under periodic lateral wind, they proposed an "idealized sailboat model" to explain this passive behavior.

Crall et al. (2017) studied the flight performance of a bumblebee both in both open turbulent field and a controlled turbulent environment in wind tunnel (turbulent intensity 15% and integral length scale 4cm~ 2b, b being wingspan). Bumblebees showed a small but statistically significant increase in wingbeat frequency in turbulence (similar to (Ortega-Jimenez et al. 2013)), indicating that a decrease in time between wing strokes may reduce the delay in updating control input to wing kinematics, an important factor in flight control. Bees also increased mean stroke amplitude in turbulence at higher speed and employ stroke amplitude asymmetry to control body orientation. When modulating wing stroke amplitude, bees mainly adjusted the angle of supination than pronation.

Numerical studies have also explored the impact of turbulent intensity and length scales on the generation of flight forces in tethered and free-flying bumblebees at timescales relevant for passive mechanism of control (Engels et al. 2016; Engels et al. 2019). Despite introducing highly intense turbulent flow, the study revealed no change in mean aerodynamic force, moment and power for tethered flight. Bees were found to be least stable about roll axis in this study as well (Engels et al. 2016). Aerodynamic fluctuations (at constant integral length) were, found to increase with turbulent intensity and decrease when integral length scales (at constant turbulent intensity) were smaller than wing length in case of both tethered and free flight (Engels et al. 2019). In the free flight case, (Engels et al. 2019) reported that smaller integral scales resulted in much smaller angular velocities and variations in orientation, while an increase in turbulent intensity increased angular velocities in bees, and also, translational motion of insect was much smaller than its rotational one.

Although turbulence and structured vortex trails are important on broader scale, isolated discrete gusts could be critical parameters of unsteady aerodynamic conditions at smaller scales and hence particularly relevant to insects. Vance et al. (2013) studied the impact of discrete gusts, (i.e. jet of high-speed air at ~5m/s) on kinematic strategies employed by honeybees and stalk-eye flies. They observed high roll rates in both insects. Stalk-eyed flies significantly changed in yaw angle as well. Both insects employed differential stroke amplitude to recover roll. Flies displayed differential change in average angle of attack and mean stroke position to regain stability. They noted that bees used ocellar pathways to actively respond to perturbations in 3-6 wing beats, while flies took 2-3 wing beats to generate any active response to the gusts.

In their study on the effects of gusts on flight trajectories of bumblebees, Jakobi et al. (2018). generated gusts in form a thin, high-velocity air sheet (~5 m/s) and directed it from three different directions (lateral, vertically upward and downward) on a free-flying bee. Irrespective of the gust direction, bees always pitched up and slowed down upon encountering gusts, indicating an active response. Downward gusts were most challenging for bees, whereas upward gusts were easier one to compensate. Bees overcame disturbances in lateral directions in a more robust way, although lateral gusts produced disturbance similar in magnitude to downward gusts. In the case of lateral gusts, bees extended their legs (Combes & Dudley 2009; Ortega-Jimenez et al. 2013).

Ristroph et al. (2010) harnessed the magnetic effects of a pair of Helmholtz coil as a gust. They attached a magnet on the dorsal thorax of free-flying fruit flies along its longitudinal axis and flew them across a pair of a horizontally directed Helmholtz coil. The coil was optically triggered for a period of 1 wing beat when fly is in region of interest (center of the coil). This generated a torque on the magnet and hence the body of flies. With this experimental setup, authors found that fruit flies actively responded to any yaw deviations by differentially varying angle of attack within 3 wing beats and gained complete recovery by 15 wing beats. They also formed a mechanical feed-back control loop based on proportional and derivative scheme (P-D controller) to explain recovery strategy. Feeding experimentally observed yaw rate and response time (delay time) into a model, they showed the inability of halteres to detect high body rotation rate.

Using a similar experimental setup, Ristroph et al. (2013) studied the pitch stability of fruit flies. The only difference in this study was vertical orientation of Helmholtz coil. Flies actively controlled any change in their pitch angle. The response time, in this case, was 2-3 wing beats and the recovery time was similar to that observed while correcting for any yaw deviations. They further disabled halteres in flies and observed that flies could not fly and fell straight down. However, the haltere-disabled flies followed directed path when fibers were attached at their abdomen, indicating that passive pitch stability could be restored by increasing pitch damping.

Beatus et al. (2015) used a similar setup as (Ristroph et al. 2010) to investigate the impact of gusts on roll stability of fruit flies. In this case, flies employed differential stroke amplitude asymmetry to maintain control about roll axis and extended their legs to counteract roll perturbations. Flies actively responded within 1 wing beat and completely recovered from roll disturbances within 8 wing beats. This experiment, in conjunction with earlier experiments (Ristroph et al. 2010; Ristroph et al. 2013) showed that roll responses in fruit flies were 3.5 times faster than its yaw response, 2.5 times pitch response, and 5 times visual response.

1.5 Present work: Motivation and Research question

Recent advancements in the field of miniaturization technology have brought a significant interest in the design of MAVs and their employability for civil and strategic applications. These vehicles are characterized by their small size and dimension. According to Defence Advanced Research Projects Agency (DARPA), the dimension of such vehicles should not exceed 15cm, they should be portable, their weight should be less than 65 g and they should fly at an altitude of less than 500m at a velocity around 10 m/s for at least 20-40 minutes (Schnepf 2000). They operate in aerodynamic regime of low Re (~10^5) (Roadman & Mohseni 2009). The range of their applications includes surveillance, search and rescue missions, exploration of remote landscapes, traffic monitoring, or pollution level detection. These applications can be extended considerably to their use as smart weapon, chemical and biological sensor for soldiers, electronics disabling of adversary radars, etc.

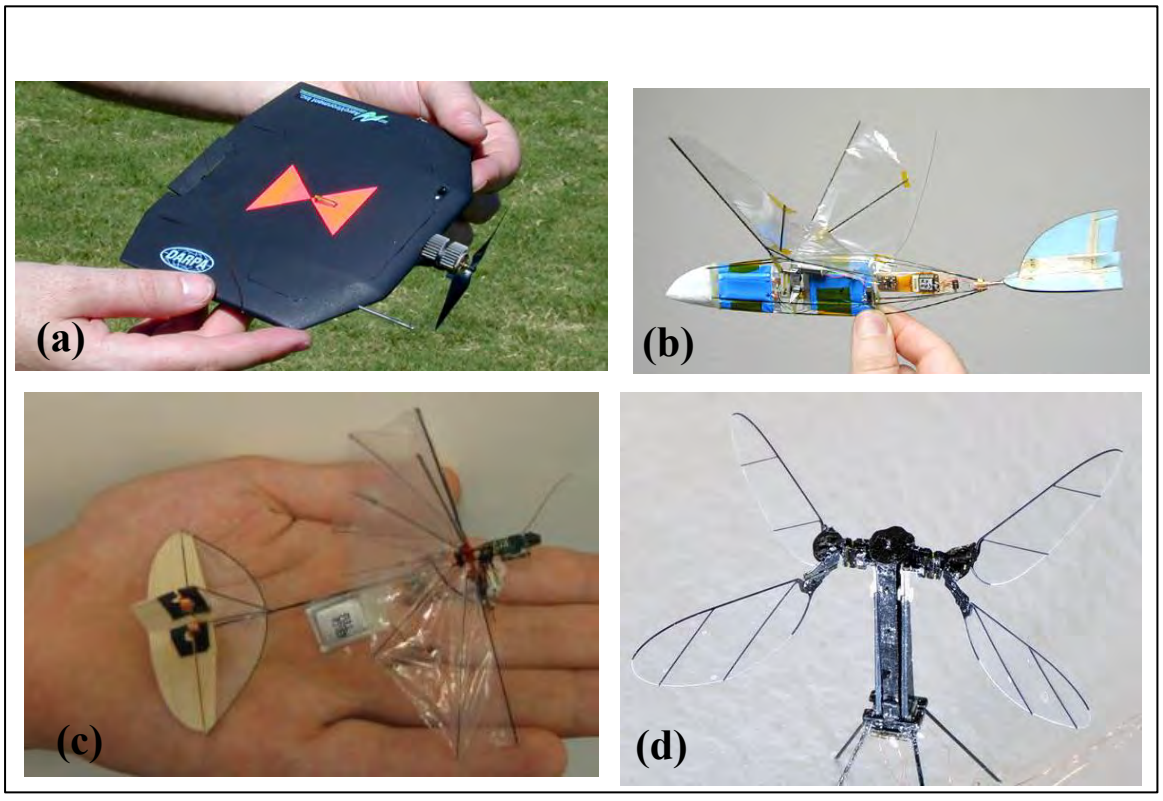

Figure 1-5: Some MAVs as per DARPA specifications. (a) is an image of black widow with 15 cm wingspan(Grasmeyer et al. 2001), (b) Microbat, a flapping MAV with 8 in. wingspan and 11.5 gm weight(Pornsin-Sirirak et al. 2001), (c) Delfly Micro, with wing span 10 cm, (d) Robo Bee, 4-wings MAV weighing 90mg (Jafferis et al. 2019).

Their smaller size is advantageous in several military applications as covertness and portability. At the same time, the small size brings with it, problems like accommodation of airframe weight, propulsion system weight, endurance, and reliability, restart capability, flight control system and communication systems together. Development in the area of miniaturization and

electronics has solved the problem of weight and lower power consumption to some extent. However, we still lack the fundamental understanding of aerodynamics and control at the range of Re and how to best design these vehicles at this scale.

Further, MAVs are developed to operate in the lower part of the earth's atmosphere (100-1000m above ground surface) (Watkins et al. 2010; Loxton 2011; Watkins et al. 2006; Deshpande et al. 2014) and generally in where direct line of sight is not possible. Such areas include hillsides, canyons, city, around street corners, residential areas, catastrophe affected areas, etc. It is thus clear that the region and environment in which these vehicles operate is very complex, and wakes of local obstructions like houses, grasslands, trees, towers, etc are significant. Their flight is consequently affected by turbulence in the environment.

Turbulent structures on a scale comparable to the size of MAVs significantly affect their body orientation (pitch, yaw, and especially roll) and flight trajectory**.** If l is the characteristic length of an MAV, tumbling forces (F) scale as l_c^2 (i.e. Force $\propto$ wing area) and the resulting torques (T) scale as Fx $l_c \propto l_c^3$, but moment of inertia $I = mass$ x $l^2 = density$ x $volume$ x $l_c^2 \propto l_c^5$. Thus, that decrease in size of the vehicle decreases its resistance to any change by 5^{th} power and consequently increases its tendency to tumble by same. This analysis holds for fixed-wing MAVs. It ignores counter-torque due to flapping wings.

A. Effect of change of wind speed on body orientation of MAVs

Let us illustrate it with a simple analysis (Klipp & Measure 2011)**.** Consider an MAV with mass 'm', wing span 'b', and acceleration 'a'.

$$Force, F = ma$$

$$Torque, T \sim mab$$

$$Moment\ of\ inertia, I \sim mb^2$$

$$Angular\ acceleration, \alpha_a = T/I$$

$$\sim (mab)\ /\ (mb^2)$$

$$= a/b$$

It can be seen that angular acceleration is inversely proportional to the characteristics length of the vehicle.

$For\ b = 10\ cm\ and\ a = 9.8\ m/s^2,$

$$\alpha_a = 98\ radians/s^2$$

Using basic equation of motion, $\gamma_{roll} = 1/2\alpha_a t^2$

For t= 0.1 s, $\gamma_{roll} = 28°$

This implies that if the resulting torque due to turbulence in environment is not compensated for 0.1 s, it can lead to a roll of 28°.

It can also be shown, using basic equations of motion, that an acceleration of 1G in vertical direction if remain uncomponsated for 0.1 s can result in loss of altitude by 4.9 cm. This displacement becomes 4.9 m if the acceleration is uncomponsated for 1 second.

B. Effect of change of wind speed on lift of MAVs

Similarly, turbulence variations in wind speed and direction can also lead to change in lift force (Klipp & Measure 2011)**.**

The basic equation of aerodynamic lift is

$$L_f = \frac{1}{2}\rho U^2 S C_L \quad (5)$$

Where L_f is lift, ρ is density of air, U is forward speed, S is planform area of wing and C_L is coefficient of lift.

For thin airfoil, at smaller angle of attack(α), $C_L = 2\pi\alpha$ (6)

Any fluctuation in wind speed appears as fluctuation in forward speed and angle of attack of the airfoil. The consequent change in lift can be expressed as follow:

$$dL_f = \frac{1}{2}\rho U^2 S \left[\frac{\partial C_L}{\partial \alpha}\right] d\alpha + C_L \rho S U dU \quad (7)$$

Where dU indicates change in forward speed and $d\alpha$ is the change in angle of attack of airfoil.

Using (5) and (7), $$\frac{dL_f}{L_f} = \frac{1}{C_L}\left[\frac{\partial C_L}{\partial \alpha}\right] d\alpha + \frac{2UdU}{U^2} \quad (8)$$

Using thin airfoil approximation for small angle of attack,

$$\frac{\partial C_L}{\partial \alpha} = 2\pi \quad (9)$$

For small change in angle of attack, $d\alpha \approx sin(d\alpha) = \frac{|(U+dU) \text{ x } U|}{|U+dU||U|}$ (10)

Maximum change in $d\alpha$ occurs when wind velocity changes in direction perpendicular to forward speed. For this case,

$$d\alpha \approx \frac{|dU|}{|U|} \tag{11}$$

and using (6) and (11), (8) becomes $\frac{dL_f}{L_f} = \frac{1}{\alpha}\frac{|dU|}{|U|} + \frac{2UdU}{U^2}$ (12)

For U= 4 m/s, dU = .25 m/s and α = 6°,

$$\frac{dL_f}{L_f} = 72.2\% \tag{13}$$

Similarly, when change in wind speed takes places in direction parallel to forward speed, (10) becomes zero and (8) takes the following form:

$$\frac{dL_f}{L_f} = \frac{2UdU}{U^2}$$

For same conditions of velocity as considered above,

$$\frac{dL_f}{L_f} = 12.5\% \tag{14}$$

Equations (13) and (14) gives us a quantitative change in lift due to change in flow normal and parallel to forward speed respectively. A change of even 6.25% in forward speed due to fluctuations in wind speed changes lift by 72.2% when occurred in normal diection, and 12.5% if occurred in parallel direction. Change in lift by such amount can not lead to abrupt changes in flight trajectory, while also structurally affecting the vehicles, and hence leading to failure of mission objective.

Thus, MAVs are more vulnerable to environmental fluctuations than their bigger counterparts for both dynamics and environmental reasons. Dynamically, even small changes in wind speed and direction at length scale comparable to MAVs can severely upset their flight trajectory and body orientation. Environmentally, MAVs are expected to operate at a lower altitude from ground surface, full of turbulence and transient gusts. Maneuvering in a chaotic environment through complex terrain of hills, canyons, trees and street corners is thus a challenging task, but one that insects, birds and bats routinely tackle. For success of any operations, the autonomous controllability of MAVs using real-time on-board sensing of environmental

turbulence, gust and unsteadiness is therefore crucial, and raises the fundamental question of sensor and actuator placement in MAVs. Study of insects, from aerodynamics and control point of view, can help us answer the question. However, very little is known about the flight of insects in turbulent and gusty environment. With this motivation and curiosity to understand their flight response in the natural environment, we investigated the flight performance of insects subjected a transient discrete gust on the flight trajectory, and body and wing kinematics of a normal flying insect in a controlled environment.

Based on the earlier findings that the roll axis is most unstable in insects (Combes & Dudley 2009; Ravi et al. 2013; Beatus et al. 2015), we conjectured that insects respond to perturbations along roll axis in order to maintain a stable flight. To examine the hypotheses, a free-flying soldier fly was perturbed by a strong head-on gust. Most methods reported in the literature in relation to the impact of gusts on the flight performance of insects are either not well characterized or too extreme by natural standards. Vance et al. (2013), for example, used an unsteady and non-uniform jet as a gust to study the response of insect, which was not easy to characterize. Similarly, Beatus et al. (2015), Ristroph et al. (2010), and Ristroph et al. (2013) studied the insect's response by applying impulsive force using a pair of Helmholtz coil. The force so generated is unrealistic. To present insects with a controlled and well-characterized gust, we used a discrete vortex ring to perturb the fly. This method is well characterized in terms of its flow properties. Moreover, it also ensures the steadiness and uniformity of flow in the region where insect encounters gust. This method would, thus, eliminate any ambiguity in analyzing the response of insect, arising from the ambiguity in flow properties.

The flight motion of insects before, during, and after gust was recorded using high-speed videography. Each video was calibrated, digitized, and analyzed. The time and 3-D position coordinates so obtained were then used to study any change in flight trajectory, body, and wing kinematics of insects due to gust. Also, the time taken by the fly to respond to the perturbations (i.e. response time) was noted and used to characterize the mechanism fly employed to regain stability along different body axes.

Structure of Thesis

The organization of the thesis is as follows. Chapter 2 presents the details of the experimental setup, gust generator used for generating the head-on gust, along with the instrumentation and the experimental methods such as insect selection, flow visualization, high-speed videography, video processing and analysis techniques, signal conversion unit, detection of insect flight and electronic synchronization. The results obtained from the characterization of gust are presented in chapter 3. This includes the results on position and velocity of gust with time and space, obtained from smoke flow visualization and bead method, by using high-speed videography. The results on the impact of a gust on insect flight are presented in chapter 4. This includes the results on flight trajectories, body and wing kinematics of fly before, during, and after gust. Finally, chapter 5 presents the main conclusions from the present study and directions and scope for future work.

Chapter 2. **Materials and Method**

The present study has two parts- (a) generation of a well-studied and highly controllable gust, and (b) experimentation and analysis of the interaction of insects with the gust. We generated gust in two different ways- (a) using a pair of pitching foils and (b) vortex ring. This chapter, however, discusses the methodology for generation and characterization of vortex ring to be used as a gust, and the materials and techniques used for experimentation and analysis of insects with the vortex ring. The generation of gust using the former is discussed in detail in Appendix A.

Adult soldier fly was used as a model insect for this study. The flies were reared and cultured in the lab. A Speaker (100W, 8 Ohm) was used to generate gust in the form of a vortex ring. First, a digital signal of trapezoidal form was generated and converted into analog using appropriate NI-DAQ modules (Ni-c9263 and Ni-c9401). The signal was then amplified using an amplifier and fed to the speaker. Flow visualization, useful for characterization of the gust, was done using fog particles of size 1-2 μm.

Flight motion was captured at 4000 FPS using two synchronized, non-orthogonal high-speed cameras (Phantom VEO 640L and Phantom V611) and for flow visualization, Phantom Miro eX4 was used at 1200 fps. Nikon lenses 24-85 mm and 18-70 mm were both used for filming flight motion, while only the latter one was used for visualization purpose. Two Halogen lamps (1000W) were used for illumination. The calibration and the digitization of the videos were done using MATLAB based routines - easywand5 (Theriault et al. 2014) and DLTdv7 (Hedrick 2008) respectively.

An in-house infrared motion detector was used to trigger the camera and Ni- DAQ with a pre-specified delay. All the recordings were done between 0900 and 1600 hours on a sunny day to ensure daylight is present. Daylight attracts the fly and provides directionality to insect flight, which improves the success rate of an insect being hit by a gust.

2.1 Insect

A. Rearing

Soldier flies (*H. illucens*) were reared in a large mesh cage, maintained at 28° C (Sheppard et al. 2002). A bucket filled with compost was placed in the center of the mesh. The bucket was covered on the top with a lid having a small opening to facilitate the flies to fly into the bucket and lay eggs on cardboard papers hanging from the lid. The eggs after hatching into the larva would fall down in the compost and feed insatiably on the compost. The sixth instar larva would climb the wall and reach crevices like opening on the sidewall. There is another tray containing dry sawdust, placed such that the larva would fall into it once it gets out of crevices. Until the complete pupation takes place, the larva would hide in the sawdust. The pupae are then transferred into the mesh cage where they grow into an adult.

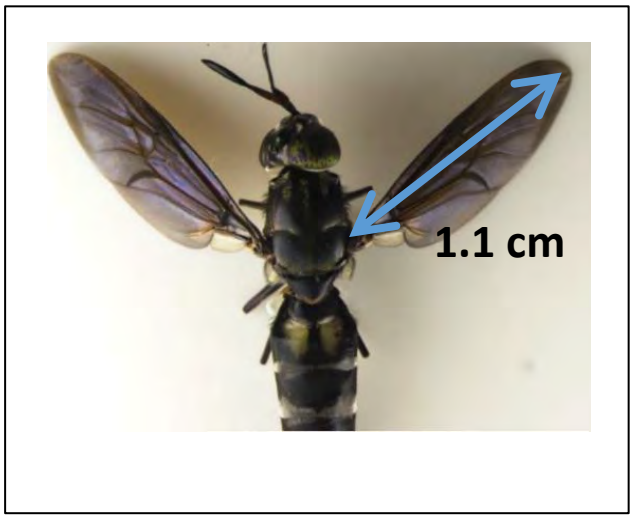

Figure 2-1: A soldier fly with wing length of 1.1 cm

B. Insect Selection criteria

Their characteristic feature to fly towards light is one of the main reasons we chose the soldier fly for our study. This makes the control of their flight trajectory easier. For consistency across all the trial, a certain set of criteria was set to select an insect before subjecting it to gust:

- No body parts (wings, halteres, etc.) were damaged.
- Insect should be able to fly for at least 30 cm across the test section.
- Its body length was minimum of 1cm and maximum of 1.5cm.

C. Experimentation with insects

A group of 5-6 insects was collected at a time from the large mesh cage (See 2.1A**)** using a plastic disposable centrifuge tube. The group was then released into a test chamber using fly

releasing duct (FRD). Releasing a group of insects together increases the probability of them being hit by a gust. After releasing, I would wait for the insects to fly themselves. It was observed that all insects would, in some cases, fly at the same time just after release into the test chamber, while in other cases only one or none at all would fly into the test chamber. In latter cases, when an insect would remain stationary in FRD for more than 5 minutes, the lower internal wall of the duct was slightly hit with a plastic ruler to instigate its flight. However, while doing so, care was taken to ensure insects weren't directly hit and any body parts weren't damaged.

2.2 Gust generation

2.2.1 Experimental Set-up

The experimental set-up used for the generation of a gust is shown in Figure 2-2**.** It consists of a 60 cm long, 30cm square cross-section dismountable clear Perspex chamber, a 40 cm long, 3.76 cm internal diameter (D_0) cylindrical PVC nozzle (2mm thick), a 12-inch 100W, 8 Ω speaker, a 15cm long, 5cm square cross-section clear Perspex fly releasing duct (FRD), a digital to analog converter NI-DAQ, a high voltage high current direct coupled (DC) amplifier, two synchronized high-speed cameras (Phantom VEO 640L and V611) and an infrared (IR) motion detector.

The large Perspex chamber serves as a test section where the vortex ring forms and propagates. The large dimension of the Perspex chamber (test chamber) compared to the diameter of vortex ring aids in maintaining a still ambient fluid, and also reduces any effects of external air currents on experimental observations (Das et al. 2017). The experiments were carried in a closed room with a controlled level of humidity and an ambient temperature of 20°C.

FRD and nozzle are placed co-axially and opposite each other on the longer sides of the test chamber. To accommodate these, a 5cm square cross-section is cut on one wall to support FRD and a 5cm diameter hole is cut on the opposite wall for the nozzle. FRD and nozzle are not permanently fixed to the test section, rather they are dismountable and can be reassembled when required. The speaker is enclosed in a 40cm x 40cm x 5cm wooden chamber (driving section) on the diaphragm side and each side of the chamber is glued with fevicol and pin hammered to ensure air-tightness. A 5cm diameter hole is cut at the center of the 40cm x 40cm face of the wooden chamber to facilitate attachment of the nozzle via a PVC flange. A rubber gasket is used in between flange and wooden chamber to eliminate any air leakage. The nozzle is sharp chamfered by an angle of 9° at the exit and smooth chamfered at entry.

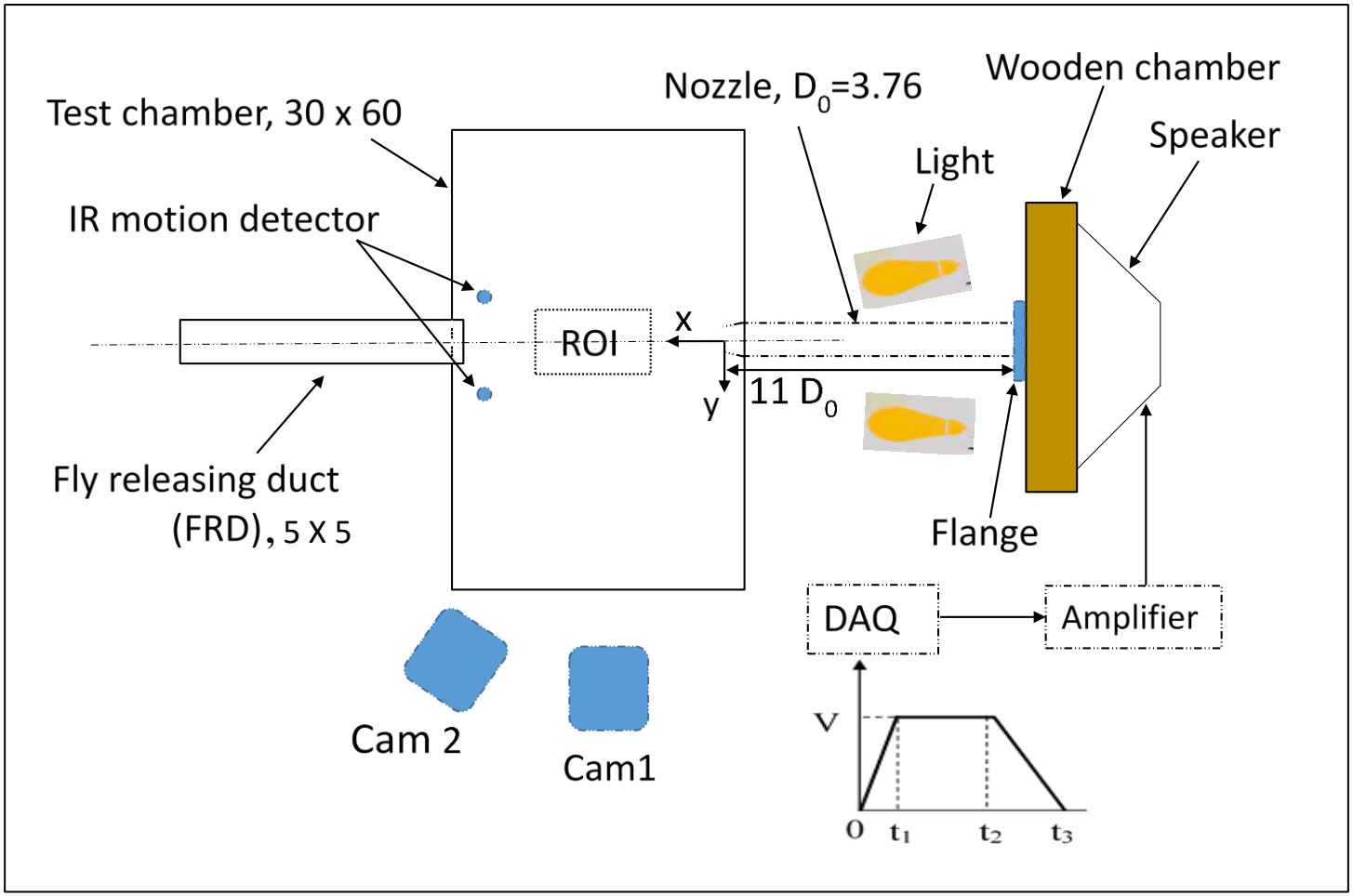

Figure 2-2: Gust generator system. Different components of the experimental setup and their arrangement. Test chamber, Speaker, nozzle, Infrared (IR) motion sensor, Fly releasing dust, halogen lamp cameras, DAC and amplifier together constitute the gust generator system. Right bottom shows input signal to DAC with rising time, t_1, constant duration t_2-t_1 and fall time t_3-t_2-t_1. This signal is converted into analog form, amplified by amplifier and fed to the speaker for gust generation. All dimensions are in cm.

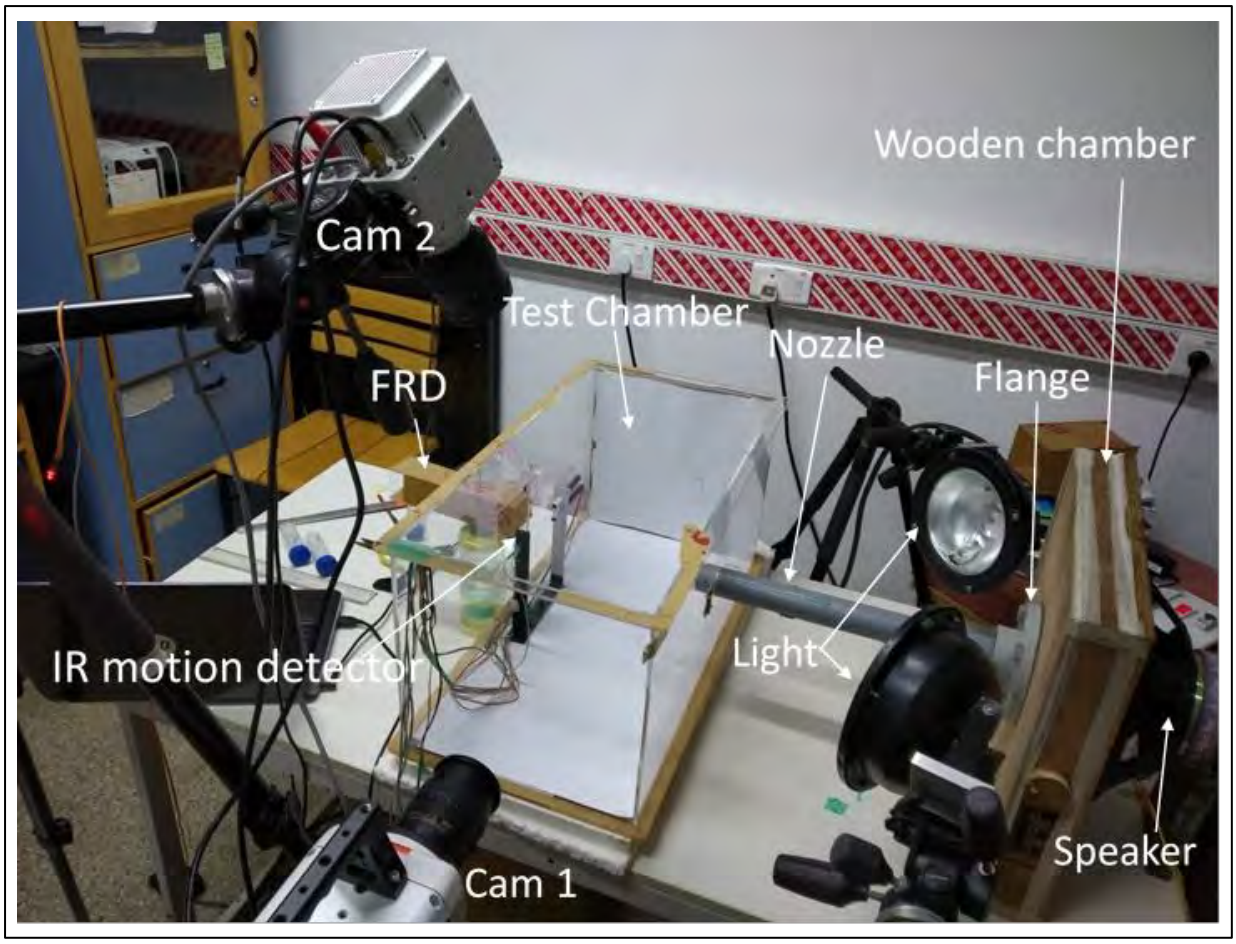

Figure 2-3: Experimental setup showing important components. Cam 1 and Cam 2 are side and top cameras respectively. FRD is a fly releasing duct. Lights were placed opposite to FRD to direct the insects straight towards gusts. FRD and nozzle are placed co-axially and opposite each other to study the effect of head-on gust on insect flight.

The present experimental set-up, unlike conventional piston-cylinder configuration for vortex ring generation (Didden 1979; Lim & Nickels 1995; Pullin & Perry 1980; Weigand & Gharib 1997; Kumar et al. 1995; Maxworthy 1974; Auerbach 1991; Irdmusa & Garris 1987; Glezer 1988; Gharib et al. 1998; Glezer & Coles 1990; Cater et al. 2004; Sullivan et al. 2008; Maxworthy 1977; Auerbach 1987) has speaker diaphragm (analogous to piston) in the driving section outside the nozzle, thus eliminating the generation of piston vortex (Das et al. 2017). Piston vortex (Allen & Auvity 2002; Glezer 1988; Glezer & Coles 1990; Cater et al. 2004) is formed in front of the piston as it moves ahead in the tube, due to removal of a boundary layer of the tube wall as the piston advances forward (Allen & Auvity 2002). Further, the long nozzle (11 times its diameter) forces the slug of fluid coming out only from the front part of nozzle, not from the entry region where the nozzle is attached to the wooden chamber, thereby ensuring the elimination of possibility of having any disturbances similar to the orifice generated vortex ring (Das et al. 2017).

Two synchronized high-speed cameras (Phantom VEO 640L and V611) were used to record the events before, during, and after gust. The details of the camera position, orientation, and its setting are explained in section 2.4**.** The cameras were focused in the region of interest (ROI). The uniformity and steadiness of the velocity of gust govern the distance of ROI from the nozzle exit plane. ROI ($2D_0$ x $2D_0$ x $2D_0$) was selected at a distance of $3D_0$ from the nozzle exit plane. The velocity of the gust becomes nearly invariant with space and time after this distance. Its volume was so chosen that the insect wouldn't possibly go beyond the focal volume of the camera, even after its encounter with gust. The video images were calibrated using a glass capillary of known length (see section 2.5.3).

An in-house infrared (IR) motion detector was used to detect any flight motion of insects towards ROI. Electronic detection served as an automatic trigger for gust generator and cameras. Detection, automatic triggering of gust generator, and cameras were electronically synchronized using an in-house electronics circuit (see section 2.7.3 and 2.7.4).

2.2.2 Input Signal

A trapezoidal signal, as shown in Figure 2-2 was initially synthesized and stored in computer memory using NI-LabVIEW. The signal consisted of three parts: acceleration (i.e. rise), constant velocity and deceleration (i.e. falling). The time period of each part (t_1, t_2- t_1 and t_3- t_2- t_1) of the signal and the signal's amplitude (V) were so chosen that required velocity(U) of the gust was achieved. Certain choice of time period of each portion of the signal (t_1= 100µs, t_2- t_1 = 30 ms and t_3- t_2- t_1=100 ms) resulted a vortex ring velocity with maximum velocity = 6 m/s. Such a large deceleration time eliminates the formation of opposite sign stopping vortex (Das et al. 2017) which is formed, on abrupt stopping of piston, due to separation and rolling of the secondary boundary layer formed on the outer surface of the tube due to induced velocity of primary vortex ring (Didden 1979; Lim & Nickels 1995; Pullin & Perry 1980; Weigand & Gharib 1997; Shariff & Leonard 1992).

This signal was converted into analog form for physical output using NI –c9263 card (see section 2.7.1 for detail) and triggered by a transistor-transistor logic (TTL) signal using NI-c9401, upon automatic detection of insect flight by IR motion sensor (see section 2.7.3 for detail). The signal is then amplified using an in-house DC power amplifier (see section 2.7.2 for detail) and finally fed to the speaker, resulting in the formation of a vortex ring at the exit of the nozzle.

2.2.3 Formation of vortex ring

The signal, when fed to the speaker impulsively, displaces its diaphragm by some distance in the wooden chamber. An equivalent volume of air is pushed from the chamber into the nozzle,

generating a layer of vorticity (boundary layer) in the inner wall of the nozzle to satisfy a no-slip condition. As the high-speed slug of air comes out of the nozzle, this boundary layer forms a cylindrical vortex sheet that immediately starts rolling up into a spiral form, giving rise to a vortex ring (Lim & Nickels 1995).

2.3 Characterization of gust

The gust was characterized using two different techniques: fog visualization and Styrofoam bead method. Both the methods were carried out independently and flow properties were characterized for each method.

A. Fog visualization

Antari fog particles from a fog generator (Antari Z-1000II) were used as seeding particles for visualization of the vortex ring. The average particle size of the fog was of an order of 1μm. The fog was first filled into a 500 ml wash bottle and injected through a small port on the nozzle. The fog injection port was made on the upper circumference of the nozzle, at 18 cm ($4.5D_0$) away from its exit plane. The circumferential (lower, upper, or sidewise) position of the port didn't seem to affect the visualization. Its longitudinal position, however, determined whether any fog particles would be present at the exit of the nozzle before ring formation (i.e. background fog at nozzle exit). The choice of its position ($4.5D_0$) eliminated the possibility of any background fog formation at the nozzle exit.

A 12-bit CMOS camera (Phantom Miro EX4) was used to capture the flow images using Nikon 18-70 mm focal length lens. The frame rate was set to 1200 fps and exposure time to 50 μs (see section 2.4). To take care of such a low exposure time, the background was illuminated using two 1000W halogen lamps. The camera was placed horizontal such that a lateral view of vortex ring propagation would be captured in a plane perpendicular and vertical to the nozzle exit plane. The external diameter served as a calibration scale for the images.

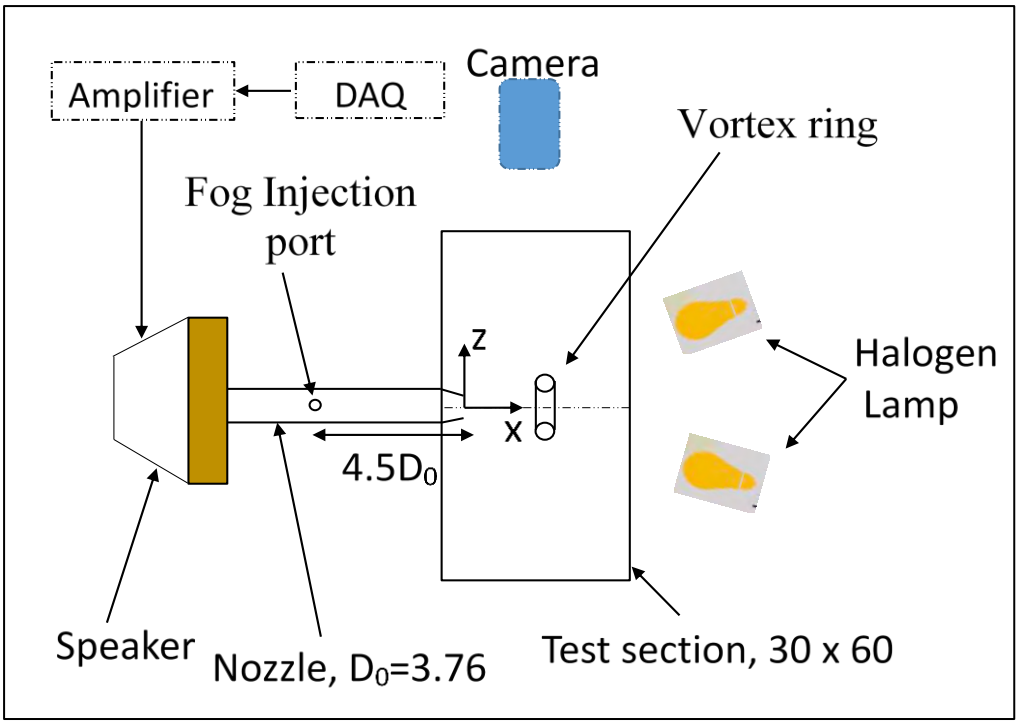

Figure 2-4: Experimental setup for flow visualization and characterization. Fog particles were used to visualize the flow. These particles were injected into nozzle through a port at a distance $4.5D_0$ from nozzle exit. Camera was placed horizontal to record the lateral view of the flow. The background was illuminated using a pair of high-power halogen lamp. All dimensions are in cm.

The vortex ring generator and other electronics like DAQ and amplifier were the same as that used for experimentation with insects. To prevent fog accumulation inside the test chamber, a 5cm square window was hinged on the longer side opposite to nozzle. The window was kept closed during visualization to eliminate any effects of external air current on the ring propagation and its trajectory. It would be opened only after the completion of the recording. This ensured no fog inside the chamber before the start of the next trial. A schematic of the experimental setup is shown in Figure 2-4**.**

Visualization of gust at two different non-dimensional time instances are shown in Figure 2-5.The visualization was carried out at Re ($U_{avg}D_0/\nu$)=4700. Time (t) is non-dimensionalized with average velocity of gust (U_{avg}) and exit diameter of nozzle (D_0) and is given by $T_n = U_{avg} * t/D_0$.

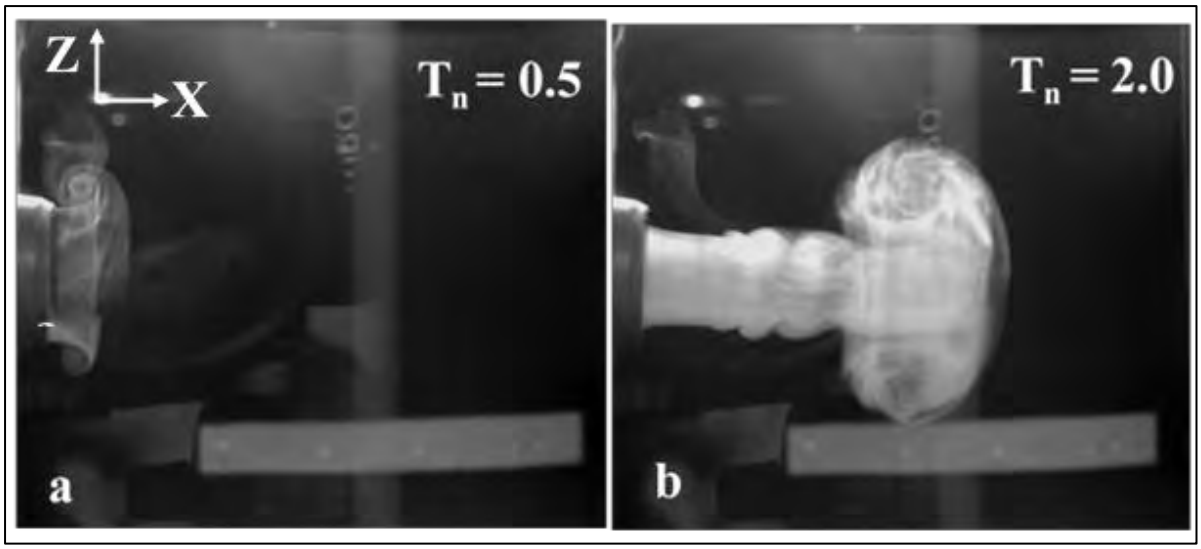

Figure 2-5: Flow visualization at different time instances for Re 4700. The gust propagates from left to right along X in each figure. X and Z are axial and vertical directions of gust respectively.

B. Styrofoam Bead method

In this method, a Styrofoam bead was used to determine the average velocity of the gust. The experimental setup was the same as that for fog visualization (see Figure 2-4). This method is discussed, in detail, in the next chapter.

2.4 High-Speed videography

Fly beats its wing at an average of 110 Hz. Considering the Nyquist frequency, we need to capture the flight motion at a speed of at least ≥ 220Hz to ensure there is no missing of any useful quantitative information like stroke angle, angle of attack, and deviation angle during a wing beat. Further, to get the 3D position of fly in space and time, we require at least two cameras with minimum frame speed as specified earlier. It is always advisable to use the cameras in orthogonal positions, as it eases the reconstruction of a 3D position. It is, however, not a necessary condition and not possible on the present experiments.

2.4.1 Frame per second (FPS)

FPS denotes the number of images taken in 1 second. The higher the FPS, the smoother is the video and the lower is the probability to miss any details of the information during a wing stroke. But, higher FPS also requires large memory space and a longer time to analyze the images. Considering these two factors, 4000 FPS was chosen on each camera for insect flight motion and 1200 FPS for flow visualization. The insect moves by an average of 0.2mm (~0.9 pixels) for each frame period, while the gust by about 5mm (~13 pixels).

2.4.2 Resolution

The resolution of any image determines its detailed content. The higher the resolution, the more detailed the image is. A resolution of 1280x 800 was chosen for insect flight and 800 x 600 for flow visualization.

2.4.3 Exposure time and aperture

The time period for which the camera sensor is exposed is called exposure time. The maximum exposure time is inverse of the FPS. Based on the average peak to peak amplitude of wing (2x110°), wingbeat frequency (f) 110 Hz and average wing radius (R) of 1cm, the tip velocity (U_t) of the wing is approximately 4.5 m/s ($11\pi U_t \mathrm{Rf}/9$). The choice of exposure time should be such that the wingtip doesn't move by a large distance, i.e. multiple pixels during the exposure time, else a blurred image is obtained. Considering these parameters, an exposure time of 70μs was chosen for flight motion during which the wing tip moves by 0.3 mm (~1.3 pixels ~ 2% of body length), and 50μs for flow visualization during which the gust moves by 0.3 mm (~ 0.8 pixels). The intensity of the image decreases as exposure time is reduced. We used two halogen lamps (1000W) to illuminate the background to obtain sufficiently well-lit images.

Aperture denotes the area over which light can pass through the camera lens. Exposure time, aperture, and background luminescence determine the quantity of light the camera sensor receives.

2.4.4 Multi-camera Setup

While considering a multi-camera system, it is necessary to consider whether frame rate, spatial resolution, field of view, and synchronization ability of the cameras are appropriate for the size and speed of the organism under study (Theriault et al. 2014). Two synchronized high-speed cameras (Phantom VEO 640L and V611) were used to capture flight motion. The two cameras were synchronized, with the sensor of one camera put in a Master mode, generating the timing signal and that of the other in Slave mode. This enforces the same number of FPS on each camera (F-sync) with no time lag. To ensure each camera was f-synced accurately, a 2cm LED bulb was turned ON in the region of interest common to both cameras. The glowing of the light was captured from switch ON to switch OFF mode. The frames of the image were then compared in both cameras when the light just glowed, remained ON and just went off. The synchronization was considered accurate when, in each camera, the light turned on and off at the same time and remained on for the same number of frames.

Due to the large experimental setup and limited space, these cameras couldn't be placed orthogonal to each other. To ensure the cameras don't capture coplanar views, one camera was

placed such that it would capture the side view of the flight motion while the other would capture an oblique top view. It is noted that the non-orthogonality was taken care of by employing a rotation matrix that was determined using two orthogonal axes common to all the images (see section 2.5.1). Only one camera was used for flow visualization.

2.5 Video processing

The cameras were calibrated using a wand of 75mm long using direct linear transformation (DLT) implemented in DLTdv7 and easywand5 MATLAB routines (Theriault et al. 2014; Hedrick 2008). Each step involved in video processing is briefly explained below.

2.5.1 Finding Rotation Matrix

We need perfectly orthogonal spatial coordinates of the fly to obtain its trajectory. But, because we couldn't place the cameras perfectly orthogonal to each other and to the flight path, the first step in the processing of the videos was to rotate the captured views from each camera. The rotation ensures no projection error and also the same origin point across all videos that can ease the analysis of data. This was achieved by finding a rotation matrix common to both side and top views for each experiment. Also, because the orientation of cameras can be different in different experiments, a separate rotation matrix was found for each experiment.

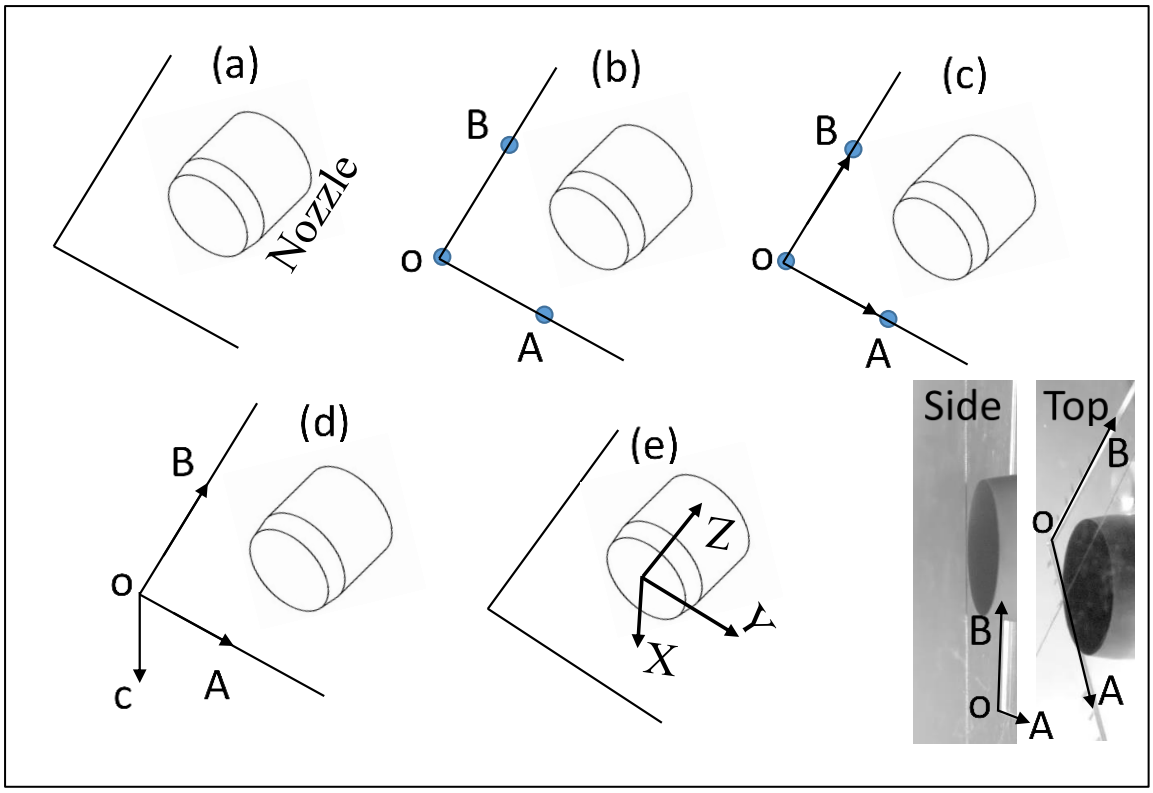

Figure 2- 6:Finding rotation matrix for each experiment using both top and side views. Inplots in right bottom shows physical orthogonal axes from experimental setup that serve as a basis of rotational matrix in each image for different experiments.

The rotation was achieved using the following steps:

a. Two orthogonal physical axes passing through each other in a plane parallel to the plane of nozzle exit were first traced across all videos (see Figure 2- 6 (a) and inplots).

b. Three points-1) being the point of intersection of these axes as an origin (**O**), 2) on the horizontal axis (**A**) and 3) on the vertical axes (**B**) were digitized (see Figure 2- 6 (b)).

c. The position vectors of horizontal (***OA***) and vertical points (**OB**) with respect to origin were found and normalized with their magnitude to get unit position vectors (see Figure 2- 6 (c)).

$$\widehat{OA} = \frac{\boldsymbol{OA}}{|\boldsymbol{OA}|}$$

$$\widehat{OB} = \frac{\boldsymbol{OB}}{|\boldsymbol{OB}|}$$

d. To ensure the digitized position vectors of vertical and horizontal points are orthogonal in recorded images as well, the orthogonality was cross-checked using vector dot product and vector addition (i.e. Pythagoras theorem).

Orthogonality test of $\widehat{OA}$ and $\widehat{OB}$ in recorded images:

1. Dot product = 0	$\widehat{OA}.\widehat{OB} = 0$
2. Pythagoras theorem	$OA^2 + OB^2 = AB^2$

e. Once **OA** and **OB** satisfy the conditions in (d), a third vector (**OC**) perpendicular to both OA and OB was found using vector cross-product (see Figure 2- 6 (d))

$$\widehat{OC} = \widehat{OA} \, X \, \widehat{OB}$$

f. Using these three mutually orthogonal unit vectors, a rotation matrix, **R** was then found such that it transforms the coordinates in the recorded views into orthogonal one with respect to the physical world. This implicitly made the point of intersection of these position vectors as the origin.

$$\begin{bmatrix} \widehat{\boldsymbol{OA}} \\ \widehat{\boldsymbol{OB}} \\ \widehat{\boldsymbol{OC}} \end{bmatrix} [\boldsymbol{R}] = [\, \boldsymbol{I} \,]$$

Where R and I are rotation and identity vectors respectively.

g. The origin was then translated to the center of nozzle exit across all videos (see Figure 2- 6 (e)).

2.5.2 Principle: Direct Linear Transformation (DLT)

The process of getting the 3D position of any object from its 2D coordinate points, captured using at least 2 cameras is called reconstruction. Reconstruction requires calibration of the cameras and for calibration, we need to relate the image plane coordinates to the object space coordinates. This relation is obtained using Direct Linear Transformation (DLT). A figure showing the principle of DLT is shown for two cameras in Figure 2-7.

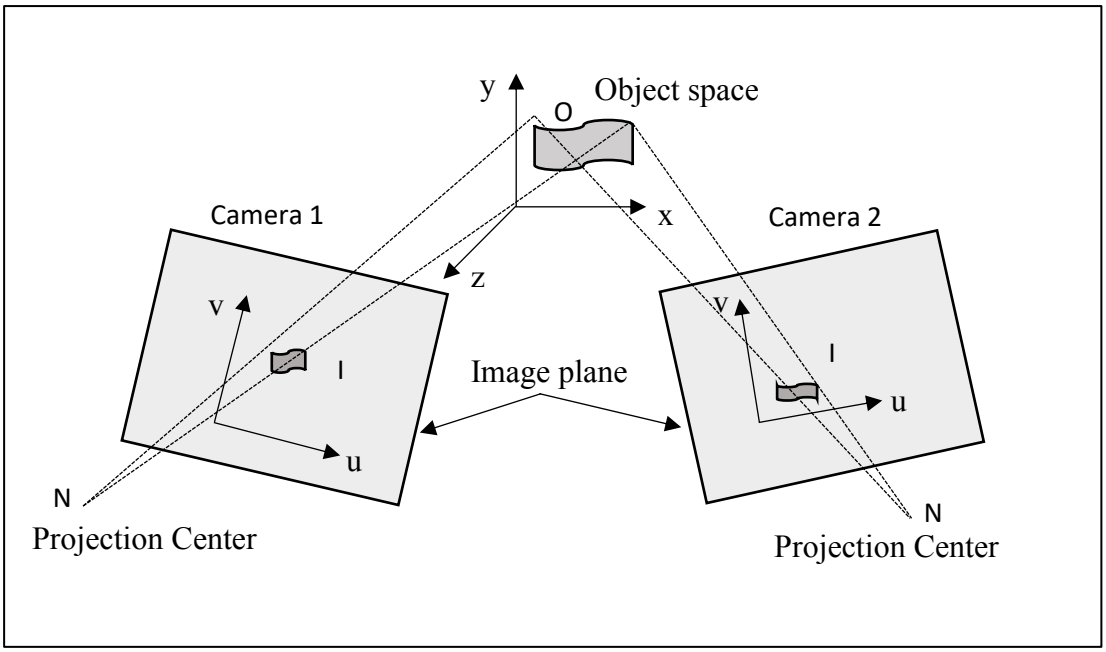

Figure 2-7 Principle of Direct linear Transformation showing collinearity of projection center, image point and object point in each of two cameras. Object-space reference system and image-plane reference system are defined in the figure. Camera sensor maps the object space points (x, y, z) onto the image plane as (u, v).

Each object space point (x, y, z) is projected onto the image plane (u, v) by camera sensor (CMOS) or projector. The basis of DLT is collinearity of projection center, image point and object point (i.e. all three points lie on the same line). Based on this principle and using six different points common to all the cameras, DLT finds 11 calibration coefficients (L_i) relating physical object space and the camera image plane.

$$\begin{matrix}\text{Point 1}\\ \\ \text{Point 2}\\ \\ \\ \text{Point } N\\ \\ \end{matrix}\left\{\begin{bmatrix} x_1 & y_1 & z_1 & 1 & 0 & 0 & 0 & 0 & -u_{L1}x_1 & -u_{L1}y_1 & -u_{L1}z_1 \\ 0 & 0 & 0 & 0 & x_1 & y_1 & z_1 & 1 & -v_{L1}x_1 & -v_{L1}y_1 & -v_{L1}z_1 \\ x_2 & y_2 & z_2 & 1 & 0 & 0 & 0 & 0 & -u_{L2}x_2 & -u_{L2}y_2 & -u_{L2}z_2 \\ 0 & 0 & 0 & 0 & x_2 & y_2 & z_2 & 1 & -v_{L2}x_2 & -v_{L2}y_2 & -v_{L2}z_2 \\ & & & & & \vdots & & & & & \\ x_N & y_N & z_N & 1 & 0 & 0 & 0 & 0 & -u_{LN}x_N & -u_{LN}y_N & -u_{LN}z_N \\ 0 & 0 & 0 & 0 & x_N & x_N & x_N & 1 & -v_{LN}x_N & -v_{LN}y_N & -v_{LN}z_N \end{bmatrix}\right.$$

$2N \times 11$

$$\begin{bmatrix} L_1 \\ L_2 \\ L_3 \\ L_4 \\ L_5 \\ L_6 \\ L_7 \\ L_8 \\ L_9 \\ L_{10} \\ L_{11} \end{bmatrix}$$

11×1

$$= \begin{bmatrix} u_{L1} \\ v_{L1} \\ u_{L2} \\ v_{L2} \\ \vdots \\ u_{LN} \\ v_{LN} \end{bmatrix}$$

$2N \times 1$

The equation can be written as AL=B.

Calibration is achieved by solving for L. Since A and B are not square, their inverse can't be obtained. So, the least-squares method is employed to calculate L as follows.

$$\mathbf{L = (A^T A)^{-1} A^T B}$$

DLTdv7 (Hedrick 2008), MATLAB based routine, was used to determine L and hence calibrate the video images (see next section for a detailed discussion).

2.5.3 Calibration Technique

Camera calibration is the process of creating a camera model that can be used to obtain 3D information from the images. It comprises matching corresponding points on a calibration object across all the camera views. A 75 mm long and 1mm diameter glass capillary was used as a calibration object (wand) to calibrate the cameras. One end of the wand was marked with black color, for the distinction between its endpoints, and before any flight experiments, it was moved randomly throughout the calibration volume and recorded, so that it ends points can be digitized and used as an aid for calibration.

To obtain the 11 DLT coefficients, at least 120 calibration points were digitized using easywand5, a MATLAB based calibration tool (Theriault et al. 2014). The software, using user-fed approximate intrinsic parameters like focal length, principal points and spatial resolution for each camera, and 8-point algorithm (Hartley & Zisserman 2004), estimates relative 3D position, orientation, and intrinsic parameters of each camera. It uses an 8-point algorithm, meaning it requires at least 8 wand points for a good calibration. It then applies Sparse Bundle Algorithm (SBA) to further refine the estimates of calibration parameters. Finally, it converts the calibration parameters in the form of DLT coefficients for 3D reconstruction. The reprojection error (RMS distance between reprojected and original calibration points) and wand score (ratio of the estimated standard deviation of wand length to its mean), each was less than 1 pixel in all the cases. The intrinsic parameters required for calibration are tabulated in Table 2-1.

Table 2-1: Intrinsic Parameters of the camera (Phantom) and lens

Camera model	**Lens focal length (mm)**	**Sensor pixel size (µm)**	**Resolution (pixel)**
VEO 640L	24-85	10	1200 X 800
V611	18-70	20	1200 X 800

2.5.4 3D Reconstruction

Reconstruction is the process of using camera models obtained by calibration to generate 3D position of any object across camera views. It involves employing DLT coefficients and known pixel coordinates to reconstruct a 3D location.

Six different points (head, abdomen, right and left-wing bases, and the corresponding wingtips) were manually digitized on the body of a fly as shown in Figure 2-8. DLTdv7, a custom code written by T.L. Hedrick in MATLAB (MathWorks Inc) was used to obtain 3D coordinates of the fly. The DLT residual was kept less than 2 for each point and across videos.

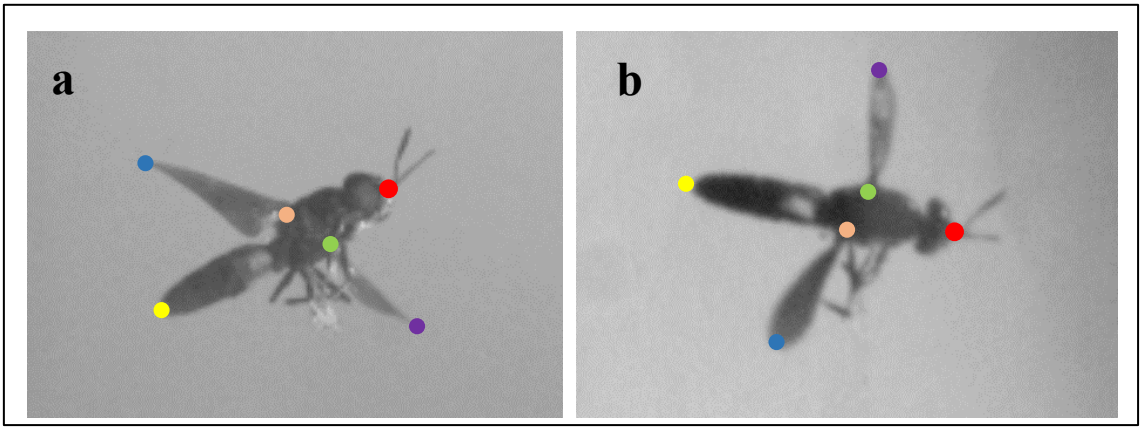

Figure 2-8: Digitization of different body parts of soldier fly. Head, abdomen, wing tips and wing bases are digitized in each frame. (a) Side view and (b) Top view of the fly.

2.6 Video analysis

Videos (700-1500 frames each) from 14 experiments were analyzed using custom code written in MATLAB. The code is given in Appendix B-***5***. The data were first down-sampled to a frequency of 1000Hz and then each of the six different points on the body was tracked in the global reference frame. The code provided measures of fight trajectory, pitch, yaw, and roll orientation. Further, the digitized points were transformed into a body coordinate system to calculate the wing position with respect to fly. This gives us a measure of wing stroke and wing deviation about the horizontal plane.

The time period and hence the frequency of a wing beat were calculated from the videos by counting the number of frames in a wing beat. A minimum of 20 wing beats (5 wingbeats before gust hit and 15 wing beats after gust hit) were analyzed for each video.

2.7 Electronics

A number of electronic components were required to achieve the objective of driving and triggering the gust generator and event recording system. The important electronics used for the experimentation are discussed below briefly.

2.7.1 Digital-to-Analog Converter (DAC)

The objective of DAC is to convert a digital signal to an analog one. Gust was generated by feeding a trapezoidal signal of definite time scales to a speaker. This signal was digitally produced using a computer program the NI-LabVIEW. The speaker requires an analog input. To achieve this objective, the NI-c9263 module was used. A simple LabVIEW program was used to generate a digital signal, store it in a volatile memory of DAQ and convert it into analog form. The program is given in Appendix B-***1***.

2.7.2 Linear Amplifier

The signal that can be produced and stored in a memory of the DAQ is limited to 10V and 50 mA, which is not sufficient to drive the diaphragm of the speaker by the required amount. An in-house direct coupled (DC) amplifier built using commercially available OPA 548T (high voltage high current operational amplifier) was employed to drive the speaker. The use of the DC amplifier ensured the amplification of the signals with very low and even zero frequency. The circuit diagram for the amplifier is given in Appendix B-***3***.

2.7.3 Motion detector/Trigger

The success of perturbing the insect with a gust lies in triggering the gust generator and camera system when the insect is in the region of interest. Triggering the system manually, based on the visual aid, wasn't possible. Moreover, the success of the event can't be ascertained. To overcome this difficulty, an in-house infrared (IR) motion detector was used to detect any motion of the insect between two fixed points in a plane parallel to and at a certain distance from the exit plane of fly releasing duct (FRD). The distance between the IR motion detector and exit plane of FRD was determined based on the average flight speed of the insect and the region of interest where the interaction of insects with gust was intended.

Once the flight of an insect is detected, another crucial step is to trigger the gust generator and camera system. The same IR motion detector circuit was used to trigger NI-c9401and camera, each with a pre-specified delay after detection of motion. NI module then triggers the NI- c9263 module to generate an analog output signal. Based on the average flight speed ($u =$

70 cm/s), and distance between IR motion detector and region of interest ($s = 9\ cm$), the pre-specified delay, Δt was given by

$$\boldsymbol{\Delta t = s/u = \sim 130\ ms}$$

A LabVIEW program to trigger the gust generator is given in Appendix B-***2***.

2.7.4 Electronic Synchronization

Electronic synchronization is necessary to make the events like detection of insect motion, trigger of camera recording, and activation of gust generation system appear nearly simultaneous, each with pre-specified delay as per requirement. It was accomplished using an in-house electronic circuit as shown in Appendix B-***4.***

Chapter 3. **Characterization of Gust**

3.1 Introduction

This chapter discusses the flow properties of the gust obtained using the methods discussed in the previous chapter. Gust was generated in the form of a vortex ring. This method of gust generation, unlike other methods like the use of jet, magnetic torque and von Karman vortices, is a well-studied unsteady flow and eliminates any ambiguity that may result in the analysis due to ambiguity in flow properties. This dictated the use of a vortex ring as a gust in the present study. The formation and flow properties of a vortex ring-like its position and velocity are discussed in detail below. The terms gust and ring are interchangeably used hereafter.

Some of the non-dimensional terms used in the chapter are listed below.

A. Reynolds number

Reynolds number (Re) shows whether inertial force or viscous force is dominant in the flow. We define Re based on exit diameter of nozzle (D_0) and average velocity of ring (U_{avg}) and kinematic viscosity of air, as $\boldsymbol{Re} = \frac{\boldsymbol{U_{avg} D_0}}{\boldsymbol{\nu}}$. Characterization of the gust was carried out for Re=1000, 3000,4700,6800,8600,9200,11700,11900,13700 and 15000. However, only results for Re=4700 and 15000 are reported here.

B. Propagation time and axial distance, diameter and velocity of vortex ring

We define non-dimensional time based on exit diameter of nozzle and ring average velocity, time **(t)** as $\boldsymbol{T_n} = \frac{\boldsymbol{U_{avg} t}}{\boldsymbol{D_0}}$.

Similarly, axial distance from nozzle exit is non-dimensionalized with the exit diameter and is given by $\boldsymbol{X_n} = \frac{\boldsymbol{X}}{\boldsymbol{D_0}}$. The dimensionless diameter of the is given by $\boldsymbol{D_n} = \boldsymbol{D/D_0}$, where D is the instantaneous diameter and dimensionless velocity of the ring is given by $\boldsymbol{U_n} = \frac{\boldsymbol{U_r}}{\boldsymbol{U_{avg}}}$ where $\boldsymbol{U_r}$ is instantaneous ring velocity .

3.2 Flow Visualization

Flow visualization was carried using fog particles of size 1-2 μm. Figure 3-1 shows the formation of the vortex ring at Re=4700 at different time instances. It can be observed that vortex sheet emanates from the edge of the nozzle and rolls up to form a spiral, as the slug of fluid gets ejected through the nozzle. The vortex ring continues to propagate while drawing more fluids from the surrounding ambient (see Figure 3-1 (c) to (f)).

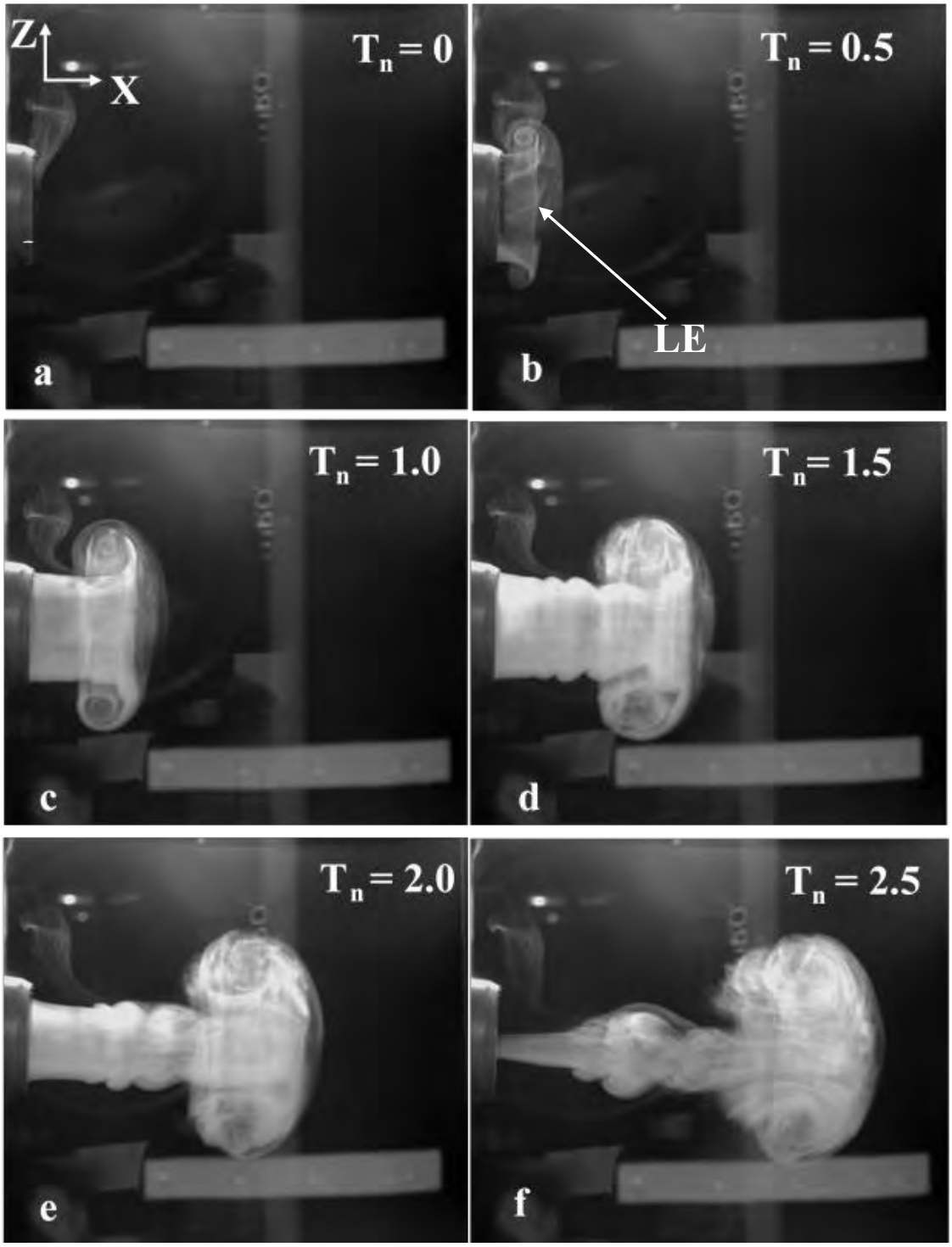

Figure 3-1: Flow visualization of vortex ring at different time instances for Re = 4700. The ring propagates from left to right along X in each figure. X and Z are axial and vertical directions of ring respectively. T_n=0 indicates the time instance when no ring is formed. LE in (b) indicates the point on vortex ring that was followed to track the position of the ring.

3.3 Bead Method

The density of a Styrofoam bead is slightly higher than that of air. To find the density of the bead, its weight was measured using a weighing balance and considering it to be a sphere, its volume was calculated. The so calculated mass and volume were then used to find the density of the bead. The trial was carried out for 5 different beads, the diameter and mass of which are listed in table 3-1.

Table 3-1: Physical measurement of Styrofoam beads used for flow characterization

Diameter (m) x 10^{-3}		Mass (kg) x 10^{-7}	Density (Kg/m^3)
	6.527	8.7	5.98
	6.150	9.5	7.80
	6.653	6.6	4.28
	5.856	8.3	7.89
	6.091	7.9	6.67
Mean	6.26	8.2	6.52

Table 3-1 shows the density of the bead to be of the same order as that of air. So, the velocity of the bead, on an encounter with gust can be expected to be of the same order as that of the gust. With this expectation, this method was employed to determine velocity of gust at different axial locations.

The bead was freely suspended using thin sewing thread from the roof of the test chamber, such that it rests on the centerline of the nozzle exit. The nozzle was filled with fog as described in fog visualization technique and the system was triggered to generate gust. The gust brings an impulsive motion of the bead as it propagates past the bead. The motion of the bead was recorded, processed, and analyzed. This process was repeated by hanging bead at different axial locations on the centerline of nozzle exit to find the velocity of the bead and hence, the gust. Figure 3-2 shows bead locations after being hit by a vortex ring.

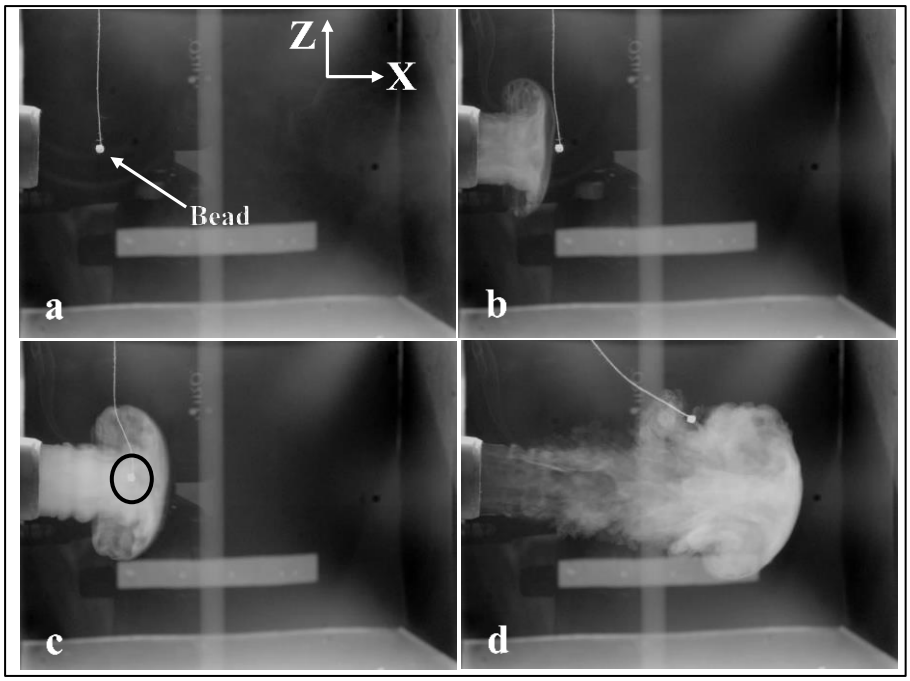

Figure 3-2: Effect of gust (Re=15000) on a freely hanging bead. Position of bead (a) when there is no any gust, (b) just before the gust, (c) during gust and (d) just after gust. The bead translates with the gust as seen in (c) unless it reaches the position where it can no longer carried by gust due to finite length of the thread. Black circle in (c) shows the position of the bead when it is at the core of the vortex ring.

3.4 Calibration of gust generation system

In order to calibrate the gust generation system, the average velocity of the ring was measured for the different input voltage to the speaker. For fog visualization, the average velocity was of the ring was obtained when the flow becomes steady and uniform, while for the bead method, the maximum velocity of bead was considered, which it attains in the first 5 frames of the image sequences.

Average velocity (U_{avg}) and maximum input voltage (V_{in}) in the trapezoid (see section 2.2.2 and Figure 2-2) are plotted in Figure 3-3 (a). It shows a linear relationship between them. Moreover, it shows that the bead velocity is equal to the ring velocity for different input voltages.

3.5 Characteristics of Ring

Parameters like propagation speed, circulation, and vorticity of the ring are some of the important flow properties to consider for its characterization. Considering the aim of the experiment, only its propagation speed is characterized here though.

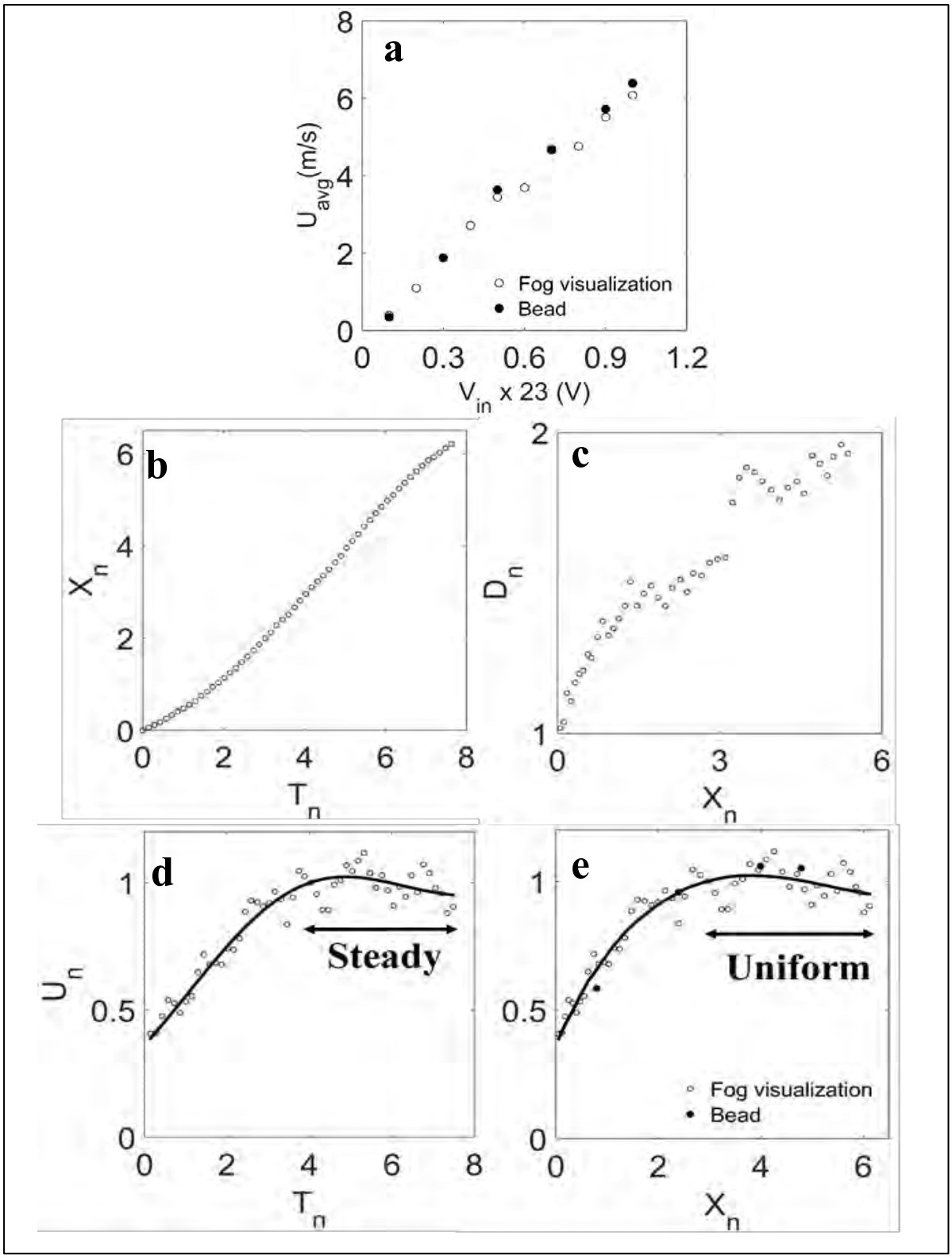

Figure 3-3: Flow properties of a vortex ring at Re=15000. (a) calibration of gust generator. Average velocity of the ring obtained using fog visualization and bead method, versus input voltage. (b) non-dimensional position of ring with time. (c) non-dimensional diameter with axial distance (d) non-dimensional ring velocity with time showing steady nature of flow after T_n=3.5. (e) Ring velocity with axial distance, showing uniformity of flow after X_n= 3 from nozzle exit. Ring velocity from fog visualization and bead method are nearly same. See section 3.1 for non-dimensional parameters.

Figure 3-3 (b) shows the position of vortex ring with time where X_n=0 and T_n=0 indicate position and time just before the spiral rolling takes place respectively. Because the core was not visible in all images and across all videos, the point LE, shown in Figure 3-1 (b) was used to track the position of the ring. The diameter of the ring, as it grows with axial distance is shown in Figure 3-3 (c). The reason for the sudden jump in ring diameter at T_n=3.1 isn't known. The jump may be due to digitization error.

The propagation velocity of the vortex ring was calculated by differentiating the spatial data, obtained from frame analysis of the recorded videos. Second-order central differencing scheme was followed to differentiate the position data. The instantaneous velocity (U_r (t)) of the ring at any position x(t) is given by

$$U_r(t) = \frac{\mathrm{x}\,(t+\Delta t)-\mathrm{x}(t-\Delta t)}{2\Delta t}$$

Figure 3-3 (d) and (e) show the velocity of the ring with time and axial location respectively. The ring attains constant velocity at T_n=3.5 and becomes uniform at X_n= 3 from the nozzle exit. The time and position when the ring becomes steady and uniform are indicated in the figures. Figure 3-3 (e) also shows the speed of bead at different axial locations from the nozzle exit. The speeds measured using the two methods agree well.

Some important parameters of the vortex ring considered for the experiment with the fly are listed in the table below.

Table 3- 2: Important parameters of the vortex ring, all units are in *SI*

Re	15000
Nozzle exit diameter, D_0	3.76 x 10^{-2}
Average velocity, U_{avg}	6.00
Maximum diameter of ring	$2D_0$
Axial Distance where flow becomes uniform	3D0
Time when flow becomes steady	3.5 D_0/U_{avg}
Time duration of ring at any axial location	9.3 x 10^{-3}

Chapter 4. **Results and Discussion**

In this chapter, the experimental results for the effect of gusts on an insect flight have been presented. The results are divided into two parts. The first part deals with the effect of a gust on body kinematics, while the second one on the effect on wing kinematics of insects. Some inferences from the results are also discussed.

The success rate of insect encounters with gust in the test chamber was less than 1:10. Further, repeatability is one of the major issues while working with insects. To take care of this, a total of more than 1000 experiments were carried out, out of which data on 80 experiments, fulfilling the selection criteria, were stored and results of only 14 trials, which were enough to depict some general trends, are presented here. The following criteria needed to be satisfied- sharp antennal deflection of insect indicating successful gust hit, only one insect encountering a gust at a time, gust encounter in a region where gust velocity is nearly constant and obtaining focused images. All the experiments were carried out in similar ambient conditions (See Methods and materials). It was ensured that the insect would get hit by a vortex ring in a particular region, called a region of interest (ROI) in the test chamber. The volume of ROI was kept $2D_0$ X $2D_0$ X $2D_0$ at an axial distance of $3D_0$ from the nozzle exit. At this axial length, the velocity of the vortex ring becomes uniform and steady and the diameter of the ring is in the range $1.5D_0 – 2D_0$, i.e. 4-6 times body length and 3-4 times wingspan of the fly (See 3.5, and Figure 3-3). The ROI volume ensured that focused and high-resolution images of the fly were obtained.

Table 4-1: Important parameters of insect, All units are in *SI*

Average body length,L	1.54×10^{-2}
Wing Radius (length), R	1.1×10^{-2}
Wing Span,b	2.2×10^{-2}
Wing Mean Cord length, $\bar{c}$	3.5×10^{-3}
Wing Aspect Ratio, AR=2R/$\bar{c}$	6.25
Wing Beat Frequency,f	110
Time period of one Wing Beat (WB)	9×10^{-3}
Stroke amplitude,θ_0	115°
Fly avg. velocity, U_{fly}	0.72±0.14
Wing tip velocity, $U_t = 2\theta_0 Rf$	4.85
Re_{fly}, $4\theta_0 R^2 f/ (\nu * (AR))$	1.1×10^3
Time period of gust	1WB

The Reynolds number of the fly is calculated based on its wing stroke amplitude, radius and aspect ratio, and wingbeat frequency, and is given as

$$Re_{fly} = \frac{4\theta_0 R^2 f}{\nu * AR}$$

Some of the important parameters regarding the fly are given in Table 4-1.

4.1 Body kinematics

The study of body kinematics focuses on the study of flight trajectory, velocity and acceleration, body angles, angular rates, and trajectory angle, results on each of which are discussed below.

4.1.1 Flight Trajectories

The primary question that we asked is how the gust affects the flight trajectory of the insect. Any change in the flight trajectory would also give us an idea of the change in velocity and acceleration of the insect due to gust. The velocity and acceleration are discussed in the next section.

Figure 4-1 (a to n) shows flight trajectories for the cases with time and axial distance. The axial direction is considered X, vertical is Z, and normal to X-Z plane is Y. Origin is at the center of the nozzle exit. One-third of body length from the head towards the abdomen was considered as the center of mass and is represented as CoM. As the insects fly towards the nozzle, its X-location decreases with time. Figure 4-2 shows the flight trajectories for all the cases in the Y-Z plane. Let us define some terms used in Figure 4-2 to understand the results better. We define response time as the time when the fly starts opposing the change in velocity induced by a gust on its flight motion, while recovery time as the time when the fly starts flying with near-constant velocity after the response phase.

Before being hit by a gust, the CoM along the axial direction, in all of the cases, changed mostly linearly with time, as shown in Figure 4-1 (a - n). CoM was at most 1L offset in Y and Z directions from X-axis.

During the period of gust, the initial trend continued, and no any significant change was observed in the position of CoM along three directions.

A relatively small change was observed along the axial direction ($X_L < 1$) for six wing beats after gust. Linear change was noted along axial direction afterward. This trend was observed for 9 cases (see Figure 4-1 (a to h and n)), while for other cases, initial trend (before being hit by gust) continued with slight change in slope, as shown in Figure 4-1 (i to m). Maximum change along lateral and vertical directions after gust was ± 6L, as shown in Figure 4-1 (a-n).

The flies were observed to fly at a higher altitude just after being hit by gust till response time as seen in Figure 4-2 (a to k and m) and at lower altitude as seen in Figure 4-2 (l, n), while the final flying altitude of the flies decreased after recovery in all the cases except some as shown in Figure 4-2 (a, c, d, i and k). It is also noted that the flies, in majority of the cases, flew outside the circumference of vortex ring due to gust as can be seen in Figure 4-2 (a, b, c, d, e, I, k, l, m and n)

It is noted that the flies didn't recover along Y and Z directions after gust in any of the cases (i.e. after gusts, they didn't regain to their original positions as they were initially before gust), as shown in Figure 4-2. Our results vary from results from earlier experiments on the effects of a gust on flight trajectory on Bumblebees (Jakobi et al. 2018), where recovery of initial trajectory was reported in case of upward and lateral gusts. The difference may be attributed to different perturbation method (thin continuous air sheet in that case), body and wing morphology, flapping frequency and wing loading.

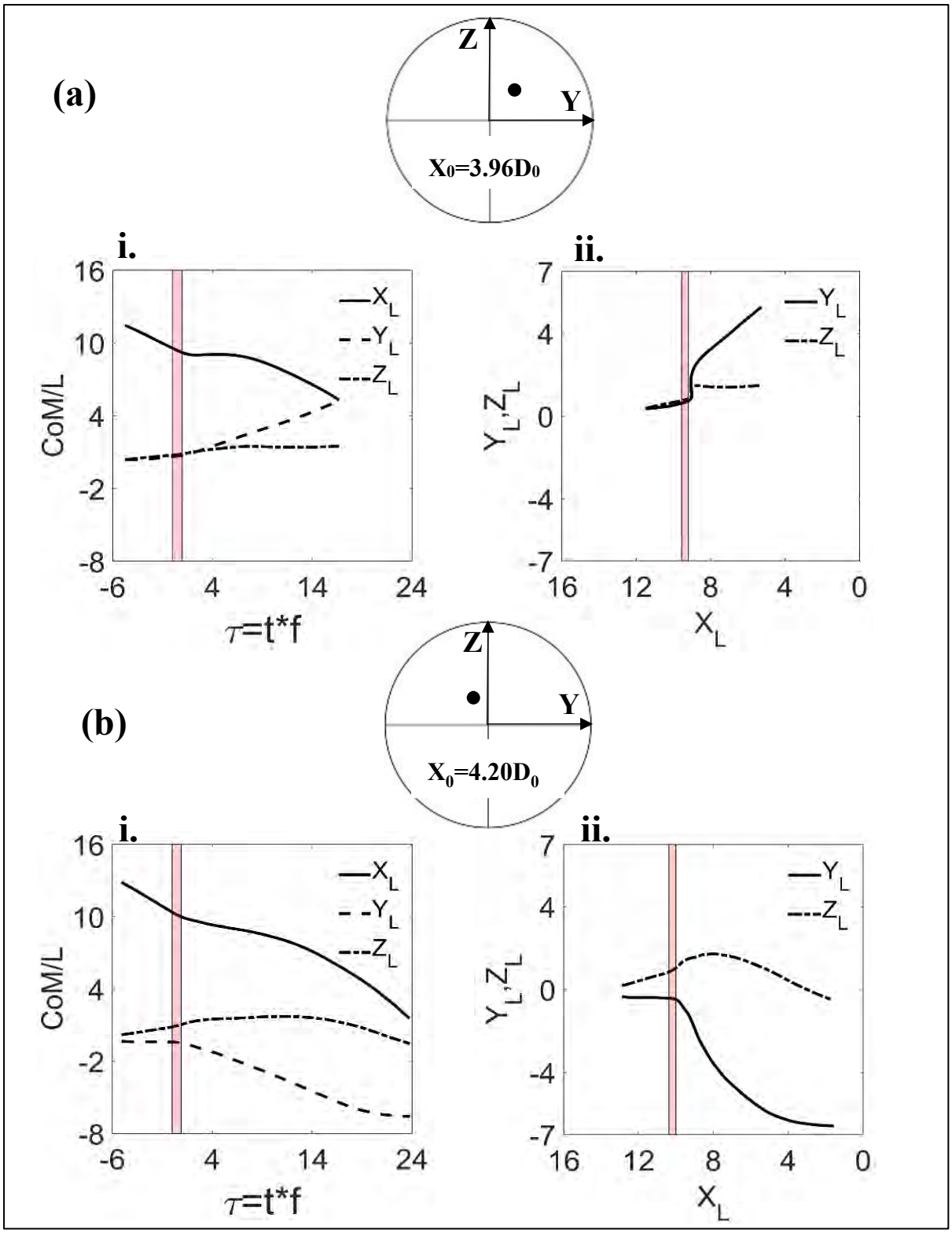

Figure 4-1: Flight trajectory. Vertical strip denotes time instance of vortex ring. Circle represents front view of the ring and black dot inside it the relative position of insect, with its axial distance from nozzle exit represented by X_0. Small alphabets within parenthesis ((a), (b)) indicate trials, while (i) and (ii) are flight trajectory with time and axial direction resp. Position and time are non-dimensionalized with body length and wing beat frequency respectively. CoM is center of mass of fly. X_L is axial distance from nozzle exit, Y_L is normal lateral distance and Z_L is vertical distance, following Right-handed coordinate system. $\tau = 0$ indicates the instance when fly was just hit by gust.

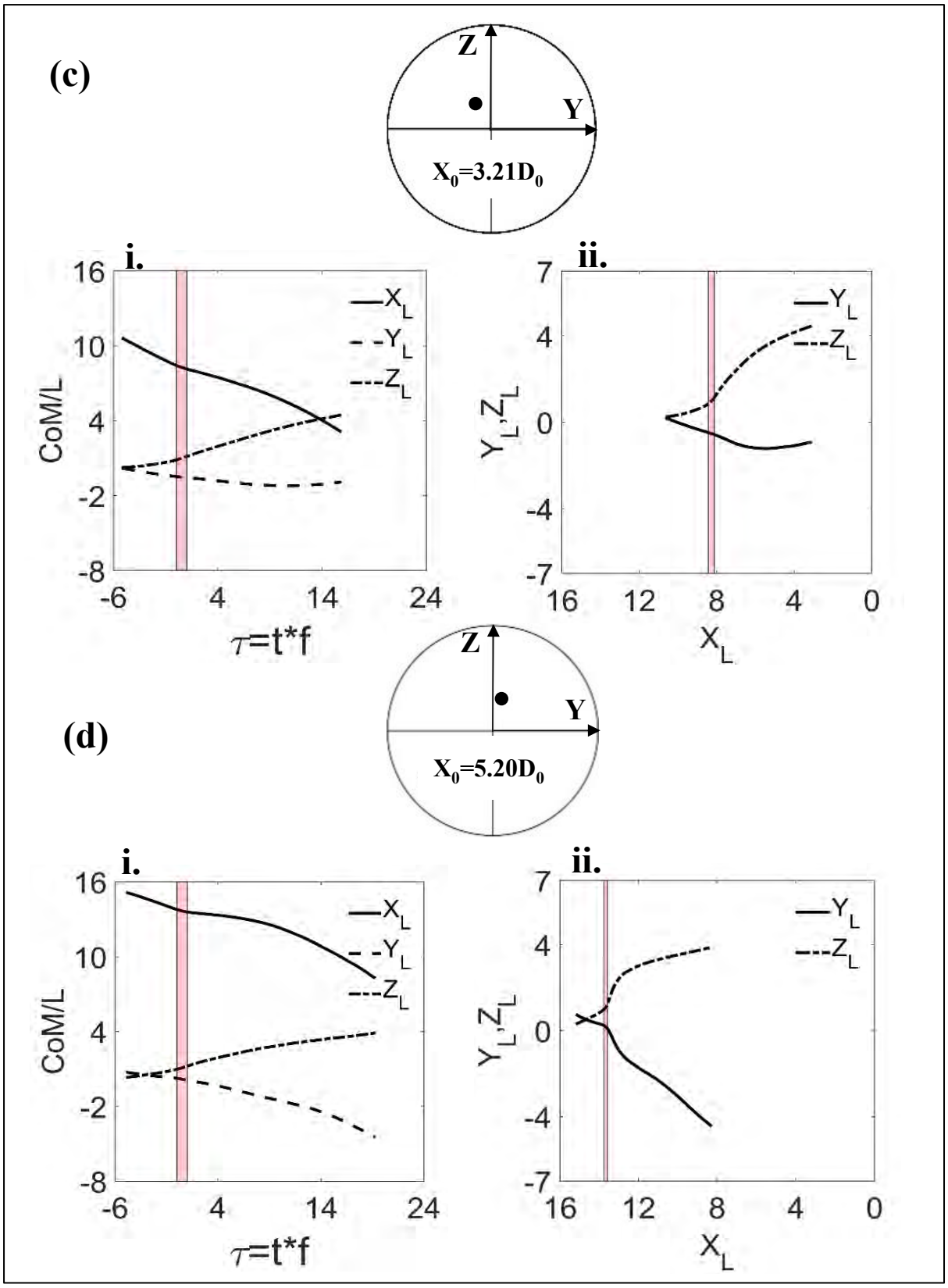

Figure 4-1: (continued)

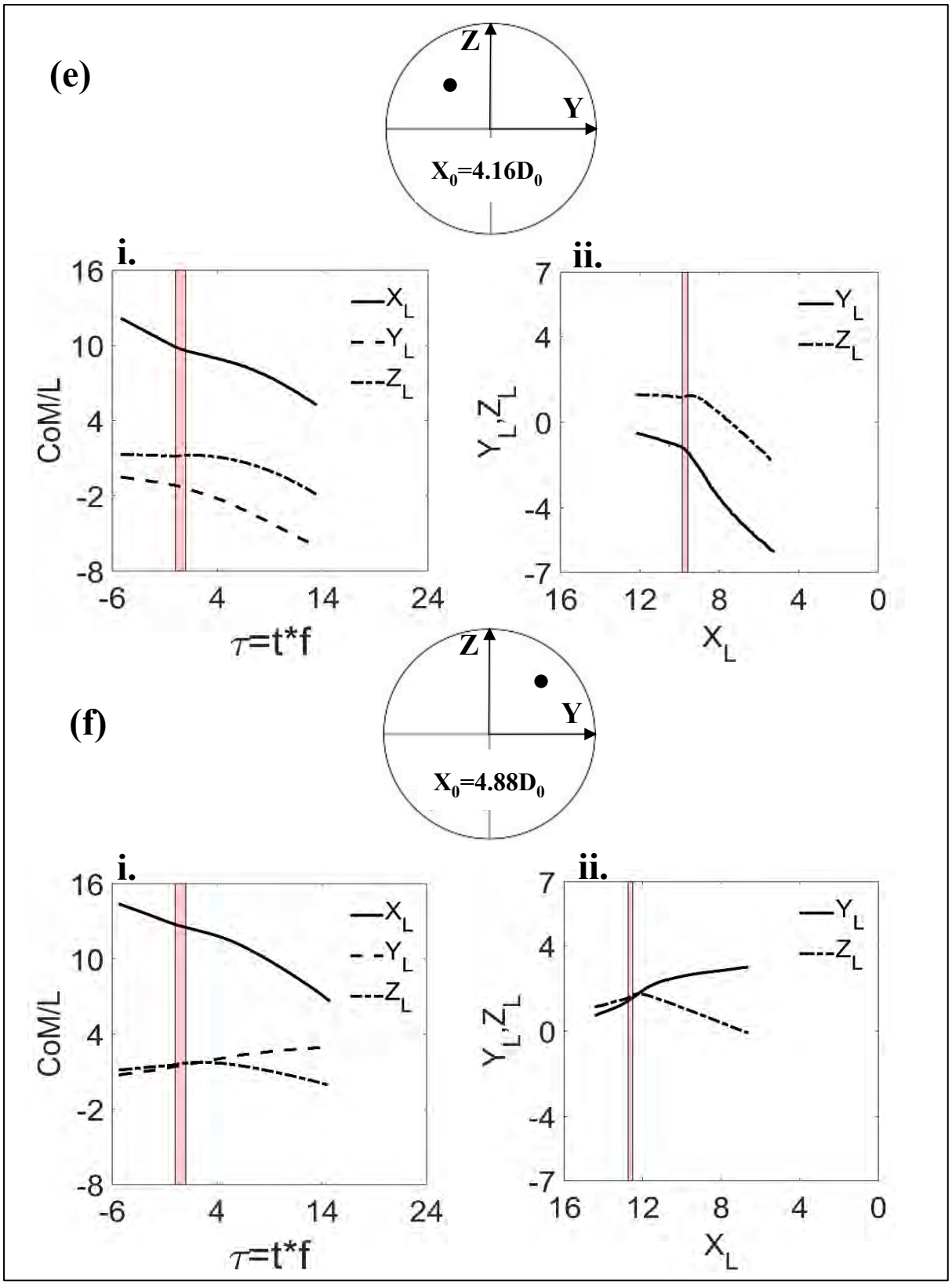

Figure 4-1: (continued)

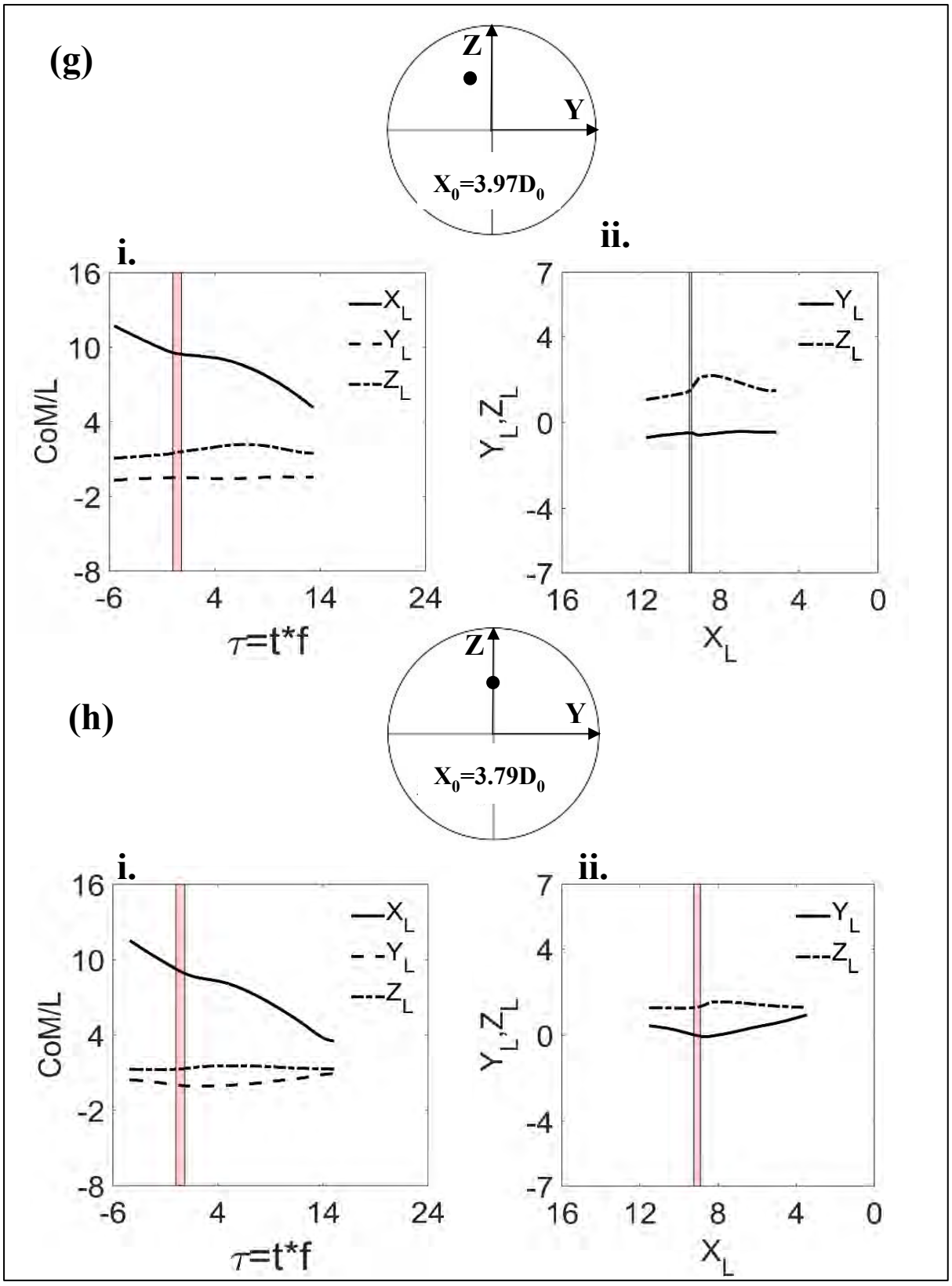

Figure 4-1: (continued)

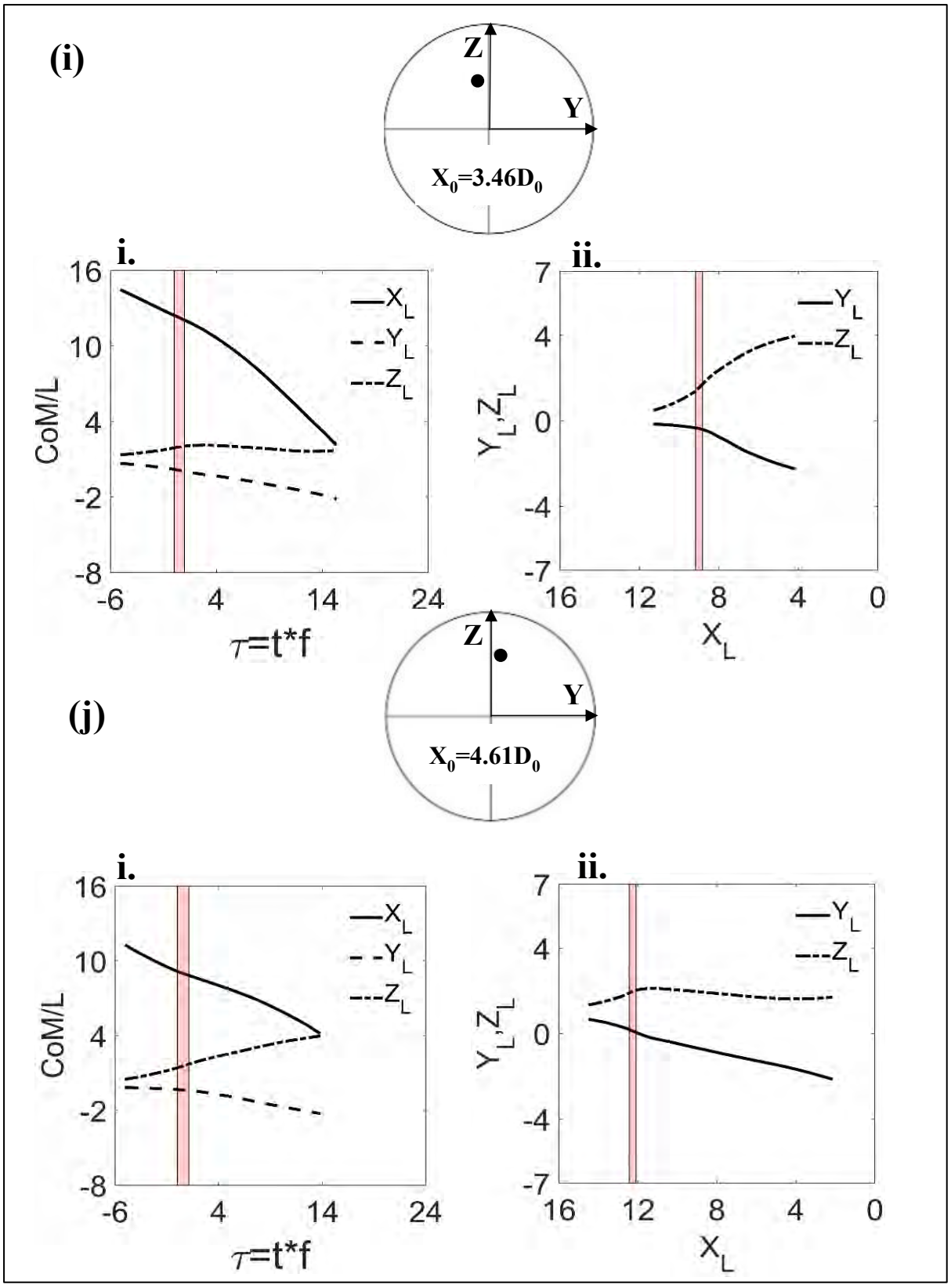

Figure 4-1: (continued)

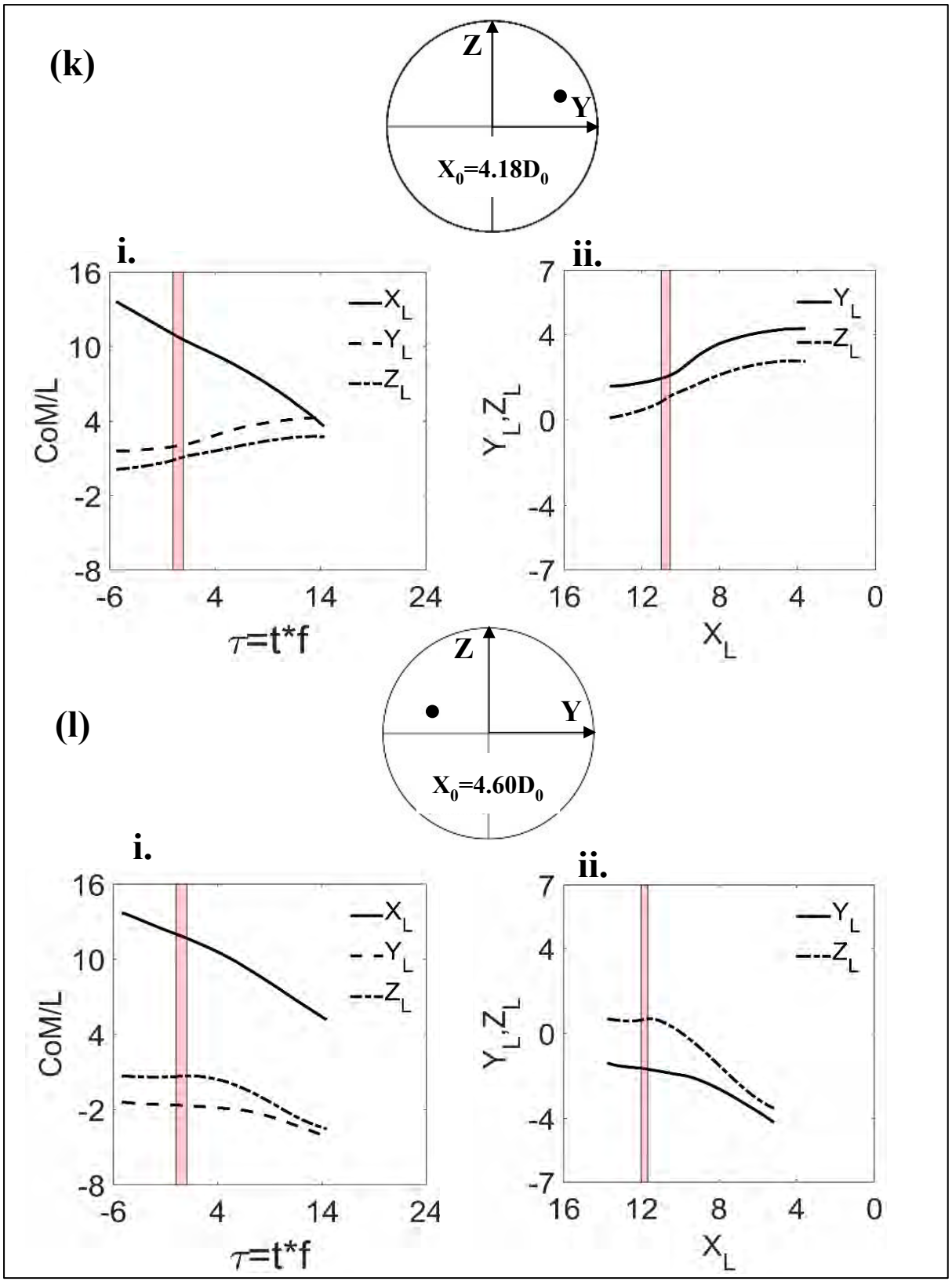

Figure 4-1: (continued)

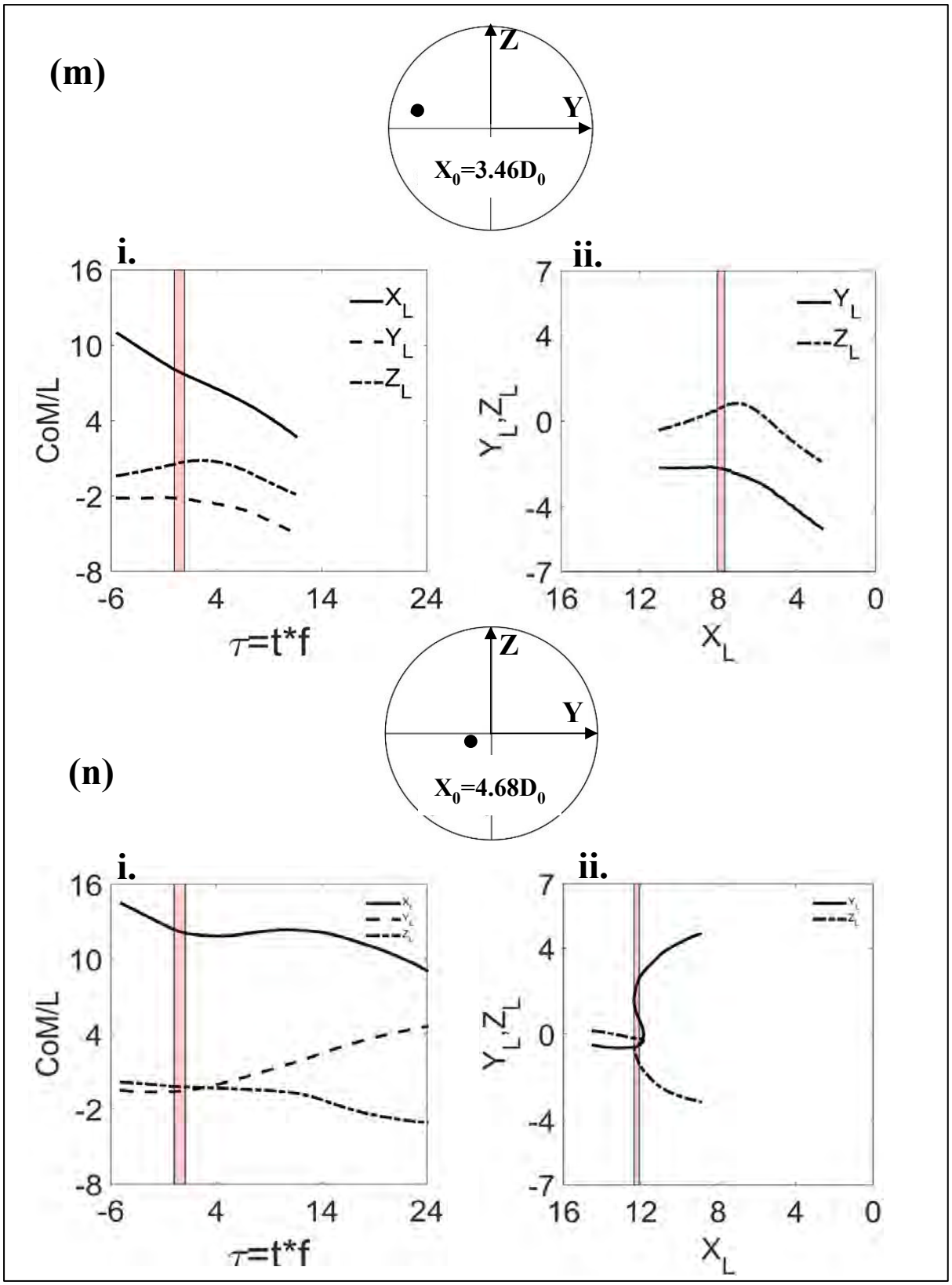

Figure 4-1: (continued)

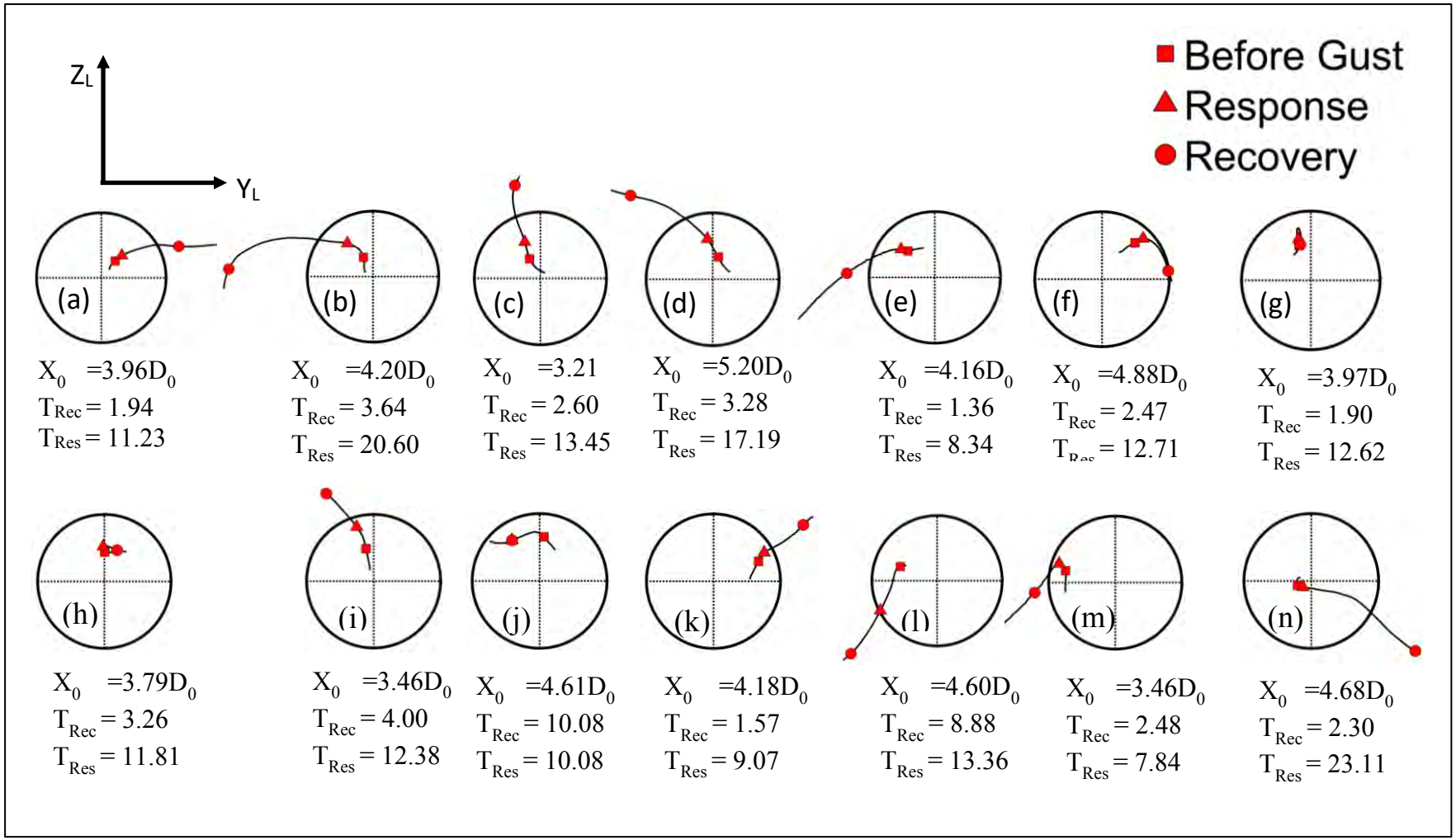

Figure 4-2: Flight trajectory, Z_L vs Y_L. Circle represents the circumference of the vortex ring when viewed from front. The axial distance where insect was hit by gust is represented by X_0 in terms of nozzle exit diameter D_0 and is given below each figure. $\mathbf{T_{Res}}$ and $\mathbf{T_{Rec}}$ deonte response and recovery time in wing beats. Small alphabets within parenthesis ((a), (b)) indicate trials. Z and Y are non-dimensionalized with body length and are represented by Y_L and Z_L respectively. Y_L is lateral distance and Z_L is vertical distance. Filled square, triangle and circle represent the time instances before gust, after response and recovery respectively.

4.1.2 Flight velocity and acceleration

Figure 4-3 shows, for each case, the three dimensionless velocity components and the velocity magnitude while dimensional velocity and acceleration values are shown in (ii) of each figure. Velocity is non-dimensionalized with the product of the average body length of fly and its average wingbeat frequency. The velocity components along axial, lateral and vertical directions are represented by u_n, v_n, and w_n respectively, while their magnitude is represented by U_n. Plotting all the components and magnitude of the velocity together gives an idea of the contribution of each component in the flight speed of the fly. The dimensional velocity and acceleration are represented by **"U"** and **"a"** respectively. A fourth-order low pass Butter-worth filter with cut-off frequency 200Hz was first applied to the CoM position data and the velocity and acceleration were then calculated using second-order central difference scheme as discussed in section 3.5. We follow the same definition for response and recovery time as defined in section 4.1.1. It is noted that response and recovery time can be different for each parameter, but on average they agree well with those for forward speed of flight. The response and recovery time based of forward velocity change are listed in Table 4- 2.

Before being hit by gust, the dimensionless axial velocity of the fly was 0.36 ± 0.08, i.e. 60 ± 13 cm/s (mean ± SD), lateral velocity -0.03 ± 0.11 (-5 ± 18 cm/s) and vertical velocity 0.14 ± 0.09 (23 ± 15 cm/s), indicating low velocity in transverse direction compared to the axial one, as can be seen in Figure 4-3 (i) . The velocity magnitude of the forward flight was 69 ± 14 cm/s before gust, while the acceleration was near zero (see Figure 4-3 (ii)).

During the period of gust(~ 1 wing beats), velocity along the axial direction decreased by 26% (see Figure 4-4 (i)), while it increased by 53% and 4% on average along Y and Z directions respectively as shown in Figure 4-4 (ii and iii). The overall velocity magnitude decreased by 15% on average during the gust as shown in Figure 4-4 (iv).

During response time (~ 3.5 wing beats after gust), axial velocity on average decreased by 36% while lateral velocity increased by 150% and vertical velocity decreased by 83%, as shown in Figure 4-4. The velocity magnitude during this period decreased on average by 30% in all cases, except for two cases j and k (see Figure 4-3 (j, k), where the flight velocity increased by 90% and 135% respectively.

After recovery time (~ 13 wing beats after gust), the axial, lateral and total velocity (velocity magnitude) when compared to that before gust increased by 47%, 250% and 55% respectively and the vertical velocity decreased by 225% (see Figure 4-4). The flies after recovery mostly maintained constant velocity for cases a to l (see Figure 4-3 (a to n)), except in two cases j and k (see Figure 4-3 (j and k)), where they further accelerated.

Two main observations in the flight velocity are (a) sudden decrease in forward speed due to gust till response time, the maximum deceleration reached to 22 m/s^2 after gust as shown in Figure 4-3 (a and n) and (b) velocity after recovery period is higher than that before gust in all cases as can be seen in Figure 4-3 (a to n).

The deceleration of fly due to gust in the present study is consistent with the findings of Combes & Dudley (2009), Jakobi et al. (2018) and Ravi et al. (2013) where they report turbulence and gust as a limiting parameter on the forward speed of insects (especially bees).

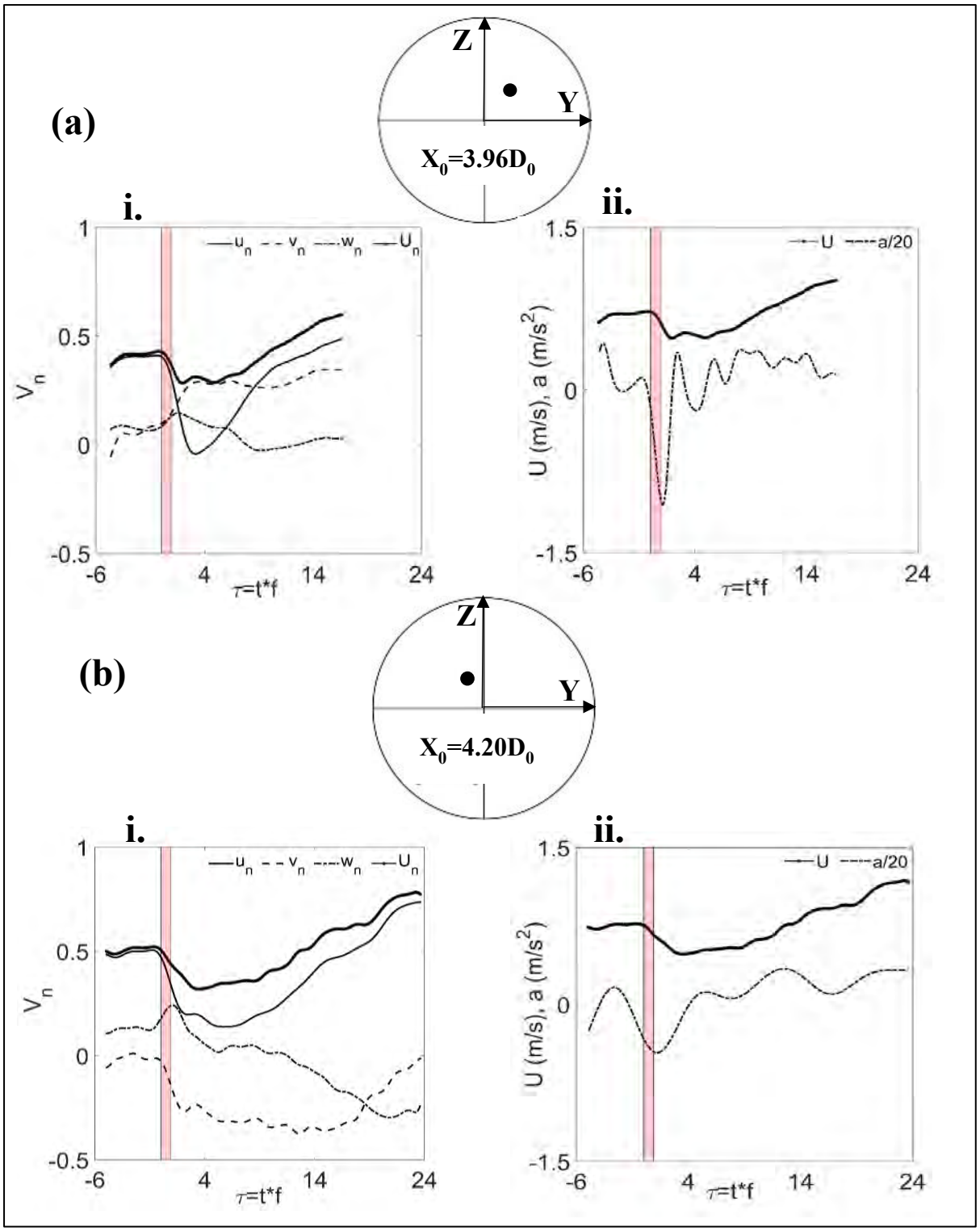

Figure 4-3: Flight velocity and acceleration. Vertical strip denotes time instance of vortex ring. Circle represents front view of the ring and black dot inside it the relative position of insect, with its axial distance from nozzle exit represented by X_0. Small alphabets within parenthesis ((a), (b)) indicate trials, while (i) and (ii) are non-dimensional velocity components (V_n), and dimensional velocity (U) and acceleration (a) plotted against time (T) resp. u_n, v_n, w_n are dimensionless velocity components along X, Y and Z axes. U_n is dimensionless velocity magnitude. Vn = V/(L*f) and τ=t*f. V is respective velocity component. $\tau = 0$ indicates the instance when fly was just hit by gust. Note acceleration is scaled down by 20 to fit in the plot together with velocity magnitude.

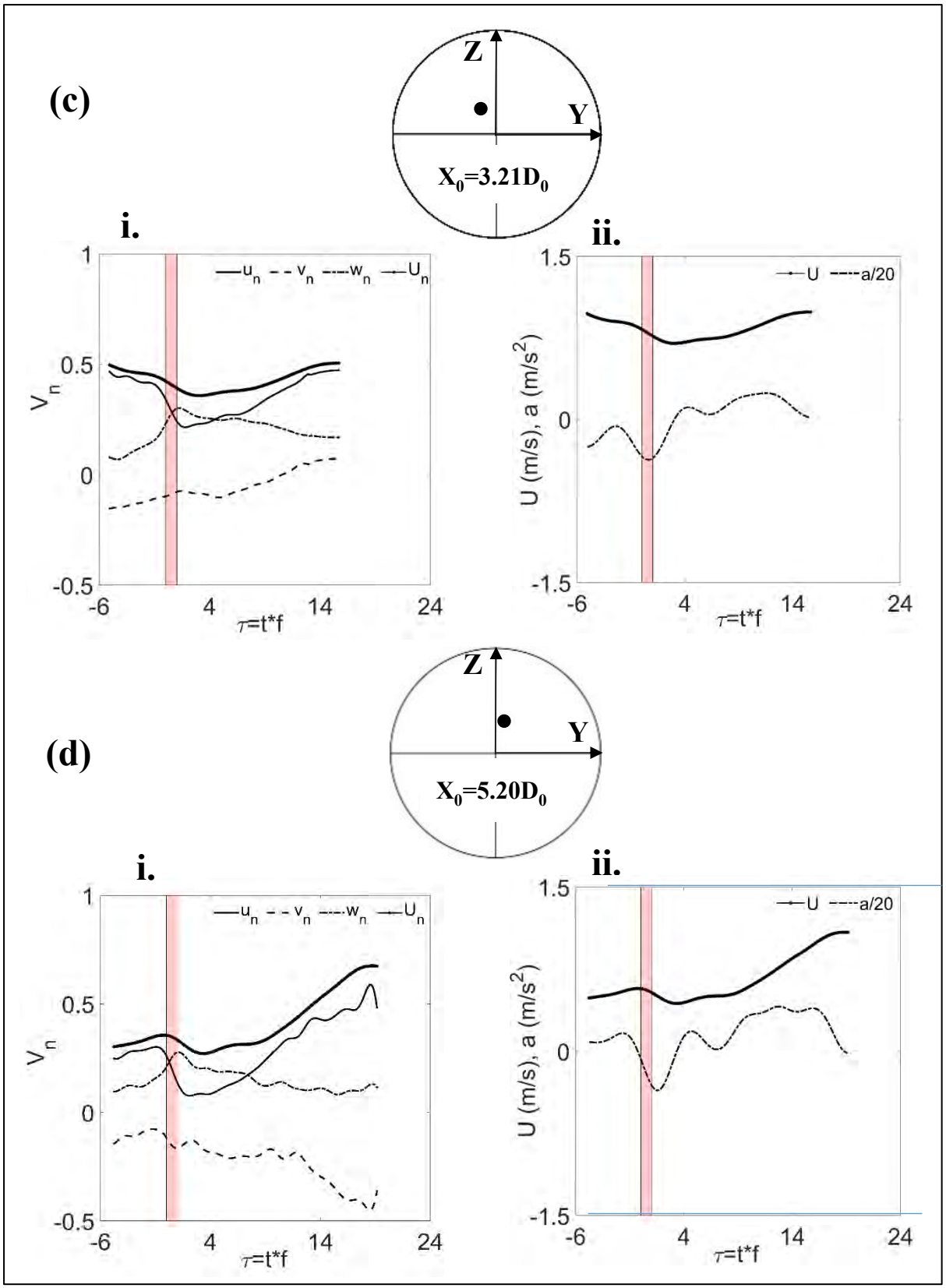

Figure 4-3: (continued)

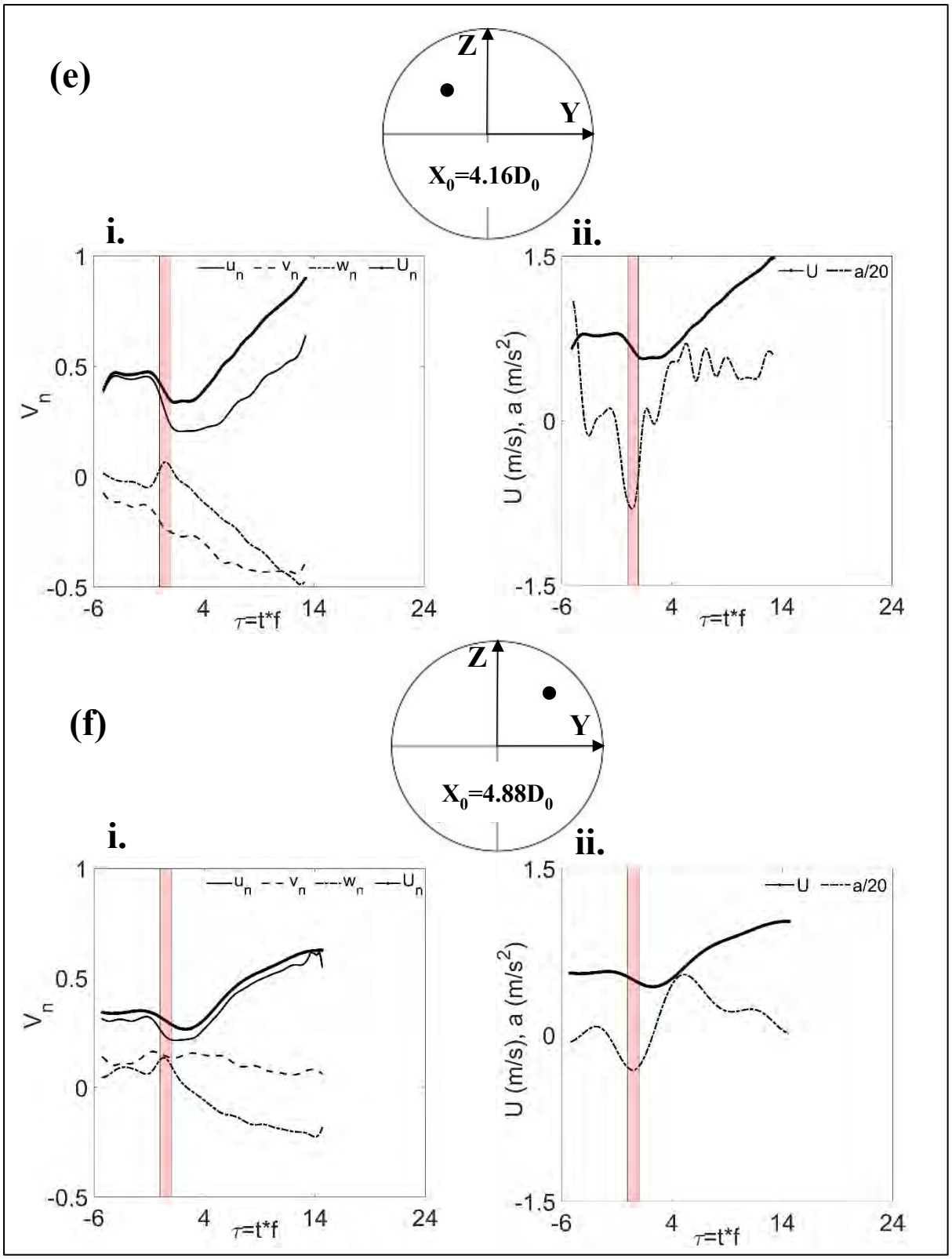

Figure 4-3: (continued)

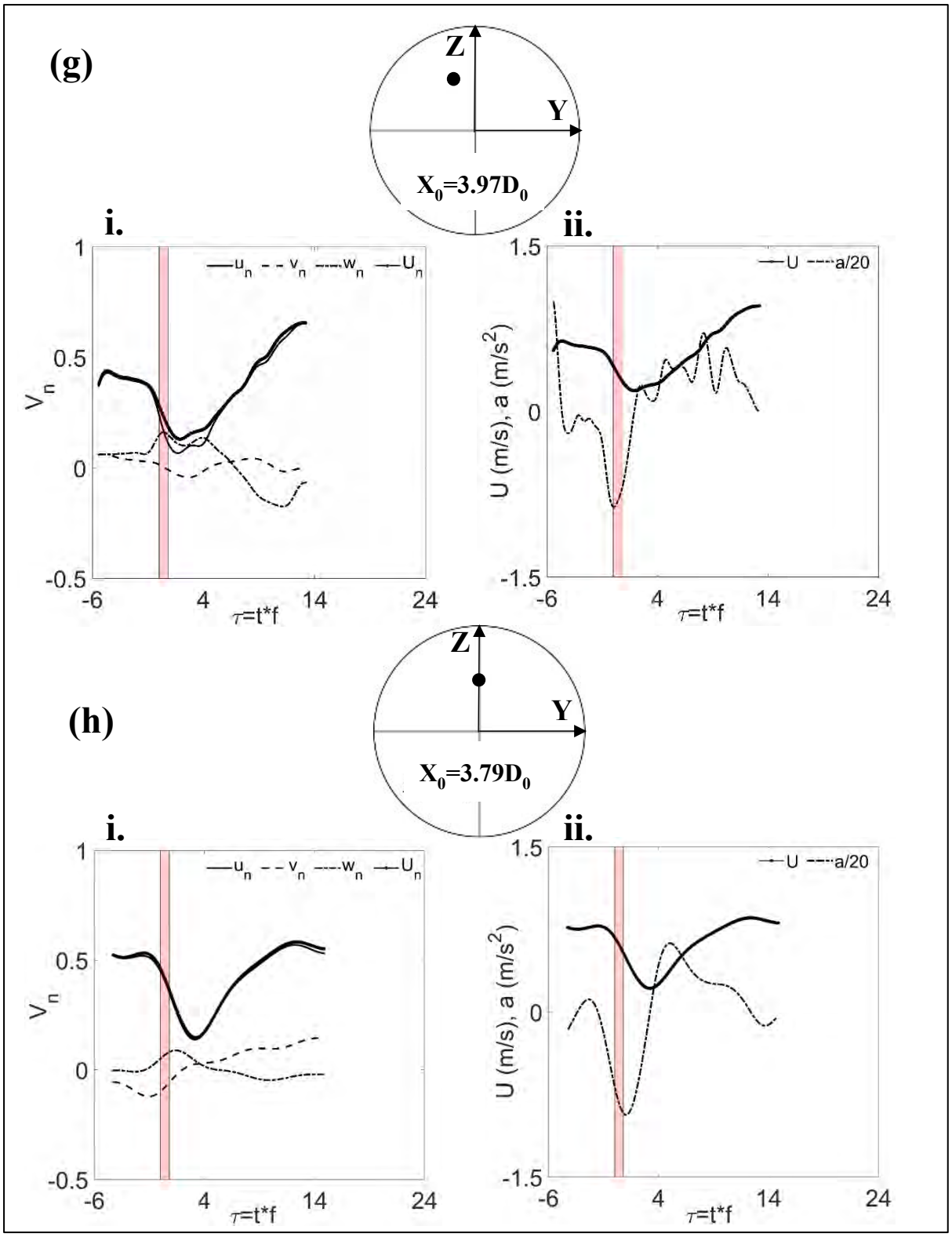

Figure 4-3: (continued)

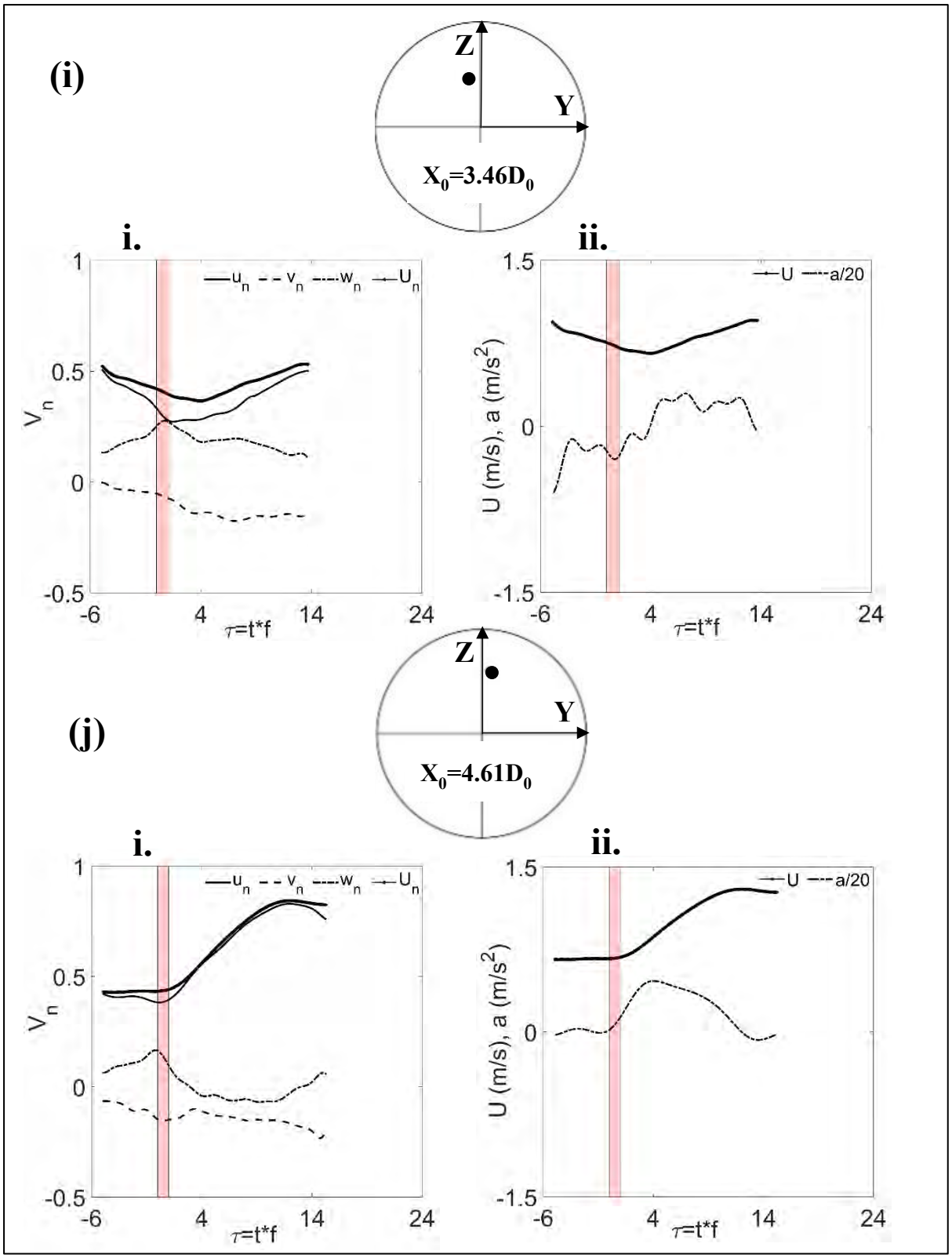

Figure 4-3: (continued)

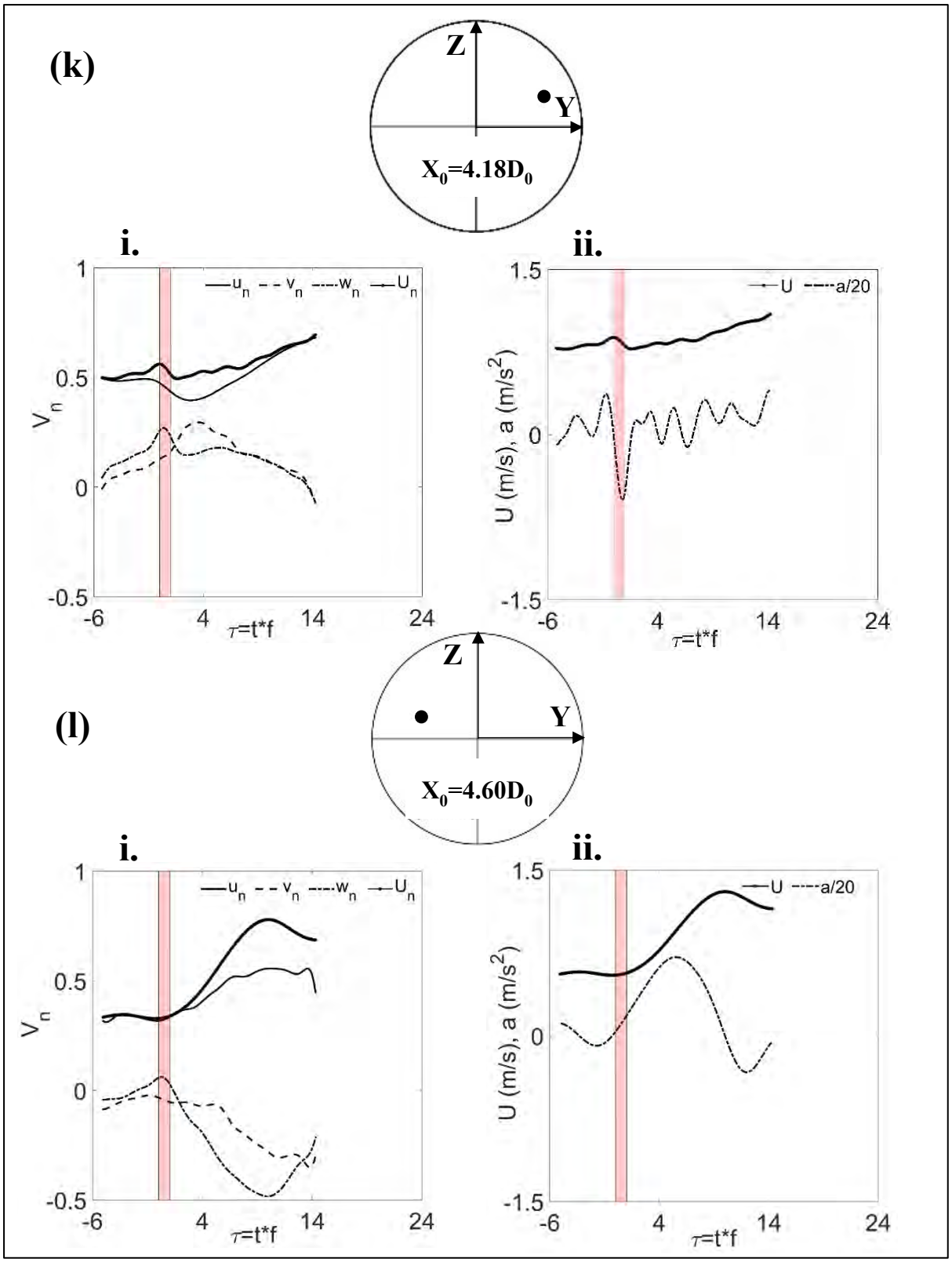

Figure 4-3: (continued)

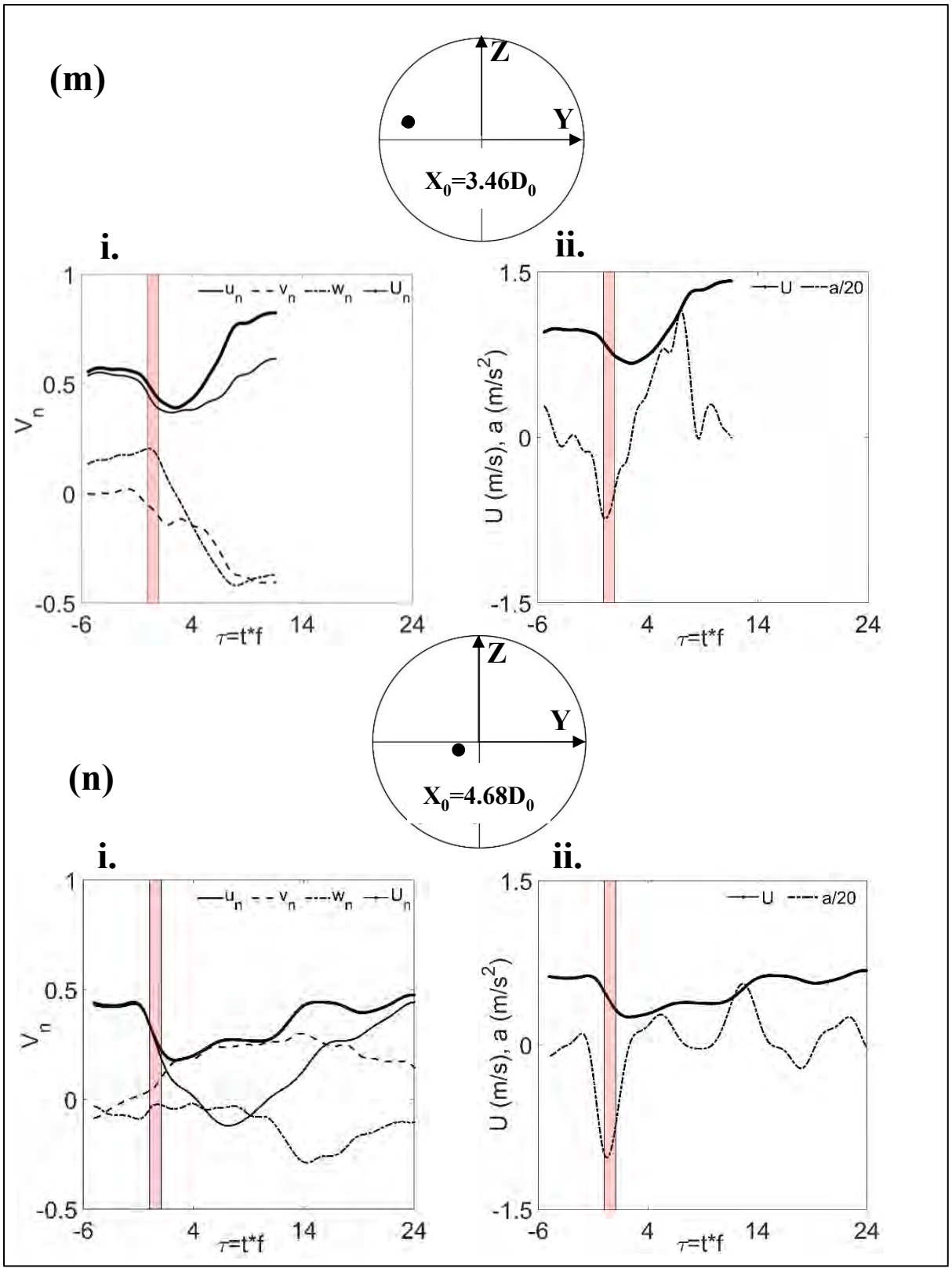

Figure 4-3: (continued)

BG – Before Gust **AG** – After Gust **Res**- Response time **Rec**- Recovery Time

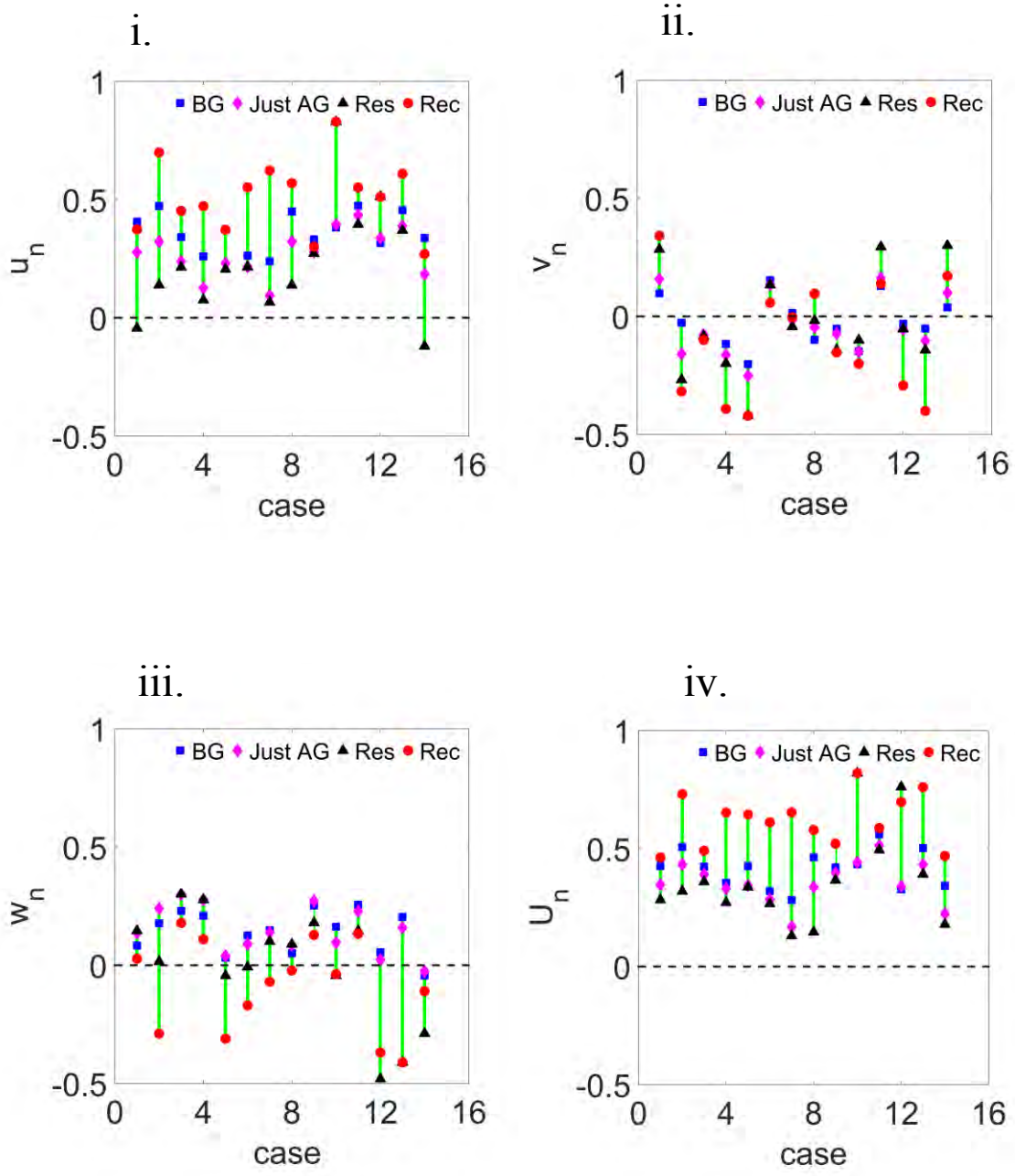

Figure 4-4: Velocity components and magnitude for different trials. BG, AG, Res and Rec are used to denote time instance just before gust, after gust, response time and recovery time respectively. Dashed line in each plot denotes zero value of the corresponding velocity. Non-dimensional velocity components in (i) axial, (ii) lateral, and (iii) vertical directions respectively. (iv) Total velocity (magnitude). u_n, v_n, w_n are dimensionless velocity components along X, Y and Z axes. U_n is dimensionless velocity magnitude, each non-dimensionalized with the product of body length and wing beat frequency.

Table 4- 2: Response and recovery times of insects for different cases. Response time is the time when the fly starts opposing the change in forward speed induced by a gust on its flight motion, while recovery time as the time when the fly starts flying with near-constant forward speed after the response phase.

# Expt	Response time (wing Beats)	Recovery time (wing Beats)
a	1.94	11.23
b	3.64	20.60
c	2.60	13.45
d	3.28	17.19
e	1.36	8.34
f	2.47	12.71
g	1.90	12.62
h	3.26	11.81
i	4.00	12.38
j	10.08	10.08
k	1.57	9.07
l	8.88	13.36
m	2.48	7.84
n	2.30	23.11
μ	3.55	13.13
σ	2.63	4.27

4.1.3 Body angles

Figure 4- 5 gives the definition of the three body angles (yaw (φ), pitch (β), and roll (γ)). The respective angular rates are denoted by $\dot{\varphi}$, $\dot{\beta}$ and $\dot{\gamma}$. Pitch was calculated as the elevation angle of a vector joining head and CoM of the body, relative to the horizontal plane. Similarly, the azimuthal angle of the same vector on the horizontal plane gives yaw, and the elevation angle of the vector joining either wing base to the CoM gives a roll of the body with respect to the horizontal plane (see Figure 4- 5 for details of these angles). It is noted that the yaw angle so calculated gives the rotation of the body with respect to the global axis, i.e. absolute yaw. Counterclockwise rotation (i.e. rotation of insect from its right to left) in yaw and roll is considered positive. Similarly, pitched up is taken positive as shown Figure 4- 5. A fourth-order low pass Butter-worth filter with cut-off frequency 200Hz was applied to the raw body angle data to smoothen out high-frequency noise due to digitization. Angular rates were then calculated using a second-order central difference scheme as discussed in section 3.5. A MATLAB code for calculating body angles from raw position data is presented in Appendix B-*5*.

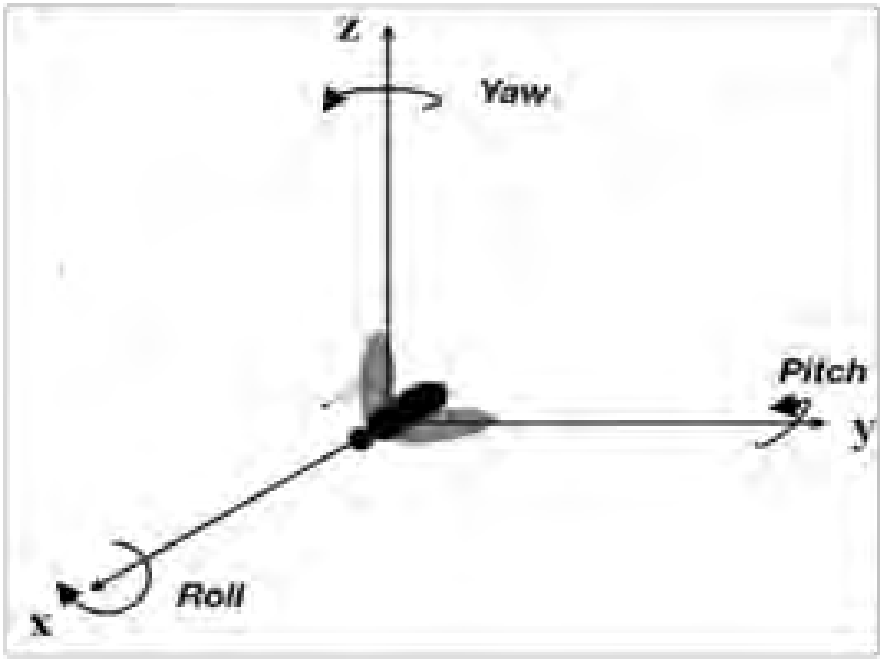

Figure 4- 5: Body axis system. Roll occurs about X-axis, pitch about Y and yaw about Z axes respectively. Counterclockwise rotation about X and Z axes are considered positive roll and yaw respectively, while pitch up rotation about Y axis is positive pitch.

In this context, we define *response time* as the time when the fly starts to rotate opposite to the rotation of the body induced by the gust, while *recovery time*, as the time when the angular rates become zero or constant. The main reason we chose to consider response and recovery time separately for velocity, body angles, and wing angle (to be discussed later) is that we can compare the response and recovery times for each kinematic parameter (as we'll see later in this section) and this can further help us discover if the fly responds to gust on a different time scale for each body and wing kinematic parameters. Figure 4-6 (i) and Figure 4-6 (ii) show body angles and angular rates of the fly respectively. Figure 4-7 shows the response and recovery time along body axes and for wing stroke amplitude (to be defined later) for the different cases. Similarly, we define *maximum change* as the difference in maximum body orientation induced due to gust and the value of body orientation of the fly before being hit by a gust. The difference in body orientation before gust and after recovery from gust is called here as *error*.

In most of the cases analyzed, the body roll angle underwent the largest change, that happened on an average, in two wing beats ($\sim 20\ ms$), and recovered to near-zero body roll angle in about 9 wing beats. We will discuss the response of the insect to the gust in terms of each body angle in detail.

Before being hit by gust, the initial orientation of the fly across the trials, along yaw, pitch and roll axes was 1 ± 37° (mean ± SD), 25 ± 13° and 7.2 ± 9.6 ° respectively with maximum and minimum values were 57° counterclockwise (CCW) (Figure 4-6 (j-(i))) and 60° clockwise (CW) along yaw axes (Figure 4-6 (a-(i))), 46° pitched up (Figure 4-6 (i-(i))) and 2° pitched up (Figure 4-6 (e-(i))) along pitch axis, and 21° CCW (Figure 4-6 (l-(i))) and 3° CW (Figure 4-6(i- (i))) along roll axes.

Due to gust, the change (mean ± SD) in roll was 35.8 ± 86.7°, with a maximum value 161.4° CW (see Figure 4-6 (m-(i))). Similarly, body yaw changed by 8.8 ± 33.1°, with maximum 68.8° CW (see Figure 4-6 (n -(i))) and pitch changed by -25.4 ± 23° with maximum 60.2° pitched down (see Figure 4-6(e (i))).

After recovery, the error calculated as the difference between the body orientation after recovery and that before gust was 5 ± 13.6° in roll with maximum 30° CCW (see Figure 4-6 (k-(i))) and minimum 18° CW (see Figure 4-6 (b-(i))), 3.4 ± 28.8° in yaw with maximum 56° CCW (see Figure 4-6 (k-(i))) and minimum 30° CW (see Figure 4-6 (b-(i))), and -22.7 ± 15.4° in pitch with maximum 15° pitched up (see Figure 4-6 (n-(i))) and minimum 47° pitched down (see Figure 4-6 (e-(i))). It was also observed that the fly would mostly attain zero roll angle (< 30°) after recovery (see Figure 4-6 (i)).

Response time was 2.1 ± 0.4 wing beats (WB), 5.4 ± 2.8 WB and 5.5 ± 1.3 WB along roll, yaw and pitch axes respectively, as shown in Figure 4-7 (a), indicating the least response time along roll axis, followed by yaw and pitch. Similarly, recovery time, as shown in Figure 4-7 (b), was noted 8.1 ± 2.6 WB, 9 ± 4.7 WB and 9.3 ± 3.4 WB along roll, yaw and pitch axes respectively, indicating the flies take approximately same time (~ 9 WB) to correct its body orientation along the three axes. The initial and final orientation, response time, recovery time along each body axis for the different cases are listed in Table 4- 3, Table 4- 4, and Table 4-5. The tables also show maximum change and error value for each trial. It is noted that value tabulated in the bold face was not considered while calculating mean and SD for roll angle.

Table 4-6 shows the maximum angular rates along each axis for the different trials. The roll rate was 21 ± 86°/WB, yaw rate 2 ± 11°/WB and -9 ± 13°/WB with maximum 250°/WB (see Figure 4-6 (m-(ii))), 20°/WB (Figure 4-6 (n-(ii))) and -26°/WB (Figure 4-6 (h-(ii))) along roll, yaw and pitch axes respectively.

Distinct change in body roll angle on such a short time scale across all trials shows that the fly is highly susceptible to gusts along the roll axis. The observation agrees with the findings of experiments carried out on other insects (Bees and flies) by different researchers (Combes & Dudley 2009; Ravi et al. 2013; Vance et al. 2013; Beatus et al. 2015). This suggests that not only in flies but also in other insects, body roll is quite sensitive to gust. The fly recovering to near-zero roll orientation after recovery time suggests that it is the preferred orientation. Some literature reports that the recovery in roll is accompanied by an extension of legs (Taylor 2001; Combes & Dudley 2009; Ortega-Jimenez et al. 2013; Jakobi et al. 2018; Beatus et al. 2015). Such observations are observed in the present study as well. Similarly, asymmetry in wing stroke amplitude was observed (to be discussed later).

Results show that the fly responds to gust along pitch and yaw axis as well, but the change is not as significant as that in roll. Further, unlike in roll, it never attains the initial orientations, but mostly stabilizes to new body orientations exhibiting neutral stability along these axes. Abdominal deflection (inward deflection of rearmost part of the body), as noted by Ravi et al. (2013), Taylor & Thomas (2002) and Taylor (2001), for pitch stability was not observed in the present study. The difference may be attributed to a different body and wing morphology, flapping frequency and wing loading.

Highest angular velocity was found along roll axis, followed by that along pitch and yaw axes, as shown in Figure 4-6-(ii) and Table 4-6. This observation, at least along roll axes, is consistent with findings of Beatus et al. (2015) and Vance et al. (2013), despite the employability of different methods of perturbation (i.e., magnetic field in case of Beatus et al. (2015) and air-jet in case of Vance et al. (2013)). The observations regarding pitch and yaw rates are in contrast to that in stalk-eyed flies studied by Vance et al. (2013), where the authors reported

yaw angular rate higher than pitch angular rates by ~3 times, while the present study shows that yaw and pitch average angular rates are approximately same.

Response time along roll axis is on average 2.5 times faster than that along pitch and yaw axes as shown in Figure 4-7 (a) and agrees well with the findings of Beatus et al. (2015). Beatus et al. (2015) also compared the roll response time in fruit fly with existing literature on yaw (Ristroph et al. 2010) and pitch (Ristroph et al. 2013) correction in gust and found that it was 3.5 times faster than yaw response and 2.5 times than pitch response. In contrast, the present result suggests approximately equal response time along both yaw and pitch axis in the gust. Also, the recovery time is approximately the same along the body axes as shown in Figure 4-7 (b).

Such a short response time, high angular rates and short recovery time along each axis suggest that passive mechanism alone cannot be accounted for these observations. Fly must also be employing an active mechanism to recover from perturbation caused by the gust (Sherman & Dickinson 2003; Vance et al. 2013; Jakobi et al. 2018; Ristroph et al. 2010; Ristroph et al. 2013).

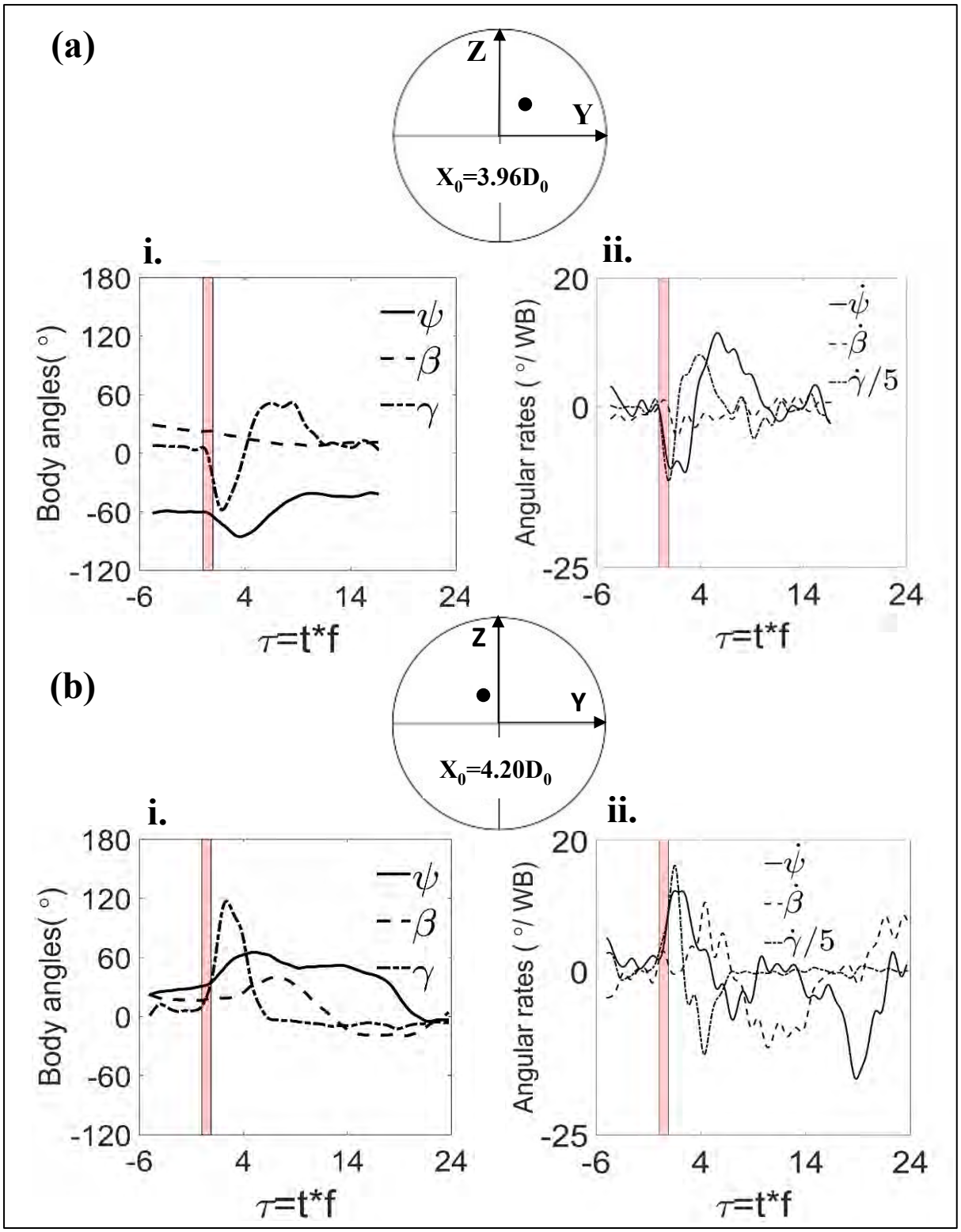

Figure 4-6: Body angles and angular rates. Ψ, β and γ represent yaw, pitch and roll respectively, while $\dot{\Psi}$, $\dot{\beta}$ and $\dot{\gamma}$ are respective angular rates. Vertical strip denotes time instance of vortex ring. Circle represents front view of the ring and black dot inside it the relative position of insect, with its axial distance from nozzle exit represented by X_0. Small alphabets within parenthesis ((a), (b)) indicates trials while (i) and (ii) are body angles and angular rates plotted against dimensionless time (τ) respectively. τ=0 indicates the instance when fly was hit by gust. Note angular rates are expressed in degree per wing beats. Roll rate is scaled down by 5 times. Counterclockwise rotation in yaw and roll and pitched up rotation are considered positive here.

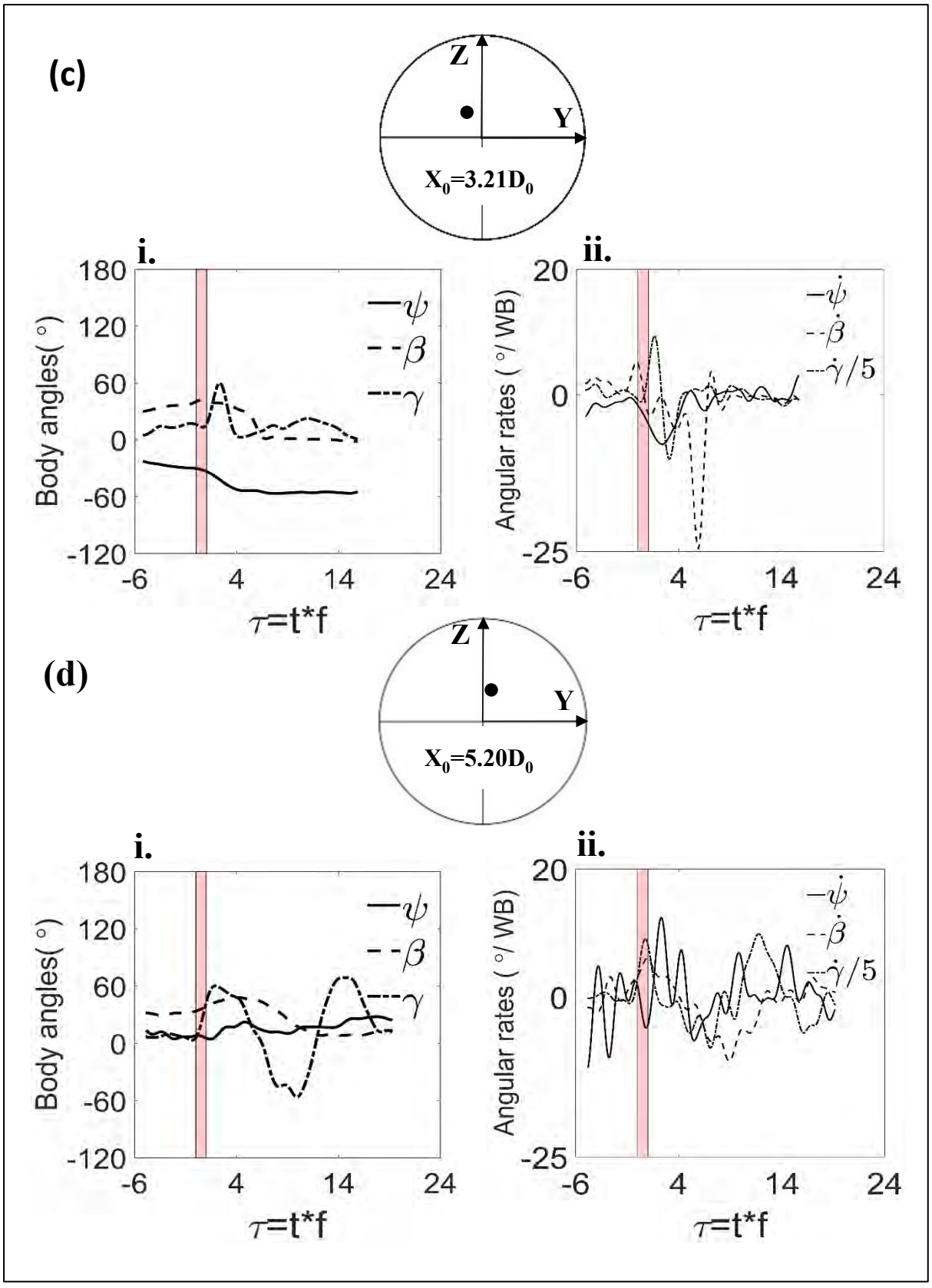

Figure 4-6: (continued)

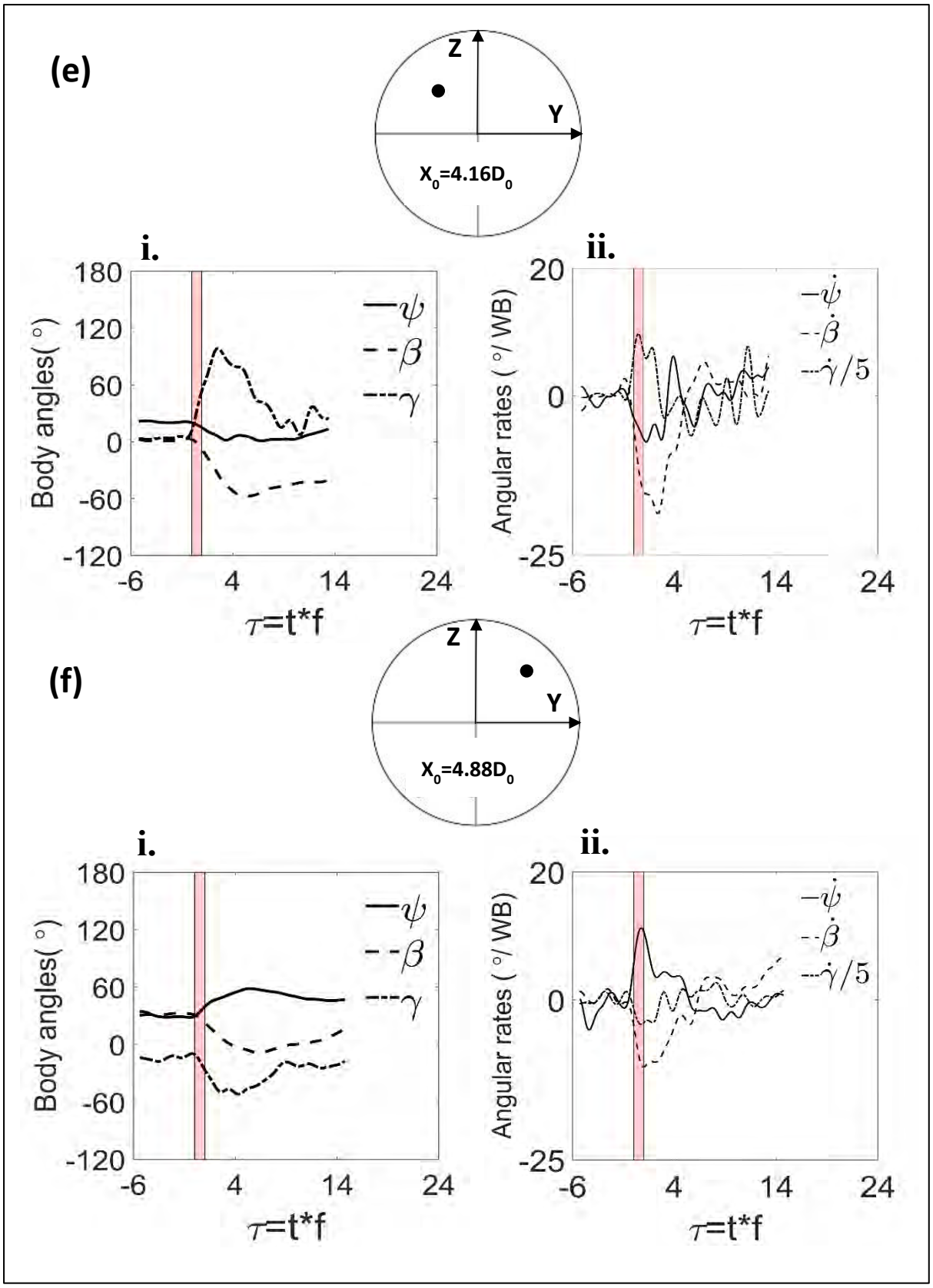

Figure 4-6: (continued)

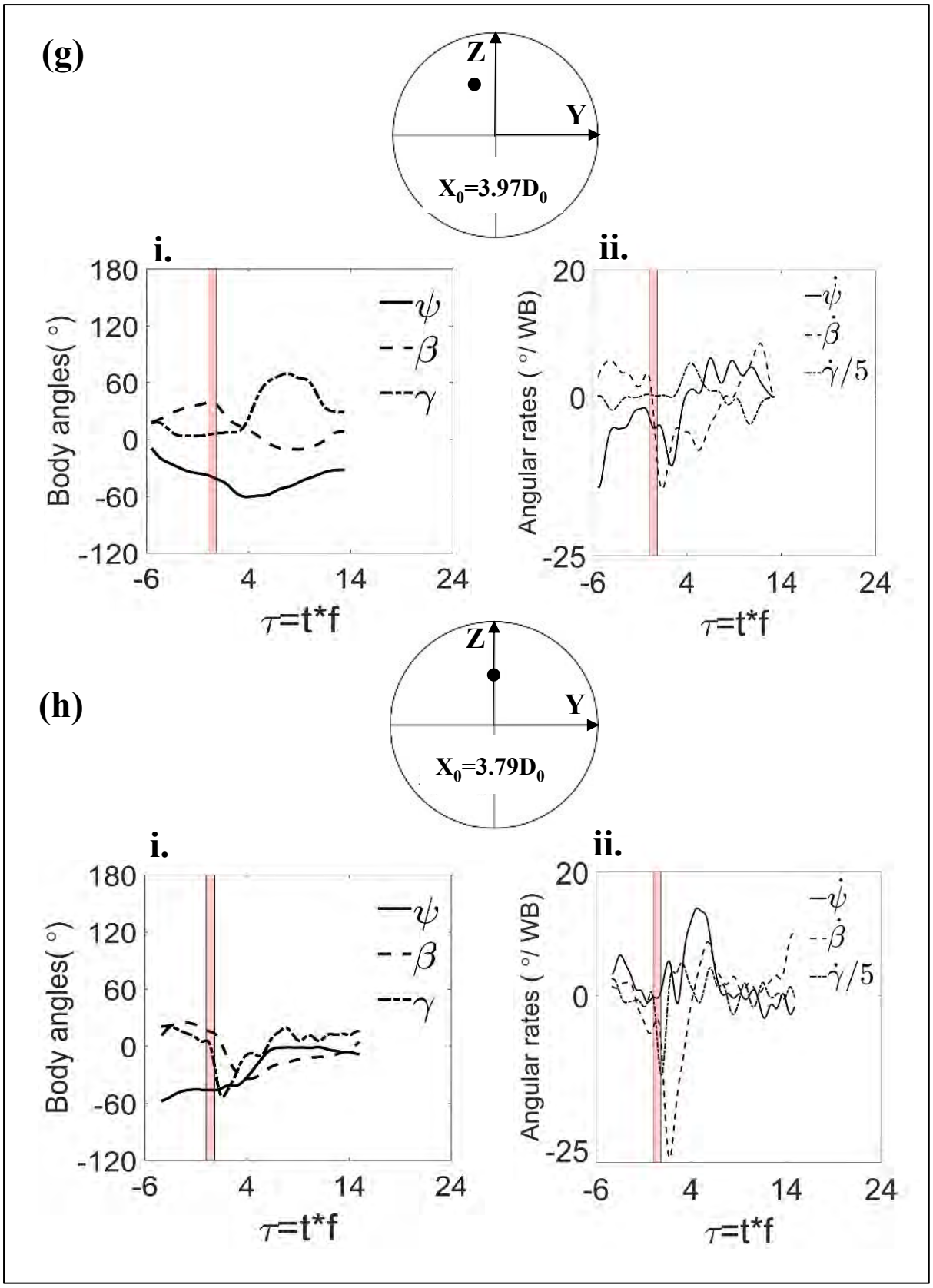

Figure 4-6: (continued)

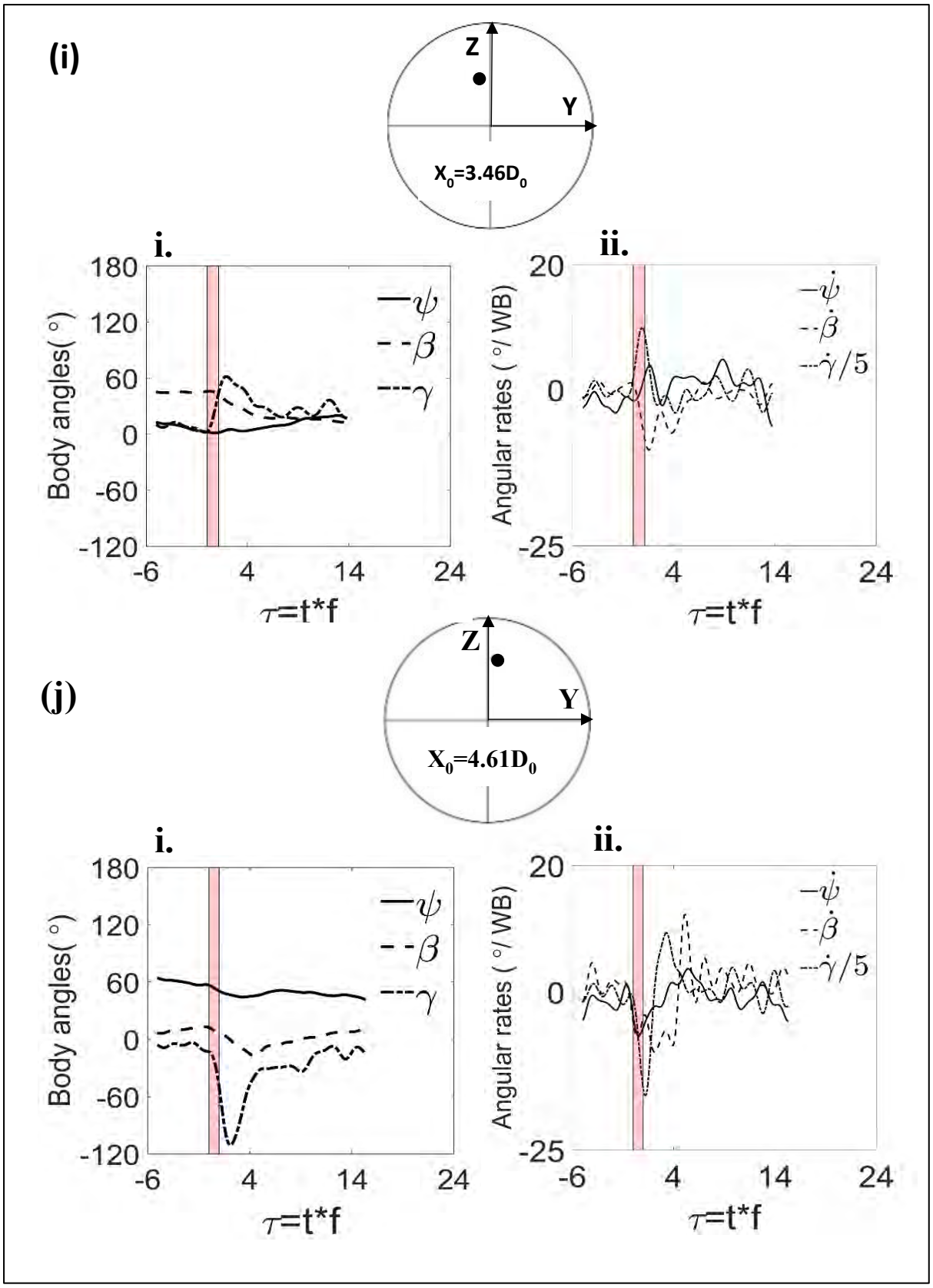

Figure 4-6: (continued)

c

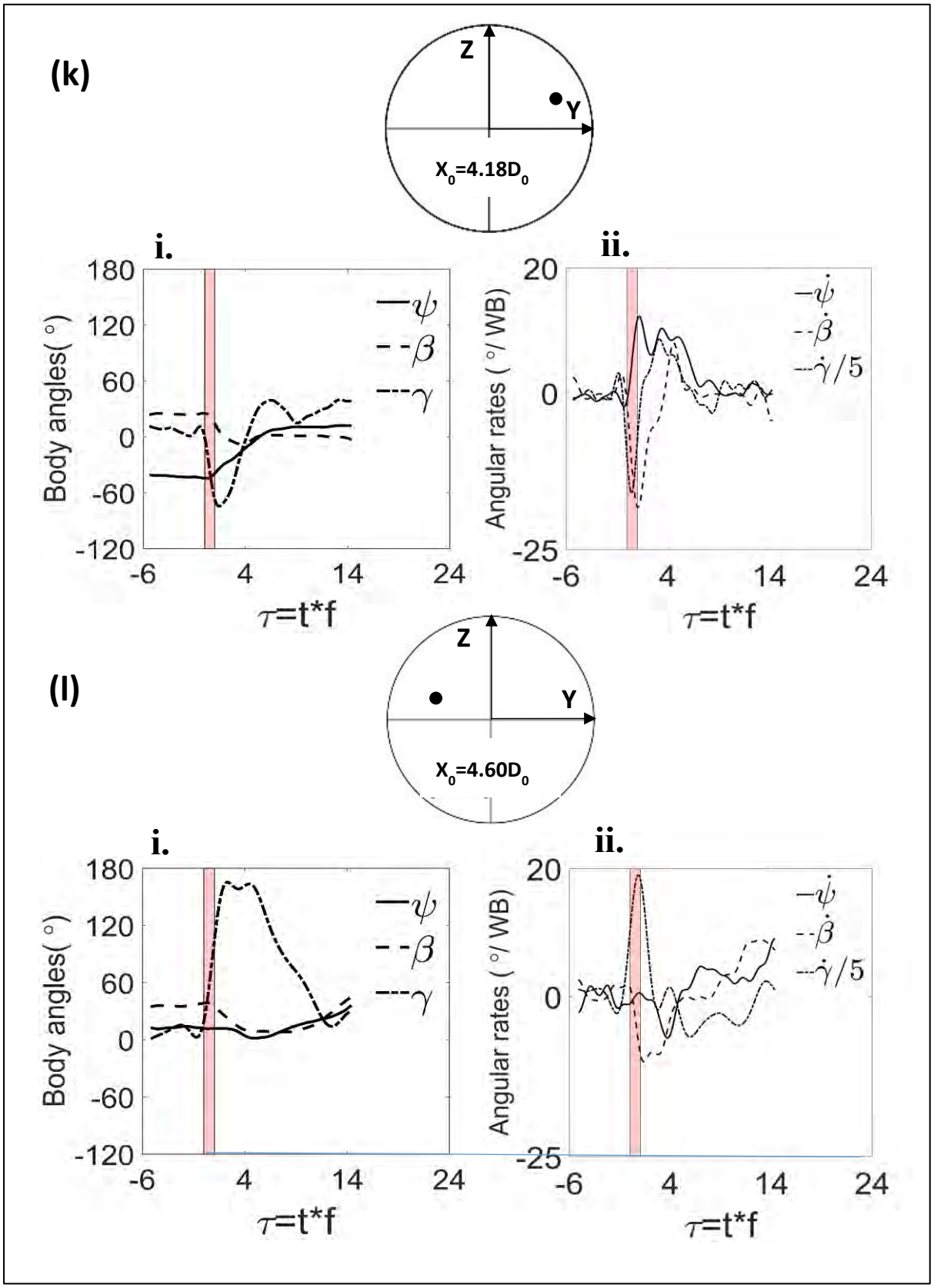

Figure 4-6: (continued)

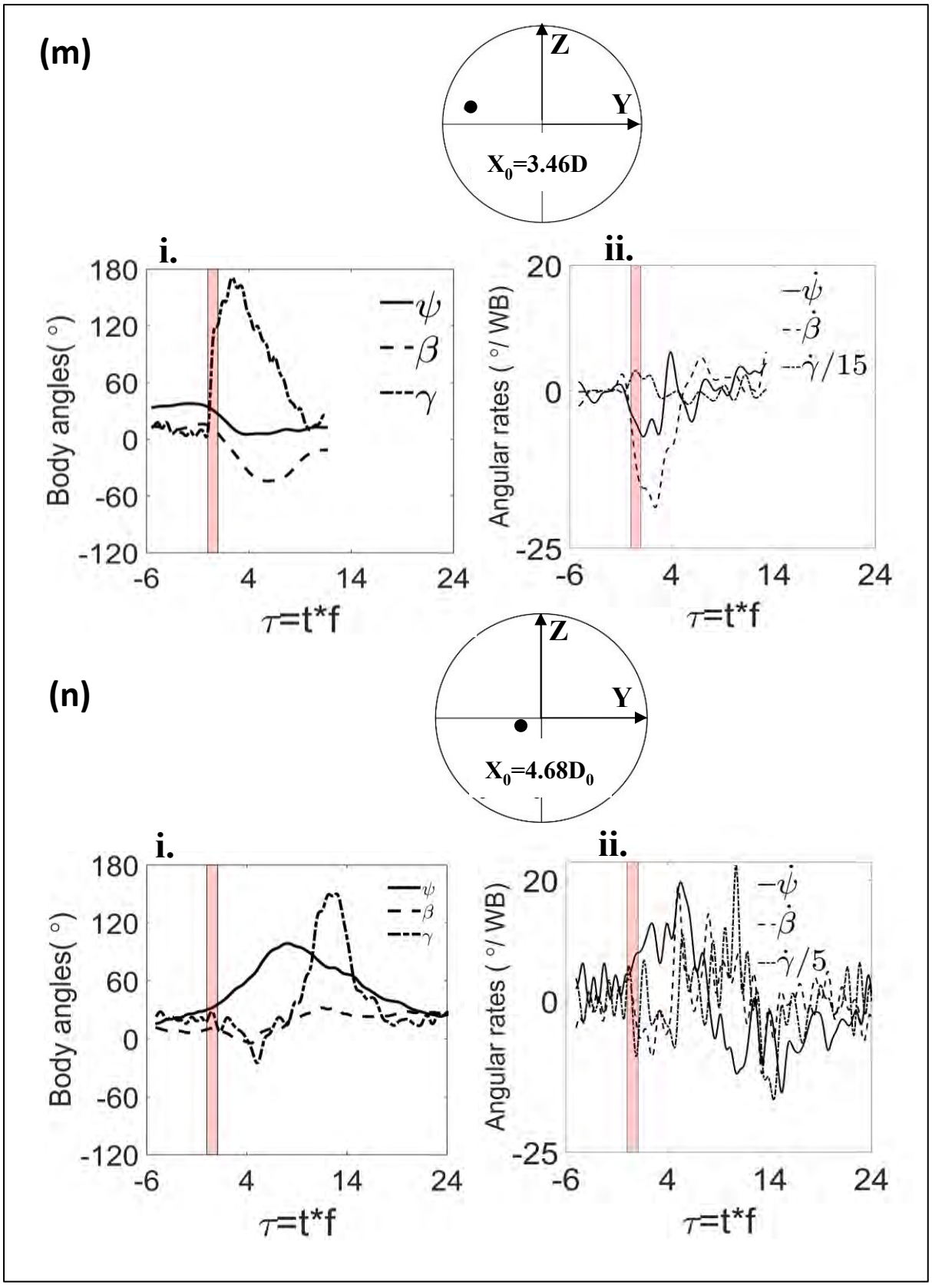

Figure 4-6: (Continued.) Note that roll rate is scaled down by 15 times in m (ii).

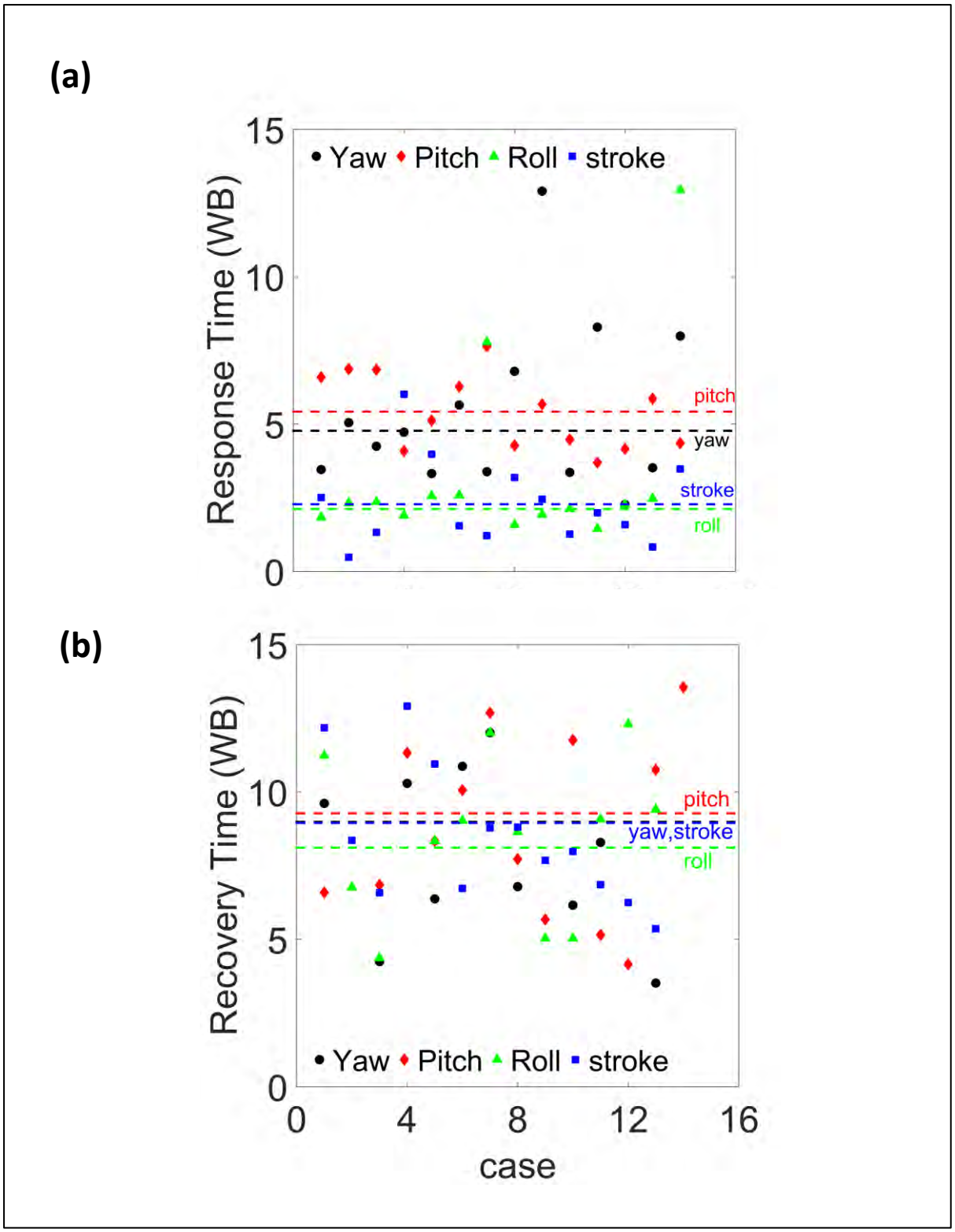

Figure 4-7: Response and recovery time along body axes and wing stroke amplitude (to be defined later) for different trials. Dashed lines in (a) and (b) show the mean response and recovery times along each body axes and for wing stroke amplitude. (a) Response time for different trials showing maximum and minimum values along pitch and roll axes respectively. (b) Recovery time for different trials showing similar observation as that in (a), except here time for recovery along yaw axis and for wing stroke amplitude coalesce, while response time is higher along yaw axis, compared to that for wing stroke amplitude.

Table 4- 3: Roll data for different trials, indicating wing beat frequency, initial and final body orientation, maximum change and error, and response and recovery time, Initial orientation is the body position just before gust. Final orientation denotes the body orientation after recovery. Response time is when the fly arrested the rotation induced by gust and recovery time is when angular rate is zero or constant. Error=Final -initial orientation, Max Δ=(Maximum value just before response time -initial value just before gust). Negative sign indicates clockwise rotation (i.e. towards right of fly) along roll axis.

#Expt	WB Frequency (f)	Orientation-Roll (°)		Recovery time		Response time		Error (°)	Max Δ (°)
		Initial	Final	sec	Wing Beats	sec	Wing Beats		
a	108	6.07	8.80	0.017	11.23	0.017	1.84	2.73	-64.13
b	100	10.67	-7.43	0.067	6.77	0.023	2.32	-18.11	106.48
c	118	16.24	12.60	0.037	4.37	0.02	2.36	-3.64	43.60
d	115	6.32	13.00	0.1535	**17.65**	0.0165	1.90	6.68	53.91
e	109	12.00	23.93	0.0765	8.34	0.0235	2.56	9.93	86.66
f	115	-10.72	-21.53	0.0785	9.03	0.0225	2.59	-10.81	-38.76
g	94	5.24	29.43	0.1278	12.01	**0.083**	**7.78**	24.19	64.60
h	93	5.97	10.71	0.093	8.65	0.017	1.58	4.74	-58.93
i	129	2.60	25.23	0.039	5.03	0.015	1.94	22.64	59.23
j	112	-12.91	20.98	0.045	5.04	0.019	2.13	-8.08	-97.97
k	112	11.12	29.74	0.081	9.07	0.013	1.46	29.98	-74.21
l	118	20.51	20.96	0.1043	12.30	0.0193	2.27	0.45	144.82
m	110	8.66	16.99	0.0855	9.41	0.0225	2.48	8.32	161.36
n	121	18.55	19.92	0.15	**18.15**	**0.011**	**12.95**	0.87	113.80
μ	111	7.17	14.52	0.0658	8.11	0.019	2.12	4.99	35.75
σ	10	9.59	14.17	0.0273	2.57	0.0034	0.38	13.63	86.65

Table 4- 4: Pitch Data for different trials, indicating wing beat frequency, initial and final body orientation, maximum change and error, and response and recovery time, Initial orientation is the body position just before gust. Final orientation denotes the body orientation after recovery. Response time is when the fly arrested the rotation induced by gust and recovery time is when angular rate is zero or constant. Error=Final -initial orientation, Max Δ=(Maximum value just before response time -initial value just before gust). Negative sign indicates pitched down motion along pitch axis.

# Expt	WB Frequency (f)	Orientation-Pitch (°)		Recovery time		Response time		Error (°)	Max Δ (°)
		Initial	Final	sec	Wing Beats	sec	Wing Beats		
a	108	22.29	9.60	0.061	6.59	0.061	6.59	-12.69	-11.72
b	100	16.39	-18.89	0.151	15.25	0.068	6.87	-35.27	23.04
c	118	40.37	0.59	0.058	6.84	0.058	6.84	-39.78	-39.78
d	115	33.92	8.84	0.0985	11.33	0.0355	4.08	-25.08	14.07
e	109	2.46	-43.81	0.0765	8.34	0.0475	5.12	-46.28	-60.20
f	115	31.12	6.12	0.0875	10.06	0.0545	6.27	-18.20	-39.98
g	94	28.14	1.33	0.1345	12.68	0.0813	7.64	-26.81	-41.70
h	93	17.06	-9.71	0.083	7.72	0.046	4.28	-14.37	-51.00
i	129	45.80	16.05	0.044	5.68	0.044	5.68	-29.75	-27.99
j	112	12.37	7.45	0.105	11.76	0.04	4.48	-4.92	-30.01
k	112	25.36	0.60	0.046	5.15	0.033	3.70	-24.70	-19.50
l	118	38.54	8.84	0.0353	4.16	0.0353	4.16	-29.71	-28.54
m	110	14.85	-11.42	0.0978	10.75	0.0533	5.86	-26.27	-28.30
n	121	9.75	25.11	0.112	13.55	0.036	4.36	15.36	-14.16
μ	111	24.17	0.05	0.085	9.28	0.0495	5.42	-22.75	-25.41
σ	10	12.76	16.95	0.0344	3.41	0.0141	1.28	15.44	22.95

Table 4-5: Yaw Data for different trials, indicating wing beat frequency, initial and final body orientation, maximum change and error, and response and recovery time, Initial orientation is the body position just before gust. Final orientation denotes the body orientation after recovery. Response time is when the fly arrested the rotation induced by gust and recovery time is when angular rate is zero or constant. Error=Final -initial orientation, Max Δ=(Maximum value just before response time -initial value just before gust). – denotes the fly continued changing orientation and didn't attain any constant value. Negative sign indicates counterclockwise rotation along yaw axis.

# Expt	WBF (f)	Orientation-Yaw (°)		Recovery time		Response time		Error (°)	Max Δ (°)
		Initial	Final	sec	Wing Beats	sec	Wing Beats		
a	108	-60.15	-42.70	0.089	9.61	0.032	3.46	14.45	-25.35
b	100	30.76	-3.32	0.205	20.71	0.05	5.05	-30.31	34.60
c	118	-30.27	-55.34	0.036	4.25	0.036	4.25	-25.07	-22.92
d	115	8.08	16.80	0.0895	10.29	0.0415	4.72	8.89	14.29
e	109	19.99	2.28	0.0585	6.38	0.0305	3.32	-18.34	-18.23
f	115	29.64	46.77	0.0945	10.87	0.0475	5.65	17.13	28.93
g	94	-37.74	-32.33	0.1278	12.01	0.036	3.38	5.40	-22.30
h	93	-45.99	-1.25	0.073	6.79	0.073	6.79	44.40	44.40
i	129	2.37	-	-	-	0.1	12.90	-	17.64
j	112	56.79	50.20	0.055	6.16	0.031	3.36	-6.59	-12.51
k	112	-44.56	11.09	0.074	8.29	0.074	8.29	55.65	54.61
l	118	11.87	-	-	-	0.0403	2.27	-	-10.16
m	110	34.21	8.90	0.032	3.52	0.032	3.52	-28.74	-28.74
n	121	30.11	-	-	-	0.066	7.99	-	68.79
μ	111	0.37	0.10	0.0849	8.99	0.0493	5.35	3.35	8.79
σ	10	37.00	33.38	0.0484	4.74	0.0211	2.84	28.82	33.09

Table 4-6: Maximum angular rates for different trials. Values are rounded off to next whole number. Negative sign indicates counterclockwise rotation along roll and yaw axes and pitched down along pitch axis.

# Expt	Yaw rate (°/WB)	Pitch Rate (°/WB)	Roll rate (°/WB)
a	-10	-5	-60
b	12	10	80
c	-8	-25	47
d	10	6	43
e	-8	-19	50
f	11	-10	-20
g	-10	-15	25
h	14	-26	-64
ij	4	-10	50
j	-7	-10	-80
k	12	-19	-80
l	-6	-10	93
m	-10	-15	250
n	20	19	-46
μ	2	-9	21
σ	11	13	86

4.1.4 Body pitch and forward speed

Analysis of body pitch and forward speed of the fly separately revealed that the fly, on average, decelerated and pitch down due to gust. This led us to check if there is any correlation between body pitch and velocity magnitude of the fly.

Figure 4-8 shows body pitch and forward speed of the fly plotted together against wing beats. In majority of the cases, a similar trend was observed in both body pitch and forward speed just after gust period, i.e. if pitch decreases, forward speed also reduces, as shown in Figure 4-8 (a-(i) to n-(i)), except some cases as Figure 4-8 (b -(i), d-(i), j-(i) and l-(i)). This is in accordance with the helicopter model. According to the helicopter model, insects alter the direction of motion by changing their body attitude and in doing so, they keep the net aerodynamics vector fixed relative to the body (Ravi et al. 2016; Taylor & Thomas 2002). It was observed that the fly pitched down and decelerated immediately after the gust in all the cases except the one discussed above. The fly pitched down by 200 % on average, compared to its initial pitch orientation before gust, while it reduced its speed on average by 30% due to gust. It is however noted that opposite trend, i.e. pitch down and acceleration (see Figure 4-8 (j-(i) and l-(i)) or pitch up and deceleration was observed for few cases as shown in Figure 4-8 (b- (i) and d - (i)).

However, when forward speed was plotted against body pitch as shown in Figure 4-8 (a- (ii) to n-(ii)), no correlation was observed. Considering the general observation that following a gust, the forward speed of the insect reduced and the pitch angle also Figure 4-8(a-(i) – n-(i)), lack of quantitative correlation between them is surprising.

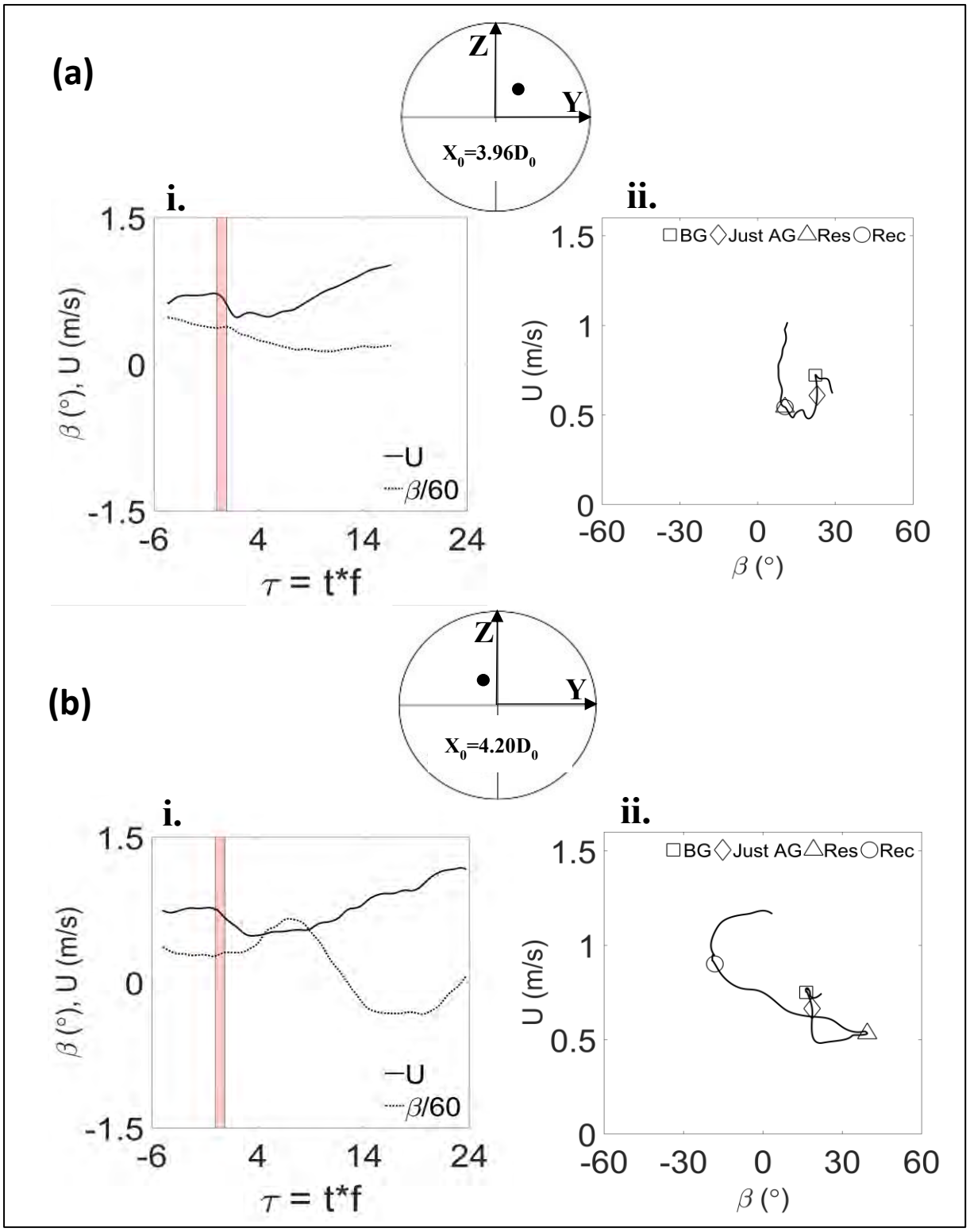

Figure 4-8: (i) Body pitch(β) and forward speed (U)of the fly versus wing beats. (ii) Forward speed versus body pitch. Small alphabets within parenthesis (a, b) denote trials. Vertical strip in (i) denotes time instance of vortex ring. Circle represents front view of the ring and black dot inside it the relative position of insect, with its axial distance from nozzle exit represented by X_0. Small alphabets within braces ((a)) indicates trials. $\tau = 0$ indicates the instance when fly was just hit by gust. Note, in (i), β is called down by 60 times. In (ii) BG denotes before gust, AG - after gust time, Res - after response time and Rec - after recovery time.

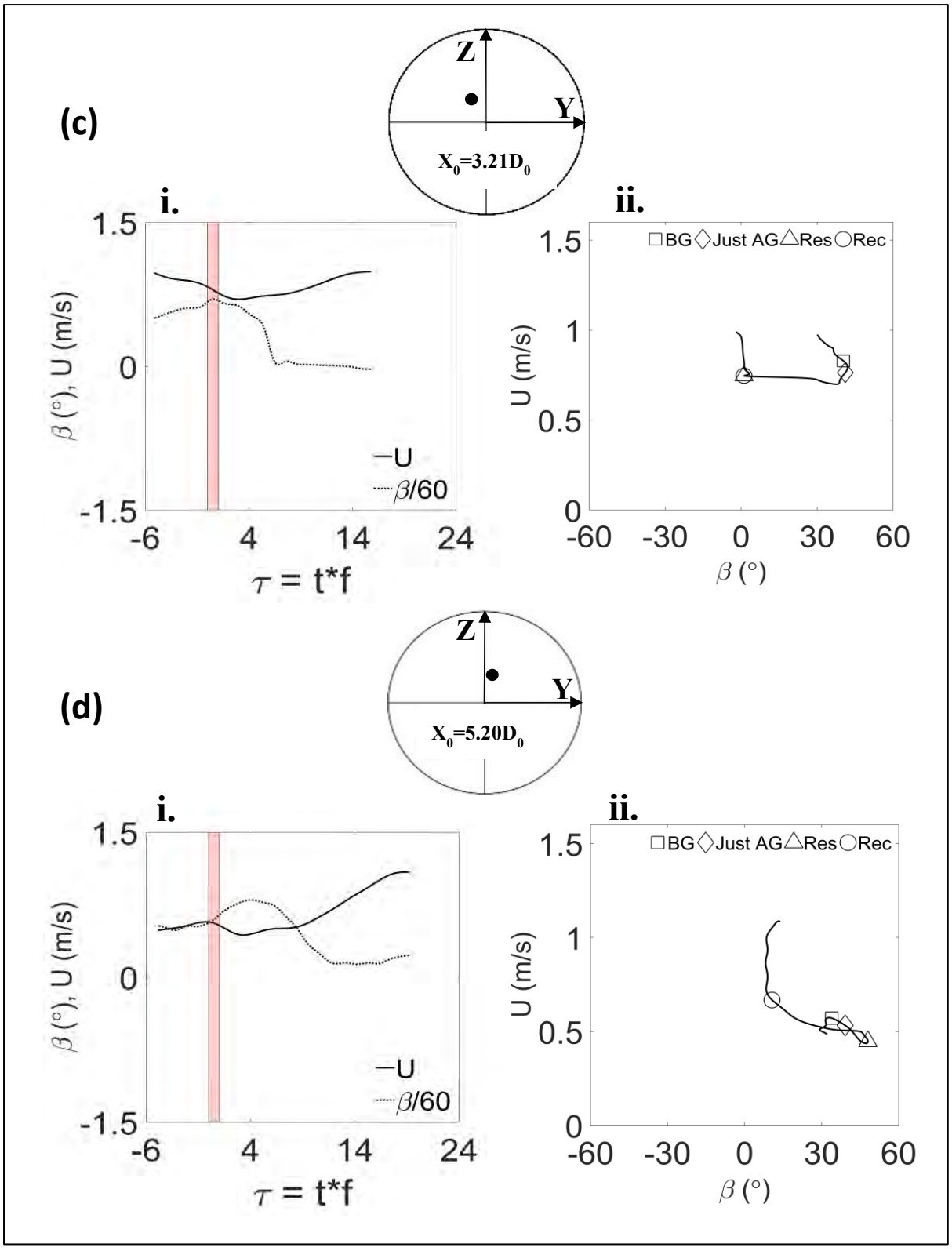

Figure 4-8: (continued)

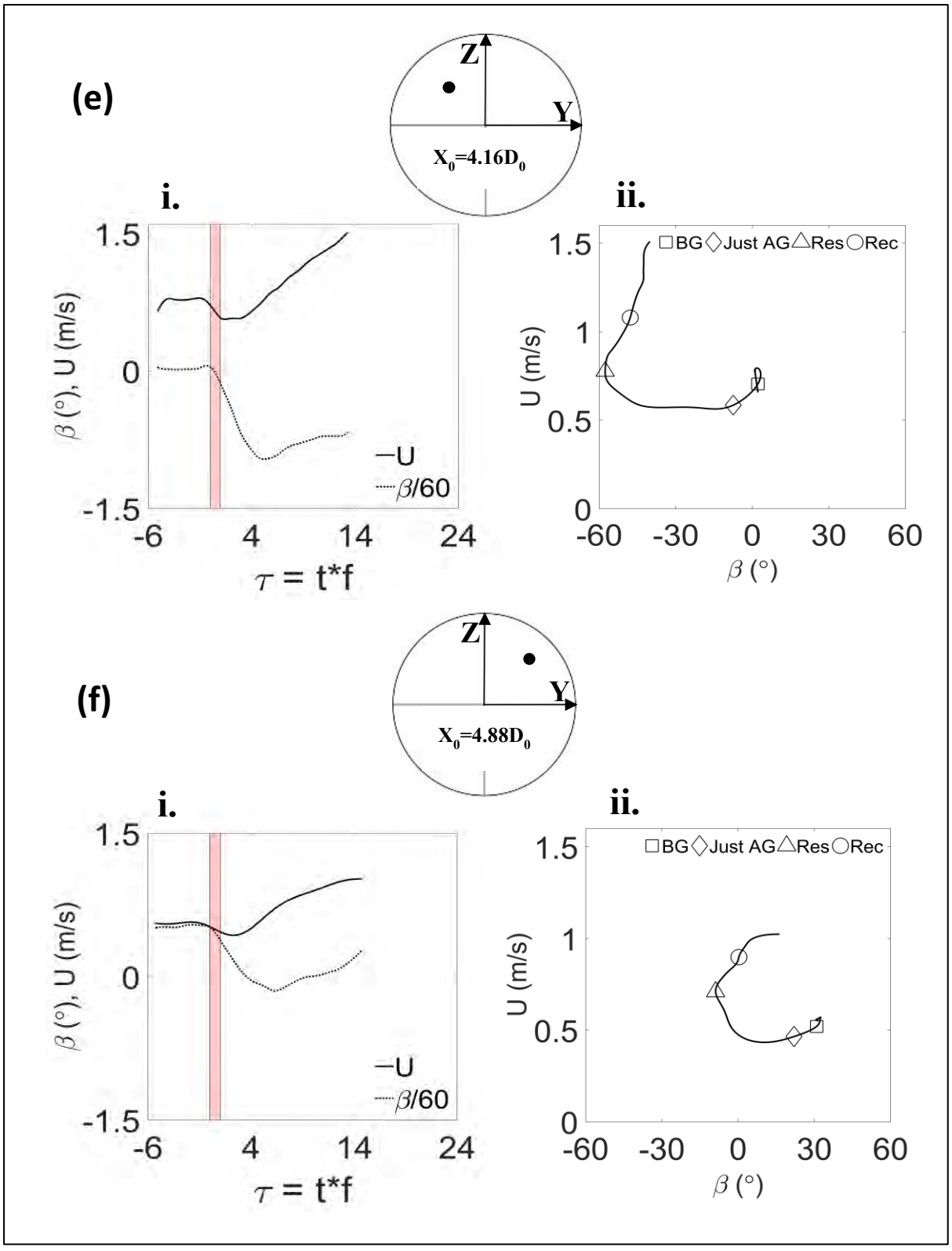

Figure 4-8: (continued)

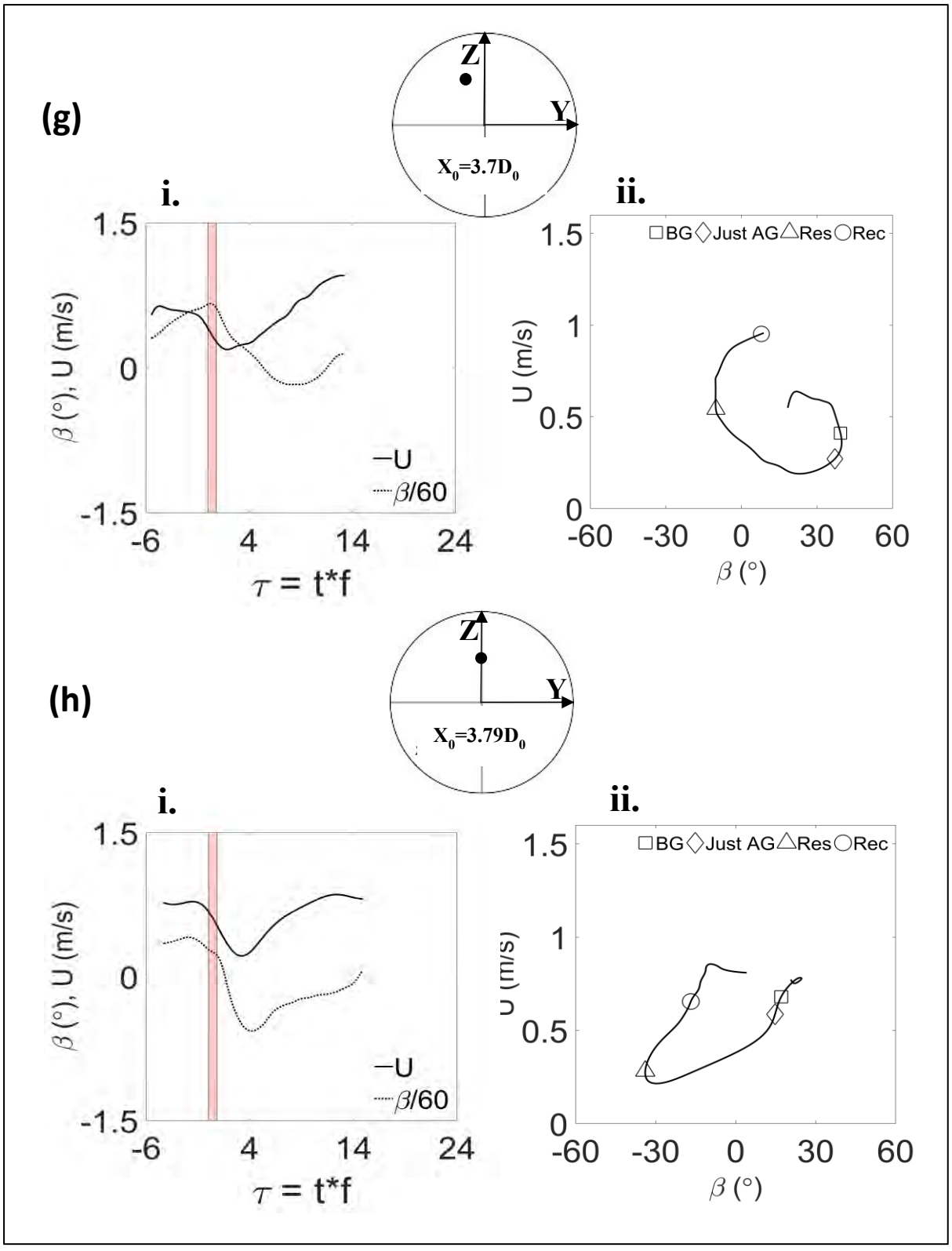

Figure 4-8: (continued)

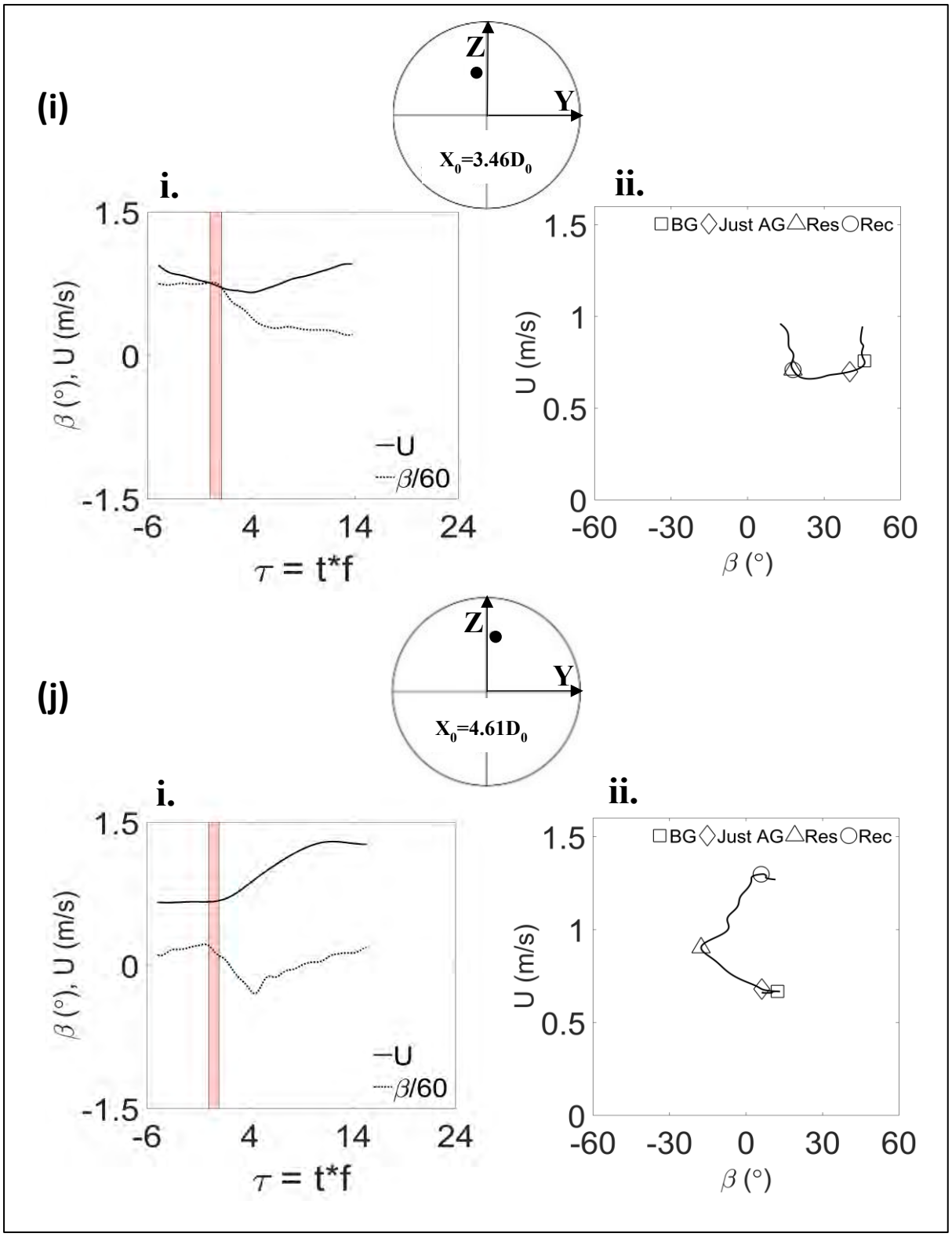

Figure 4-8: (continued)

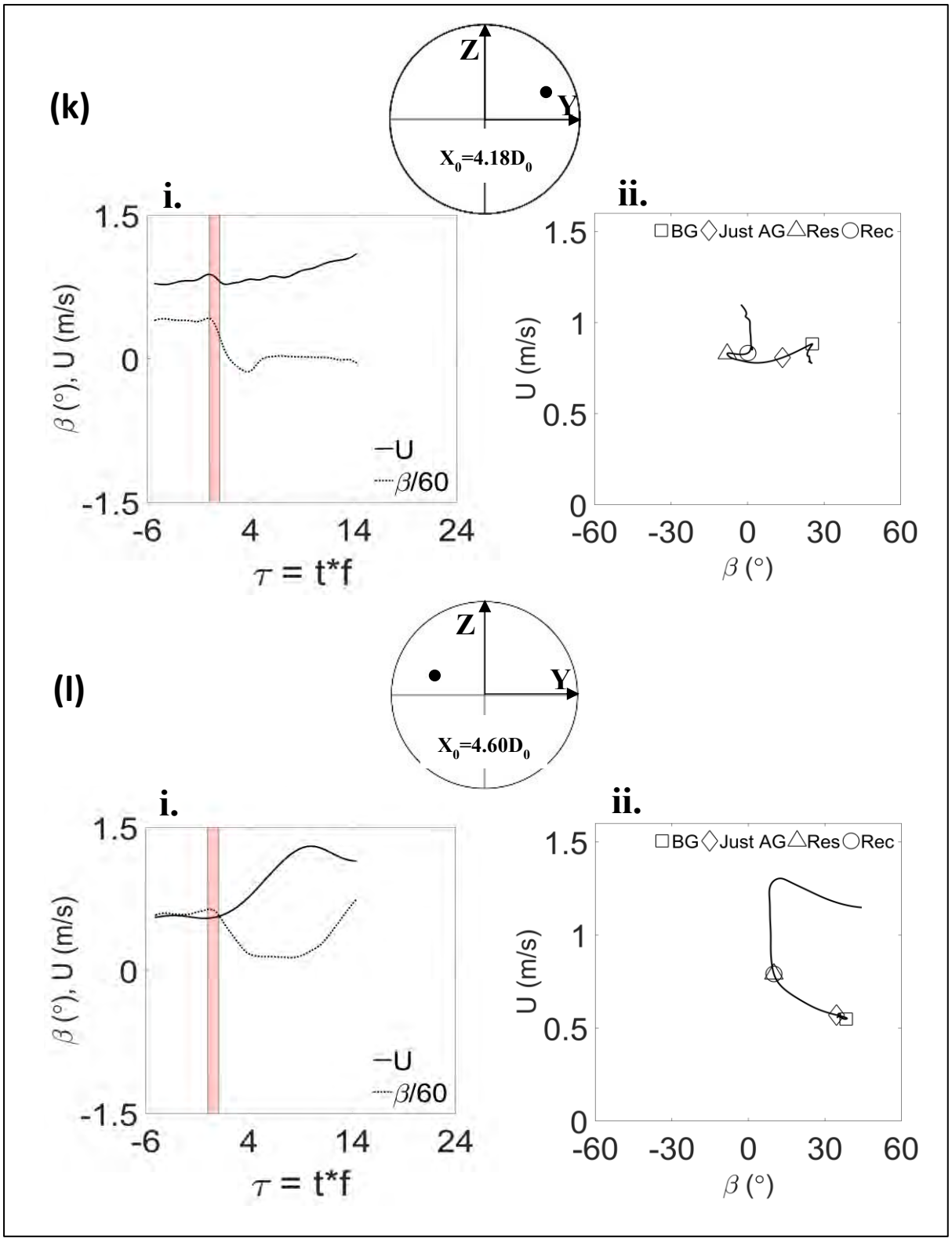

Figure 4-8: (continued)

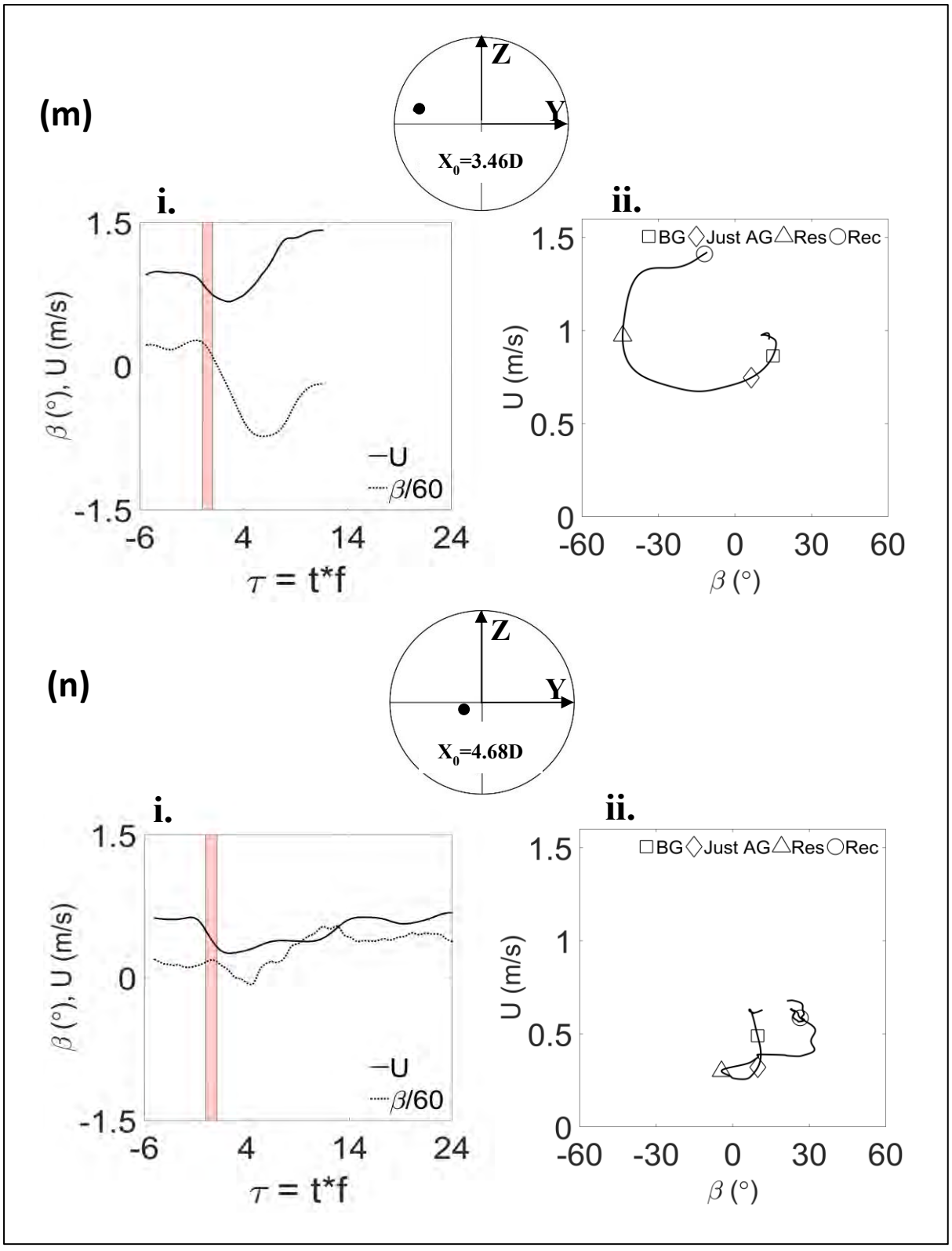

Figure 4-8: (continued)

4.1.5 Trajectory angles

This section is to determine if there is any relation between the body angles and trajectory angles. We may define lateral and vertical trajectory angles as shown in Figure 4-9 and are termed trajectory yaw (Ψ_T) and trajectory pitch (β_T) respectively.

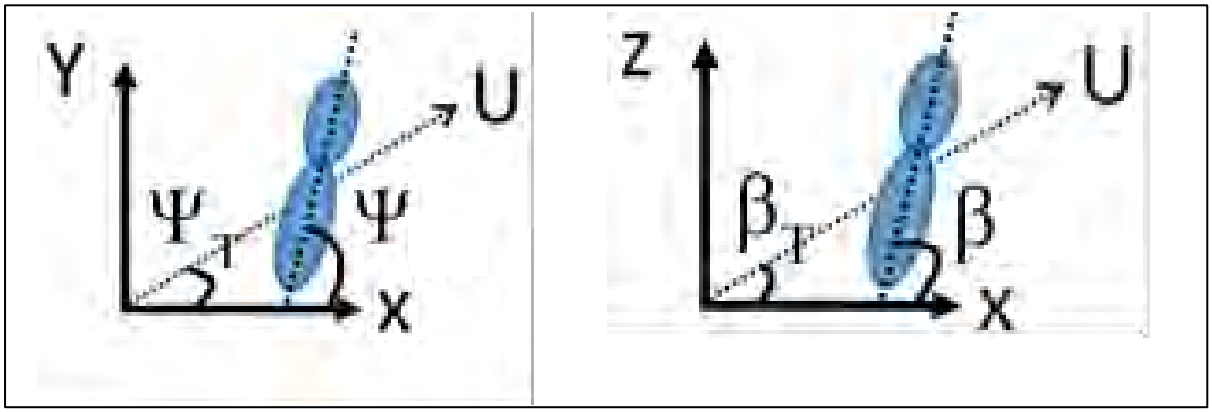

Figure 4-9: Determination of trajectory angles. Subscript T represents corresponding trajectory angle. U is forward speed of the fly. Ratio of lateral to axial velocity of fly gives trajectory yaw while that of vertical to axial velocity gives trajectory pitch.

The ratio of lateral to axial velocity gives trajectory yaw, while that of vertical to axial velocity gives trajectory pitch. Physically, trajectory yaw means that the body is moving in lateral direction as the insect flies forward. Similarly, trajectory pitch implies the motion of the body in both vertical and forward direction simultaneously. The idea of analyzing these angles was to see if the body and trajectory angles are the same, at least before gust, as one would expect under normal flight when they are not performing any maneuvers. To my knowledge, such comparison of trajectory and body angles, at least in the context of insects, have not been reported in the literature.

Flight trajectory angles are plotted together with body angles and are shown in Figure 4-10 (a to n). Initial and final values of trajectories angle averaged over four wingbeats before and after gusts respectively for the different cases are tabulated in Table 4- 7. The difference in trajectory and body angles are also listed in Table 4-8. Though the mean difference in trajectory yaw and body yaw across different realizations is less than 5° in both cases before and after gust, the standard deviation is significant. Similar is the case for the difference in trajectory and body pitch, and trajectory yaw and body roll. In all except 4 cases (see Figure 4-10 (b, c, e, m)), the direction of trajectory yaw and body yaw are opposite, meaning it moved towards right despite

yawing towards left and vice-versa, which is not expected. The cause may be attributed to the confined environment of the experimental test chamber.

On the other hand, the fly, in the majority of the cases, flew downward if it has a downward body pitch, except for two cases as shown in Figure 4-10 (b and c). Also, body roll and trajectory yaw happened in the same direction in most of the cases, i.e. if the fly was flying laterally towards the right, the roll was also observed in the same direction in all but three trials just after gust (see Figure 4-10 (h, k and m)). This indicates that trajectory pitch and body pitch, and trajectory yaw and body roll may be coupled to some extent. From the present results, however, we cannot conclude if there exist cause and effect relationship between them.

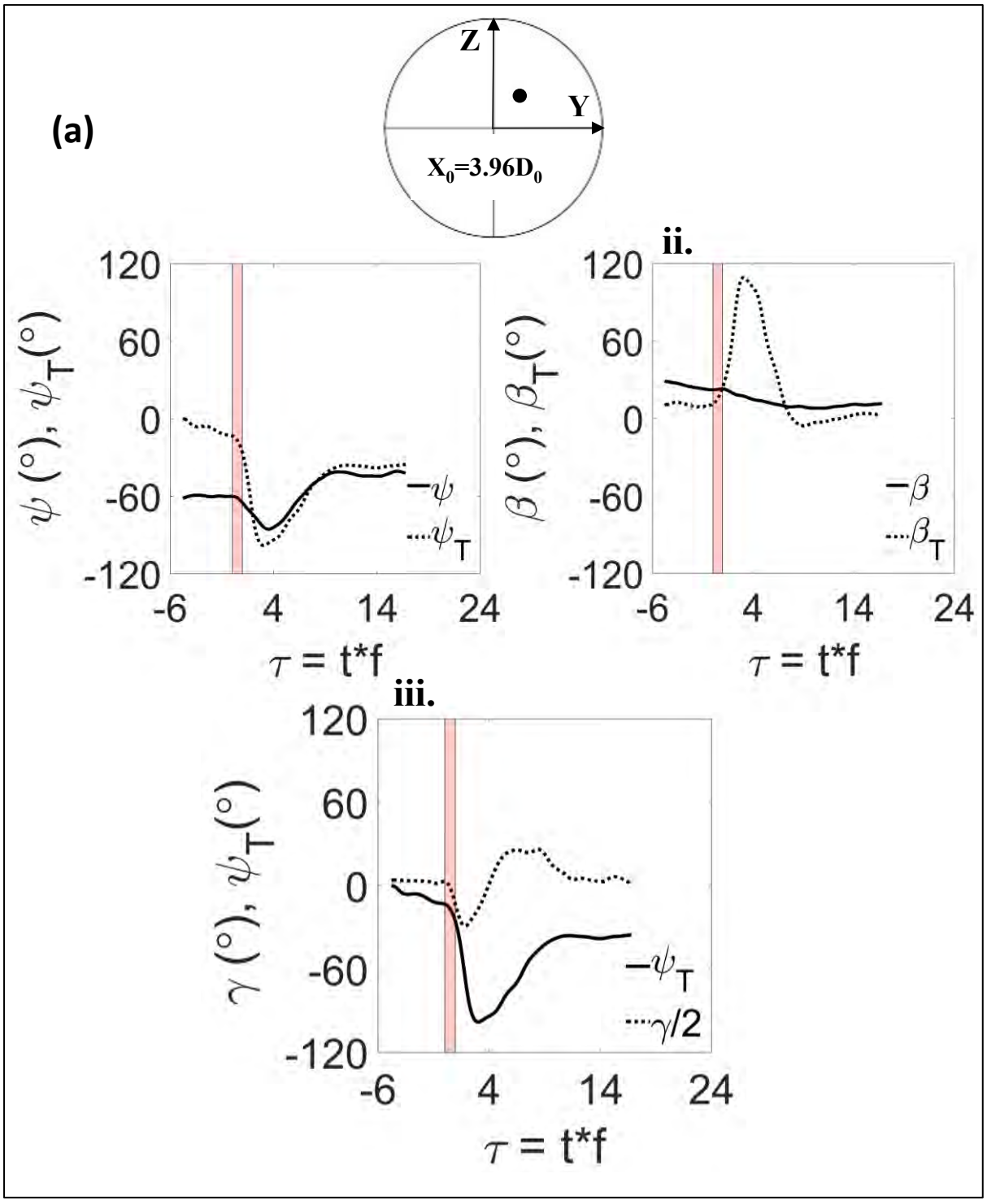

Figure 4-10: Body and trajectory angles. φ, β and γ represent absolute yaw, pitch, and roll of the body respectively, while φ_T and β_T are yaw and pitch trajectory angles. Vertical strip denotes time instance of vortex ring. Circle represents front view of the ring and black dot inside it the relative position of insect, with its axial distance from nozzle exit represented by X_0. Small alphabets within braces ((a)) indicates trials, while (i), (ii) and (iii) are comparison of body yaw and trajectory yaw, body pitch and trajectory pitch, and roll and trajectory yaw respectively. τ=0 indicates the instance when fly was just hit by gust. Note. Roll is scaled down by 2 times. Counterclockwise rotation in yaw and roll and pitched up rotation are considered positive here.

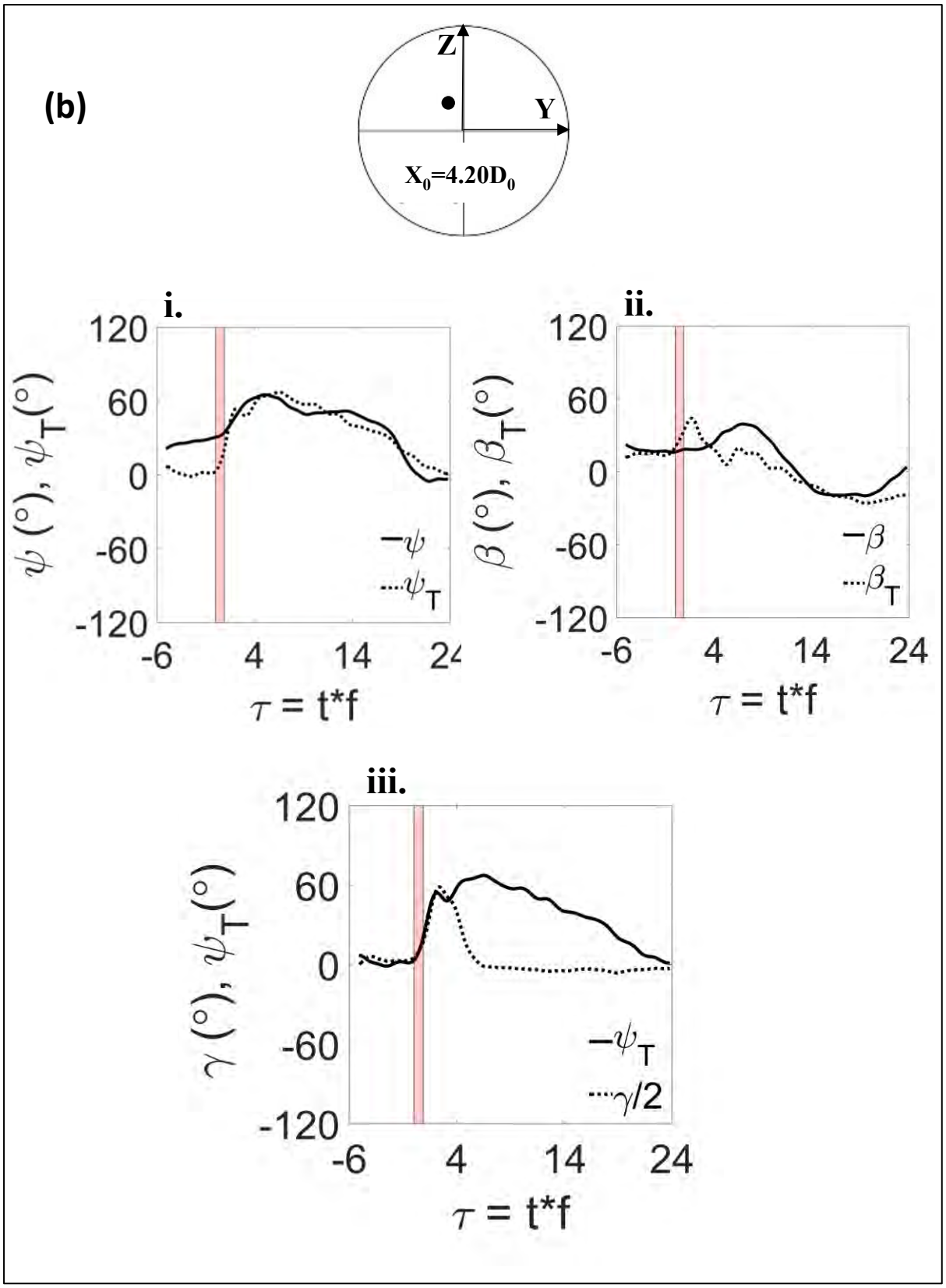

Figure 4-10: (continued)

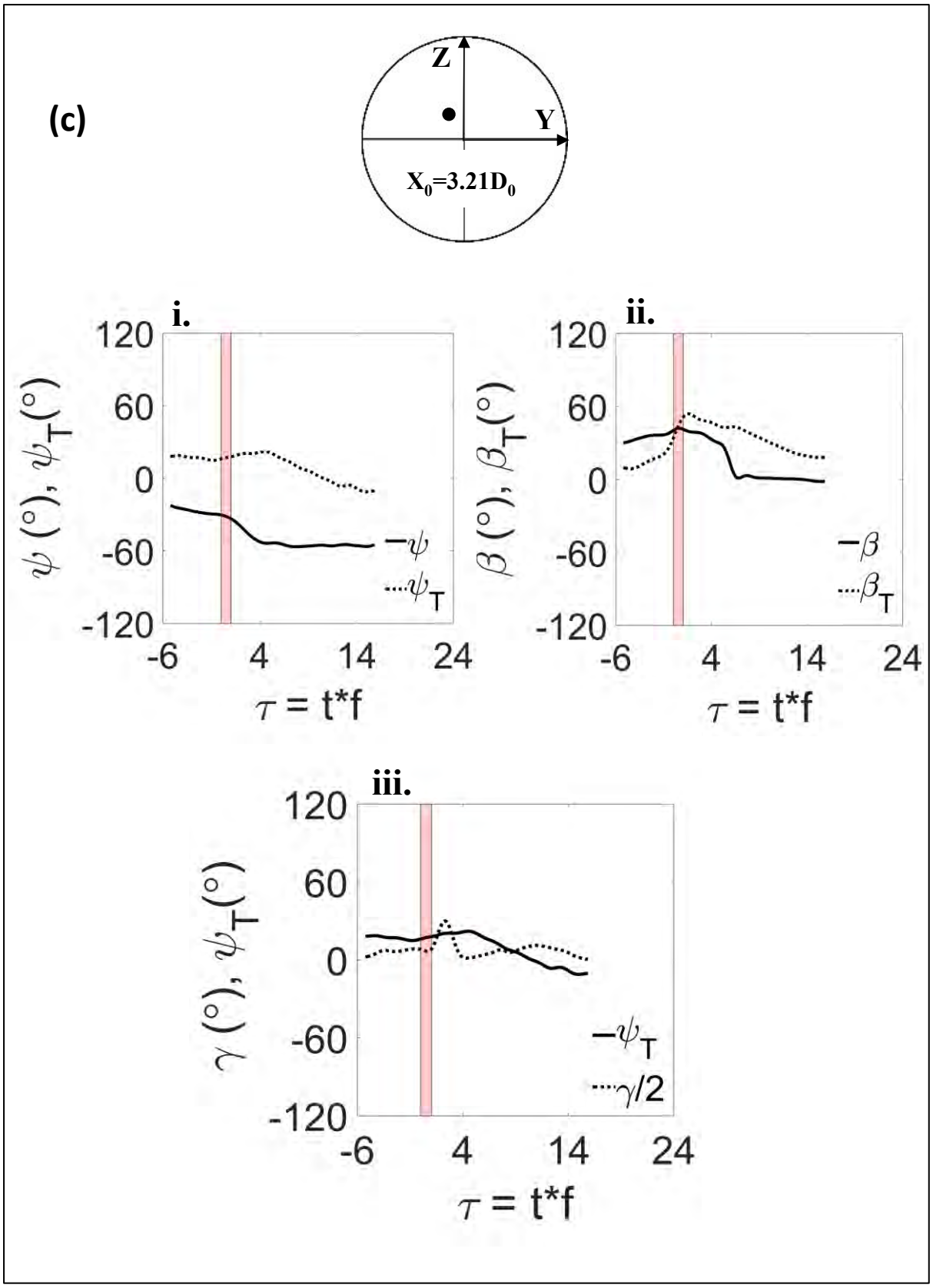

Figure 4-10: (continued)

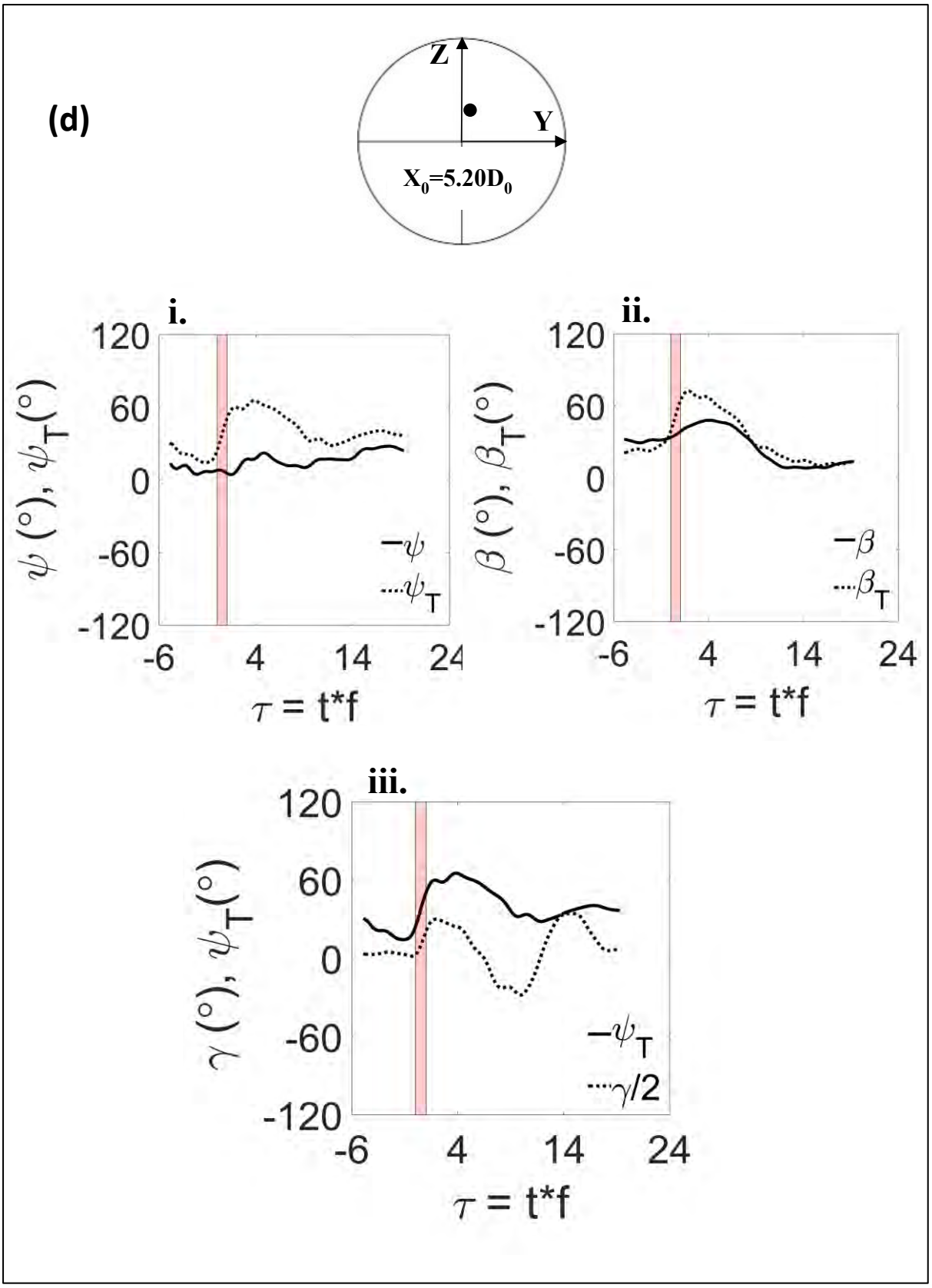

Figure 4-10: (continued)

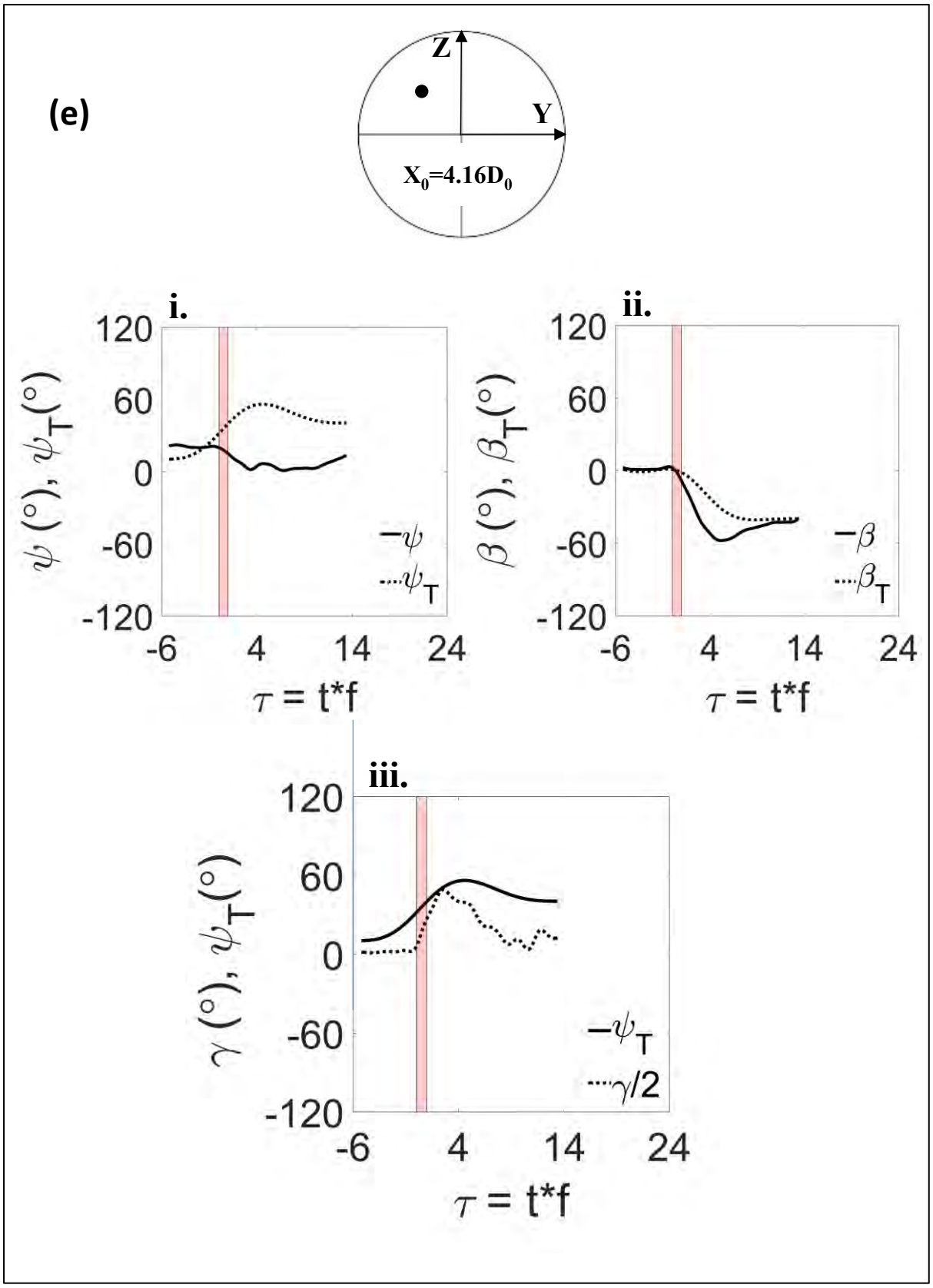

Figure 4-10: (continued)

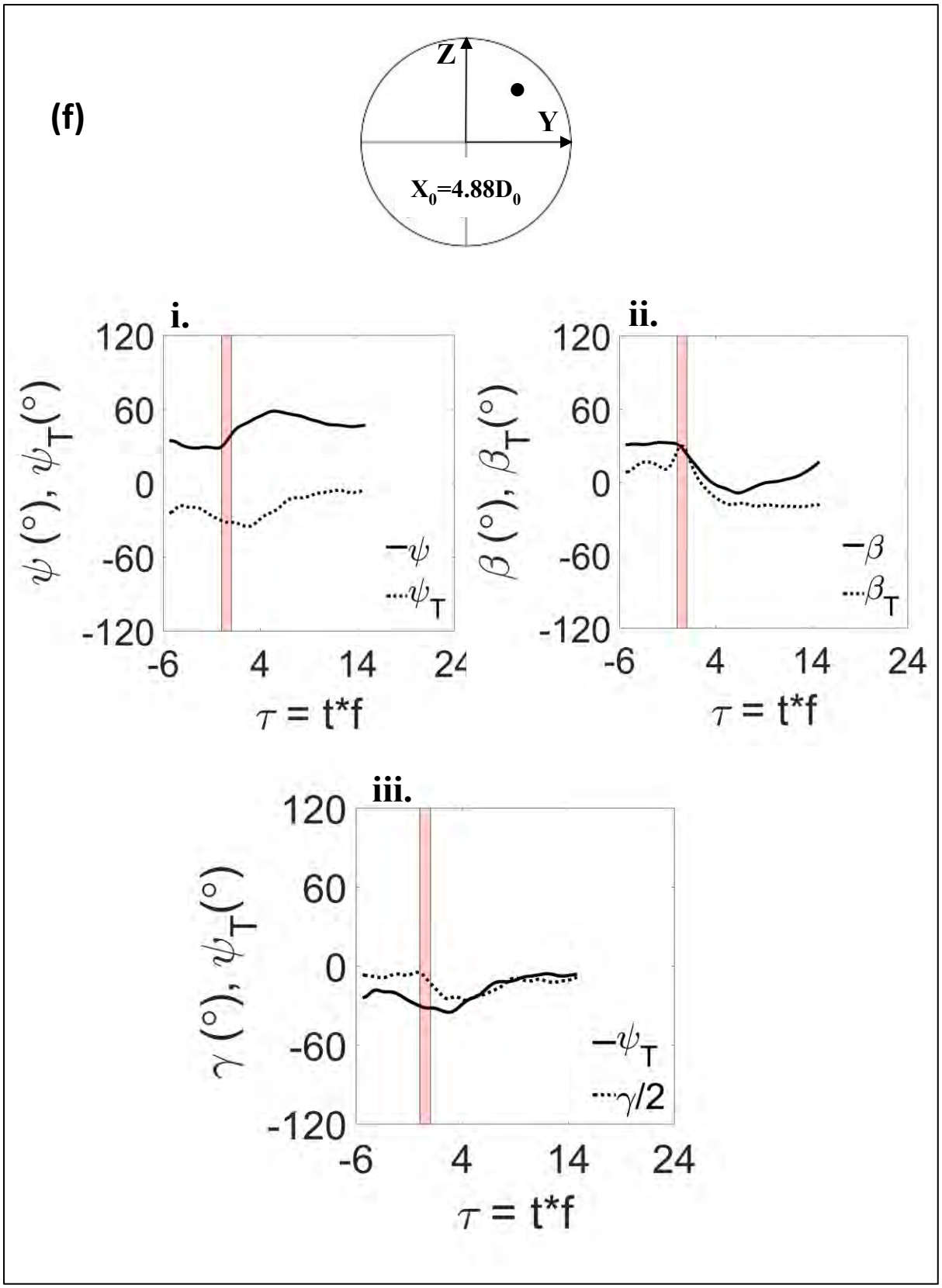

Figure 4-10: (continued)

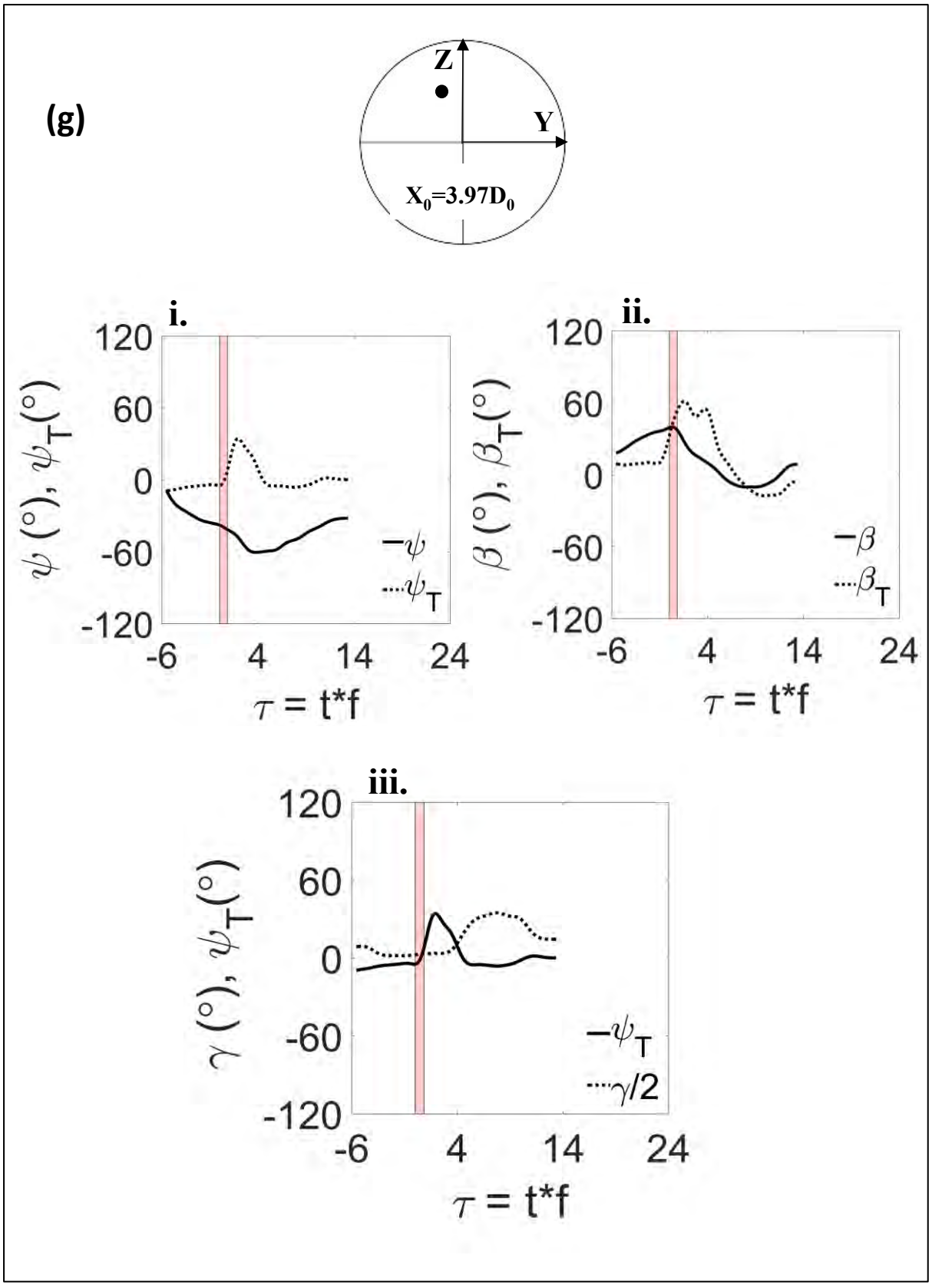

Figure 4-10: (continued)

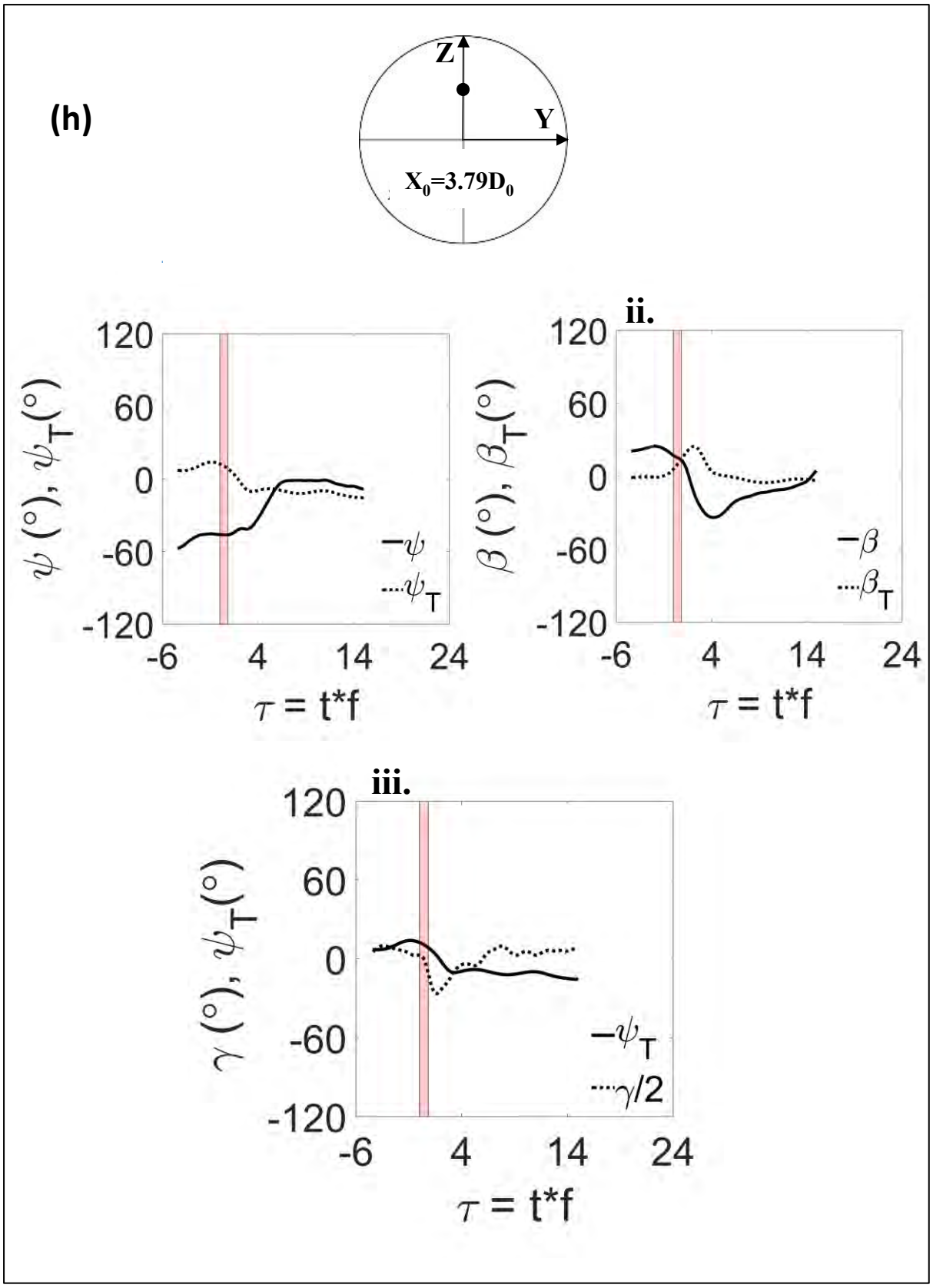

Figure 4-10: (continued)

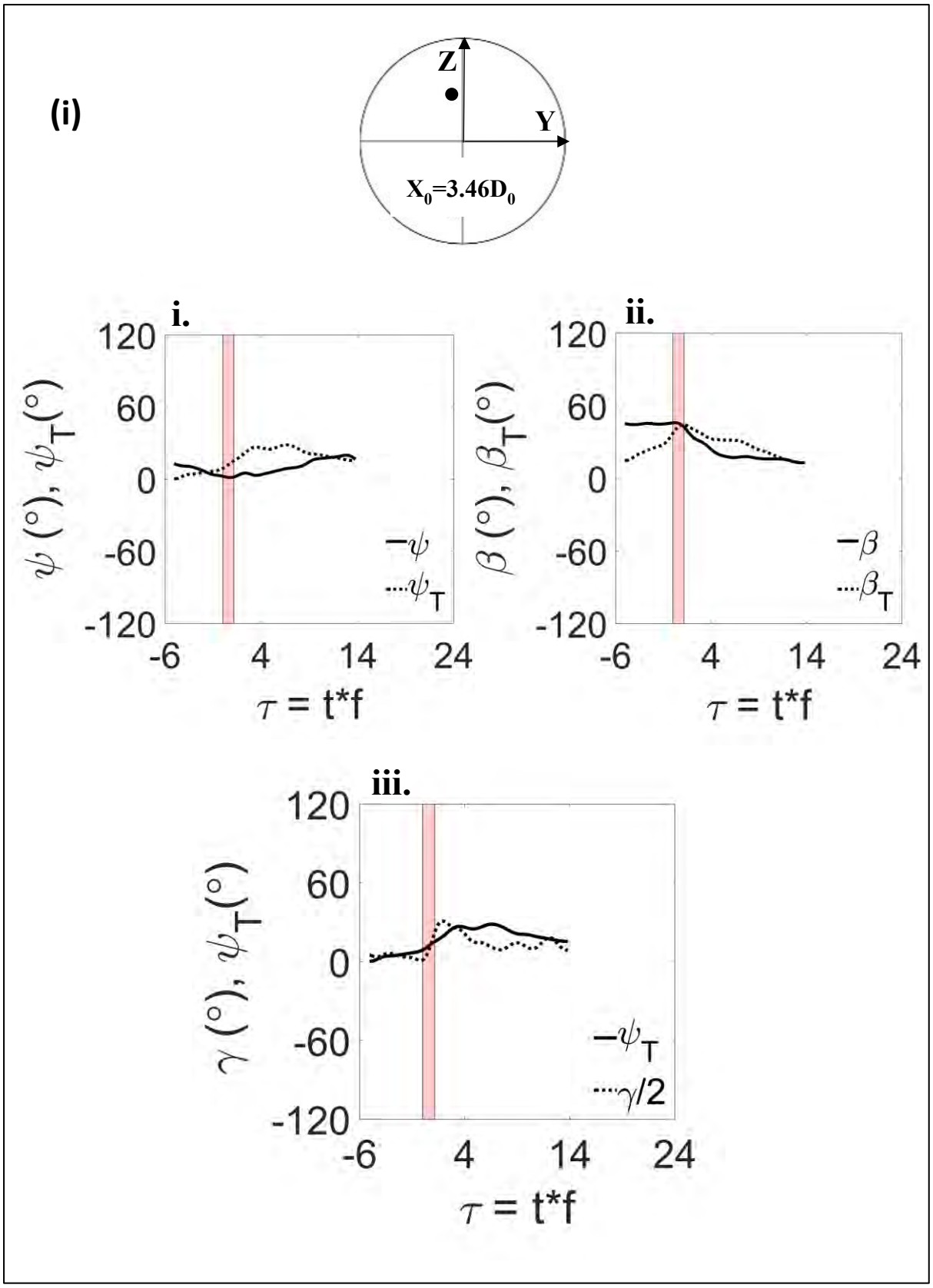

Figure 4-10: (continued)

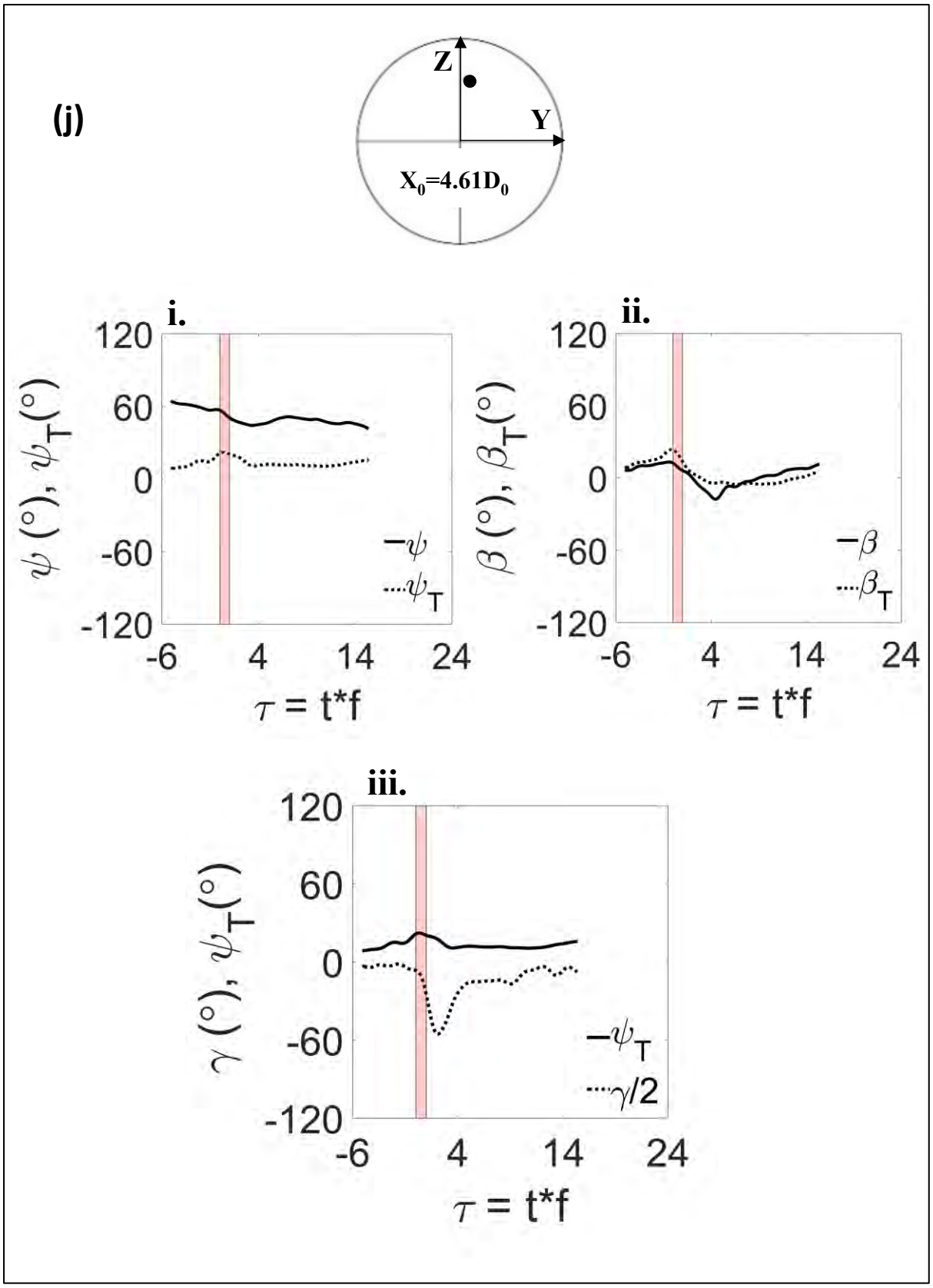

Figure 4-10: (continued)

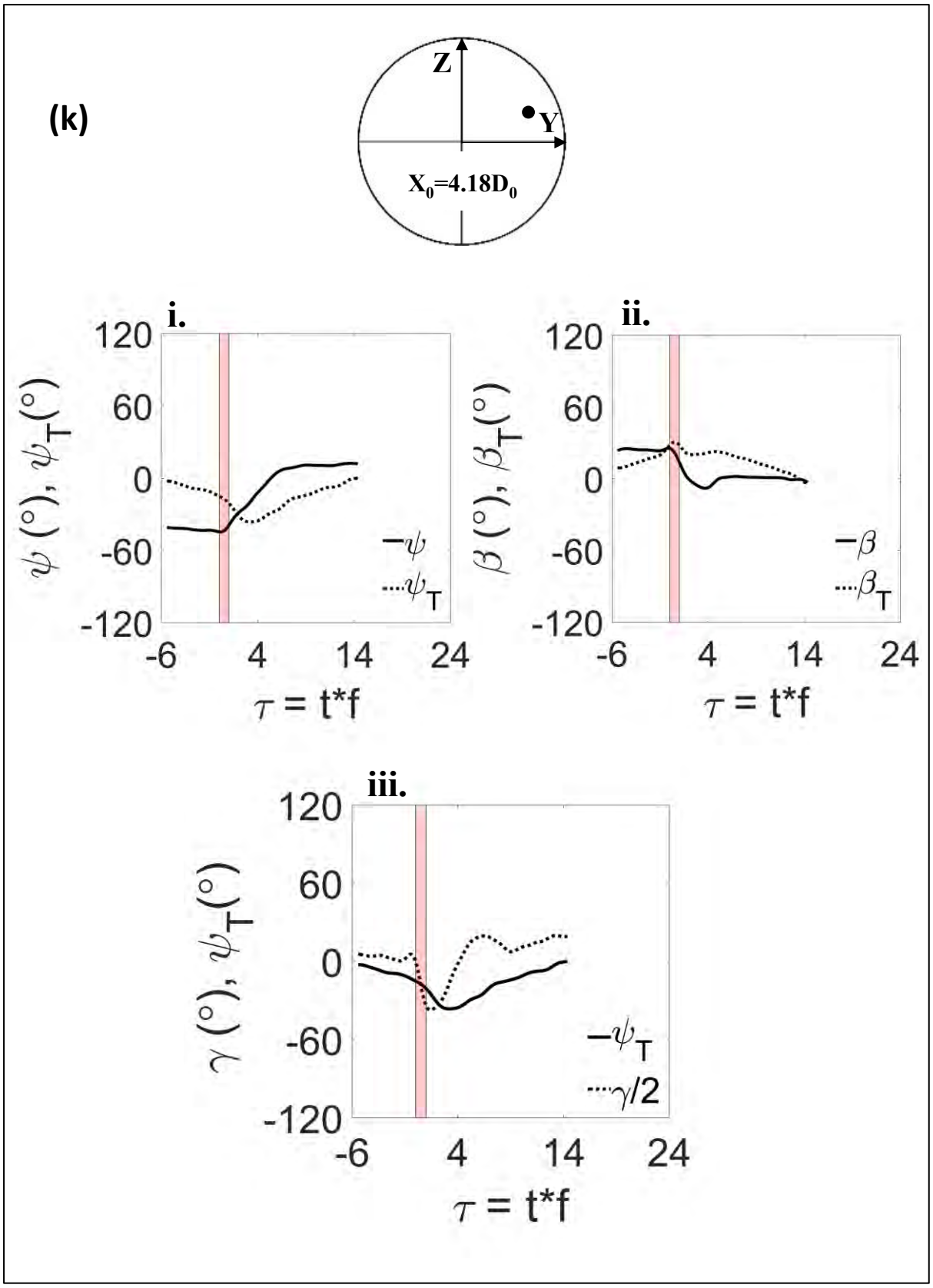

Figure 4-10: (continued)

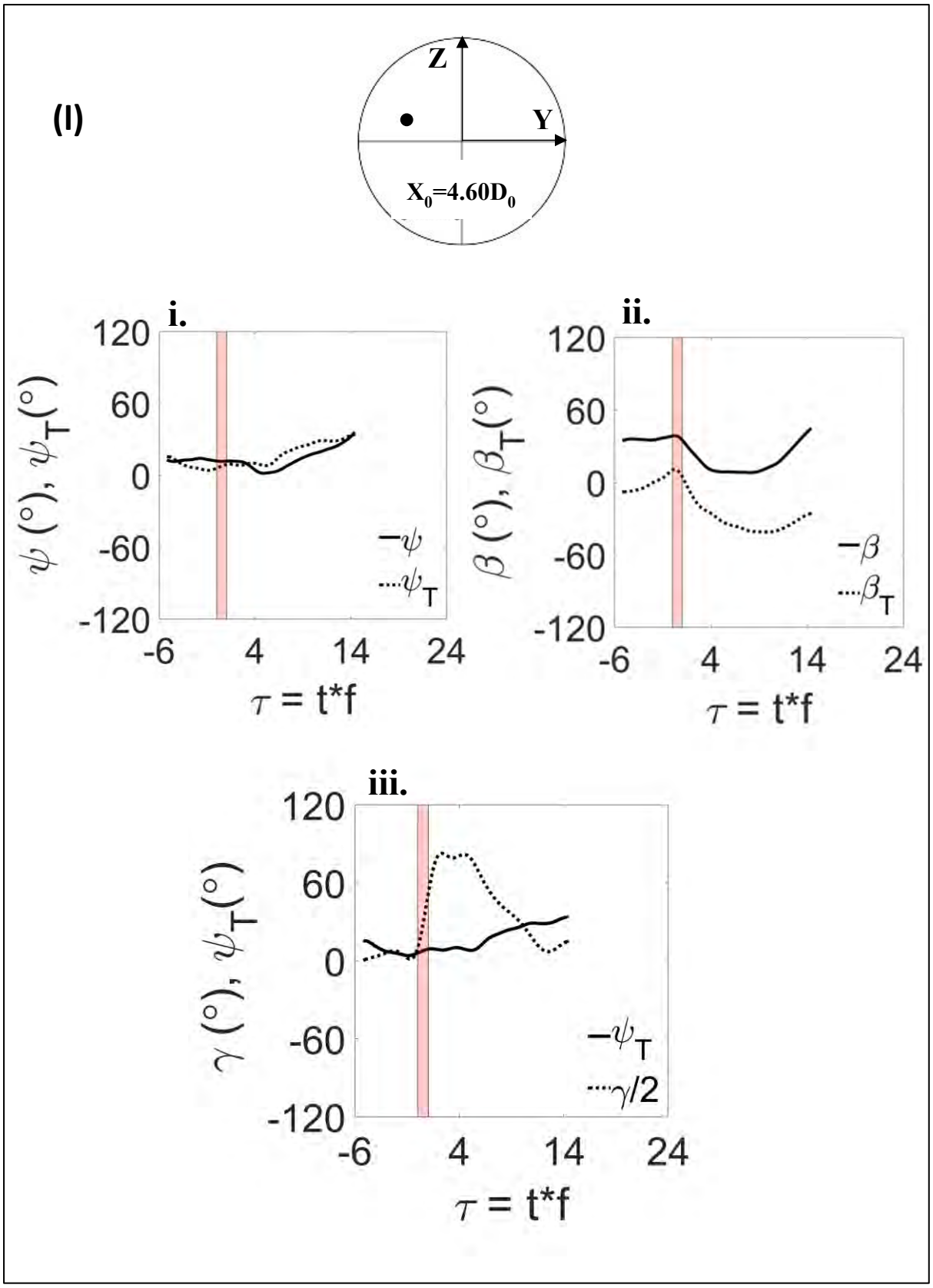

Figure 4-10: (continued)

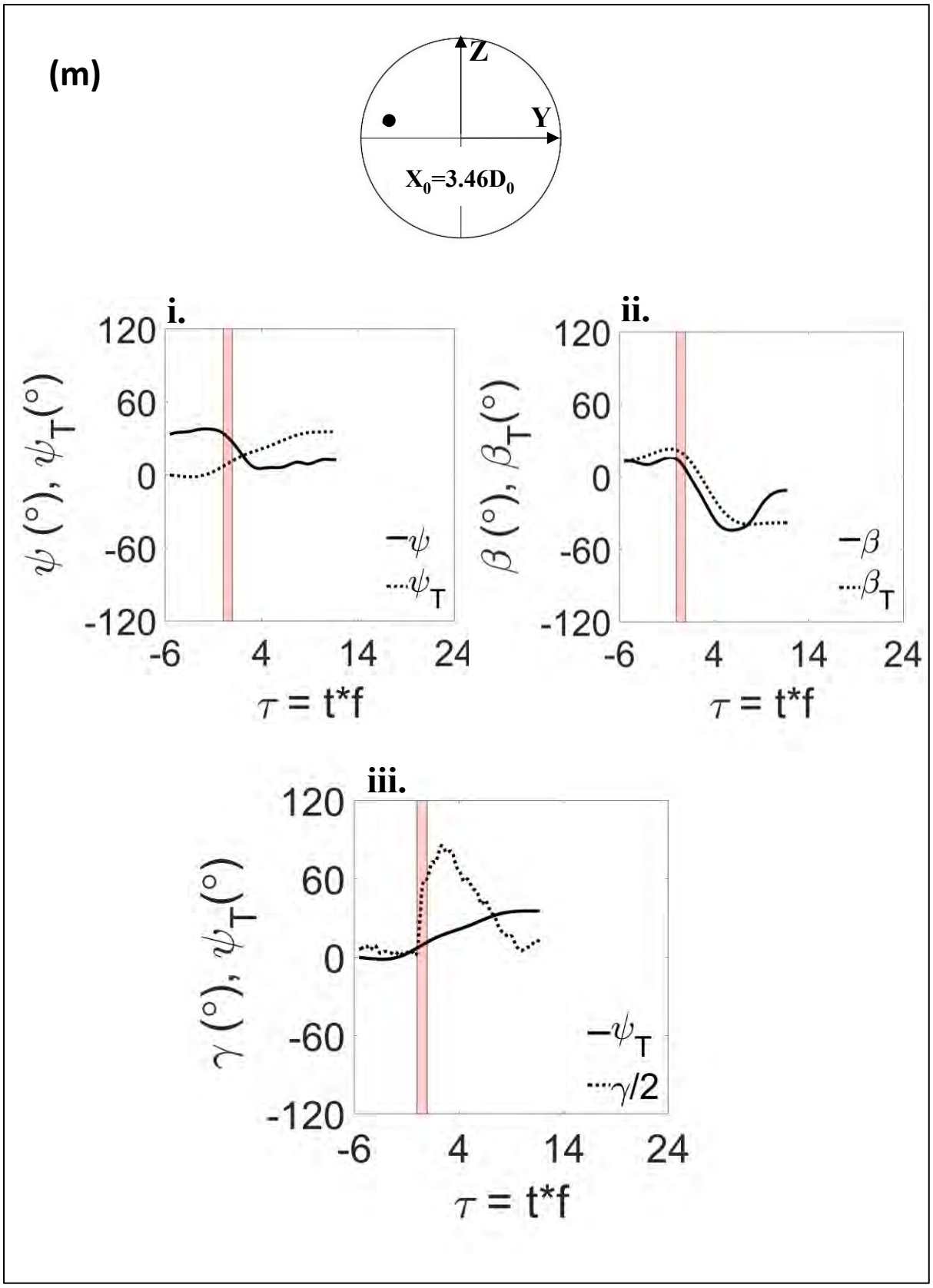

Figure 4-10: (continued)

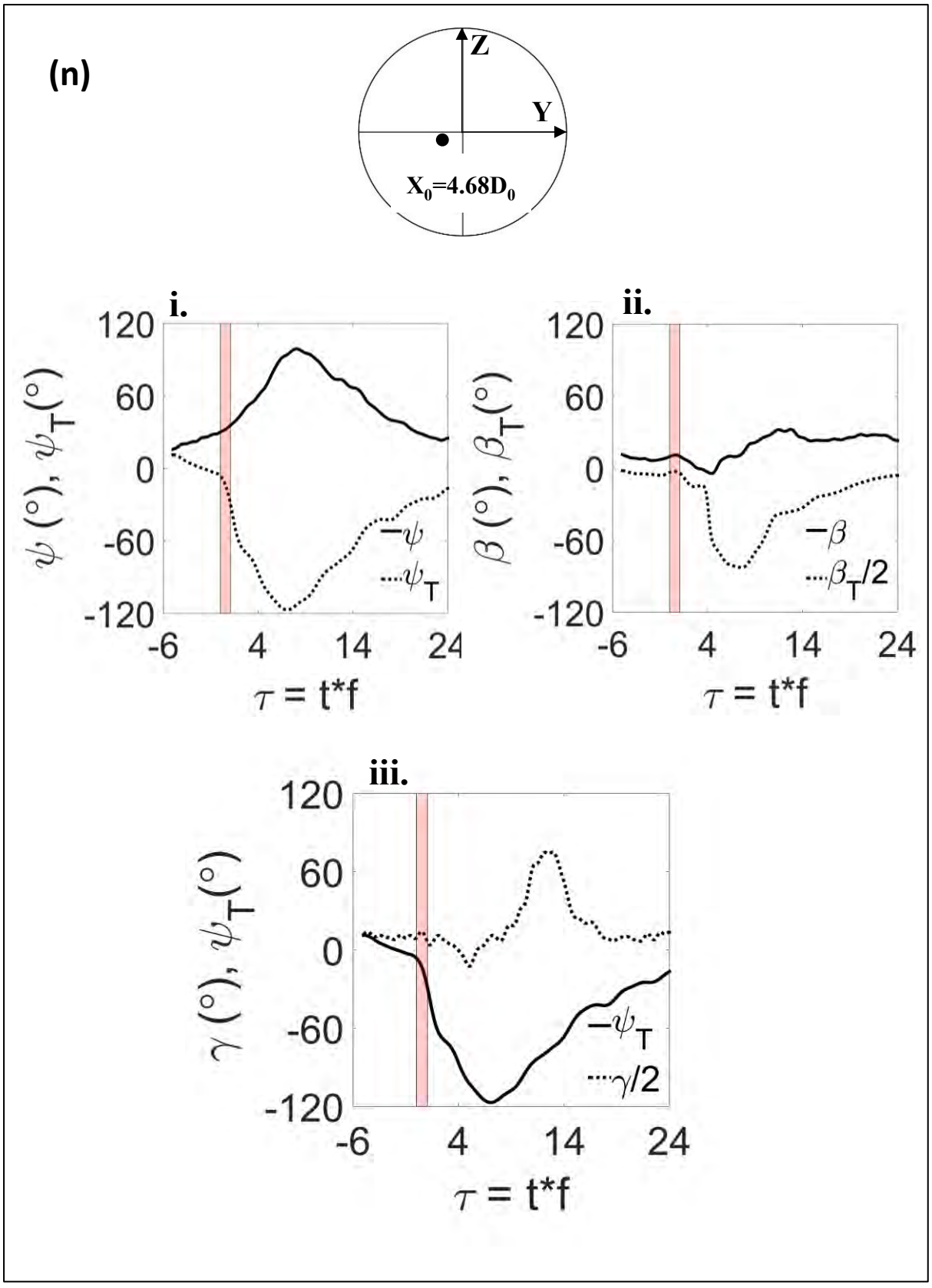

Figure 4-10: (continued)

Table 4- 7: Initial and final values of trajectory angles. Ψ_T and β_T represent trajectory yaw and pitch respectively. Values before and after gust are averaged over four wing beats.

# Expt	Ψ_T		β_T	
	Before Gust	After Gust	Before Gust	After Gust
a	-8.55	-64.63	10.59	65.77
b	0.85	5.24	20.07	5.52
c	-5.07	18.89	11.93	52.66
d	18.65	46.70	0.10	-8.83
e	10.81	-1.05	0.29	15.67
f	0.97	40.26	15.16	30.67
g	16.45	19.31	17.96	48.91
h	-9.49	-28.41	17.75	23.66
i	5.57	20.04	25.44	39.30
j	-22.76	-32.54	15.11	7.36
k	6.31	8.73	0.00	-7.93
l	18.61	54.84	25.76	64.67
m	0.80	-53.57	-9.81	-23.81
n	14.20	16.51	16.50	6.23

Table 4-8: Difference between trajectory angle and body angles values before and after gust averaged over four wing beats. $\Delta\Psi$ = Trajectory yaw – Body absolute yaw; $\Delta\beta$ = Trajectory pitch – Body pitch; $\Psi_T - \gamma$ = Trajectory yaw – Body roll

#Expt	$\Delta\Psi$		$\Delta\beta$		$\Psi_T - \gamma$	
	Before Gust	After Gust	Before Gust	After Gust	Before Gust	After Gust
a	51.32	9.60	-14.03	46.23	-14.65	-34.88
b	-35.84	-11.95	7.02	13.66	-6.38	-131.32
c	27.10	68.58	-21.43	28.46	-10.14	10.14
d	-2.02	37.41	-1.43	16.87	14.18	-25.24
e	59.10	40.73	-22.02	25.41	-2.55	25.89
f	-26.65	-7.20	-2.04	11.25	-6.41	-36.98
g	44.59	59.63	-18.17	9.97	1.79	-11.05
h	33.42	0.61	-6.48	20.28	-15.55	17.88
i	-1.37	16.79	-19.58	4.05	-2.31	-24.42
j	-51.80	-77.60	-16.75	-5.72	-9.10	4.83
k	-6.72	-1.88	-36.11	-33.82	-3.70	-119.60
l	10.72	43.94	-5.30	22.16	11.53	8.85
m	-23.75	-98.14	-17.52	-28.29	-19.03	-67.67
n	-45.00	-31.43	5.26	7.38	20.86	86.77
μ	2.36	3.51	-12.04	9.85	-2.96	-21.20
σ	36.50	48.27	11.99	21.27	11.64	57.18

4.2 Wing Kinematics

This section deals with the wing kinematics of the insect. Let us define some terms used here to understand the results better. We define response time, for wing kinematics, as the time when asymmetry in right- and left-wing stroke asymmetries is more than ± 20° in response to the gust, while recovery time as the time when sustained stroke asymmetry is less than ± 20°. The reason to consider response time and recovery time separately for body and wing kinematics is discussed in sec. 4.1.3. Here, an active response is defined as any voluntary motion or kinematic change (like change in wing stroke) performed by insects in response to the gust, while passive motion as one induced just by the flow disturbances. Similarly, the maximum angle the wing moves in a half cycle is termed half-stroke amplitude, denoted by θ_0, as shown in Figure 4- 11 and we define peak difference as the difference in stroke amplitude of right and left wings.

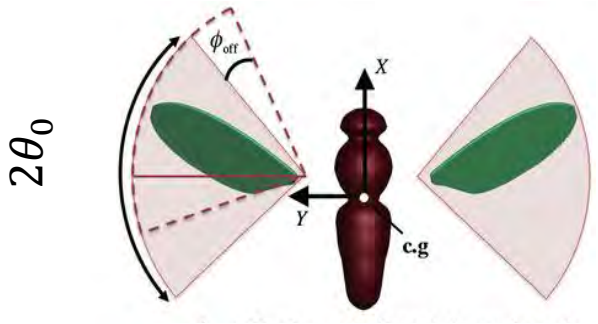

Figure 4- 11: Wing stroke angle. θ_0 denotes half – stroke amplitude and is given as the maximum angle, the wing moves in the plane swept by the line joining wing tip and its base.

In order to find the stroke angle, the position data of different digitized parts of the fly were first converted from a global coordinate system to a body reference system, beginning with a right-handed yaw rotation about the global vertical axis, followed by pitch and roll rotation about the global axis. The azimuthal angle of a vector joining wing tip and its base in stroke plane relative to body reference system gives the measure of wing stroke angle. Figure 4- 12 (a to n) show wing stroke and peak difference plotted against time for the different cases.

Before being hit by gust, the wing stroke amplitude was observed to be 115 ± 17° (mean ± SD) and the peak difference was near zero across the different cases, as shown in Figure 4- 12 (a-(i, ii) to n-(i, ii)). The wing stroke amplitude for each case are listed in Table 4-9.

Peak difference was noted in each case to study if the fly responds actively to the gust. Results show that stroke asymmetry occurs in 2 ± 1.5 wing beats (18.2 ±13.6 x 10^{-3} ms), as shown in Figure 4- 13. The asymmetry continued for 9 ± 3 wing beats (81.9 ± 27.3 x 10^{-3} ms), as shown

in Figure 4- 13, after which either stroke became symmetric or asymmetricity if existed, was less than ± 20°. The value for response and recovery time for each trial are listed in Table 4-9. Moreover, the response time along roll axis and for wing stroke are approximately same (see section 4.1.3 and Figure 4-7). Also, the fly recovered its body attitude, on average, after this recovery period, suggesting that kinematic change in wing stroke directly or indirectly affects the body attitude and orientation.

Considering the time latency for any passive response in a fly (> 5 – 6 wing beats)((Dickinson & Muijres 2016; Sherman & Dickinson 2003)), beginning of stroke asymmetry on such a short timescale (~ 2 wing beats) is believed to be an active mechanism employed by insects (flies and bees) to correct for perturbations ((Dickinson & Muijres 2016; Ortega-Jimenez et al. 2014; Crall et al. 2017; Vance et al. 2013; Ristroph et al. 2010; Ristroph et al. 2013; Beatus et al. 2015).

Existing literature also reports that insects employ differential angle of attack to correct for yaw in response to gusts ((Ortega-Jimenez et al. 2014; Vance et al. 2013; Ristroph et al. 2010) and also employ differential wing excursion forward or backward on each wing to correct for pitch (Dickinson & Muijres 2016; Ristroph et al. 2013). The present study was not focused on dissecting this aspect of wing motion.

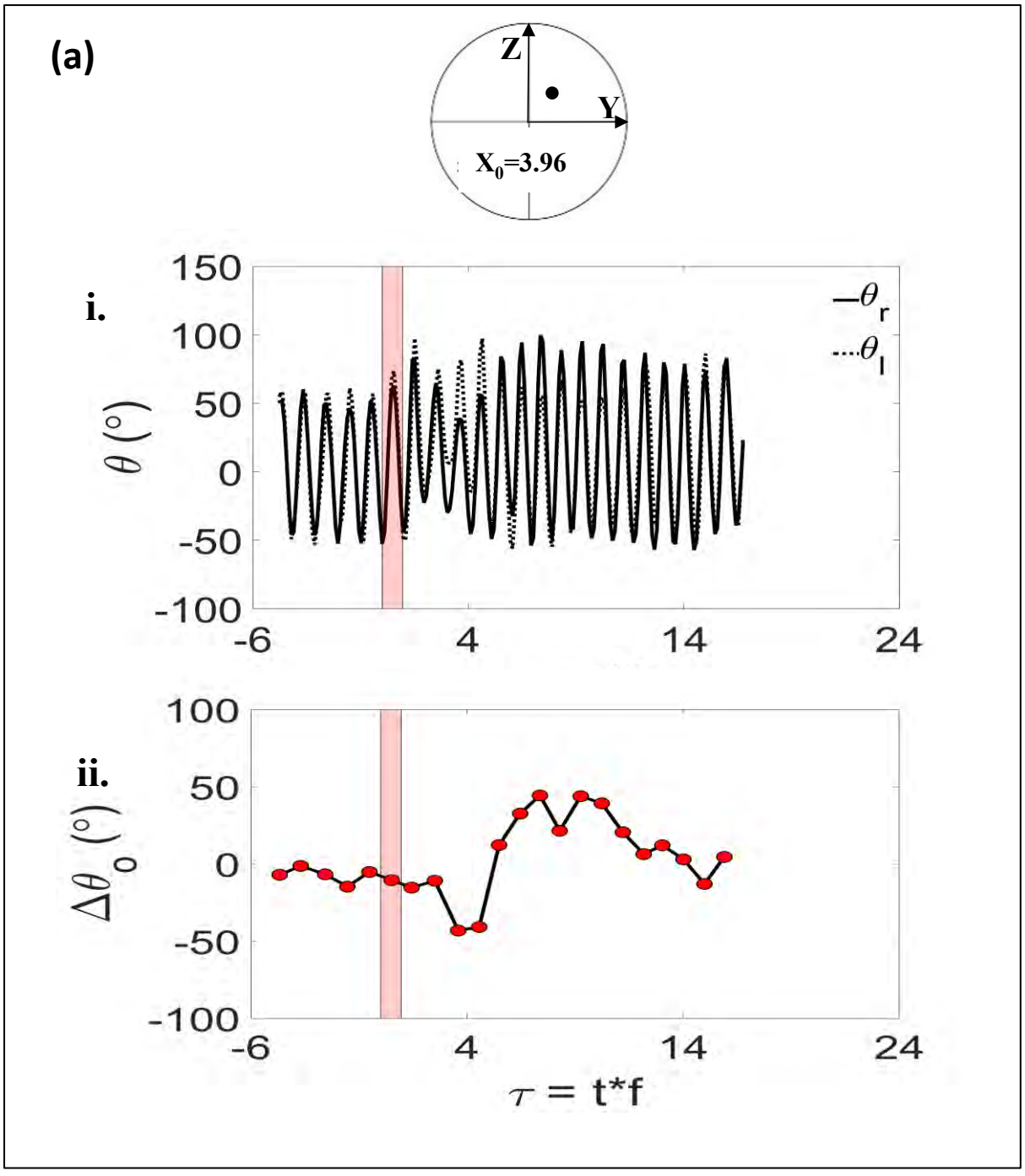

Figure 4- 12: Wing stroke and peak difference. θ and $\Delta\theta_O$ represent wing stroke angle and difference in stroke amplitude of right and left wings. Vertical strip denotes time instance of vortex ring. Circle represents front view of the ring and black dot inside it the relative position of insect, with its axial distance from nozzle exit represented by X_0. Small alphabets within braces ((a)) indicates trials while (i) and (ii) are wing stroke and difference of stroke amplitude plotted against dimensionless time (τ) respectively. τ=0 indicates the instance when fly was hit by gust.

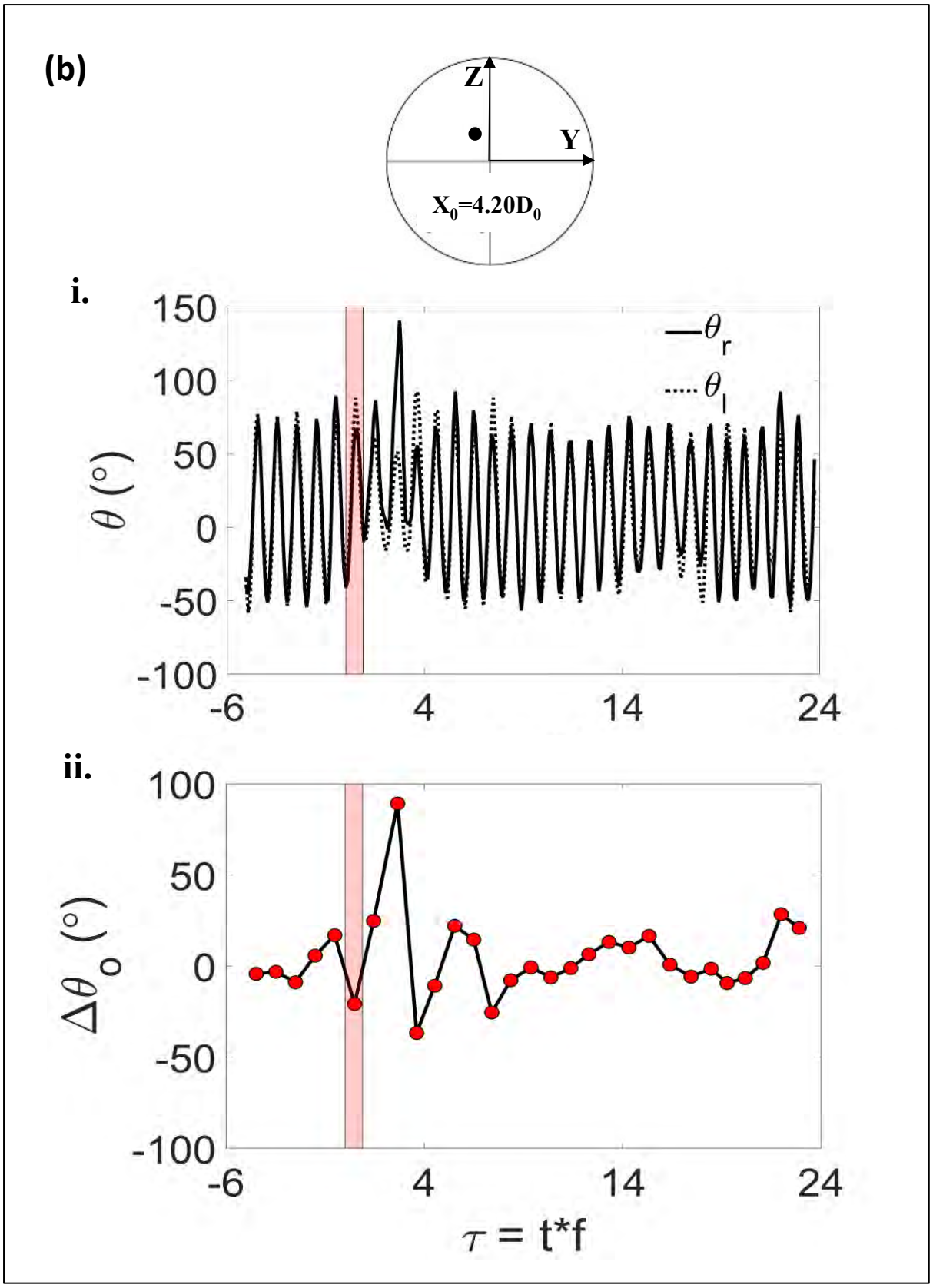

Figure 4-12: (continued)

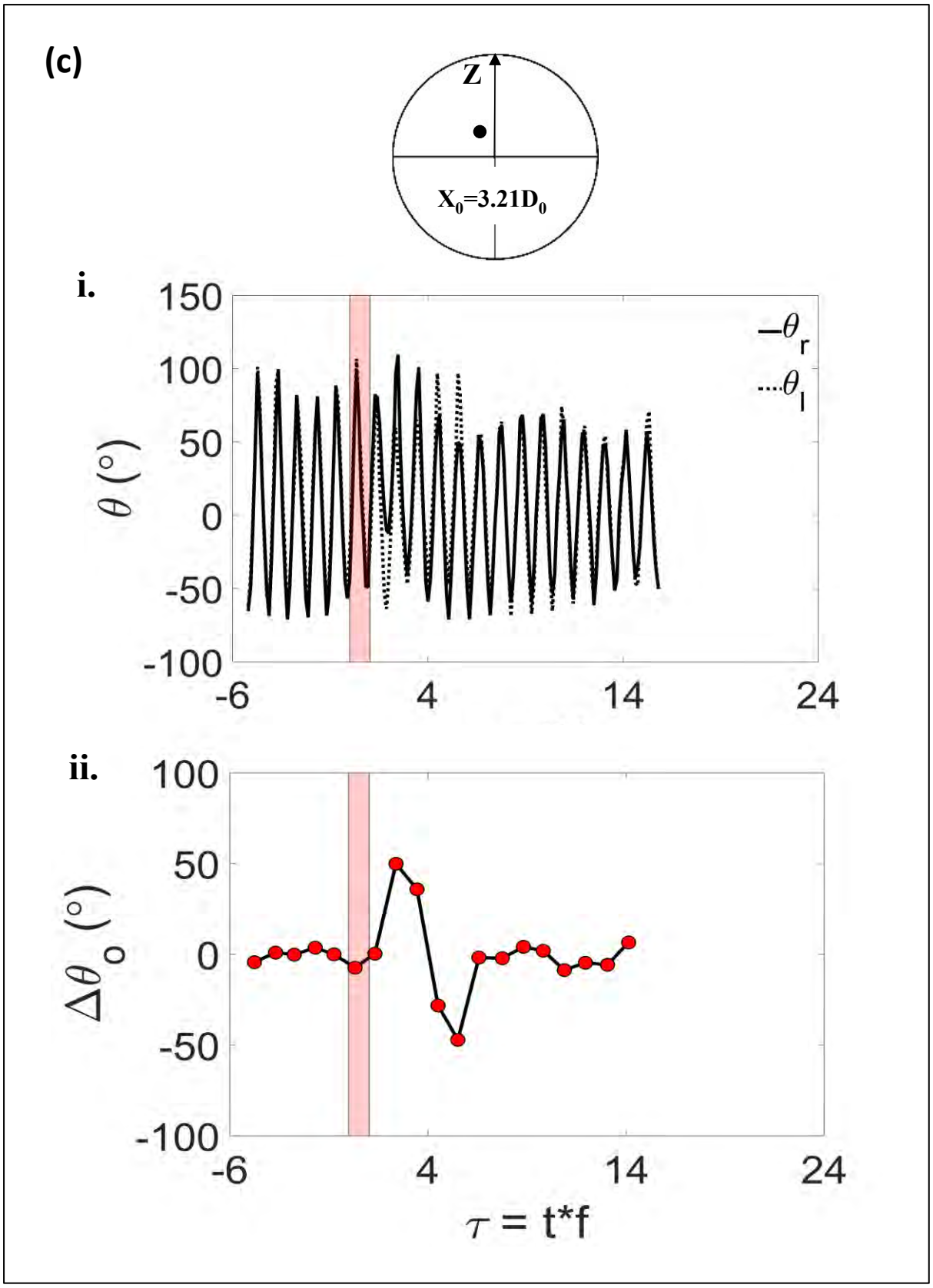

Figure 4-12: (continued)

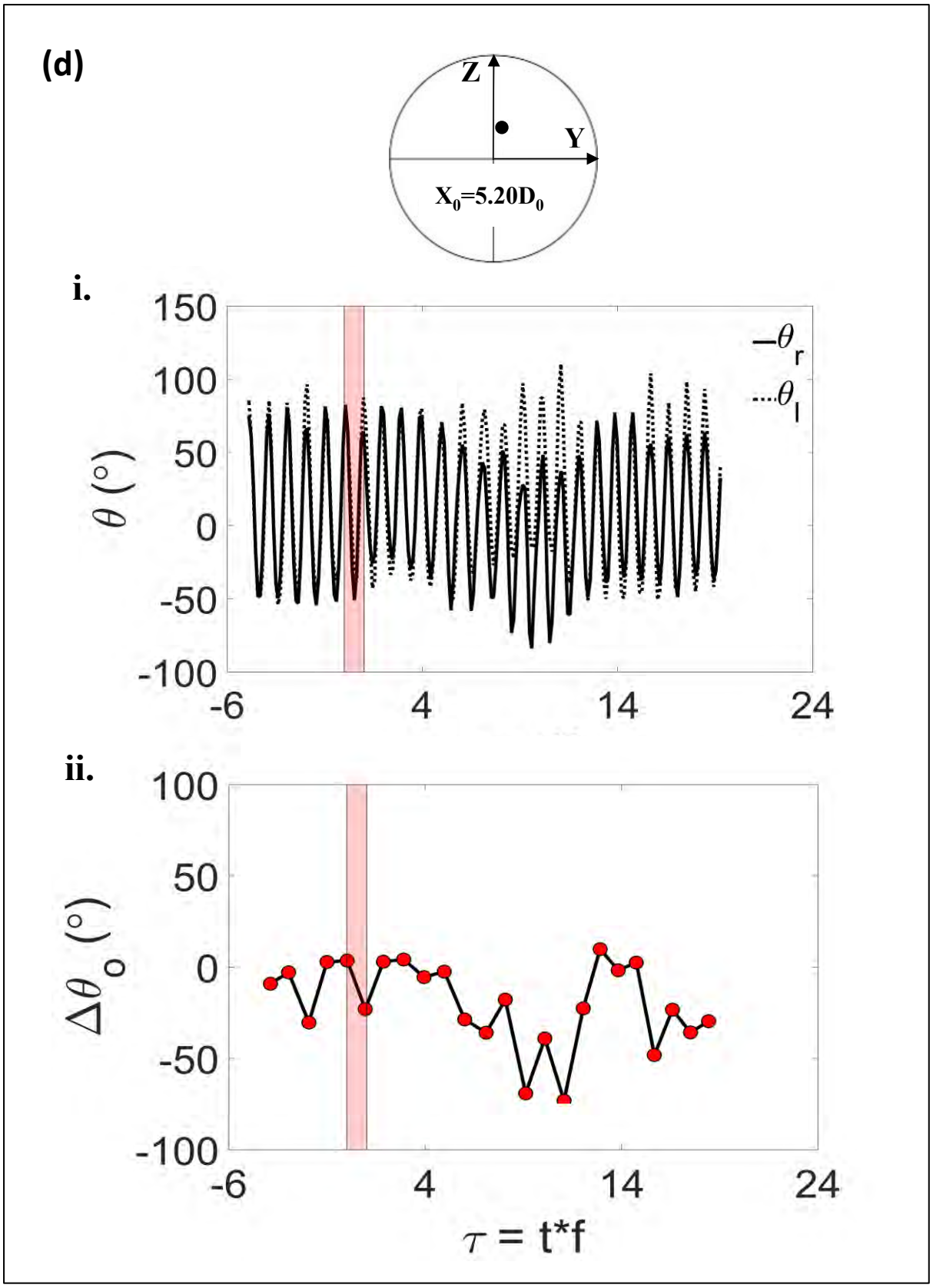

Figure 4-12: (continued)

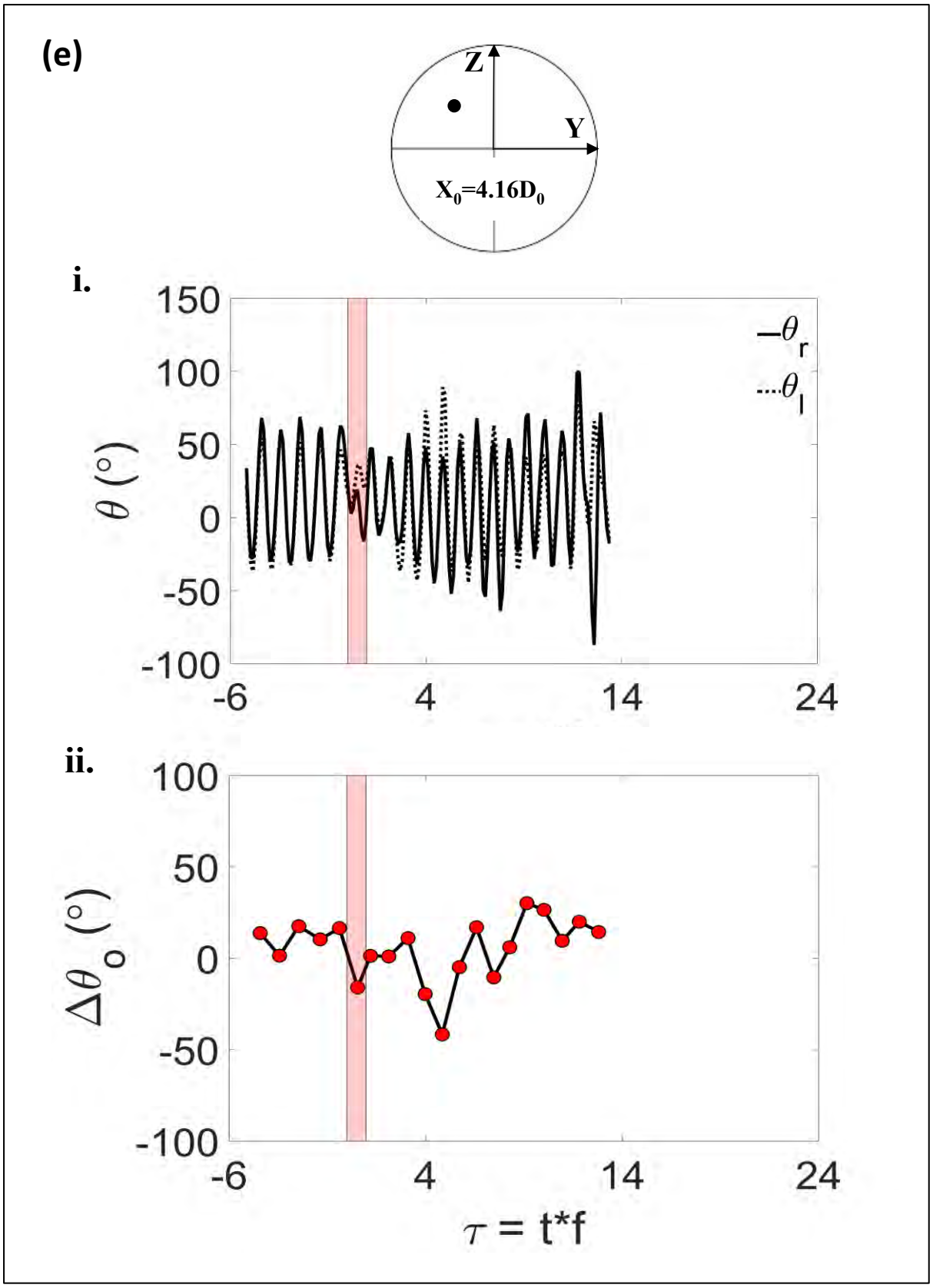

Figure 4-12: (continued)

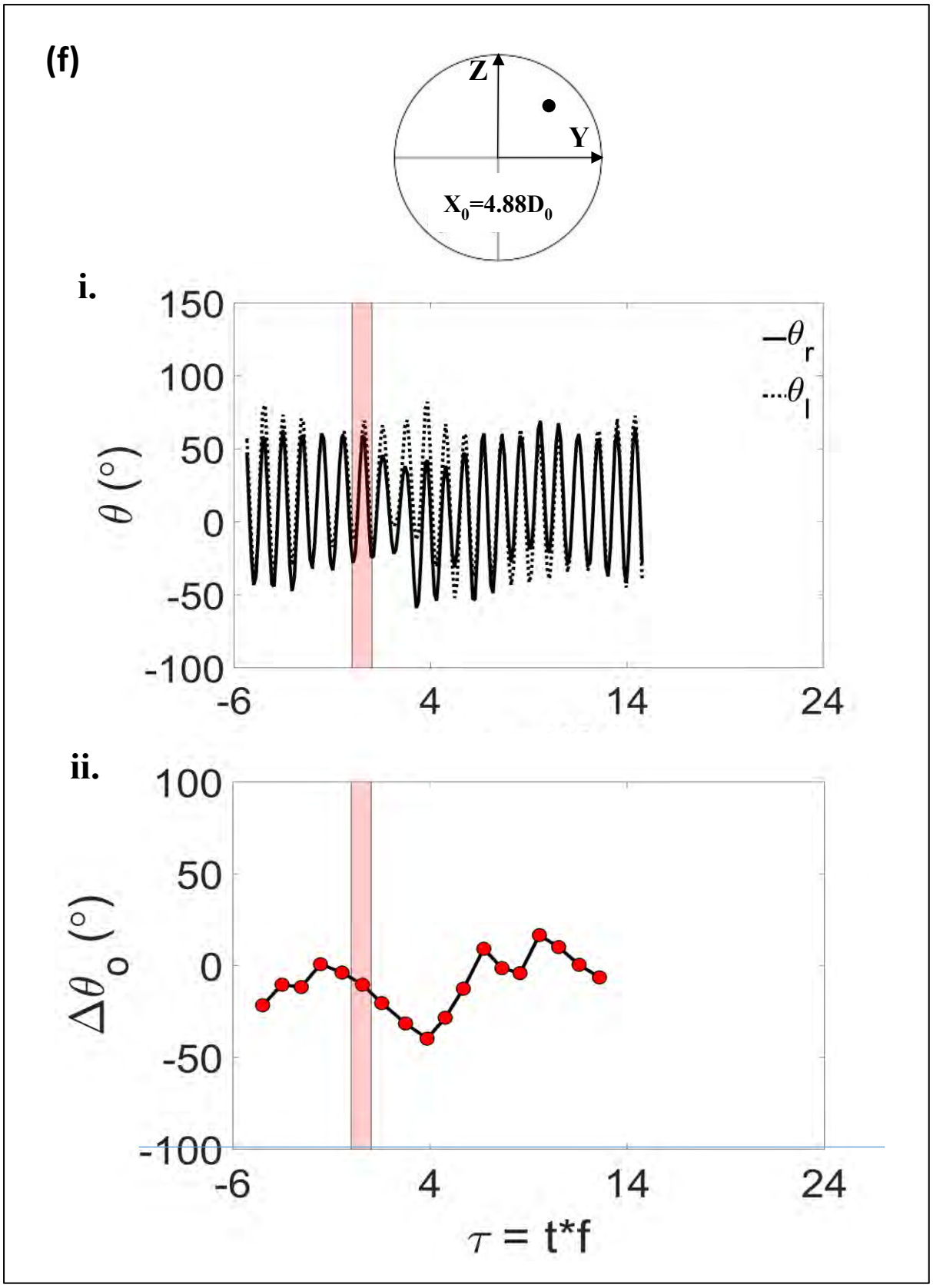

Figure 4-12: (continued)

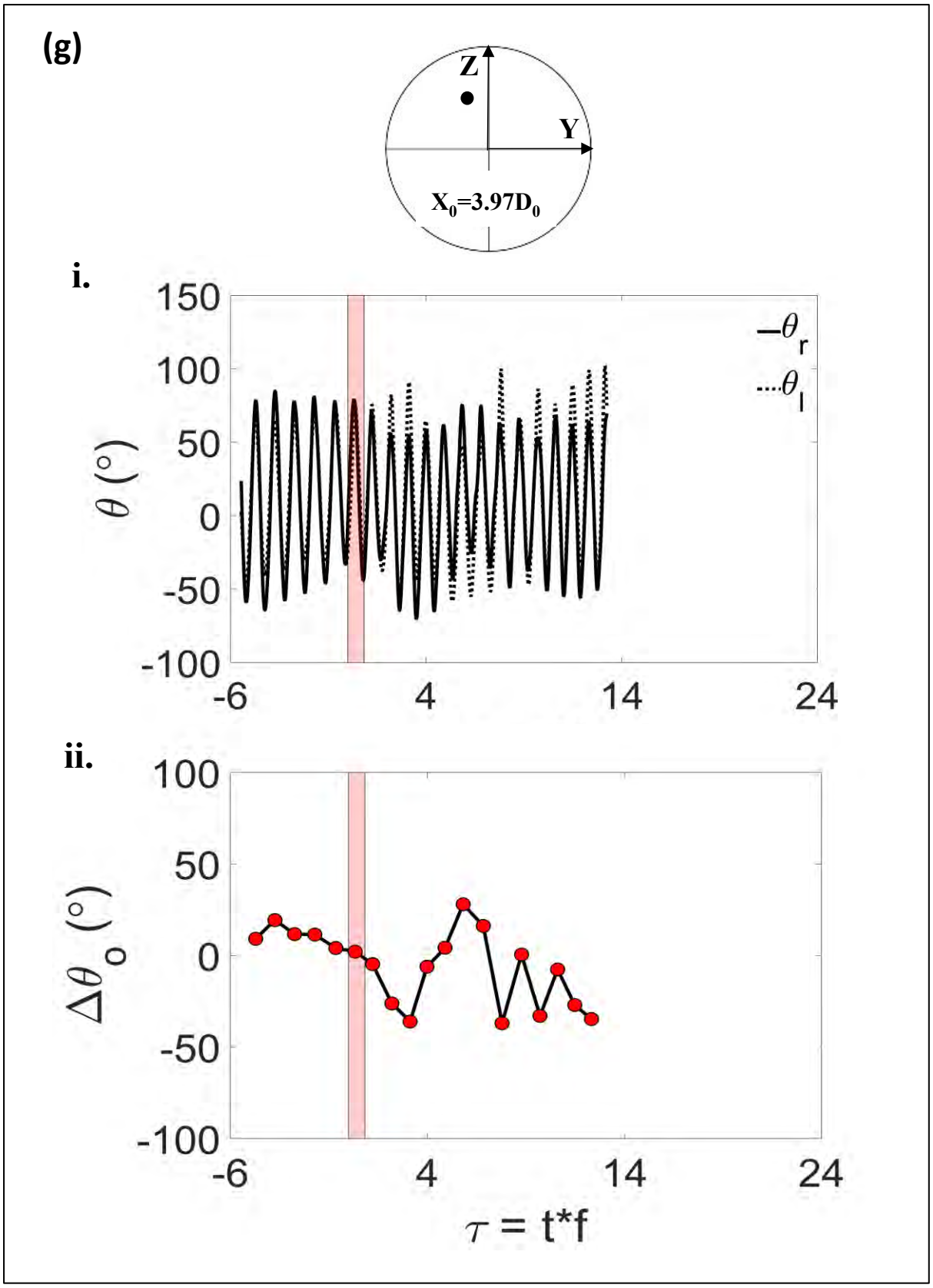

Figure 4-12: (continued)

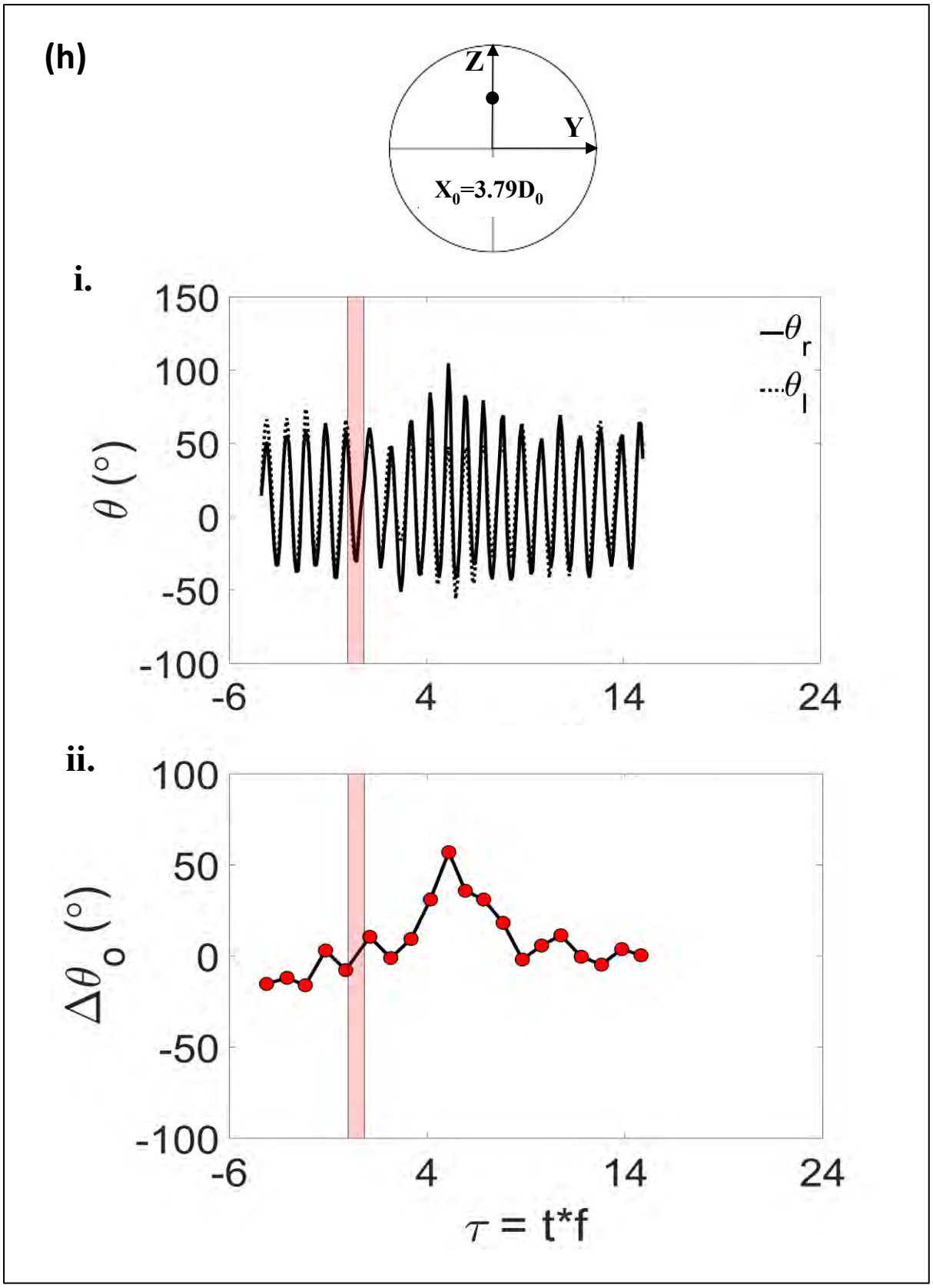

Figure 4-12: (continued)

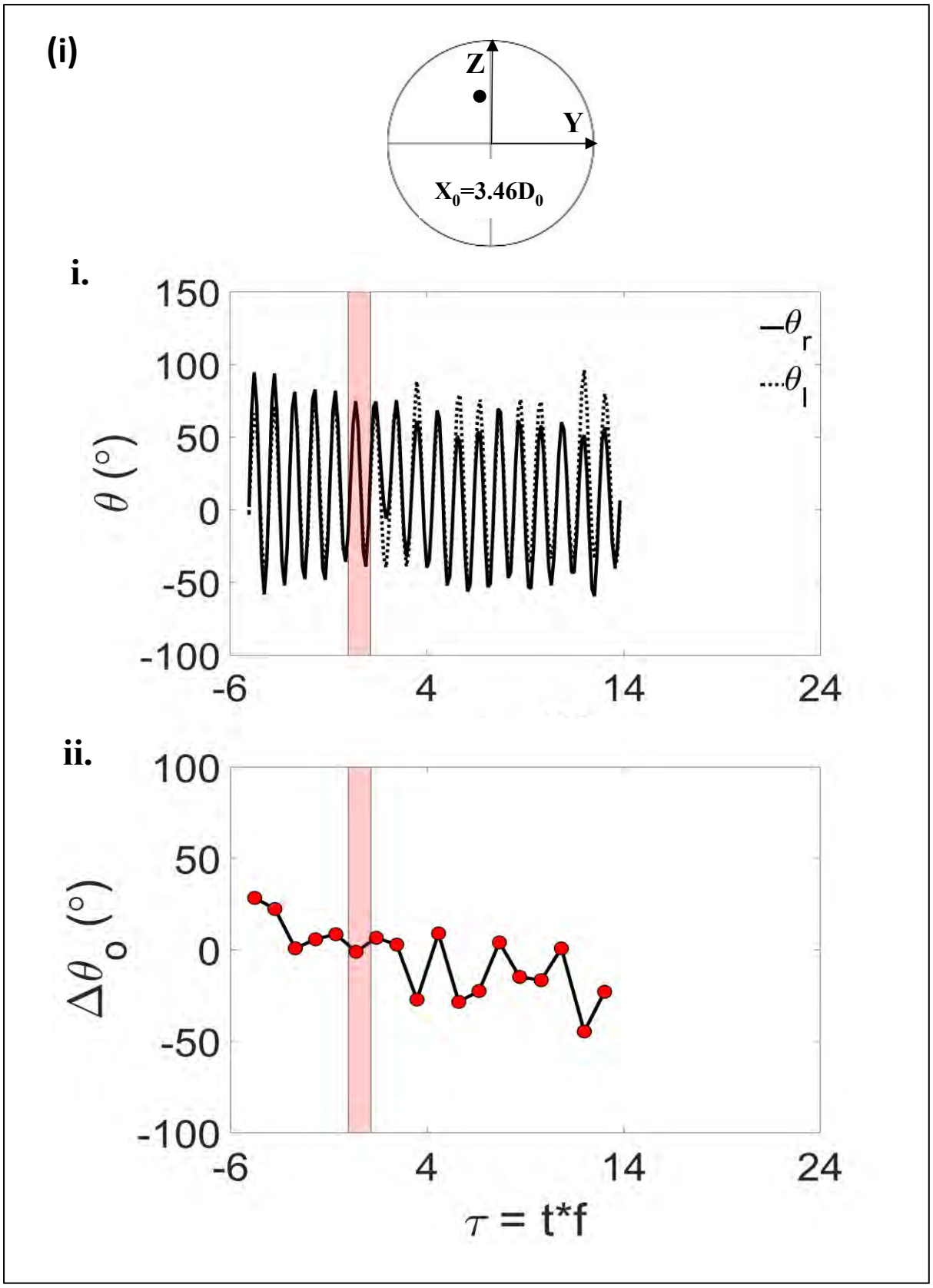

Figure 4-12: (continued)

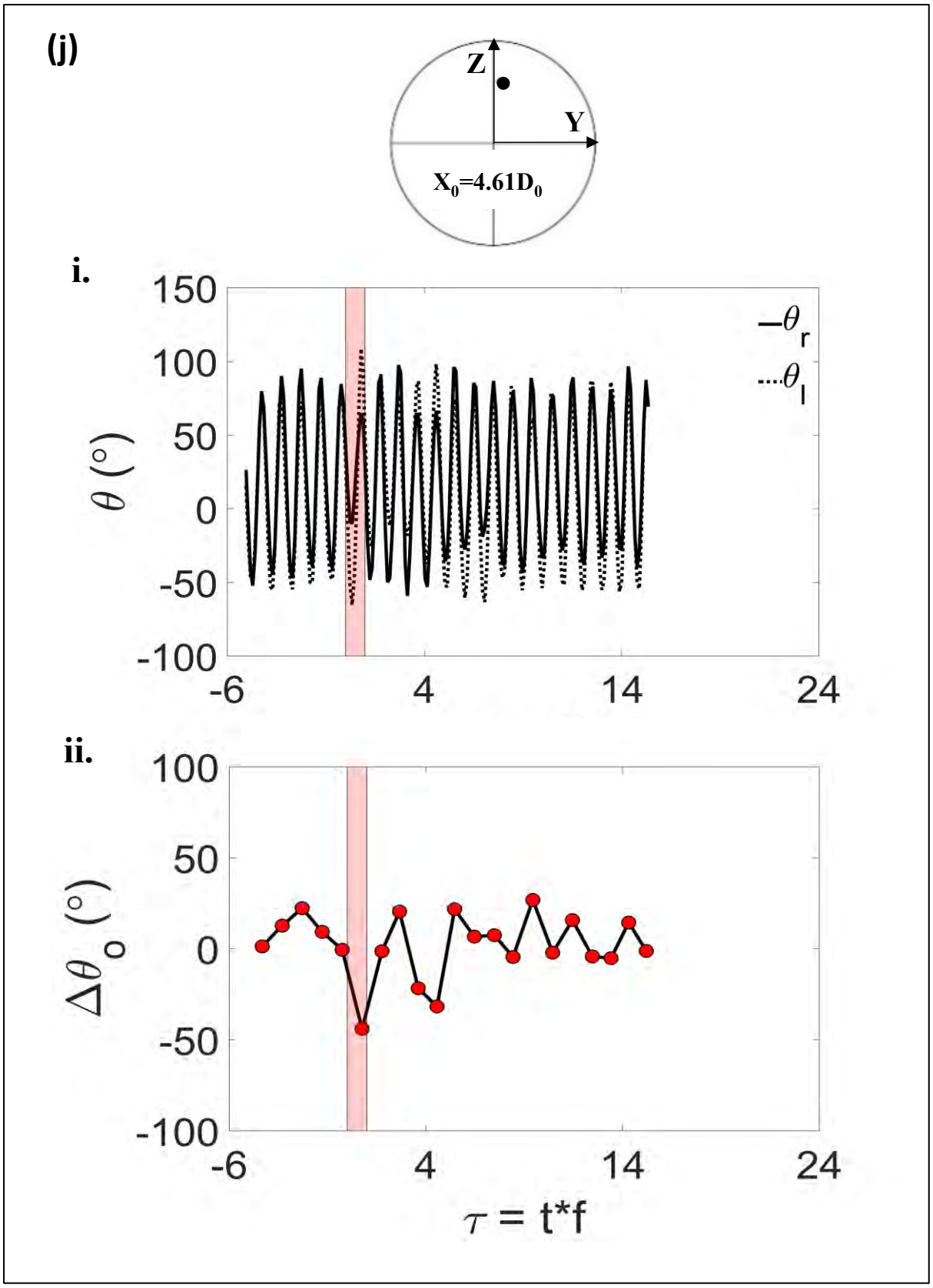

Figure 4-12: (continued)

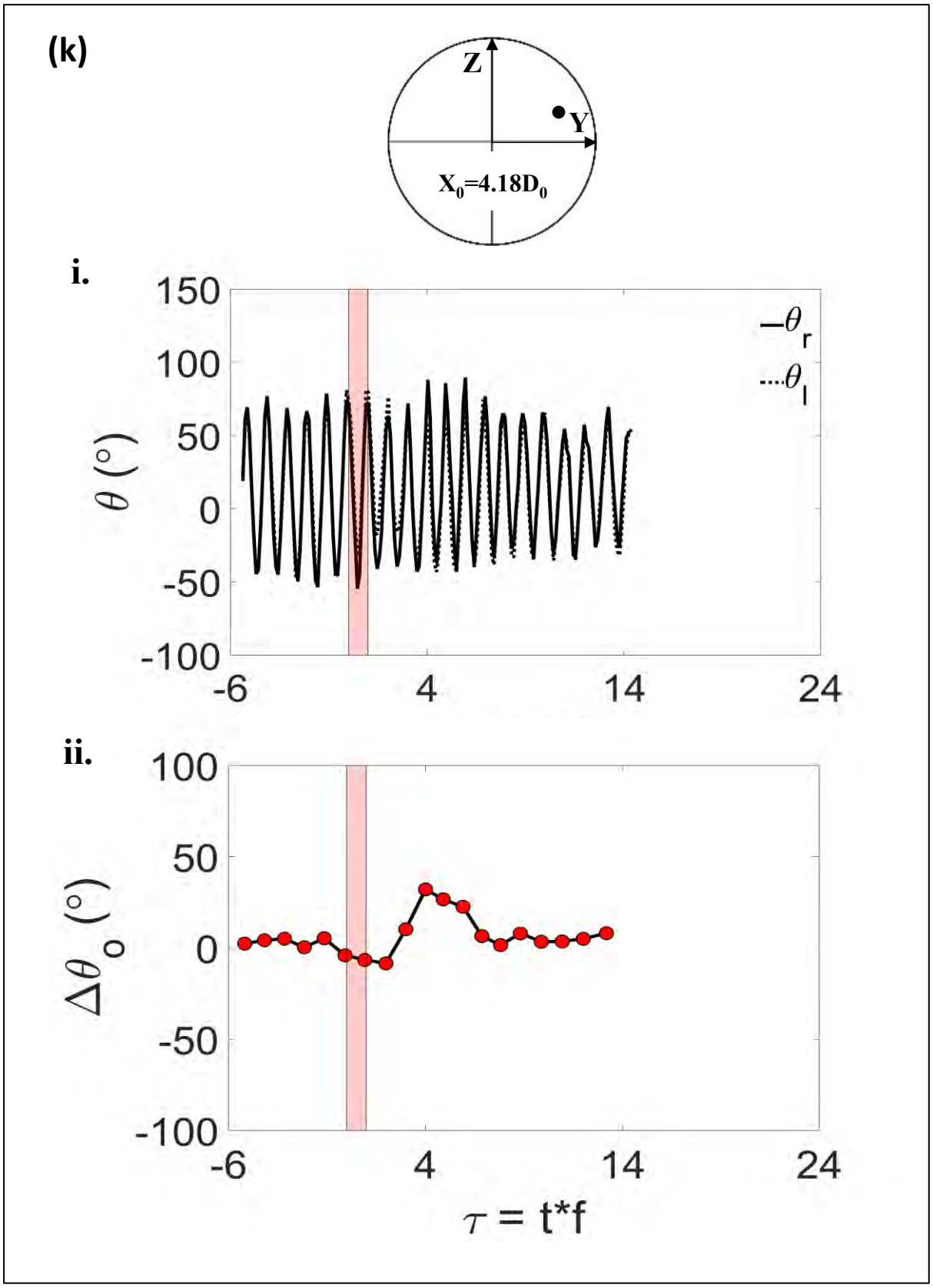

Figure 4-12: (continued)

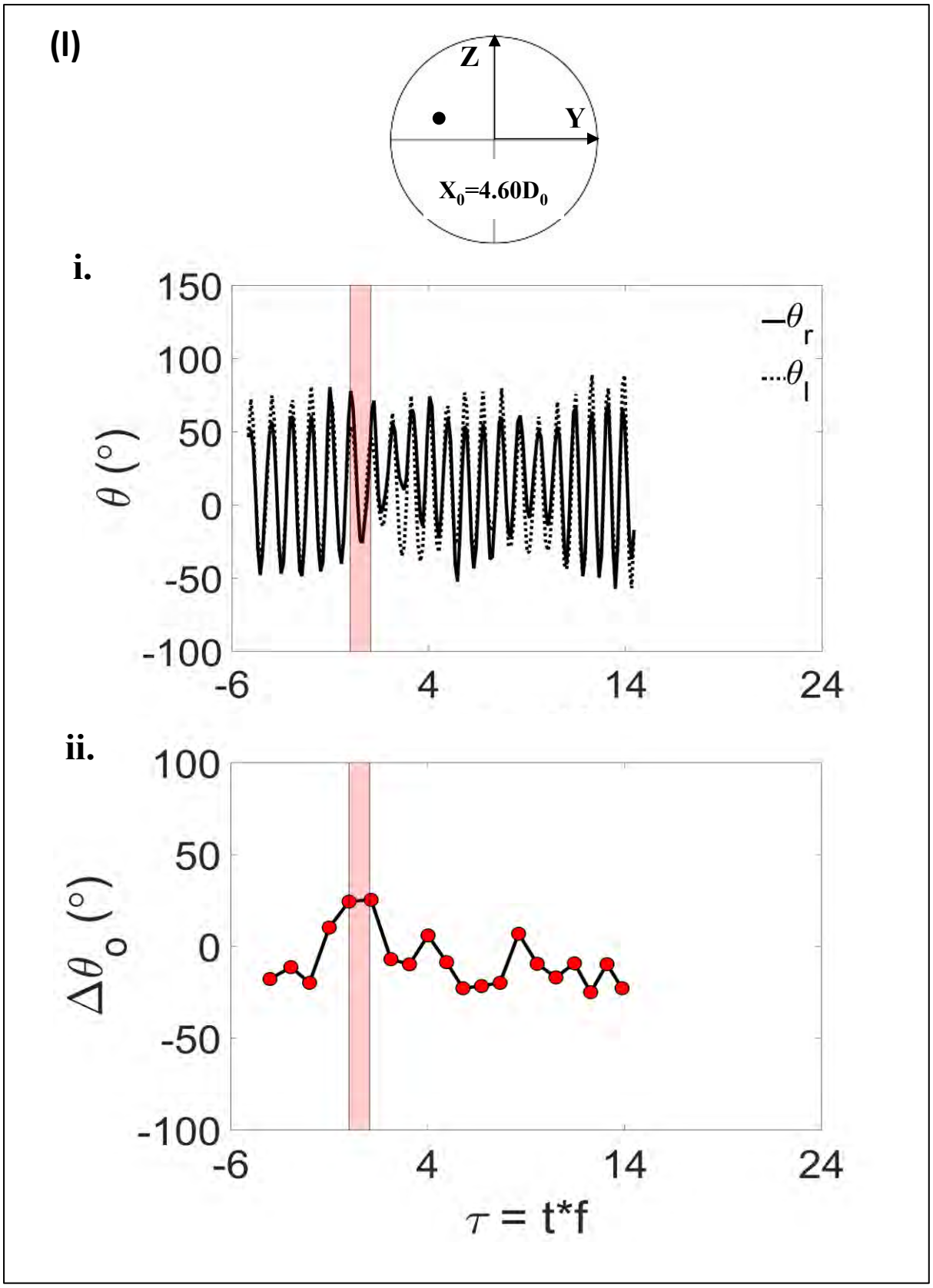

Figure 4-12: (continued)

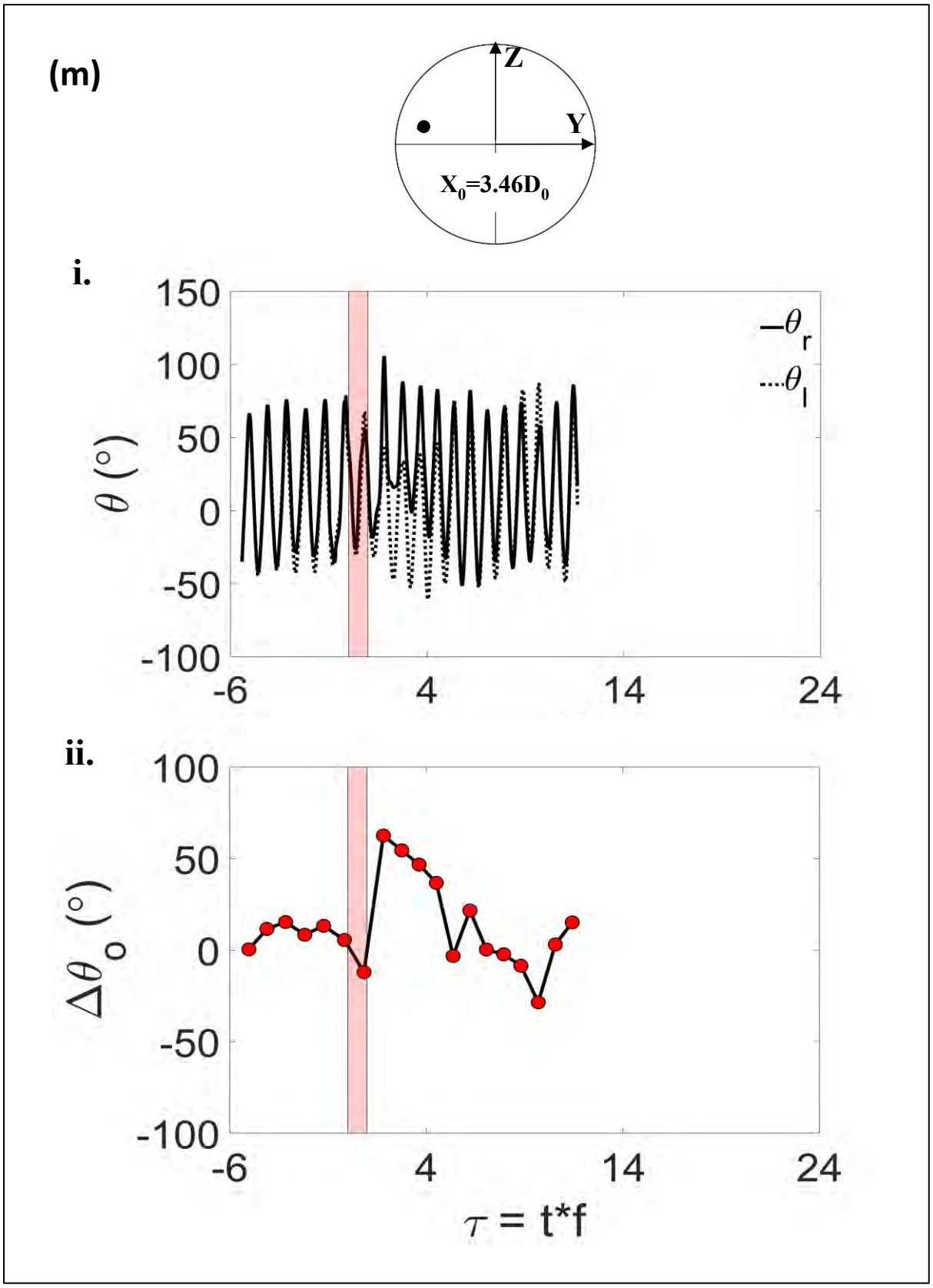

Figure 4-12: (continued)

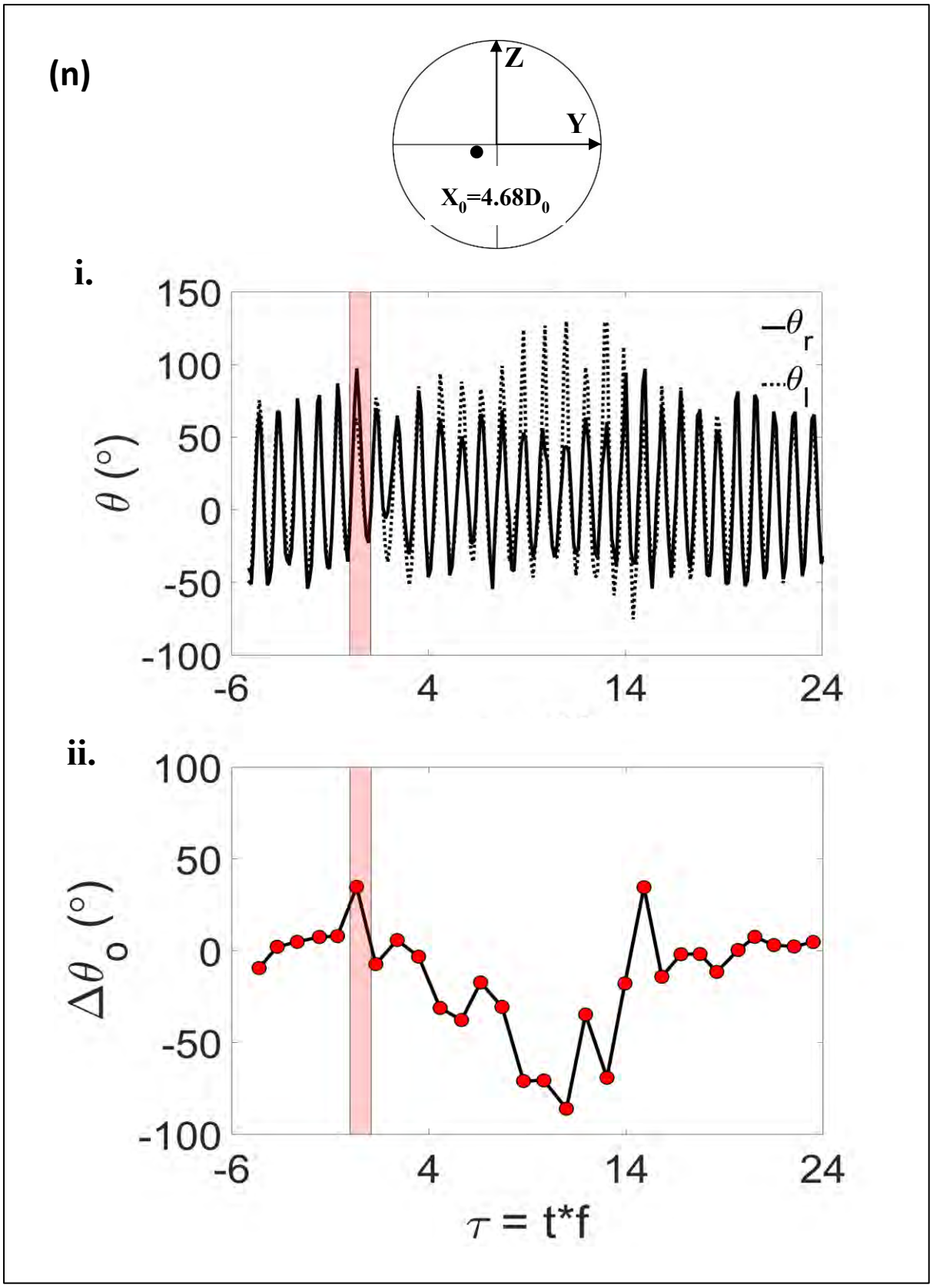

Figure 4-12: (continued)

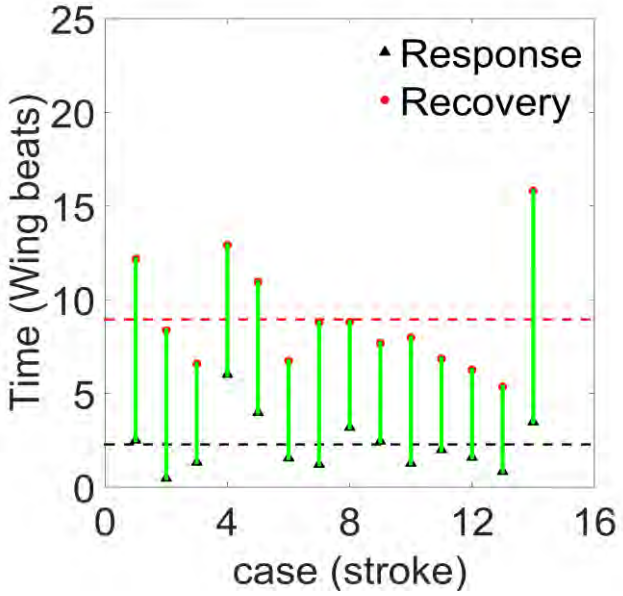

Figure 4- 13: Response and recovery times for wing stroke amplitude for different trials. Dashed lines show the mean response and recovery times for wing stroke amplitude.

Table 4-9: Average Stroke amplitude before gust and response and recovery time observed in different realizations. Note time is given in terms of wing beats (WB).

#Expt	Average Stroke amplitude Before Gust(θ_o) (°)	Response time (WB)	Recovery time (WB)
a	106.85	2.51	12.18
b	124.94	0.48	8.36
c	152.43	1.33	6.58
d	126.30	6.01	12.91
e	88.99	3.98	10.95
f	97.26	1.55	6.73
g	118.60	1.22	8.78
h	92.85	3.19	8.81
i	123.17	2.45	7.68
j	127.88	1.27	7.98
k	115.23	1.99	6.86
l	111.53	1.59	6.25
m	102.03	0.83	5.36
n	117.96	3.48	15.82
μ	**114.71**	**2.28**	**8.95**
σ	16.66	1.48	2.98

4.3 Summary

We note the following major responses of the insect to the gust in the cases that were studied.

I. Large displacement in Y and Z directions in the majority of the cases.

II. Large change in the body roll, as much as by 160°, that happens, on an average, in two wing beats (~ 20 ms), and with recovery in about 9 wing beats.

III. Change to pitch down attitude in about 5.5 wing beats in response to gust.

IV. No recovery in yaw and pitch attitude in the majority of the cases

V. Deceleration in flight direction

VI. Asymmetry in wing stroke amplitude by more than 20° in about 2 wing beats in response to gust. This asymmetry reduced to less than 20° in about 9 wing beats.

VII. Possible positive correlation between body pitch and forward speed, and body roll and trajectory yaw.

Chapter 5. **Conclusions**

The effect of a head-on aerodynamic gust on flight kinematics of insects was studied experimentally. Vortex ring was used as a gust to perturb a freely flying insect (Black soldier fly) in a confined test chamber. The ring was generated by an impulsive motion of the diaphragm of an electronic speaker. Advantage of this perturbation method lies in well-understood physics and the high-controllability of its flow properties. The flow properties of the gust were characterized using fog visualization and bead method. The flight motion of the insect was recorded using high-speed cameras. The images were then analyzed to study changes in body and wing kinematics of insects due to gust.

The fly pitches down and decelerates on encountering the gust which is in accordance with the helicopter model of insect flight, which suggests some correlation between body motion and its orientation. It is highly sensitive to gust along the roll axis, exhibiting a maximum roll of 160° clockwise at an angular rate 28000°/s. Despite these large changes in roll angle, it usually regains its initial orientation and successfully maintains near-zero roll after gust in nine wing beats. However, the same is not the case along pitch and yaw axes. It attains new sustained pitch and yaw orientation after gust suggesting neutral stability along these axes. Trajectory angles were also analyzed with a hypothesis that trajectory and body angles should be quantitatively the same before gust, at least along the vertical axis. But, to our surprise, a significant difference exists between body and trajectory angles along both lateral and vertical axes, and between body roll and yaw trajectory as well. However, analysis shows that body roll happens mostly in the direction of trajectory yaw, indicating a possible correlation between roll and trajectory yaw. Study of wing kinematics revealed that stroke asymmetry begins in about two wing beats after gust; stroke symmetry is recovered in nine wing beats. Response to roll also happens on a time scale that matches the beginning of stroke asymmetry. However, it responds approximately 2.5 times slower to correct pitch and yaw orientations. Also, the recovery time for body orientation along three axes and time when wing stroke asymmetry ceases after gust are approximately equal, indicating wing stroke indeed play a major role in stabilization of insects in gusts. Further, such a short response time, high angular rates and short recovery time along roll axis5 imply that, in addition to passive mechanism, it also employs an active mechanism to counteract the effects of the gust.

FUTURE WORK

The present work focused mainly on the study of the kinematic response of insects in a gust. It, however, didn't report the role of angle of attack and aerodynamics of the wing for stabilization. Aerodynamics of insect flight under such a severe environment is still missing in

the existing literature. This can be accomplished by carrying out a volumetric particle image velocimetry (PIV) with a freely flying insect subjected to gust. It is a complex and daunting task though. Simplification may result by subjecting a robotic insect model to such perturbations and directly measuring the force using load cells while carrying out planar PIV at the same time. Understanding the flow physics of insect flight under such conditions may provide us better insight in the design of MAVs and NAVs.

Appendix A: Generation of gust by pitching foils

Introduction

In this section, we first present a numerical simulation of a pair of sinusoidally pitching two dimensional thin foils which can produce transverse and/or streamwise velocity fluctuations superimposed over the mean flow. The unsteady flow is generated in the region behind and between the wakes of the foils. The flow so generated and superimposed over mean flow is called here as a ***gust***. The results and their validation, limitations and some gust enhancement techniques are then discussed. Finally, we discuss the proposed technique for gust enhancement and, with the help of some results, how this technique proves to be better compared to the conventional ones is also discussed.

Method

Two NACA 0015 foils with chord length (c) 20 cm was used, with a separation of 2.3c and 3c in between them. The point of oscillation was fixed at mid-chord point, which also served as the origin for the numerical simulation. The geometry creation was carried out in commercially available Ansys workbench. The geometry and dimensions are given in Figure A (1)**- (i)**. The distance between the sidewalls of the geometry was chosen based on the dimension used by Stapountzis (1982) to ease validation. The whole domain was discretized using an unstructured grid that was generated using Tetrahedral elements in Ansys workbench. To simulate the pitching motion of the foils, sliding mesh technique was used. In sliding mesh technique, the pitching foils are fixed to the surrounding domain and the domain rotates by the specified angle. This method has the advantage of preserving grid quality over dynamic mesh technique in which just the airfoil pitches up and down, thereby leading to tearing up of mesh for high rotation angle. Before solving the flow over pitching foils, grid convergence was carried out for steady and non-rotating airfoil for different angles of attack in Ansys FLUENT employing inviscid, laminar and turbulence models like S-A, k-ε, and k-ω. It was found that realizable k-ε model (with inlet turbulence intensity 5%) gives the result that agrees well with thin airfoil theory (grid convergence and results not shown here).

Once we chose the suitable turbulence model (i.e. realizable k-ε), further spatial and temporal grid convergence was carried out for a different number of nodes and different time steps. The instantaneous transverse velocity calculated at 6c downstream on the centerline between the foils is shown in Figure A (1)-(ii) for the different number of grids for a pitching frequency of 9.7Hz. The maximum velocity changed by not more than 2% after 2.6 x 10^5 number of nodes, as can be seen in Figure A (1)-(iii). Also, because the flow is unsteady, the simulation was run

for different time steps(Δt) for 2.6 x 10^5 number of nodes and it was observed that the change in maximum velocity was lesser than 2% for (Δt) less than 0.2 ms (See Figure A (1)-(iv)) and, hence, this spatial and temporal resolution was used for further calculations. Here, the amplitude of transverse sinusoidal velocity is considered as maximum velocity and is denoted by V_{max}. V_{max} is considered only after the unsteadiness due to starting motion subsides (to be discussed later in detail). The data is shown for the foils separation of 3c. A similar convergence test was carried for Y=2.3c. It is also noted that uniform grid spacing was employed around each airfoil in a rotating domain with a grid growth rate of 1.2 outside this domain, and the boundary layer was not resolved. Considering that the focus of the present work not on boundary layer or drag calculation, but on gust generation due to vortices shedding (to be discussed later in detail), usage of uniform grid spacing is justified.

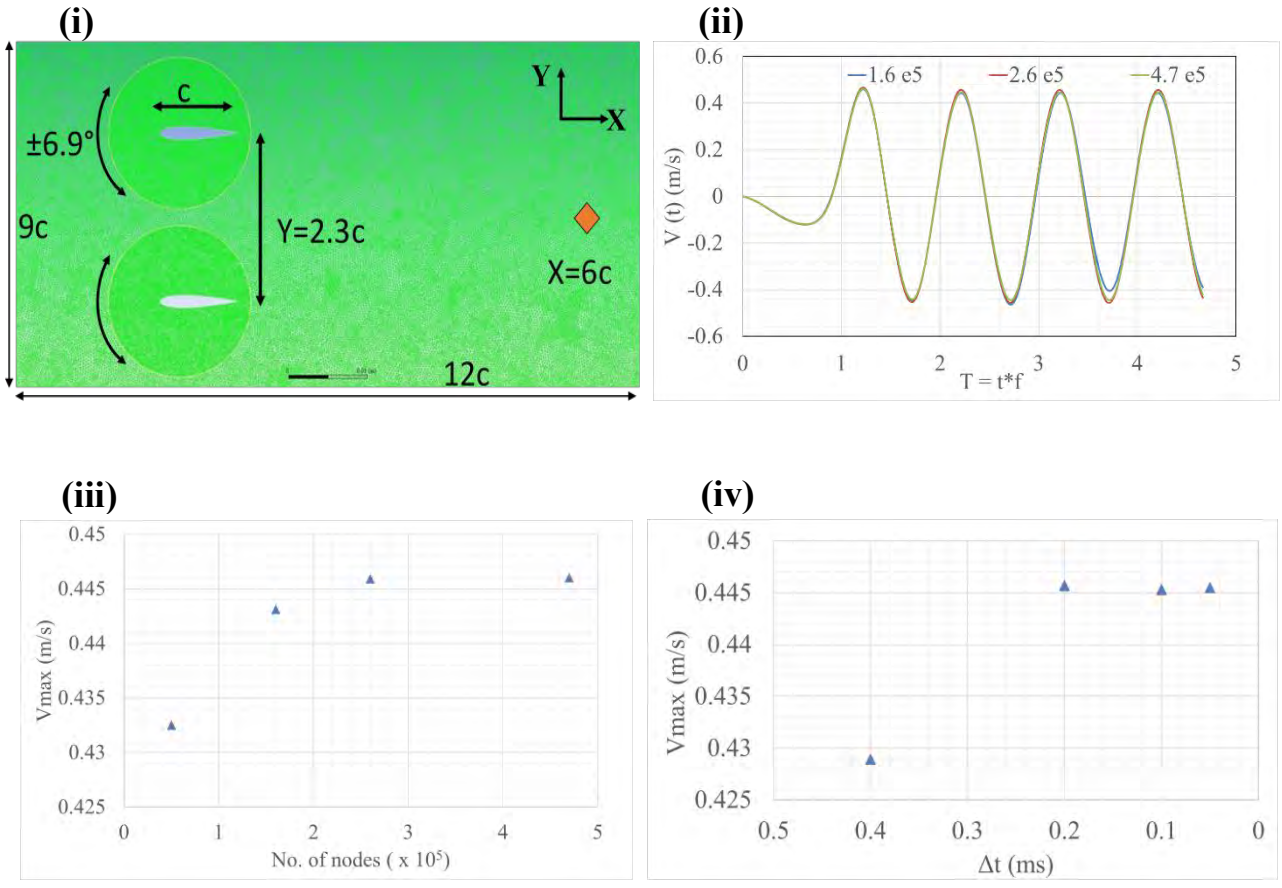

Figure A (1): Numerical geometry and grid convergence. (i) Geometry creation. X and Y are streamwise and transverse directions respectively. A pair of NACA foils are placed at a separation of 2.3 chord length (c), both pitching up and down by 6.9° in-phase. he foils pitch about mid-chord point, enforced by a custom written UDF. X_0 is the location where values of interest are calculated. The distance between sidewalls is 6c and that between inlet and outlet is 12c. (ii) Instantaneous transverse velocity, V(t) calculated at X_0 = 6c for 1.6 x 10^5, 2.6 x 10^5 and 4.7 x 10^5 nodes for pitching frequency of 9.7 Hz. Time is normalized with pitching frequency. (iii) Maximum transverse velocity (V_{max}) versus number of nodes(N). Change in V_{max} is < 2% for N > 2.6 x 10^5. (iv) V_{max} versus time step (Δt) used for simulation. Change in V_{max} is < 2% for Δt < 0.2 ms.

Boundary conditions

The mean flow velocity (U) was chosen so that Reynolds number ($Re = Uc/\upsilon$), based on chord and mean flow velocity was 1.6 x 10^5. No-slip boundary condition was imposed on all wall surfaces, while velocity and pressure boundary conditions on inlet and outlet respectively. Transient pressure-based solver employing first order SIMPLEC upwind and second-order implicit formulation were used.

Pitching motion of the foils was achieved using a custom UDF that specified type of motion, maximum rotation angle (α_0) and rotation frequency (f). The instantaneous motion of the foils was given as below.

$$\alpha(t) = \alpha_0 \sin(2\pi f t)$$

Both the foils pitch sinusoidally in-phase. Vortices shed from the pitching foils induce velocity normal to the line joining their center and any point in the neighborhood, as per Biot-Savart law. Resolving the velocity into components results that in-phase sinusoidal motion gives rise to sinusoidal transverse gust, as the velocity induced in streamwise direction gets canceled out as shown in Figure A (2), and Out-of-phase pitching motion would cancel out transverse velocity component and results into only streamwise gust. We, here, aim at generating transverse sinusoidal gust. So, an in-phase sinusoidal motion was imposed on both the airfoils via UDF.

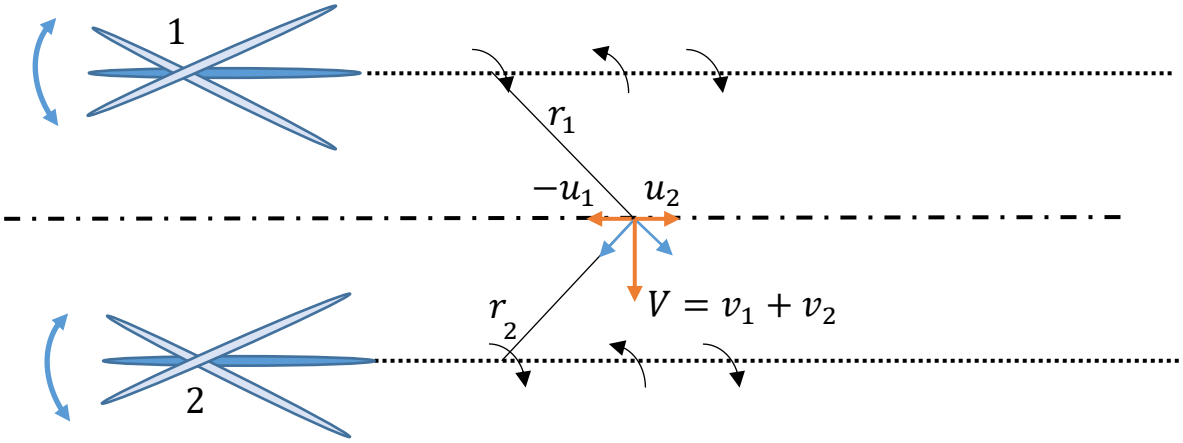

Figure A (2): In-phase sinusoidal pitch motion of a pair of foils. 1 and 2 denote upper and lower foils respectively. r is the distance from vortex center to a centerline point. The vortices shed from the foils induce velocity in the neighborhood. For ease understanding the flow physics, vortices are assumed to lie on a straight line behind trailing edge. u and V are streamwise and transverse velocity components induced by the vortices on the centerline. Streamwise velocity gets canceled out, while the transverse velocity component adds up, resulting in the transverse sinusoidal gust.

Results and discussion

We simulated pitching foils for Re = 1.6 x 10^5 at α_0 =6.9° and for a range of reduced frequencies ($k = \frac{\pi f c}{U}$) from 0.54 to 1.1 with an increment of 0.13. The choice of this range of k was dictated by two main reasons- (a) Maximum gust is obtained for 0.4 ≤ k ≤ 0.6 (Harding and Bryden, 2012). (b) Further, experimental data was available for only these reduced frequencies for given flow conditions. Each case was studied for at least 5 rotation cycles to ensure that there remained no transients due to the starting of rotation. This effect generally subsided after two rotation cycles, as shown in Figure A (1)- (ii).

Figure A (3**)** shows vorticity contour plots of flow for k = 0.54 when foils are separated by 3c. Clockwise vorticity is shed downstream into flow when the foil pitches down, while counterclockwise vorticity for pitch-up motion. Vorticity of opposite sense is, thus, shed during each half-cycle. It is also evident from (ii) that the vorticity starts decaying after x/c =5. Figure A (3)-(ii) further shows the shearless (i.e. irrotational flow) region marked by two horizontal black lines from -0.6c to 0.6c in y-direction, thus indicating a vorticity free region of 1.2c.

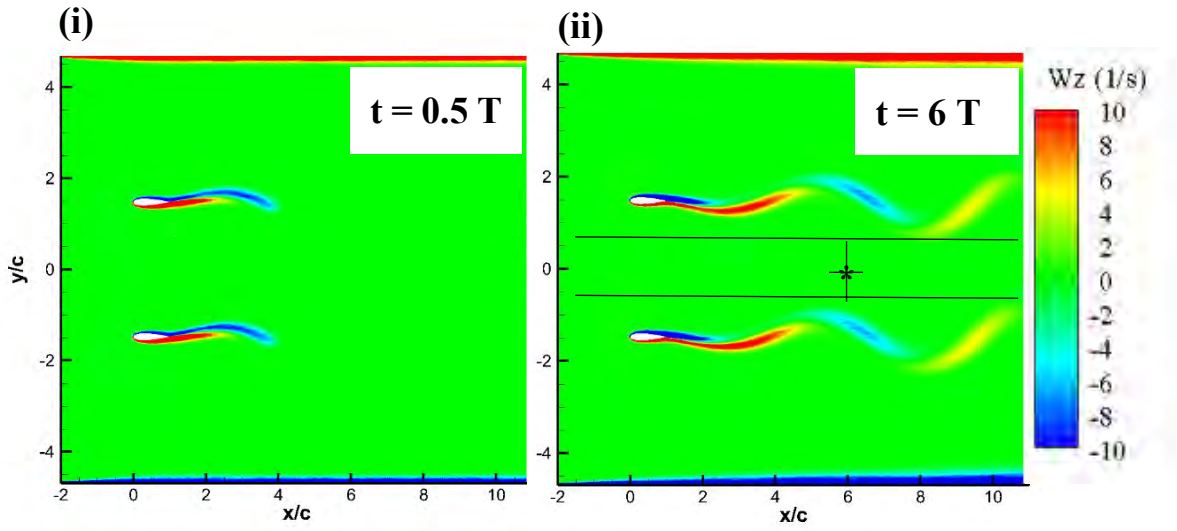

Figure A (3): Vorticity contour in X – Y plane for k= 0.54 and at foils separation of 3c. X and Y are normalized with foil chord length. Vorticity shedding at t = 0.5T (i) and t=6T (ii), where T is time period of foil pitching. Vorticity decays as it moves downstream of the foils. A pair of horizontal black line in (ii) indicates the irrotational region, while the vertical line denotes X_0 =6c and * point on centerline where induced velocity and hence, gust intensity was calculated.

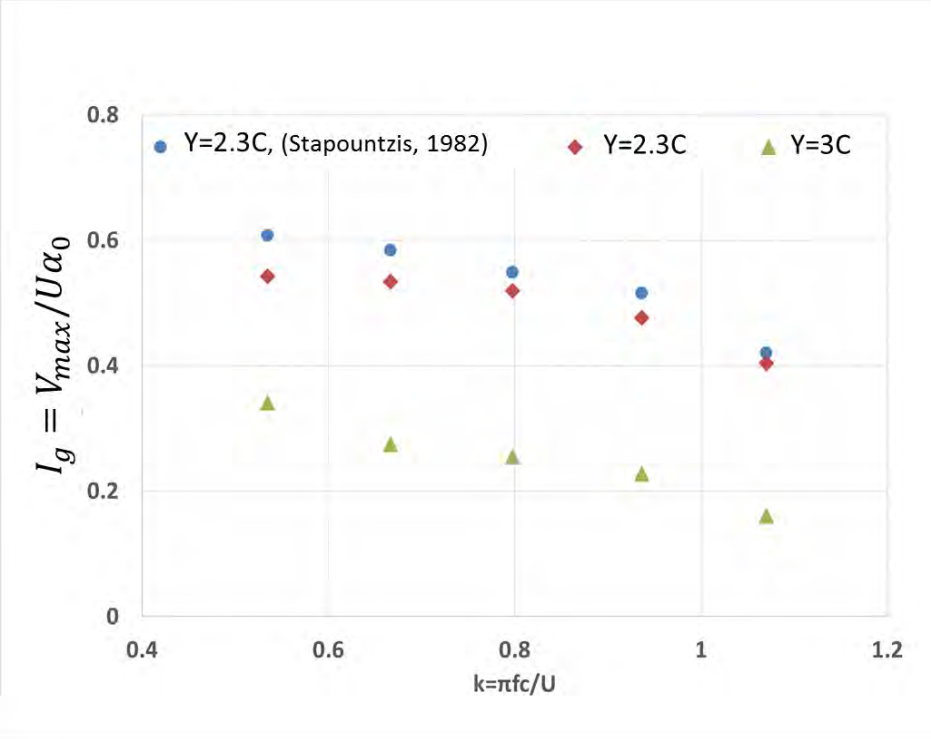

Figure A (4): Gust intensity (Ig) for a range of reduced frequencies (k), for Y = 2.3C and 3c. The computed data for Y= 2.3c matches reasonably well with experimental data (Stapountzis 1982) for Re = 1.6 x 10^5. Ig reduces with an increase in k and Y.

We define gust intensity as the maximum transverse velocity (V_{max}) divided by the product of mean flow (U) and maximum pitching angle (α_0), given by

$$I_g = \frac{V_{max}}{U\alpha_0}$$

Figure A (4) shows gust intensity for different reduced frequencies and for two different foil separation Y= 2.3c and 3c calculated at X_0 = 6c. The reasons for choosing this downstream distance for calculation of gust intensity are (a) the effect of bound circulation over foils becomes minimal after X_0=5c and (b) the shed vorticities decay rapidly after X_0 = 10c (Stapountzis 1982).

Results show that the gust intensity computed for Y=2.3c agrees reasonably well with experimental data reported by (Stapountzis 1982)for identical flow conditions with maximum error 15 % at k=0.54 as seen in Figure A (4). The error reduces to 2% at higher k. Also, unexpectedly, the gust intensity reduces with an increase in reduced frequency. The shed vortices take some time to fully develop. With an increase in reduced frequency, the formation of fully developed vortices is hindered, as there is less time for them to develop and hence, the circulation induced due to the vortices may also reduce. The reduction in circulation may be

the reason for the decrease in gust intensity with increasing reduced frequency (Harding & Bryden 2012).

Figure A (4**)** further shows that gust intensity reduces with an increase in spacing between the foils. For Y=3c, the gust intensity reduces by (40 – 60) % compared to that for Y= 2.3c. This reduction in gust intensity can be explained using Biot-Savart law, according to which, the velocity induced by a vortex at any point in its neighborhood reduces as the radial distance between the vortex and the point increases. An increase in spacing between foils causes the radial distance of vortex from any centerline point to increase and hence, decrease in induced velocity.

One of the main limitations of this technique of gust generation is low gust intensity ($Ig \leq 0.6$). The maximum transverse velocity corresponds to approximately 7% of the mean flow velocity, which may not be enough to simulate the gust an aircraft or MAV may experience in a natural environment.

Trailing edge jet

The gust intensity can be enhanced by increasing mean flow Re, number of pitching foils (Saddington et al. 2015; Buell 1970) rotation angle and/or pitching frequency. Each enhancement technique, however, comes with its own limitation – deviations from intended flow conditions for high Re, high cost and loss of smooth flow region for a large number of foils, flow separation for high rotation angle and maximum gust intensity for only a range of pitching frequency, after which it starts decreasing (Harding & Bryden 2012; Stapountzis 1982). The results discussed above in Figure A (4), however, shows that gust intensity decreases monotonically with k, because of the range of k ($1.2 > k > 0.5$) considered here.

Considering the limitations of each enhancement technique, we, here, propose a new method for gust enhancement. A momentum deficit region is formed behind the foils. The deficit region may be the reason for low gust intensity. Introducing an external jet into the mean flow increases mass flux and momentum into the flow, and hence, diminish the momentum deficit region behind the foil. This additional mass and momentum flux may also strengthen the vorticity shed from the foils and thus, enhance the gust intensity compared to that obtained using the conventional technique discussed above. With this hypothesis, we enforce a high-speed external continuous jet at the exit of the trailing edge of the pitching foils. Due to the inherent flow entrainment property of a jet, we further conjectured that usage of trailing jet would increase the smooth irrotational region between the pitching foils.

The numerical geometry and grid generation details are the same as explained in section ***Method***, except the longitudinal length of the domain was increased from 10c to 14c and the

number of grid nodes was increased to 5.4 x 10^5 to satisfy spatial grid convergence. The time-step was kept the same (0.2 ms) as that for the case without trailing jet. The results discussed here are considered only after verifying spatial and temporal grid convergence (not shown here).

To enforce jet at trailing edge (TE) of the foils, we first introduce a slit source at mid-chord point of the foils, as shown in Figure A (5)-(i). TE was cut in a plane perpendicular to the chord line. The area of the source and TE cut were chosen such that the jet velocity was three times the mean flow velocity at TE exit as shown in Figure A (5)-(ii). This magnitude of jet velocity was used as the starting case for the present study.

Velocity inlet boundary condition was used on the face of source facing TE, as shown by arrows on the corresponding face in Figure A (5)-(i), while on all other faces , no-slip boundary condition was enforced. The main reason for introducing the source, rather than using velocity inlet condition directly at TE cut was to simulate the real experimental condition where the mass will be added inside the foil by rotating source fixed to it at mid-chord point.

All other boundary conditions were kept the same as explained above in section ***Boundary conditions.***

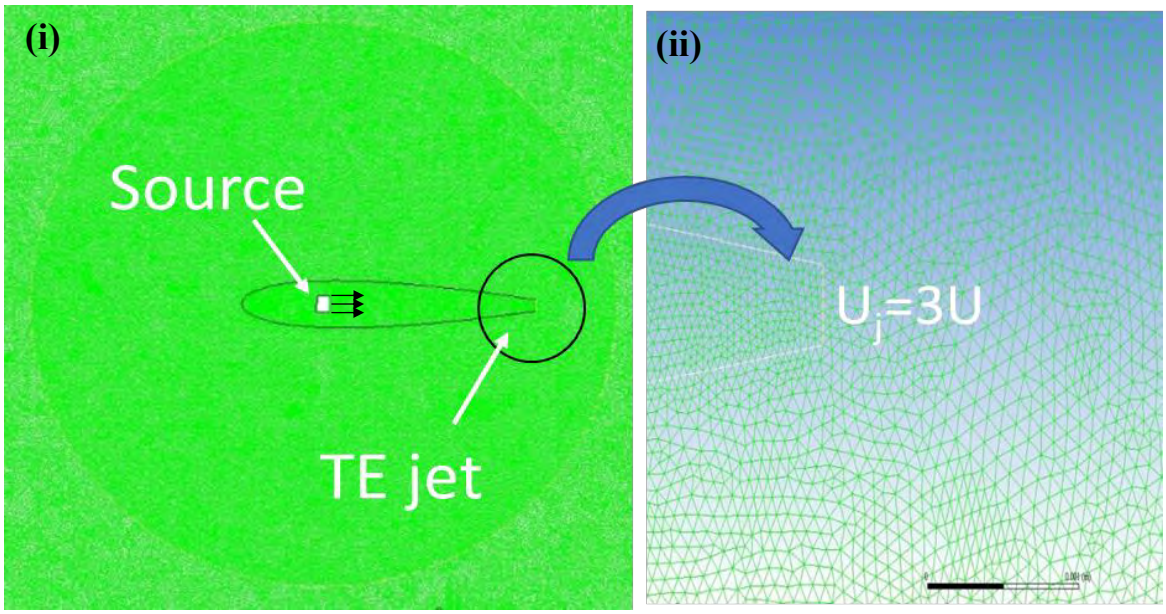

Figure A (5): Jet introduction at trailing edge (TE) of foil. U_j is jet velocity at TE. (i) A source of mass flow is placed at mid-chord point and TE is cut normal to the chord line. Arrows on source show that air was ejected into airfoil through that face only, and all other faces were treated as wall. The area of the source and TE cut is selected such that velocity at jet is 3-times mean flow velocity (ii).

Figure A (6) shows a comparison of instantaneous transverse velocity for cases with and with jet at foils spacing of 3c and k=.54. The maximum velocity with the jet is at least twice as higher as that without the jet. Also, a distinct phase difference exists between the induced transverse velocity for the cases with and without jet, the latter leading the former. Such observation was noted in all cases. It is evident that the introduction of jet is the cause for this phase difference, but understanding the flow physics requires further study.

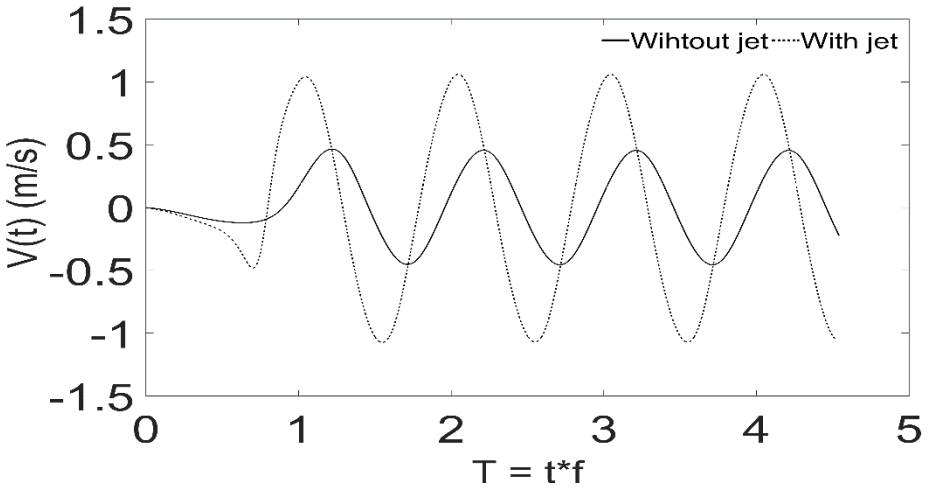

Figure A (6): Transverse velocity comparison with and without jet for k=0.54 at foils spacing of 3c. Maximum velocity with jet is higher than that without jet by more than 2 times.

Figure A (7) shows vorticity contour in X-Y plane at two time instances (T = 0.5 and T = 6) for k = 0.54 and foils spacing 3c. Formation of staring vortex can be seen as a blob of fluid in Figure A (7)-(i). Similarly, two layers of vorticity forms dur to jet addition and the strength of the vortex starts decaying 8c downstream of foils (see Figure A (7)-(ii)), in contrast to that observed for the case without jet (i.e. after x/c = 5) (see Figure A (3)-(ii)). Also, the strength of vorticity at any spatial location is higher in case of flow with the jet, as compared to that without jet as shown in Figure A (3)-(ii).

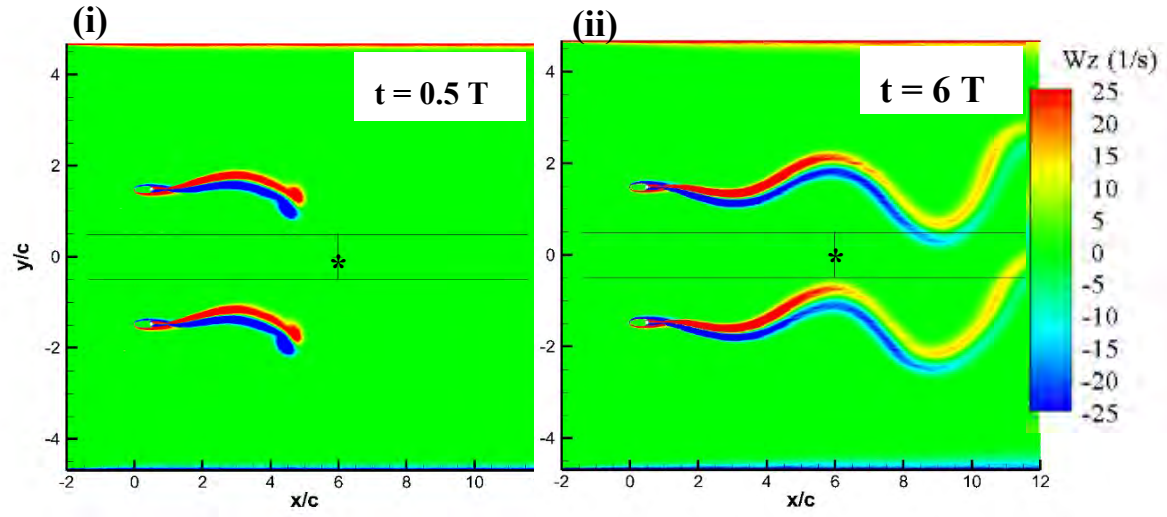

Figure A (7): Vorticity contour in X – Y plane for k= 0.54 and at foils separation of 3c. X and Y are normalized with foil chord length. Vorticity shedding at t = 0.5T (i) and t=6T (ii), where T is time period of foil pitching. A pair of horizontal black line in (ii) indicates the irrotational region, while vertical line denotes X_0 =6c and * point on centerline where induced velocity and hence, gust intensity was calculated.

This implies that the addition of a trailing jet indeed serves to increase the circulation shed by the foils. The region of smooth flow, however, to our surprise, gets confined to 0.5c above and below the centerline (total 1c) (see Figure A (7)-(ii)), which is 20% lower compared to that without jet as shown in Figure A (3)- (ii). Considering the entrainment property of jet, reduction in the smooth flow region isn't expected. The smooth region between the foils should have instead increased.

Figure A (8) shows the comparison of gust intensity for the cases with and without jet for two different foils spacing. For each spacing, the gust intensity increases linearly with an increase in reduced frequency, in contrast to that without jet (see Figure A (4)). The increase in gust intensity is higher for lower foil spacing at a higher reduced frequency, while at a lower reduced frequency, large spacing dominates the gust generation. The gust intensity increases by 2-7 times for foils spacing 2.3c, and by 5.5 times for foils spacing of 3c.

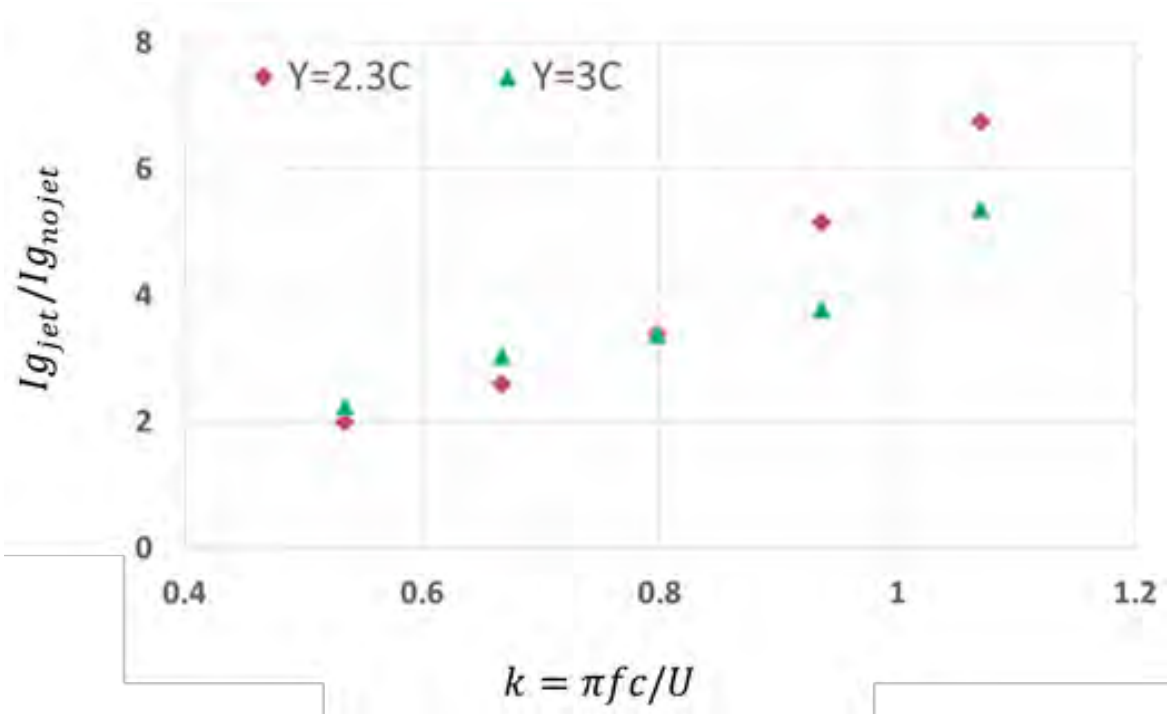

Figure A (8): Comparison of gust intensity with and without TE jet. Ig_{jet} and Ig_{nojet} denote gust intensity with and without TE jet respectively. Y is the spacing between foils. Gust intensity with jet increases by 2-7 times compared to that without jet for both cases Y=2.3c and 3c. Increase in gust intensity is higher for Y=2.3c than Y=3c at k ≥0.8, and lower at other cases.

Conclusion

We carried out a numerical simulation of a pair of sinusoidally pitching two dimensional thin foils to generate a sinusoidal gust in the region behind and between the foils. The pitching motion of the foils was simulated using sliding mesh technique and employing a UDF that specifies rotational motion – type, maximum rotation angle, and rotation frequency. A transient pressure-based realizable k-ε turbulence model was used to solve the flow.

The flow was simulated at Re=1.6 x 10^5 for maximum rotation angle 6.9° and a range of reduced frequencies ($0.54 \leq k \leq 1.2$). Results show that a pair of pitching foils can be useful to generate a shearless and irrotational gust. The maximum gust that can be generated by this technique is, however, limited to (5-7) % of the mean flow.

To enhance gust intensity, we propose a new method using a ***jet*** at the trailing edge of each of the pitching foils. The hypothesis is that the jet diminishes the momentum deficit behind the foil and thus would enhance the gust intensity. Compared to the case without jet, it is observed that, for identical flow conditions, (a) gust intensity increases linearly with reduced frequency

(for the range studied here), (b) gust intensity is higher for higher foils spacing only at higher reduced frequency ($k \geq 0.8$) and (c) gust intensity increases by $2-7$ times. Besides generating higher gust intensity, the proposed technique, unlike other conventional gust enhancement methods, ensures a smooth flow region in between the pitching foils and provides a simple, economical and controlled way to study gust response of MAVs and aircraft in wind tunnels.

Appendix B: Miscellaneous

B1. LabVIEW code to generate analog voltage output

The program given below accepts the digital input signal (i.e. trapezoidal) from a computer, generates, stores in volatile memory of DAQ and convert it into analog form. The analog signal is then fed to the gust generator.

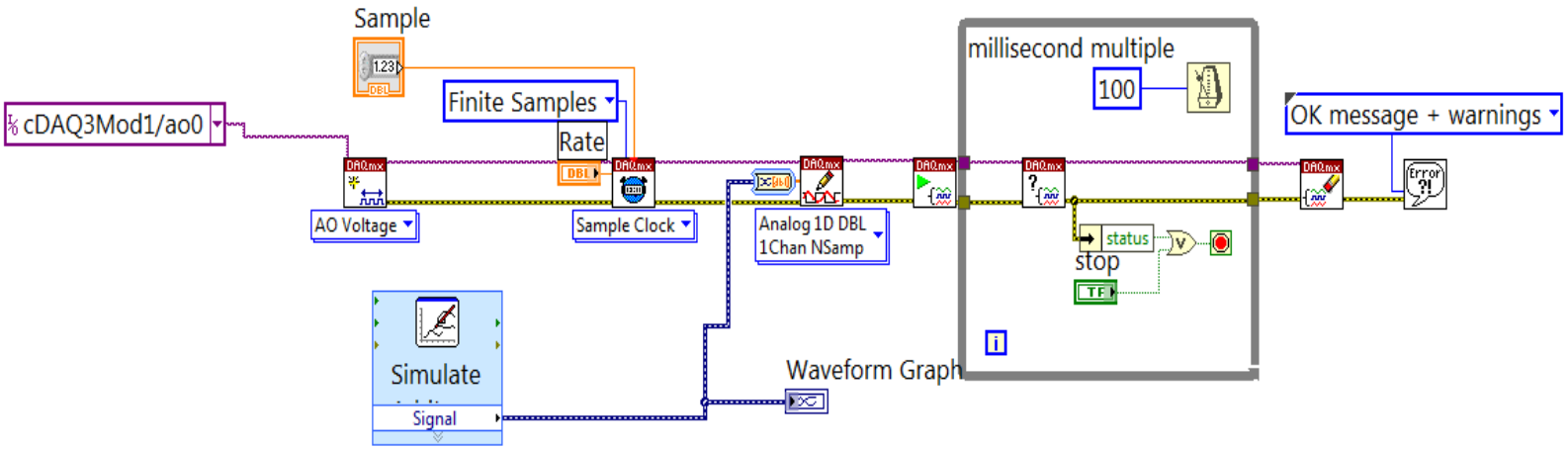

Program to generate analog output

B2. LabVIEW code to trigger the analog output

The program below is a modified form of that given in A1. This program, besides taking digital signal as input and converting it into analog form, also produces a TTL signal using NI-c 9401. The signal acts to trigger the analog output module- Ni-c9263.

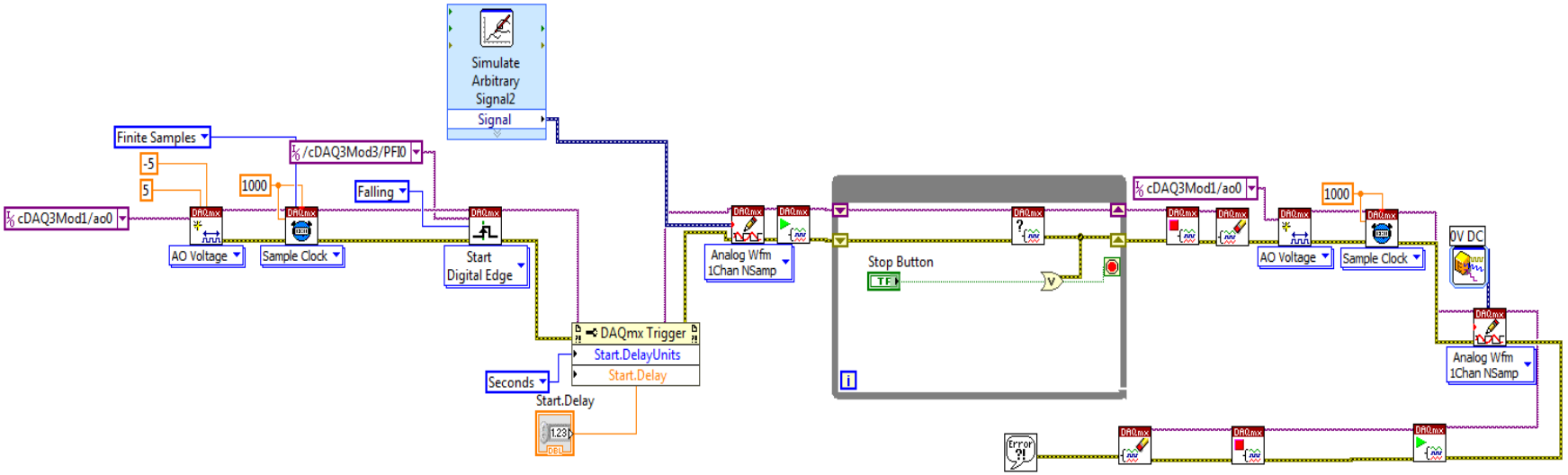

Program to trigger gust generator

B3. Electronic circuit for Linear Amplifier

The signal generated by DAQ is not sufficient to drive the diaphragm of the speaker by the required amount. An in-house DC amplifier was built using commercially available OPA 548T and using electrical components like resistors and capacitors. The circuit diagram is given below.

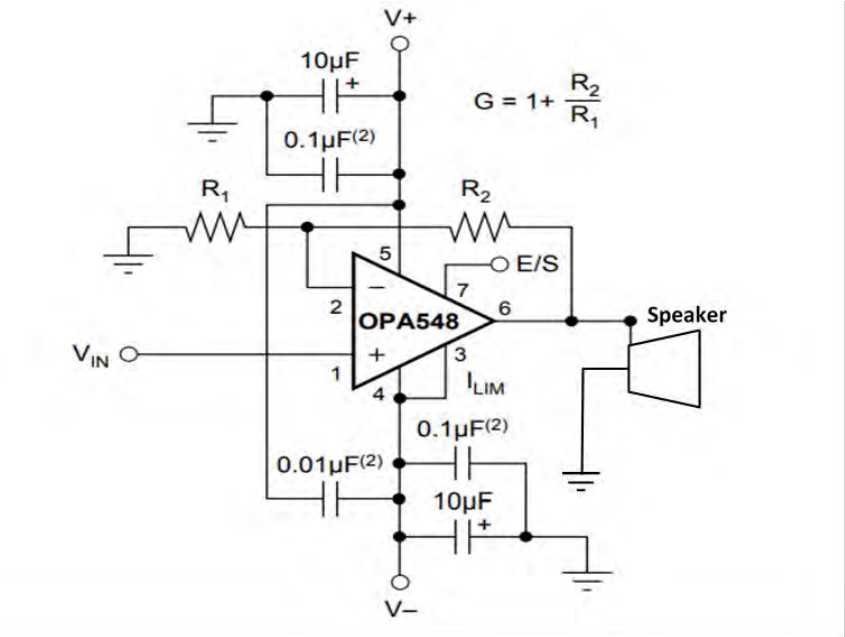

Linear Amplifier

(www.ti.com/general/docs/suppproductinfo.tsp?distId=26&gotoUrl=http%3A%2F%2Fwww.ti.com%2Flit%2Fgpn%2Fopa548)

B4. Electronic circuit for IR motion sensor

The success of perturbing the insect with a gust lies in triggering the gust generator and camera system. Manual triggering is not possible on a short time scale (< 5 ms) when the insect is in the region of interest. To overcome this difficulty, an in-house infrared (IR) motion detector as shown below was used.

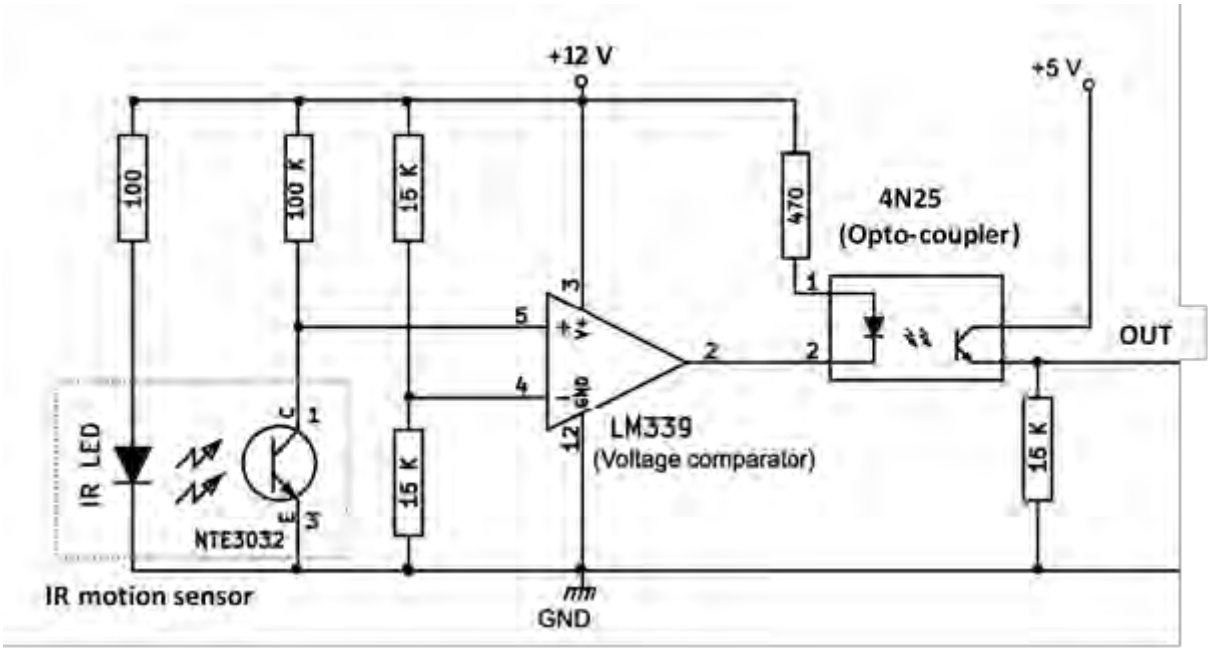

IR motion detector

B5. MATLAB code to calculate body angles and wing stroke of insect

This code was used to calculate body angles - roll, pitch and yaw, and wing angles - stroke and deviation angles. The global coordinate system was first converted into body fixed axis system, beginning with a right-handed yaw rotation, followed by pitch and roll rotation about global axis.

```
function wingAngles = calculatestrokeangle(xyz)

%

% Original code by Ty Hedrick

% Modified by Dinesh Nateshan

% Further modification by Dipendra Gupta

% constants

rwt=4; % right wing tip point #

rwb=2; % right wing base point #

head=1; % head point #

lwb=3; % left wing base point #

lwt=5; % left wing tip point #

% Get CoM

CoM= (xyz(:,rwb*3-2:rwb*3)+xyz(:,lwb*3-2:lwb*3))*(1/2); %xyz(:,head*3-2:head*3)+(1/3)*(xyz(:,abdo*3-2:abdo*3)-xyz(:,head*3-2:head*3))

xyzC=xyz-repmat(CoM,1,size(xyz,2)/3);

% compute roll from the two wing bases (attempt to equalize them at some -Z

% value by rotating about an axis passing through the CoM and head)

headpt=xyzC(:,3*head-2:3*head);

rwbpt=xyzC(:,3*rwb-2:3*rwb);

lwbpt=xyzC(:,3*lwb-2:3*lwb);

headproj=[xyzC(:,3*head-2:3*head-1),xyzC(:,3*head)*0];
```

```
pitchax=headproj*[0 1 0;-1 0 0; 0 0 1];
for i=1:size(headpt,1)
x2=headpt(i,1);
x1=0;
x3=pitchax(i,1);
y2=headpt(i,2);
y1=0;
y3=pitchax(i,2);
z2=headpt(i,3);
z1=0;
z3=pitchax(i,3);
A=det([1 y1 z1;1 y2 z2;1 y3 z3]);
B=det([x1 1 z1;x2 1 z2;x3 1 z3]);
C=det([x1 y1 1;x2 y2 1;x3 y3 1]);
D=-det([x1 y1 z1;x2 y2 z2;x3 y3 z3]);
X=rwbpt(i,:);
perp=(A*X(1)+B*X(2)+C*X(3)+D)/sqrt(A*A+B*B+C*C);
hyp=sqrt((X(1))^2+(X(2))^2+(X(3))^2);
roll(i,1)=asin(perp/hyp);
signa=sign(perp/hyp);
signb=sign(dot(X,pitchax(i,:)));
if signb<0
   if signa>0
      roll(i,1)=pi-roll(i,1);
   elseif signa<0
      roll(i,1)=-pi-roll(i,1);
   end
```

```
end
hyp=sqrt(headpt(i,1)*headpt(i,1)+headpt(i,2)*headpt(i,2)+headpt(i,3)*headpt(i,3));
perp=-headpt(i,3);
pitch(i,1)=asin(perp/hyp);
yaw(i,1)=atan2(headproj(i,2),headproj(i,1));
[Hib,~] = aeroROTM(roll(i,1),pitch(i,1),yaw(i,1));
for j=1:5
   xyzRPY(i,3*j-2:3*j)=applyAeroRotationMatrix(xyzC(i,3*j-2:3*j),Hib);
end
end
% create output variables
ypr=[yaw,pitch,roll];
xyzBRF=xyzRPY;
% Right wing
% Calculate deviation angle and stroke angle
tip=xyzBRF(:,rwt*3-2:rwt*3)-xyzBRF(:,rwb*3-2:rwb*3);
ePhi=acos(dot(tip(:,1:3),[tip(:,1:2),tip(:,3)*0],2)./(rnorm(tip(:,1:3)).*rnorm([tip(:,1:2),tip(:,3)*
0])));
idx=find(tip(:,3)>0);
ePhi(idx)=ePhi(idx)*-1;
eTheta=acos(dot(repmat([0,1,0],size(tip,1),1),[tip(:,1:2),tip(:,3)*0],2)./rnorm([tip(:,1:2),tip(:,3
)*0]));
idx=find(tip(:,1)<0);
eTheta(idx)=eTheta(idx)*-1;
% store the estimates
wingAngles(:,1,2)=ePhi;      % Deviation angle
wingAngles(:,2,2)=eTheta;    % Stroke angle.
% Left wing
```

```
% Calculate deviation angle and stroke angle

tip=xyzBRF(:,lwt*3-2:lwt*3)-xyzBRF(:,lwb*3-2:lwb*3);

ePhi=acos(dot(tip(:,1:3),[tip(:,1:2),tip(:,3)*0],2)./(rnorm(tip(:,1:3)).*rnorm([tip(:,1:2),tip(:,3)*
0])));

idx=find(tip(:,3)>0);

ePhi(idx)=ePhi(idx)*-1;

eTheta=acos(dot(repmat([0,-
1,0],size(tip,1),1),[tip(:,1:2),tip(:,3)*0],2)./rnorm([tip(:,1:2),tip(:,3)*0]));

idx=find(tip(:,1)<0);

eTheta(idx)=eTheta(idx)*-1;

% store the estimates

wingAngles(:,1,1)=ePhi;  % Deviation angle

wingAngles(:,2,1)=eTheta; % Stroke angle.

end

%%% subfunctions

function [Hib,Hbi] = aeroROTM(roll,pitch,yaw)

%

% This function generates two rotation matrices, Hib & Hbi, from the roll

% pitch & yaw angles.  These matrices are as described in Stengel, section

% 2.2.

% Vb = vector in body space

% Vi = vector in inertial space

%

% Vb = Hib*Vi

% Vi = Hbi*Vb

%

% pitchR=[cos(pitch),0,-sin(pitch);,0,1,0;sin(pitch),0,cos(pitch)];

% rollR=[1,0,0;0,cos(roll),sin(roll);0,-sin(roll),cos(roll)];
```

```
% yawR=[cos(yaw),sin(yaw),0;-sin(yaw),cos(yaw),0;0,0,1];
%
%Hib=yawR*pitchR*rollR;
Hib = [cos(pitch)*cos(yaw), cos(pitch)*sin(yaw), -sin(pitch);
   (-cos(roll)*sin(yaw)+sin(roll)*sin(pitch)*cos(yaw)), ...
   (cos(roll)*cos(yaw)+sin(roll)*sin(pitch)*sin(yaw)), ...
   sin(roll)*cos(pitch);
  (sin(roll)*sin(yaw)+cos(roll)*sin(pitch)*cos(yaw)), ...
  (-sin(roll)*cos(yaw)+cos(roll)*sin(pitch)*sin(yaw)), ...
  cos(roll)*cos(pitch)];
Hbi=inv(Hib);
end


%%%%%%%%%%%%%%%%%%%%%%%%%%%%%%%%%%%%%%%
%%%%%%%%%%%%%%%%%%%%%%%%%%
%applyAeroRotationMatrix
%
function [output]=applyAeroRotationMatrix(input,rotm)
% function [output]=applyAeroRotationMatrix(input,rotm);
%
% Applies a rotation matrix to input where input is a Nx3 matrix with each
% row being a set of [X,Y,Z] coordinates and rotm is a 3x3 rotation matrix.
% The operation is [rotm]*[X;Y;Z]=[X';Y';Z'], with [X';Y';Z'] rotated into
% column form.
%
% This function is vectorized and much faster than applying the rotation
% within a loop and quite a bit neater looking than typing the vectorized
```

```
% bit out repeatedly.
%
% Ty Hedrick
% 06/06/2007
output(:,1)=input(:,1).*rotm(1,1)+input(:,2).*rotm(1,2)+input(:,3).*rotm(1,3);
output(:,2)=input(:,1).*rotm(2,1)+input(:,2).*rotm(2,2)+input(:,3).*rotm(2,3);
output(:,3)=input(:,1).*rotm(3,1)+input(:,2).*rotm(3,2)+input(:,3).*rotm(3,3);
end
function [norms] = rnorm(matrix)
% function [norms] = rnorm(matrix)
%% Description: rnorm returns a column of norm values.  Given an input
%               matrix of X rows and Y columns it returns an X by 1
%               column of norms.
% for i=1:size(matrix,1)
%   norms(i,1)=norm(matrix(i,:));
% end
% possibly a faster method
norms=sqrt(dot(matrix',matrix'))';
end
```

REFERENCES

Allen, J. & Auvity, B., 2002. Interaction of a vortex ring with a piston vortex. *Journal of Fluid Mechanics*, 465, pp.353–378.

Auerbach, D., 1987. Experiments on the trajectory and circulation of the starting vortex. *Journal of Fluid Mechanics*, 183, pp.185–198.

Auerbach, D., 1991. Stirring properties of vortex rings. *Physics of Fluids A: Fluid Dynamics*, 3(5), pp.1351–1355.

Barber, S. & Pringle, J.W.S., 1966. Functional aspects of flight in belostomatid bugs (Heteroptera). *Proceedings of the Royal Society of London. Series B. Biological Sciences*, 164(994), pp.21–39.

Beatus, T., Guckenheimer, J.M. & Cohen, I., 2015. Controlling roll perturbations in fruit flies. *Journal of The Royal Society Interface*, 12(105), p.20150075.

Bomphrey, R.J. et al., 2006. Application of digital particle image velocimetry to insect aerodynamics: measurement of the leading-edge vortex and near wake of a Hawkmoth. *Experiments in Fluids*, 40(4), p.546.

Bomphrey, R.J., Taylor, G.K. & Thomas, A.L., 2010. Smoke visualization of free-flying bumblebees indicates independent leading-edge vortices on each wing pair. In *Animal Locomotion*. Springer, pp. 249–259.

Buell, D.A., 1970. *An experimental investigation of the velocity fluctuations behind oscillating vanes*, National Aeronautics and Space Administration.

Cater, J.E., Soria, J. & Lim, T., 2004. The interaction of the piston vortex with a piston-generated vortex ring. *Journal of Fluid Mechanics*, 499, pp.327–343.

Chin, D.D. & Lentink, D., 2016. Flapping wing aerodynamics: from insects to vertebrates. *Journal of Experimental Biology*, 219(7), pp.920–932.

Combes, S.A. & Dudley, R., 2009. Turbulence-driven instabilities limit insect flight performance. *Proceedings of the National Academy of Sciences*, 106(22), pp.9105–9108.

Crall, J. et al., 2017. Foraging in an unsteady world: bumblebee flight performance in field-realistic turbulence. *Interface focus*, 7(1), p.20160086.

Das, D., Bansal, M. & Manghnani, A., 2017. Generation and characteristics of vortex rings free of piston vortex and stopping vortex effects. *Journal of Fluid Mechanics*, 811, pp.138–167.

Deora, T., Gundiah, N. & Sane, S.P., 2017. Mechanics of the thorax in flies. *Journal of Experimental Biology*, 220(8), pp.1382–1395.

Deora, T., Singh, A.K. & Sane, S.P., 2015. Biomechanical basis of wing and haltere coordination in flies. *Proceedings of the National Academy of Sciences*, 112(5), pp.1481–1486.

Deshpande, P. et al., 2014. Experimental investigation of periodic wind gust generated in a low speed wind tunnel. In *32nd AIAA Applied Aerodynamics Conference*. p. 2306.

Dickerson, B.H., Aldworth, Z.N. & Daniel, T.L., 2014. Control of moth flight posture is mediated by wing mechanosensory feedback. *Journal of Experimental Biology*, 217(13), pp.2301–2308.

Dickinson, M.H. & Gotz, K.G., 1993. Unsteady aerodynamic performance of model wings at low Reynolds numbers. *Journal of Experimental Biology*, 174(1), pp.45–64.

Dickinson, M.H., Lehmann, F.-O. & Sane, S.P., 1999. Wing rotation and the aerodynamic basis of insect flight. *Science*, 284(5422), pp.1954–1960.

Dickinson, M.H. & Muijres, F.T., 2016. The aerodynamics and control of free flight manoeuvres in Drosophila. *Philosophical Transactions of the Royal Society B: Biological Sciences*, 371(1704), p.20150388.

Dickinson, M.H. & Tu, M.S., 1997. The function of dipteran flight muscle. *Comparative Biochemistry and Physiology Part A: Physiology*, 116(3), pp.223–238.

Didden, N., 1979. On the formation of vortex rings: rolling-up and production of circulation. *Zeitschrift für angewandte Mathematik und Physik ZAMP*, 30(1), pp.101–116.

Ellington, C.P. et al., 1996. Leading-edge vortices in insect flight. *Nature*, 384(6610), p.626.

Ellington, C.P., 1984. The aerodynamics of hovering insect flight. I. The quasi-steady analysis. *Philosophical Transactions of the Royal Society of London. B, Biological Sciences*, 305(1122), pp.1–15.

Engels, T. et al., 2016. Bumblebee flight in heavy turbulence. *Physical review letters*, 116(2), p.028103.

Engels, T. et al., 2019. Impact of turbulence on flying insects in tethered and free flight: High-resolution numerical experiments. *Physical Review Fluids*, 4(1), p.013103.

Etkin, B., 1981. Turbulent wind and its effect on flight. *Journal of Aircraft*, 18(5), pp.327–345.

Fuchiwaki, M. et al., 2013. Dynamic behavior of the vortex ring formed on a butterfly wing. *Experiments in fluids*, 54(1), p.1450.

Gharib, M., Rambod, E. & Shariff, K., 1998. A universal time scale for vortex ring formation. *Journal of Fluid Mechanics*, 360, pp.121–140.

Glezer, A., 1988. The formation of vortex rings. *The Physics of fluids*, 31(12), pp.3532–3542.

Glezer, A. & Coles, D., 1990. An experimental study of a turbulent vortex ring. *Journal of Fluid Mechanics*, 211, pp.243–283.

Grasmeyer, J.M., Keennon, M.T. & others, 2001. Development of the black widow micro air vehicle. *AIAA paper*, 127.

Harding, S. & Bryden, I., 2012. Generating controllable velocity fluctuations using twin oscillating hydrofoils. *Journal of Fluid Mechanics*, 713, pp.150–158.

Hartley, R. & Zisserman, A., 2004. *Multiple view geometry in computer vision* 2nd edition., Cambridge university press.

Hedenström, A., 2014. How insect flight steering muscles work. *PLoS biology*, 12(3), p.e1001822.

Hedrick, T.L., 2008. Software techniques for two-and three-dimensional kinematic measurements of biological and biomimetic systems. *Bioinspiration & biomimetics*, 3(3), p.034001.

Hill, R.W., Wyse, G.A. & Anderson, M., 2012. *Animal physiology*, Sinauer Associates Sunderland, MA.

Irdmusa, J. & Garris, C., 1987. Influence of initial and boundary conditions on vortex ring development. *AIAA journal*, 25(3), pp.371–372.

Jafferis, N.T. et al., 2019. Untethered flight of an insect-sized flapping-wing microscale aerial vehicle. *Nature*, 570(7762), p.491.

Jakobi, T. et al., 2018. Bees with attitude: the effects of directed gusts on flight trajectories. *Biology open*, 7(10), p.bio034074.

Klipp, C.L. & Measure, E., 2011. *Urban turbulence and wind gusts for micro air vehicle bio-inspired designs*, ARMY RESEARCH LAB ADELPHI MD COMPUTATIONAL AND INFORMATION SCIENCES DIRECTORATE.

Kumar, M., Arakeri, J. & Shankar, P., 1995. Translational velocity oscillations of piston generated vortex rings. *Physics of Fluids*, 7(11), pp.2751–2756.

Lehmann, F.-O., 2004. The mechanisms of lift enhancement in insect flight. *Naturwissenschaften*, 91(3), pp.101–122.

Lentink, D. & Dickinson, M.H., 2009. Rotational accelerations stabilize leading edge vortices on revolving fly wings. *Journal of Experimental Biology*, 212(16), pp.2705–2719.

Lim, T. & Nickels, T., 1995. Vortex rings. In *Fluid vortices*. Springer, pp. 95–153.

Loxton, B., 2011. An experimental investigation into the effects of atmospheric turbulence on the aerodynamics of micro air vehicle wings.

Maxworthy, T., 1977. Some experimental studies of vortex rings. *Journal of Fluid Mechanics*, 81(3), pp.465–495.

Maxworthy, T., 2007. The formation and maintenance of a leading-edge vortex during the forward motion of an animal wing. *Journal of Fluid Mechanics*, 587, pp.471–475.

Maxworthy, T., 1974. Turbulent vortex rings. *Journal of Fluid Mechanics*, 64(2), pp.227–240.

Ortega-Jimenez, V.M. et al., 2013. Hawkmoth flight stability in turbulent vortex streets. *Journal of Experimental Biology*, 216(24), pp.4567–4579.

Ortega-Jimenez, V.M., Mittal, R. & Hedrick, T.L., 2014. Hawkmoth flight performance in tornado-like whirlwind vortices. *Bioinspiration & biomimetics*, 9(2), p.025003.

Osborne, M., 1951. Aerodynamics of flapping flight with application to insects. *Journal of Experimental Biology*, 28(2), pp.221–245.

Pornsin-Sirirak, T.N. et al., 2001. Microbat: A palm-sized electrically powered ornithopter. In *Proceedings of NASA/JPL Workshop on Biomorphic Robotics*. pp. 14–17.

Pratt, B. et al., 2017. Neural evidence supports a dual sensory-motor role for insect wings. *Proceedings of the Royal Society B: Biological Sciences*, 284(1862), p.20170969.

Pringle, J.W.S., 1948. The gyroscopic mechanism of the halteres of Diptera. *Philosophical Transactions of the Royal Society of London. Series B, Biological Sciences*, 233(602), pp.347–384.

Pullin, D. & Perry, A., 1980. Some flow visualization experiments on the starting vortex. *Journal of Fluid Mechanics*, 97(2), pp.239–255.

Ravi, S. et al., 2016. Bumblebees minimize control challenges by combining active and passive modes in unsteady winds. *Scientific reports*, 6, p.35043.

Ravi, S. et al., 2013. Rolling with the flow: bumblebees flying in unsteady wakes. *Journal of Experimental Biology*, 216(22), pp.4299–4309.

Ristroph, L. et al., 2013. Active and passive stabilization of body pitch in insect flight. *Journal of The Royal Society Interface*, 10(85), p.20130237.

Ristroph, L. et al., 2010. Discovering the flight autostabilizer of fruit flies by inducing aerial stumbles. *Proceedings of the National Academy of Sciences*, 107(11), pp.4820–4824.

Roadman, J. & Mohseni, K., 2009. Gust characterization and generation for wind tunnel testing of micro aerial vehicles. In *47th AIAA aerospace sciences meeting including the new horizons forum and aerospace exposition*. p. 1290.

Saddington, A., Finnis, M. & Knowles, K., 2015. The characterisation of a gust generator for aerodynamic testing. *Proceedings of the Institution of Mechanical Engineers, Part G: Journal of Aerospace Engineering*, 229(7), pp.1214–1225.

Sane, S., 2003. The aerodynamics of insect flight. *Journal of experimental biology*, 206(23), pp.4191–4208.

Sane, S.P. et al., 2007. Antennal mechanosensors mediate flight control in moths. *science*, 315(5813), pp.863–866.

Sane, S.P. & Dickinson, M.H., 2002. The aerodynamic effects of wing rotation and a revised quasi-steady model of flapping flight. *Journal of experimental biology*, 205(8), pp.1087–1096.

Sane, S.P. & Dickinson, M.H., 2001. The control of flight force by a flapping wing: lift and drag production. *Journal of experimental biology*, 204(15), pp.2607–2626.

Sant, H.H. & Sane, S.P., 2018. The mechanosensory-motor apparatus of antennae in the Oleander hawk moth (Daphnis nerii, Lepidoptera). *Journal of Comparative Neurology*, 526(14), pp.2215–2230.

Schnepf, S., 2000. Micro air vehicles- The new military capability. In *AHS International, Annual Forum, 56 th, Virginia Beach, VA*. pp. 1028–1031.

Shariff, K. & Leonard, A., 1992. Vortex rings. *Annual Review of Fluid Mechanics*, 24(1), pp.235–279.

Sheppard, D.C. et al., 2002. Rearing methods for the black soldier fly (Diptera: Stratiomyidae). *Journal of Medical Entomology*, 39(4), pp.695–698.

Sherman, A. & Dickinson, M.H., 2003. A comparison of visual and haltere-mediated equilibrium reflexes in the fruit fly Drosophila melanogaster. *Journal of Experimental Biology*, 206(2), pp.295–302.

Smith, D.S., 1983. 100 Hz remains upper limit of synchronous muscle contraction—an anomaly resolved. *Nature*, 303(5917), pp.539–540.

Sotavalta, O., 1953. Recordings of high wing-stroke and thoracic vibration frequency in some midges. *The Biological Bulletin*, 104(3), pp.439–444.

Stapountzis, H., 1982. An oscillating rig for the generation of sinusoidal flows. *Journal of Physics E: Scientific Instruments*, 15(11), p.1173.

Stull, R.B., 2012. *An introduction to boundary layer meteorology*, Springer Science & Business Media.

Sullivan, I.S. et al., 2008. Dynamics of thin vortex rings. *Journal of Fluid Mechanics*, 609, pp.319–347.

Syme, D.A. & Josephson, R.K., 2002. How to build fast muscles: synchronous and asynchronous designs. *Integrative and comparative biology*, 42(4), pp.762–770.

Taylor, G. & Thomas, A., 2002. Animal flight dynamics II. Longitudinal stability in flapping flight. *Journal of theoretical biology*, 214(3), pp.351–370.

Taylor, G.K., 2001. Mechanics and aerodynamics of insect flight control. *Biological Reviews*, 76(4), pp.449–471.

Tennekes, H. & Pennycuick, C., 1996. The simple science of flight: from insects to jumbo jets. *Nature*, 381(6578), pp.126–126.

Theriault, D.H. et al., 2014. A protocol and calibration method for accurate multi-camera field videography. *Journal of Experimental Biology*, 217(11), pp.1843–1848.

Vance, J., Faruque, I. & Humbert, J., 2013. Kinematic strategies for mitigating gust perturbations in insects. *Bioinspiration & biomimetics*, 8(1), p.016004.

Wang, Z.J., 2005. Dissecting insect flight. *Annu. Rev. Fluid Mech.*, 37, pp.183–210.

Watkins, S. et al., 2006. Atmospheric winds and their implications for microair vehicles. *AIAA journal*, 44(11), pp.2591–2600.

Watkins, S. et al., 2010. On low altitude flight through the atmospheric boundary layer. *International Journal of Micro Air Vehicles*, 2(2), pp.55–68.

Watkins, S. et al., 2008. Wind-Tunnel Replication of Atmospheric Turbulence with an Emphasis on MAVs. In *46th AIAA Aerospace Sciences Meeting and Exhibit*. p. 228.

Weigand, A. & Gharib, M., 1997. On the evolution of laminar vortex rings. *Experiments in Fluids*, 22(6), p.447.

Weis-Fogh, T., 1973. Quick estimates of flight fitness in hovering animals, including novel mechanisms for lift production. *Journal of experimental Biology*, 59(1), pp.169–230.